FOSSIL ENERGY

DOE/BC/14938-12
(OSTI ID: 5127)

ADVANCED RESERVOIR CHARACTERIZATION IN THE ANTELOPE SHALE TO ESTABLISH THE VIABILITY OF CO_2 ENHANCED OIL RECOVERY IN CALIFORNIA'S MONTEREY FORMATION SILICEOUS SHALES

Annual Technical Progress Report
February 7, 1998 – February 6, 1999

By
Michael F. Morea

April 1999

Work Performed Under Contract No. DE-FC22-95BC14938

Chevron USA Production Company
Bakersfield, California

National Petroleum Technology Office
U. S. DEPARTMENT OF ENERGY
Tulsa, Oklahoma

DISCLAIMER

This report was prepared as an account of work sponsored by an agency of the United States Government. Neither the United States Government nor any agency thereof, nor any of their employees, makes any warranty, expressed or implied, or assumes any legal liability or responsibility for the accuracy, completeness, or usefulness of any information, apparatus, product, or process disclosed, or represents that its use would not infringe privately owned rights. Reference herein to any specific commercial product, process, or service by trade name, trademark, manufacturer, or otherwise does not necessarily constitute or imply its endorsement, recommendation, or favoring by the United States Government or any agency thereof. The views and opinions of authors expressed herein do not necessarily state or reflect those of the United States Government.

This report has been reproduced directly from the best available copy.

Available to DOE and DOE contractors from the Office of Scientific and Technical Information, P.O. Box 62, Oak Ridge, TN 37831; prices available from (615) 576-8401.

Available to the public from the National Technical Information Service, U.S. Department of Commerce, 5285 Port Royal Rd., Springfield, VA 22161

DOE/BC/14938-12
Distribution Category UC-122

Advanced Reservoir Characterization in the Antelope Shale to Establish the Viability of CO_2 Enhanced Oil Recovery in California's Monterey Formation Siliceous Shales

By
Michael F. Morea

April 1999

Work Performed Under Contract DE-FC22-95BC14938

Prepared for
U.S. Department of Energy
Assistant Secretary for Fossil Energy

Gary D. Walker, Project Manager
National Petroleum Technology Office
P.O. Box 3628
Tulsa, OK 74101

Prepared by
Chevron USA Production Company
5001 California Avenue
Bakersfield, CA 93309

CONTENTS

List of Tables iv
List of Figures vi
Abstract xi
Executive Summary xiii
Acknowledgements xvii
SECTION 1. Buena Vista Hills Technical Progress 1
  1.1 Buena Vista Hills Project Overview 2
  1.2 Mineralogical and Chemical Composition of Chert, Shale, and Mud-Filled Veins, Antelope Shale, 653Z-26B Well 12
  1.3 Core Analysis & Rock Properties: Estimating Initial Oil Saturation in the Antelope Shale 34
  1.4 Well Logging Summary 72
  1.5 3D Earth Model 93
  1.6 Fluid Characterization and Laboratory Displacement 110
  1.7 Flow Simulation 119
  1.8 653Z-26B Hydraulic Fracturing 126
  1.9 Surface and Downhole Tiltmeter Fracture Mapping, 653Z-26B 129
SECTION 2. Lost Hills Technical Progress 141
  2.1 Geologic Overview of the Lost Hills Field 142
  2.2 CO_2 Injectivity Test 156
  2.3 Lost Hills CO_2 Pilot 157
  2.4 Lost Hills CO_2 Simulation Study 170
SECTION 3. Technology Transfer Completed to Date 209
  3.1 Technology Transfer 210

LIST OF TABLES

Table 1.2-1. List and Descriptions of Chert Samples Selected for Detailed Study 20
Table 1.2-2. Properties of Opal-CT, 653Z-26B Well 20
Table 1.2-3. Chemical Composition of Chert and Porcelanite 21
Table 1.2-4. Mineralogical Composition of Chert and Porcelanite 22
Table 1.2-5. Comparison of ESTMIN and FTIR Mineralogical Analyses 23
Table 1.2-6. Chemical Composition of "End-Member" Shale Beds 24
Table 1.2-7. Comparison of Sum Volatiles with Loss on Ignition 24
Table 1.2-8. Chemical Composition of "End-Member" Shale Beds with Estimated H_2O^+ and Trace Elements 25
Table 1.2-9. Comparison of Revised Sum Volatiles with Loss on Ignition 25
Table 1.2-10. ESTMIN Mineralogy of "End-Member" Shale Samples (Weight %) 26
Table 1.2-11. ESTMIN Mineralogy of "End-Member" Shale Samples (Volume %) 26
Table 1.2-12. Chemical Composition of Mud-Filled Veins and Rock Matrix (Weight %) 27
Table 1.3-1. Mercury Intrusion/Extrusion Test Results. 51
Table 1.3-2. Results of USBM/Amott Wettability Tests. 52
Table 1.3-3. Results of Spontaneous Imbibition Tests. 52
Table 1.3-4. Average Properties from Routine Core Analysis by Rock Type. 52
Table 1.3-5. Initial and Movable Oil Saturations Estimated from Mercury Intrusion/Extrusion Results. 53
Table 1.3-6. Initial and Movable Oil Saturations Estimated from other special Core Analysis Tests 54
Table 1.3-7. Average Rock Properties and Initial Saturations for Tested Samples. 55
Table 1.3-8. Results of Relative Permeability. 55
Table 1.4-1. Comparison of Fully Saturated and Native State NMR Measurements. 88
Table 1.5-1. Buena Vista Hills Field Cored Wells. 97
Table 1.5-2. Buena Vista Hills United Anticline Marker Intervals Used in 2D Facies Analysis and 3D Reservoir Property Simulation. 98
Table 1.5-3. Buena Vista Hills Quarter-Pattern Marker Intervals Used in 3D Reservoir Property Simulation 100
Table 1.7-1. 3D Streamline Recovery and Fractional Flow at the End of the Run, 1825 days 121
Table 1.7-2. PREOS Parameters. 122
Table 1.7-3. Initial Oil Composition at Estimated Current Conditions. 123
Table 1.7-4. Comparison of Total Recovery after 10 Years of Injection. 124

Table 1.8-1. 653Z Stage #1 Frac Pressure Data 126
Table 1.8-2. 653Z Stage #2 Frac Pressure Data 128
Table 1.9-1. Surface Tiltmeter Mapping Results for Seven Mini Fracs, Well 653Z 134
Table 2.1-1. Average Rock Compositions from Well 166, Section 32 143
Table 2.1-2. Comparison of Lost Hills and Buena Vista Hills Rock Types 145
Table 2.3-1. Average Reservoir Properties for Lost Hills Diatomite CO_2 Pilot Area. 159
Table 2.3-2. Pros and Cons for 2-1/2 Acre Pilot Design 169
Table 2.3-3. Pros and Cons for 5/8 Acre Pilot Design 169
Table 2.4-1. Summary of Recovery Efficiency Ranges 170
Table 2.4-2. Estimated Time Required to Achieve Recovery 170
Table 2.4-3. Statistical Data of Permeability 177
Table 2.4-4. Statistical Data of Porosity 177
Table 2.4-5. Statistical Data of Water Saturation 178
Table 2.4-6. Stratigraphic Markers and their Depth in the Coarsened Model 178
Table 2.4-7. Oil and Gas Input Properties for the CHEARS Model 180
Table 2.4-8. Relative Permeability End-Points 183
Table 2.4-9. Reservoir Pressure vs. Depth at the End of Primary Depletion of the 1*K Model 186
Table 2.4-10. Reservoir Pressure vs. Depth at the End of Primary Depletion and the 2*K Model 186
Table 2.4-11. Cumulative Oil Production during History Match of the 1*K and 2*K Models 187
Table 2.4-12. Summary of Base Case Recoveries Compared to 1991 CPTC Study 188
Table 2.4-13. CHEARS Equation-of-State Parameters 190
Table 2.4-14. Overview of Case 4 Recovery Factors, 1997-2027 192
Table 2.4-15. Overview of Case 5 Recovery Factors, 1997-2027 199
Table 2.4-16. Overview of Cases 11, 12 and 13 Recovery Factors 204

LIST OF FIGURES

Figure 1.1-1. Location Map of Southern San Joaquin Valley Oil Fields. 7
Figure 1.1-2. Stratigraphic Nomenclature Used at Buena Vista Hills. 8
Figure 1.1-3. Structure Map on Top Antelope Shale, Buena Vista Hills.
Figure 1.1-4. Structure Map on Top Antelope Shale, Section 26B-T31S/R23E. 10
Figure 1.1-5. Resistivity/Density Log of 653Z-26B Well. 11
Figure 1.2-1. X-ray Diffraction Pattern of Opal-CT Porcelanite, 4784.7 ft. 28
Figure 1.2-2. X-ray Diffraction Pattern of Opal-CT Porcelanite, 4879.5 ft. 29
Figure 1.2-3. X-ray Diffraction Pattern of "End-Member" Shale Bed, 4270.8 ft. 30
Figure 1.2-4. X-ray Diffraction Pattern of "End-Member" Shale Bed, 4341.0 ft. 31
Figure 1.2-5. Photograph of Mud-Filed Veins in Porcelanite 32
Figure 1.2-6. X-ray Diffraction Patterns of Mud-Filled Veins and Rock Matrix 33
Figure 1.3-1. Typical Mercury Intrusion/Extrusion Capillary Pressure Curve for Opal-CT 56
Figure 1.3-2. Typical Mercury Intrusion/Extrusion Capillary Pressure Curve for Opal-CT/Siltstone 57
Figure 1.3-3. Typical Mercury Intrusion/Extrusion Capillary Pressure Curve for Sandstone 58
Figure 1.3-4. Typical Mercury Intrusion/Extrusion Capillary Pressure Curve for Sandstone/Siltstone 59
Figure 1.3-5. Permeability versus Porosity for all Mercury Intrusion Test Samples 60
Figure 1.3-6. Permeability versus Bulk Density for all Mercury Intrusion Test Samples 61
Figure 1.3-7. Oil/Water Entry Pressure Permeability 62
Figure 1.3-8. USBM/Amott Wettability Test Results, Opal-CT Sample, 3989.20 ft. 63
Figure 1.3-9. USBM/Amott Wettability Test Results for Sandstone/Siltstone Sample, 4315.60 ft. 64
Figure 1.3-10. USBM/Amott Wettability Test Results for Opal-CT Sample, 4355.95 ft. 65
Figure 1.3-11. Oil Recovery by Spontaneous Imbibition at Reservoir Temperature (Opal-CT Samples) 66
Figure 1.3-12. Estimated Initial Oil Saturation versus Bulk Density 67
Figure 1.3-13. Initial Oil Saturation versus Porosity 68
Figure 1.3-14. Initial Oil Saturation versus Air Permeability 69
Figure 1.3-15. Land's Trapping Constants for High-Pressure Mercury Tests 70
Figure 1.3-16. Movable Oil Saturation ($S_{oi} - S_{orw}$) Versus Air Permeability 71
Figure 1.4-1. Matrix Density from Core Variation with Depth, Well 653Z-26B. 74
Figure 1.4-2. Schlumberger ELAN Mineral Model. 77
Figure 1.4-3. Cross plot of Volume of Quartz+Feldspar – ELAN versus ESTMIN 78

Figure 1.4-4. Cross Plot of Volume of Clay+Pyrite+Organic Matter – ELAN versus ESTMIN. 79
Figure 1.4-5. Cross Plot of Volume of Opal-CT – ELAN versus ESTMIN. 80
Figure 1.4-6. Formation MicroImager Resistivity Image of Antelope Shale. 82
Figure 1.4-7. Upper Hemisphere Polar Equal Area Net of Poles to Planes of Bedding, Faults, and Fractures. 83
Figure 1.4-8. Histogram of Fracture Dip Azimuths Interpreted from FMI. 84
Figure 1.4-9. Histogram of Dip Magnitudes Interpreted from FMI. 85
Figure 1.4-10. Histogram of Fault and Healed Fracture Azimuths Interpreted from FMI. 86
Figure 1.4-11. Histograms of Dip Magnitudes of Faults and Healed Fractures Interpreted from FMI. 87
Figure 1.4-12. Carbon/Oxygen Log. 92
Figure 1.5-1. Reservoir Characterization Workflows. 101
Figure 1.5-2. Cross Plot of Core Porosity versus Vsh_SP. 102
Figure 1.5-3. Cross Plot of Drill Stem Test Permeability versus Average Vsh_SP. 102
Figure 1.5-4. Neural Net Permeability Transform Using Facies Finder. 103
Figure 1.5-5. Cross Plot of Initial Oil Saturation versus Porosity. 104
Figure 1.5-6. 1D Neural Net Analysis Using Facies Finder. 105
Figure 1.5-7. 2D Facies Analysis Using Facies Finder. 106
Figure 1.5-8. Reservoir Property Simulation for the United Anticline. 107
Figure 1.5-9. Reservoir Property Simulation and Visualization for the United Anticline. 108
Figure 1.5-10. Scale-up of the Production Simulation Earth Model. 109
Figure 1.6-1. Oil Production from Waterflood and Tertiary CO_2 Injection. 111
Figure 1.6-2. Pressure Drops from the Waterflood Experiment. 112
Figure 1.6-3. Oil/Water Relative Permeability Curves Used in Simulating the Waterflood Experiment. 112
Figure 1.6-4. Gas/Oil Relative Permeability Curves Used in Simulating the CO_2 Flood. 113
Figure 1.6-5. A Schematic of the Mixed Lithology Core Elements. 114
Figure 1.6-6. Cross Sectional View of the Mixed Lithology Core. 114
Figure 1.6-7. A Flow Diagram of the Displacement Rig. 115
Figure 1.6-8. Oil Production from CO_2 Injection. 116
Figure 1.6-9. Total Oil Production from the High Pressure CO_2 Flood. 117
Figure 1.7-1. Buena Vista Hills Permeability Distribution near Well 653Z. 119
Figure 1.7-2. 3D Streamline Model Water Saturation Distribution at Different Times. 120
Figure 1.7-3. 3D Streamline Model Water Distribution in Original High Vertical Resolution. 121
Figure 1.7-4. Oil Saturation Distribution along the South Face of the CHEARS Model. 123
Figure 1.7-5. CO_2 Fraction in Reservoir Oil along the South Face of the CHEARS Model. 124

Figure 1.8-1. Lithostatic Load..127
Figure 1.9-1. Principles of Tiltmeter Fracture Mapping..130
Figure 1.9-2. Surface Deformation for Hydraulic Fractures of Different Orientations. 130
Figure 1.9-3. Three Pictures of Raw Tiltmeter Data on Different Time Scales....................131
Figure 1.9-4. Observed and Theoretical Fracture-Induced Tilt Vectors for a Vertical and Horizontal Fracture..133
Figure 1.9-5. Tilt Signals from all Downhole Tiltmeters for 24-Hour Period from 2/19/98 at 9:00 am to 2/20/98 at 9:00 am..137
Figure 1.9-6. Tilt Signals from all Downhole Tiltmeters for 3-Hour Period from 2/23/98 12:00 pm to 3:00 pm..138
Figure 1.9-7. Map View of Surface Tiltmeter Sites in Relation to Wellhead Locations. 139
Figure 1.9-8. Plan View of Fractures created during Treatment of well 653Z. 140
Figure 2.1-1. Location Map of Major Oil Fields in the Southern San Joaquin Valley 147
Figure 2.1-2. Productive Limits of Belridge Diatomite at Lost Hills 148
Figure 2.1-3. Top Belridge Diatomite Structure Map...149
Figure 2.1-4. Lost Hills CO_2 Pilot Base Map...150
Figure 2.1-5. Lost Hills Stratigraphic Column 151
Figure 2.1-6. Generalized Cross Section along Southeast Plunge on Lost Hills 152
Figure 2.1-7. Slabbed Core of Laminated Diatomite and Bioturbated Sandy Diatomite 153
Figure 2.1-8. SEM Photomicrographs of Opal-A Frustule Starting to Convert to Opal-CT and Frustule Converted to Opal-CT 153
Figure 2.1-9. Opal-A Frustule Initiating Conversion to Opal-CT and a Frustule After Conversion to Opal-CT..154
Figure 2.1-10. Type log (12-8D) of Belridge Diatomite in the Lost Hills Pilot Location.......155
Figure 2.3-1. CO_2 Pilot Base Map..158
Figure 2.3-2. Oil Rate Comparison for Various Processes at 2-1/2 Acre Spacing 160
Figure 2.3-3. Injection Rate Comparison for Various Processes at 2-1/2 Acre Spacing 161
Figure 2.3-4. Oil Rate Comparison for Various Processes at 1-1/4 Acre Spacing 161
Figure 2.3-5. Injection Rate Comparison for Various Processes at 1-1/4 Acre Spacing 162
Figure 2.3-6. Oil Rate Comparison for Various Processes at 5/8 Acre Spacing...................162
Figure 2.3-7. Injection Rate Comparison for Various Processes at 5/8 Acre Spacing 163
Figure 2.3-8. Comparison of CO_2 vs. CH_4 Injection...163
Figure 2.3-9. 2-1/2 acre CO_2 Pilot...165
Figure 2.3-10. 5/8 acre CO_2 Pilot...166
Figure 2.3-11. 2-1/2 Acre vs. 5/8 Acre Simulation Results (Oil Production).........................167
Figure 2.3-12. 2-1/2 Acre vs. 5/8 Acre Simulation Results (Injection) 168
Figure 2.4-1. Five Prediction CO_2 Configuration Scenarios...173
Figure 2.4-2. The 2.5 Acre Pattern Model (60 x 40 x 245 layers) Extracted From

Central Part of The Original 27 Acre Model (149 x 149 x 245) 174
Figure 2.4-3. 2.5 Acre Pattern Model Extracted from the Central Part of the Original 27 Acre Model 175
Figure 2.4-4. Comparison of Single Phase Flow Results in the Fine Grid 2.5 Acre Model (60 x 40 x 245 layers) and the Scaled-up Model (30 x 20 x 55 layers) 176
Figure 2.4-5. Comparison of Permeability Distribution, Fine Pattern Model (60x40x245) and the Scaled-Up Model (30x20x55) 176
Figure 2.4-6. Comparison of Porosity Distribution, Fine Pattern Model (60x40x245) and Scaled-Up Model (30 x 20 x 55) 177
Figure 2.4-7. Comparison of Initial Water Saturation Distribution, Fine Pattern Model (60 x 40 x 245) and Scaled-Up Model (30 x 20 x 55) 178
Figure 2.4-8. Five Y Slice Rows are Added to the Coarsened Model to Represent Cell Hydraulic Fractures 179
Figure 2.4-9. Plane View and Cross Section of Hydraulic Fractures Modeled with Thin Cells (dark blue) 180
Figure 2.4-10. Relative Permeability Curves 181
Figure 2.4-11. History Adjusted Gas-Oil Relative Permeability Curves of Well #12-10 182
Figure 2.4-12. Free Imbibition Endpoints Compared to Forced Endpoints from High Pressure Drop Measurements 182
Figure 2.4-13. Oil-Gas Relative Permeability Curves Derived From Mercury Injection Data. 183
Figure 2.4-14. Primary Depletion and Waterflood History Match of 1*K and 2*K Models 185
Figure 2.4-15. Pressure of 1*K and 2*K Models, End of Depletion with RFT Results 187
Figure 2.4-16. Oil Production Rate of 1*K and 2*K Models During Early Waterflood Compared to Actual 188
Figure 2.4-17. Comparison of Compositional-CHEARS with Field GOR and WOR Trends, Before 9/97 191
Figure 2.4-18. Base Case CO_2 Recovery Performance, 2.5 Acre 5-Spot, F-L Injection, and 50 FT Fracture Half-Length 193
Figure 2.4-19. Relative Permeability from Mercury Injection Data Increases Oil Recovery 194
Figure 2.4-20. Comparison of CO_2 and Methane Injection Performance 194
Figure 2.4-21. Effect of Increased Injection Pressure on Oil Recovery 195
Figure 2.4-22. Recovery Sensitivity to Interval of Injection, Continuous CO_2. 196
Figure 2.4-23. Effect of Using WAG to Improve Conformance, F-L and D-L Injection 197
Figure 2.4-24. Effect of Fracture Length on Recovery Performance, F-L Injection 197

Figure 2.4-25. Effect of Oil Gravity on Recovery Performance, F-L and D-L Injection 198
Figure 2.4-26. Case 5 CO_2 Recovery Performance, F-L Injection, and 50 FT Fracture Half-Length 199
Figure 2.4-27. Case 5, Effect of Increased Injection Pressure on Oil Recovery 200
Figure 2.4-28. Case 5, Recovery Sensitivity to Interval of Injection, Continuous CO_2 201
Figure 2.4-29. Effect of Using WAG to Improve Conformance, F-L and D-L Injection 202
Figure 2.4-30. Effect of Fracture Length on Recovery Performance, F-L Injection 203
Figure 2.4-31. Effect of Oil Gravity on Recovery Performance, F-L and D-L Injection 204
Figure 2.4-32. Oil Recovery Performance for Various Injection Intervals, Cases 11, 12 and 13 205
Figure 2.4-33. Oil Recovery Performance for Different Fracture Half-Lengths, Cases 11, 12 and 13 206

ABSTRACT

The primary objective of our project was to conduct advanced reservoir characterization and modeling studies in the Antelope Shale. Work was subdivided into two phases or budget periods. The first phase of the project would focus on the application of a variety of advanced reservoir characterization techniques to determine the production characteristics of the Antelope Shale reservoir. Reservoir models based on the results of the characterization work would then be used to evaluate how the reservoir would respond to enhanced oil recovery (EOR) processes. The second phase of the project would be to implement and evaluate an EOR pilot in Buena Vista Hills Field. A successful project would demonstrate the economic viability and widespread applicability of CO_2 flooding in siliceous shale reservoirs of the San Joaquin Valley.

To date the project has had many accomplishments: 1) detailed reservoir characterization of Brown and Antelope shales; 2) first coreflood analysis of siliceous shales; 3) first high-resolution crosswell reflection images to be obtained in any oil field in the San Joaquin Valley, 4) mineral model to determine lithology variations and oil saturations in siliceous shales, and 5) comprehensive 3D earth model and reservoir simulation.

However, based on our study of Buena Vista Hills, we will not proceed with a Phase II field trial. Although we had numerous technical successes and completed a detailed reservoir characterization, we can not overcome the siliceous shale's very low oil saturation and lithologic heterogeneity. These reservoir characteristics make the Antelope Shale at Buena Vista Hills an unsuitable CO_2 flood candidate.

Although Buena Vista Hills turned out to be a poor CO_2 EOR candidate, our reservoir characterization has demonstrated that under the right conditions, CO_2 is a viable enhanced recovery process for siliceous shales. Therefore, we have proposed moving the pilot location to the Lost Hills Field, about 30 miles north of Buena Vista Hills.

The Lost Hills Diatomite resource is a unique reservoir and its unusual properties such as extremely small pore size (<5 microns), high porosity (45 - 70%), and low permeability (<1 millidarcy) have led to historically, low primary oil recovery (3 - 4% of OOIP). Due to the low primary recovery and large amount of remaining oil in place, Lost Hills presents an attractive target for EOR. In addition to the large resource base, there is technical and economic justification for CO_2 flooding that was developed through our reservoir characterization and simulation efforts at Lost Hills. CO_2 flooding shows tremendous oil response relative to primary, waterflood and steam flood, mainly due to improved injectivity. Based on the simulation results, CO_2 flooding has the potential for dramatically improving the 4% of OOIP recovery to date from the Lost Hills diatomite.

EXECUTIVE SUMMARY

The primary objective of our project was to conduct advanced reservoir characterization and modeling studies in the Antelope Shale. Work was subdivided into two phases or budget periods. The first phase of the project would focus on the application of a variety of advanced reservoir characterization techniques to determine the production characteristics of the Antelope Shale reservoir. Reservoir models based on the results of the characterization work would then be used to evaluate how the reservoir would respond to enhanced oil recovery (EOR) processes. The second phase of the project would be to implement and evaluate an EOR pilot in Buena Vista Hills Field. A successful project would demonstrate the economic viability and widespread applicability of CO_2 flooding in siliceous shale reservoirs of the San Joaquin Valley.

To date the project has had many accomplishments:

- Detailed reservoir characterization of Brown and Antelope shales.
- First coreflood analysis of siliceous shales.
- First high-resolution crosswell reflection images to be obtained in any oil field in the San Joaquin Valley.
- Outcrop analysis has shown how fractures can act as permeable pathways.
- Mineral model to determine lithology variations and oil saturations in siliceous shales.
- Comprehensive 3D earth model and reservoir simulation.

However, based on our studies, we will not proceed with a Phase II field trial in Buena Vista Hills. Although we had numerous technical successes and completed a detailed reservoir characterization, we can not overcome the siliceous shale's very low oil saturation, lithologic heterogeneity and relatively few natural fractures at Buena Vista Hills.

Although Buena Vista Hills turned out to be a poor CO_2 EOR candidate, our reservoir characterization has demonstrated that under the right conditions, CO_2 is a viable enhanced recovery process for siliceous shales. Therefore, we will move the Phase II CO_2 pilot to Lost Hills Field, about 30 miles north of Buena Vista Hills.

The target reservoir at Lost Hills is the Belridge Diatomite of the Monterey Formation. The Belridge Diatomite is a diatomaceous mudstone and is not present at Buena Vista Hills. This diatomaceous facies grades south from Lost Hills into the more clay rich upper Reef Ridge found at Buena Vista Hills.

The diatomite has high porosity (45 - 70%), but its low permeability (<1 millidarcy) has led to low primary oil recovery (3 - 4% of OOIP). Due to the low primary recovery and large amount of remaining oil in place, Lost Hills presents an attractive target for EOR. In addition to the large resource base, there is technical and economic justification for CO_2 flooding that was developed through our reservoir characterization and simulation efforts.

We compared the oil response on three different well spacings (2-1/2, 1-1/4, 5/8 acres) for four different recovery processes at Lost Hills:

- Primary (Hydraulically Fractured Wells)
- Waterflood
- Steamflood
- CO_2 Flood

Forecasts were then generated using Chevron proprietary reservoir simulation software. At 2-1/2 acre spacing, our analysis shows that injecting water has some benefit in arresting the primary decline. Injecting steam has more or less the same benefit as water injection. Due to the low permeability of diatomite, steam injectivity is extremely poor and cannot substantially improve recovery compared to waterflooding. However, one process does stand out. CO_2 flooding shows tremendous oil response relative to the other three processes, mainly due to improved injectivity. CO_2 injectivity is at least two to three times greater than that of water or steam at 2-1/2 acre spacing.

At tighter well spacings of 1-1/4 and 5/8 acres, oil response for waterflooding and steamflooding continue to improve relative to their 2-1/2 acre base cases. Although there is a marked improvement in these two processes, they pale in comparison to the oil response for CO_2 flooding at the same spacing. In summary, CO_2 flooding at all well spacings shows the best performance of the four processes evaluated considering the magnitude of the oil response and the acceleration of recovery.

It should be noted that although under the current pressure (300 psig to 1000 psig) and temperature ranges (105 – 120°F) for the Lost Hills diatomite, the CO_2 injection process will not be a miscible process (minimum miscibility pressure is estimated to be in the range of 2500 – 3000 psig). Nevertheless, there is significant benefit from the injection of CO_2 due to viscosity reduction and fluid expansion of the reservoir oil under these partially miscible conditions.

Based on the simulation results, CO_2 flooding looks very attractive and appears to have potential for dramatically improving the 4% of OOIP recovery to date from the Lost Hills diatomite. The following is a summary of the conclusions reached from this evaluation:

- Waterflooding does not show a “classical” peak response, only a lessening of the primary decline.
- Steamflooding does not show a significant response unless it is developed on 5/8 acre spacing.
- Of the 4 processes simulated, CO_2 flooding results in the quickest or most accelerated response.
- CO_2 injectivity is significantly higher than water and steam injectivity and is a major reason for the accelerated and higher oil rate response.

In addition to the above, there are a number of additional reasons why Lost Hills is a better target than Buena Vista Hills for CO_2 EOR relating to the following reservoir properties:

- Lost Hills is cooler at 95 – 121 ^{O}F compared to 160 ^{O}F at Buena Vista Hills, which will improve the partial-miscibility of the crude oil with CO_2.
- Lost Hills is shallower so operating pressure will be lower.
- Lost Hills has greater oil saturation and porosity compared to Buena Vista Hills.
- Lost Hills oil is heavier at 19 – 25 ^{O}API compared to the 25 - 33 ^{O}API at Buena Vista Hills, which will improve the partial-miscibility of the crude oil with CO_2.
- Lost Hills has much lower overall permeability due to the absence of thin sandstone layers in the targeted intervals.

Based on the above conclusions, Chevron is planning a 5/8 acre CO_2 pilot project at Lost Hills. The 5/8 acre CO_2 pilot will utilize a Lost Hills 2-1/2 acre waterflood pattern 12-7W and will be converted to a 5/8 acre configuration by drilling four additional producers and four additional injectors. All producers will be hydraulically fractured.

In order to proceed with a pilot project we will conduct an injectivity test in the Belridge Diatomite in Lost Hills. This test will be completed by the second quarter of 1999 as part of Phase I. The objectives of the injectivity test are:

- Inject CO_2 in a new well without hydraulically propped fractures. Because the diatomite is a low permeability reservoir all wells must be hydraulically fractured. If we can successfully inject into wells that do not have to be hydraulically propped fractured, there could be significant financial savings per injection well. Therefore we will attempt to inject into a non-fractured well to see if CO_2 can be injected at or near predicted simulation rates. Additional benefits of testing this well will be injection rate/pressure data by lithology.
- The 12-8D was drilled in December 1998. This well will be used for the injectivity test of a non-fractured well. Plans call for the injectivity test to commence on March 8, 1999. This well will be completed as a producer after the injection test. After the well is on production we will be able to observe the stimulation/production benefits from a CO_2 cyclic injection/soak/production period.
- Inject CO_2 into an existing hydraulically fractured water injection well. Data from this test will allow us to compare CO_2 injection rates and pressures with a non-hydraulically fractured well (12-8D), and compare CO_2 injection with water injection from a nearby water injection well (12-7W).
- Gain experience in CO_2 operations regarding injection profiling, corrosion monitoring, production surveillance, and breakthrough.
- Utilize data to design CO_2 pilot well completions.

This is the 3rd technical progress report and it is subdivided into three sections. The first section covers Buena Vista Hills. All tasks initiated at Buena Vista Hills are now completed. The second section includes work initiated at Lost Hills and discusses in detail the reasons why the Lost Hills diatomite is a better candidate for a CO_2 field trial than the

Antelope Shale at Buena Vista Hills. The third sections lists technology transfer performed to date.

ACKNOWLEDGMENTS

I would like to thank the following individuals for their help and participation on this project: Greg Bender, John Cooney, Mark Emanuele, Kent Gailey, Charles Horsch, Rong Hwang, Dale Julander, Aleks Marasigan, Rick Mollenkopf, Pat Perri, Deborah Piceno, Steve Smith, and Tom Zalan of Chevron USA; Angela Barker, Dave Baskin, Dale Beeson, Alden Carpenter, Bob Langan, Karen De Louraille, Ed deZabala, Chuck Magnani, Sharon Puckett, Ray Tang, Julian Thorne, Don Winterstein, and Dengen Zhou of Chevron Petroleum Technology Company; Bruce Bilodeau of Chevron Overseas Petroleum Company; Allen Britton, Frank Ene, Dan Fargo, Mike Long, and Jeff Smith of Core Laboratories; Stan Denoo, Chris Presnyk, and Bill Scanlan, of Schlumberger Wireline Services; Atilla Aydin, Sneha Dholakia, Jerry Harris, Jud Jacobs, and G. Y. Wang of Stanford University; Bob Bereskin and Barbara Marin of TerraTek; David Campagna, Ned Mamula, and Vello Kuuskraa of Advanced Resources International; David Decker of Basin Energy Development; Theresa Knox and Mike McKee.

SECTION 1.

BUENA VISTA HILLS TECHNICAL PROGRESS

1.1. BUENA VISTA HILLS PROJECT OVERVIEW

INTRODUCTION

Siliceous shale is an unusual reservoir for hydrocarbons, both because it is found in only a few hydrocarbon basins in the world and its production characteristics are unlike any other type of reservoir rock. It is composed of the diagenetically altered silica shells of ancient diatoms, a planktonic plant that thrived in the coastal waters of western North America in the Miocene epoch. Siliceous shale has relatively high porosity but very low permeability so that must be naturally or artificially fractured to produce oil at economic rates.

The Monterey Formation siliceous shale and diatomite in the San Joaquin Valley represents a major but largely underdeveloped domestic oil resource. The part of the Monterey Formation in the San Joaquin Valley, called the Antelope Shale, contains an estimated 7 billion barrels of oil in place (Chevron, 1994). Monterey Formation diatomite (i.e., Belridge Diatomite), a geologically and depositionally related siliceous sedimentary rock, contains another 5 billion barrels (Figure 1.1-1).

The overall scope of the project was to use advanced reservoir characterization on the Antelope Shale (including the overlying, locally siliceous Brown Shale) in one newly drilled and cored well in the West Dome (United Anticline) area of the Buena Vista Hills Field. After characterizing the formation and determining the most appropriate enhanced oil recovery technique, a pilot demonstration enhanced oil recovery project would be installed using the four surrounding wells as producers and the newly drilled well as an injector.

The first step was to apply a variety of advanced reservoir characterization techniques to determine the reservoir and production characteristics of the Brown and Antelope shales. These characteristics were determined by innovative core and log analyses, laboratory core floods, and well tests, which were then used to build a reservoir model to simulate how the reservoir would respond to the application of CO_2 EOR processes. The second step was to design and implement an advanced CO_2 EOR pilot demonstration in the West Dome part of the field to evaluate how effective the process is in increasing the recovery of oil.

West Dome originally was considered an excellent site for this reservoir characterization and EOR pilot project. The field has many features common not only to California siliceous shale reservoirs but many slope basin clastic reservoirs. It has been under primary production (slotted liner completions) for a long time, the reservoir pressure is low, there is a long interval of pay, and oil recovery has been low.

Little modern reservoir characterization information was available in West Dome because only 3 new wells have been drilled there since 1966. Advanced reservoir characterization tools needed to be applied to understand the reservoir rock, its storage and flow paths, and its production mechanisms.

RESERVOIR HISTORY

The Antelope Shale zone was discovered at the Buena Vista Hills field in 1952, and has been under primary production for the last 45 years. Since discovery, 161 wells have been drilled through the Antelope Shale. The Brown and Antelope shales (Antelope Shale Zone) was unitized in the East Dome area in 1954 and is currently operated by Texaco. Of the 52 wells in the West Dome part of the field, 20 are currently producing, 31 are shut-in, and 1 is abandoned. Average per well production is about 20 BOEPD, boosted recently from a low of 6 BOEPD. Average reservoir pressure is about 650 psi (-3400 ft VSS datum). Oil gravity ranges from 25° to 40° API, but averages about 30° API in the pilot area. The gross pay interval averages about 800 ft. Recovery to date has been about 9 MMBO. With the estimated 130 MMB of original oil in place, 93% of the oil in West Dome is still trapped in the reservoir.

The Antelope siliceous shale at the Buena Vista Hills field suffers from three primary problems that cause low recovery, current low production, and hamper any secondary recovery attempts. These producibility problems are common to all other siliceous shale reservoirs, with the exception of problem #1 (low pressure), since undeveloped siliceous shale reservoirs usually have high initial reservoir pressure. The three producibility problems are listed below:

- The reservoir has low pressure (650 psi), low permeability (0.08 md), and the primary recovery mechanism is solution gas drive. At Buena Vista Hills, the reservoir pressure decreased rapidly until it was below bubble point after only 6 years of production. These factors combine to cause low recovery (currently 6.5% OOIP). We need to be able to displace oil from small pores and add energy to the reservoir to increase recovery.

- Siliceous shale is a poorly understood reservoir because of complex lithology, unknown fracture patterns, low permeability matrix, interbedded sand laminae, and unknown formation damage. It is unknown how to determine "sweet spots" from log or core data for limited interval completion. It is also unknown how fractures or formation damage affect current production, although acid stimulation can improve productivity. The technology challenge is to develop a working reservoir model that will enable producers to drill, complete, and stimulate wells to maximize production at the lowest cost.

- Inadequate reservoir characterization has led to limited ability to manage the siliceous shale reservoir, as a result, many mature siliceous shale fields are considered "stripper" properties, ready for abandonment. Because the siliceous shale is still so poorly understood, the current depletion strategy is often only a variation of "harvest the investment" strategy, where operators stop spending any money on siliceous shale wells. In addition, operators of properties that have siliceous shale are often hesitant to fully develop this asset because of geologic and technical uncertainties resulting from inadequate reservoir characterization.

STRATIGRAPHIC NOMENCLATURE

Chevron's common usage for Upper Miocene stratigraphy (Figure 1.1-2) distinguishes the interval between Tmc (or N Point) and P Point as the Brown Shale, and the interval between P Point and P4 Point as the Antelope Shale. Brown Shale is equivalent to the "N Shales" at Elk Hills. We find that the term Brown Shale is useful to distinguish the production characteristics of the intervals above and below P Point so it will be used throughout this report. Upper Antelope refers to the interval from P Point to P2a Point, and lower Antelope the interval from P2a Point to P4 Point. The term "Antelope Shale Zone" refers to the Brown Shale and Antelope Shale.

DEPOSITIONAL MODEL

In the late Miocene epoch, submarine channels were common on the southwest side of the Maricopa depocenter (Webb, 1981). Many of the channels were fed with sand derived from Gabilan Range granitic rock on the southwest side of the San Andreas Fault. At that time, the Gabilan Range was about 150 miles south of its present location near the town of Salinas. The submarine channels were the pathways that turbidity currents followed to carry material from the coastal shelf to the basin floor. The coarsest material was deposited in channels on submarine fans, which formed the Stevens turbidite sands. The channels were located primarily in the low spots between submarine highs present at the time. The submarine highs were the surface expression of anticlines actively forming in the basin due to tectonic stress localized along the San Andreas Fault. The anticlines continued to grow throughout the Pliocene, later becoming anticlinal oil fields like the Buena Vista Hills and the 29R and Main structures at Elk Hills.

The basin was restricted, so tidal and storm currents were at a minimum, and much of the detritus from surrounding land areas was trapped on nearshore shelves (Graham and Williams, 1985). The water apparently was nutrient-rich, providing an ideal environment for diatom growth, so siliceous diatom tests were constantly being deposited throughout the southwest part of the basin.

Turbidity currents periodically swept down the channels, depositing sand in the submarine fans. The fine material in the turbidity current consisting of diatoms, very fine sand, silt, and clay was injected into the water column above the current. This fine detritus eventually settled out of suspension in the basin near the channels, forming siliceous graded beds. Subsequent turbidity currents eroded the siliceous graded beds that were deposited in the channels, leaving them preserved primarily on the submarine highs. Only very infrequently was sand deposited on the submarine highs when a channel formed near their base or an exceptionally large turbidity current occurred. The Antelope Shale built up over time as a thick sequence of these thin graded siliceous distal turbidite beds interbedded with hemipelagic siliceous deposits. Most of the anticlinal submarine highs were within the oxygen-minimum zone, which discouraged bioturbation and preserved the bedding and organic material (Graham and Williams, 1985).

STRUCTURE, STRATIGRAPHY AND LITHOLOGY

The Buena Vista Hills structure (Figure 1.1-3) is an elongated doubly-plunging anticline with a northwest-southeast trend containing two structural culminations, referred to as East Dome (Honolulu Anticline) and West Dome (United Anticline). The crests of the two domes are 3.5 miles apart, with East Dome 240 feet structurally higher than West Dome. The pilot area is located just north of the crest of the anticline in Section 26B (Figure 1.1-4). The Antelope Shale Zone, as defined by the Antelope Shale Zone Unit, extends from the Tmc marker to P4 Point. The reservoir consists primarily of upper Miocene siliceous shale belonging to the Monterey Formation, locally known as the Brown Shale, and Antelope Shale. Thin (1/2 to 25 cm) interbedded turbidite sands are common in the Antelope Shale, representing up to 8% of the reservoir volume. The lateral stratigraphic continuity across the Buena Vista Hills Field is legendary where channel turbidite sands are not present.

The reservoir consists of up to 1325 feet of hard, brownish gray to gray siliceous shale. Figure 1.1-5 shows a log from the 653Z-26B well and stratigraphic markers. The Brown Shale extends from the Top Miocene Cherts (TMC) marker to P Point. This 350-500 foot interval is essentially gas productive. Below the Brown Shale, is the Antelope Shale interval (P Point to P4). The best oil production comes from the Pa to P2a zone. Below P Point, there are many thin sand laminae. Sand thickness usually ranges from 1mm to 25 cm. Sand represents about 5.6% of the reservoir thickness from TMC to P2 and about 8% from P to P2.

Examination of the 653Z-26B, 522A-26B, and 621-25B core has revealed that the Antelope Shale reservoir consists primarily of thin (1-5 cm) graded beds of siliceous shale intercalated with discrete turbidite sand beds and hemipelagic beds of very finely laminated siliceous shale. Each siliceous shale bed grades upward from sand, silt, or silty siliceous shale at the base to porcelanite at the top. The basal contact of each graded bed is commonly eroded.

FRACTURE SYSTEM

The fracture system is not believed to be pervasive because of the low average permeability of 0.64 md calculated from pressure build-up analyses, small drainage radii of 76 to 554 feet calculated from the pressure build-ups, and the unfractured nature of the bulk of the core. Core recoveries in Buena Vista Hills are typically over 95%; the core in this study recovered 99.5% of the cored interval. In contrast, core recoveries in the Point Arguello Field in Monterey Formation offshore California were less than 5% in the highly fractured part of the reservoir. However, there is ample evidence of significant fracture permeability in Buena Vista Hills Field.

For example, well 555-6D was acidized in 1957 and subsequently wells 505-5D, 551-7D, and 501-8D showed an abrupt increase in oil production. Well 544-26B was drilled in 1957 and lost circulation in the Antelope Shale. Six days later, drilling mud was produced in wells 523-26B (2150 feet away), 543-26B (800 feet away), 553-26B (1130 feet away), 564-26B (1600 feet away), 566-26B (2400 feet away), and 556-26B (1900 feet away), skipping wells 554-26B and 555-26B.

Most of the fractures observed in core and microresistivity images are concentrated in dolomite beds. Small-scale "fractures" related to diagenesis are evident in core throughout the Brown and Antelope Shales. Williams (1982) described similar features as fluid escape fractures, which were formed when the sediment was compacting. They are typically 1 to 2 cm long, less than 1/2 mm thick, filled with material from adjacent beds, and parallel to each other. Core analysis in well 621-25B has found that the rock matrix is 10 times more permeable parallel to these fractures than perpendicular to them (Chevron, 1994).

REFERENCES

Chevron, 1994, Advanced reservoir characterization the Antelope Shale to establish the viability of CO2 enhanced oil recovery in California's Monterey siliceous shales, Volume IIA, U. S. Department of Energy, Class III Oil Program Proposal.

Graham, S. A., and Williams, L. A., 1985, Tectonic, depositional, and diagenetic history of Monterey Formation (Miocene), central San Joaquin basin, California: American Association of Petroleum Geologists Bulletin, v. 69, p. 385-411.

Snyder, W. S., 1987, Structure of the Monterey Formation, stratigraphic diagenetic, and tectonic influences on style and timing, *in* R. V. Ingersoll and W. G. Ernst, eds., Cenozoic basin development of coastal California, Rubey Volume VI: Prentice-Hall, Inc., Englewood Cliffs, New Jersey, p. 496.

Webb, G. W., 1981, Stevens and earlier Miocene turbidite sandstones, southern San Joaquin Valley, California: American Association of Petroleum Geologists Bulletin, v. 69, p. 385-411.

Williams, L. A., 1982, Lithology of the Monterey Formation (Miocene) in the San Joaquin Valley, California, *in* L. A. Williams and S. A. Graham, eds., Monterey Formation and associated coarse clastic rocks, central San Joaquin basin, California: Pacific Section Society of Economic Paleontologists and Mineralogists Annual Field Trip Guidebook, p. 17-36.

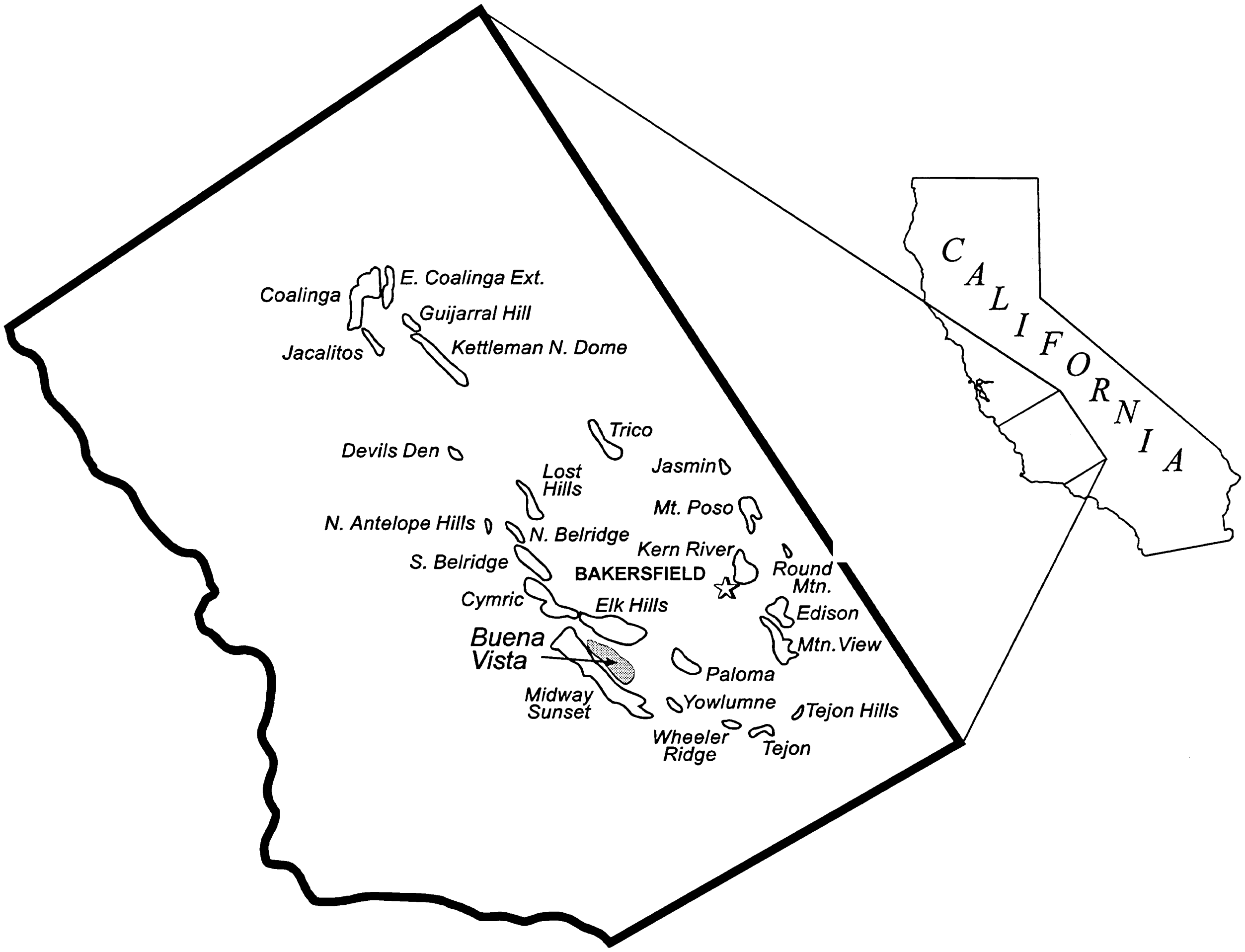
CALIFORNIA
Coalinga
E. Coalinga Ext.
Guijarral Hill
Jacalitos
Kettleman N. Dome
Trico
Devils Den
Jasmin
Lost Hills
Mt. Poso
N. Antelope Hills
N. Belridge
Kern River
S. Belridge
BAKERSFIELD
Round Mtn.
Cymric
Elk Hills
Edison
Buena Vista
Mtn. View
Paloma
Midway Sunset
Yowlumne
Tejon Hills
Wheeler Ridge
Tejon

Figure 1.1-1. Location map showing major oil fields in the southern San Joaquin Valley, California.

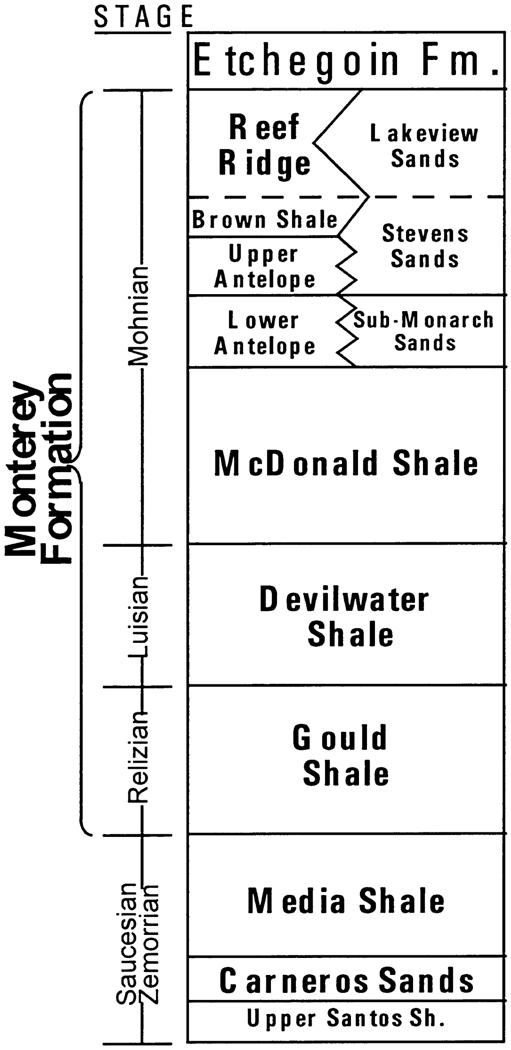
STAGE
Etchegoin Fm.
Reef Ridge
Lakeview Sands
Brown Shale
Stevens Sands
Upper Antelope
Lower Antelope
Sub-Monarch Sands
McDonald Shale
Devilwater Shale
Gould Shale
Media Shale
Carneros Sands
Upper Santos Sh.
Mohnian
Luisian
Relizian
Saucesian
Zemorrian
Monterey Formation

Figure 1.1-2. Stratigraphic nomenclature used Buena Vista Hills.

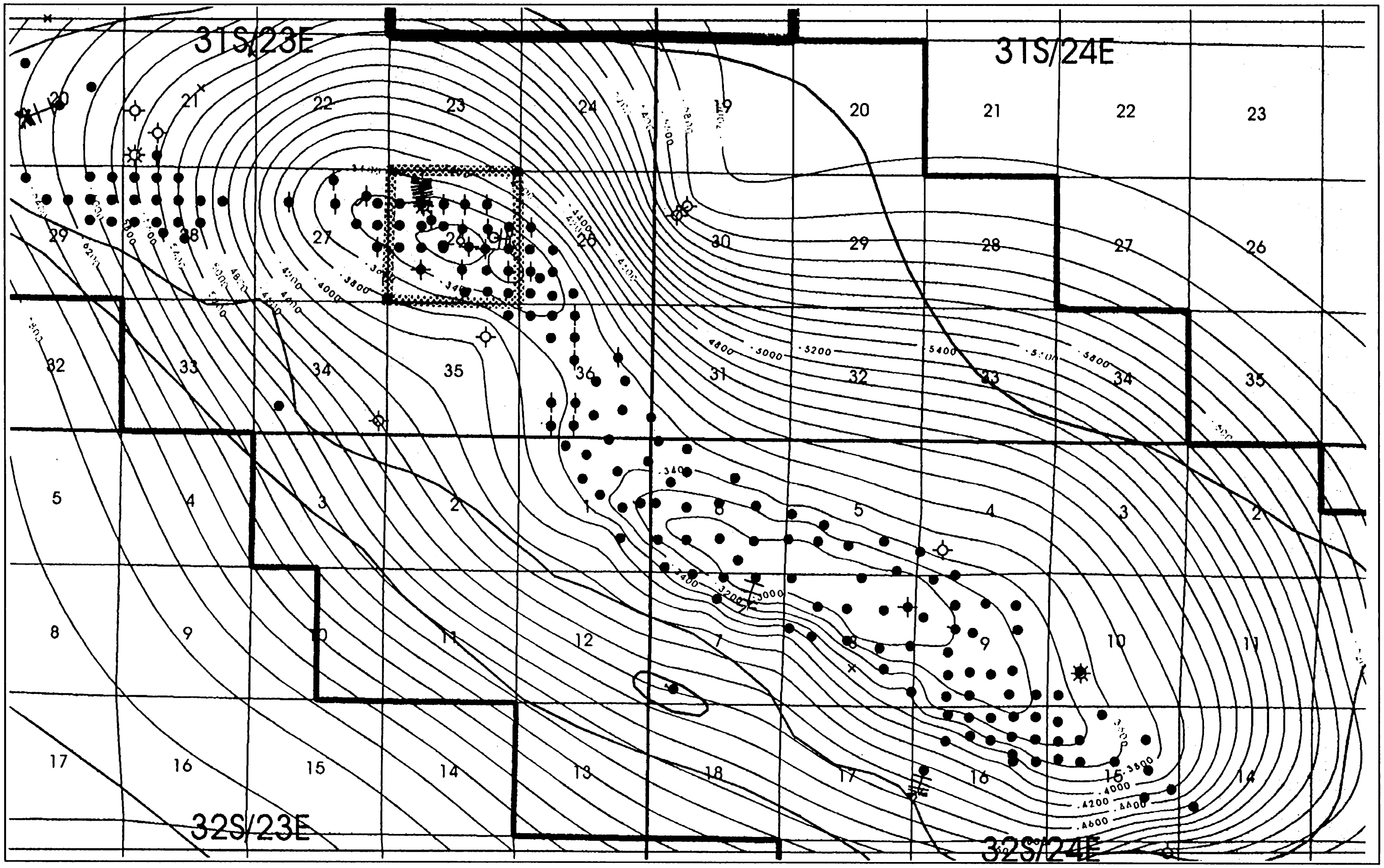
31S/23E
31S/24E
32S/23E
32S/24E
20
21
22
23
24
19
20
21
22
23
29
28
27
26
25
30
29
28
27
26
32
33
34
35
36
31
32
33
34
35
5
4
3
2
1
6
5
4
3
2
8
9
10
11
12
7
8
9
10
11
17
16
15
14
13
18
17
16
15
14
4800
5000
5200
5400
5800
3400
3800
4000
3200
3000
3600
4200
4400
4600

Figure 1.1-3. Structure contour map on the top of the Antelope Shale (P Point), Buena Vista Hills Field, Kern County, California. A stippled line outlines Section 26B.

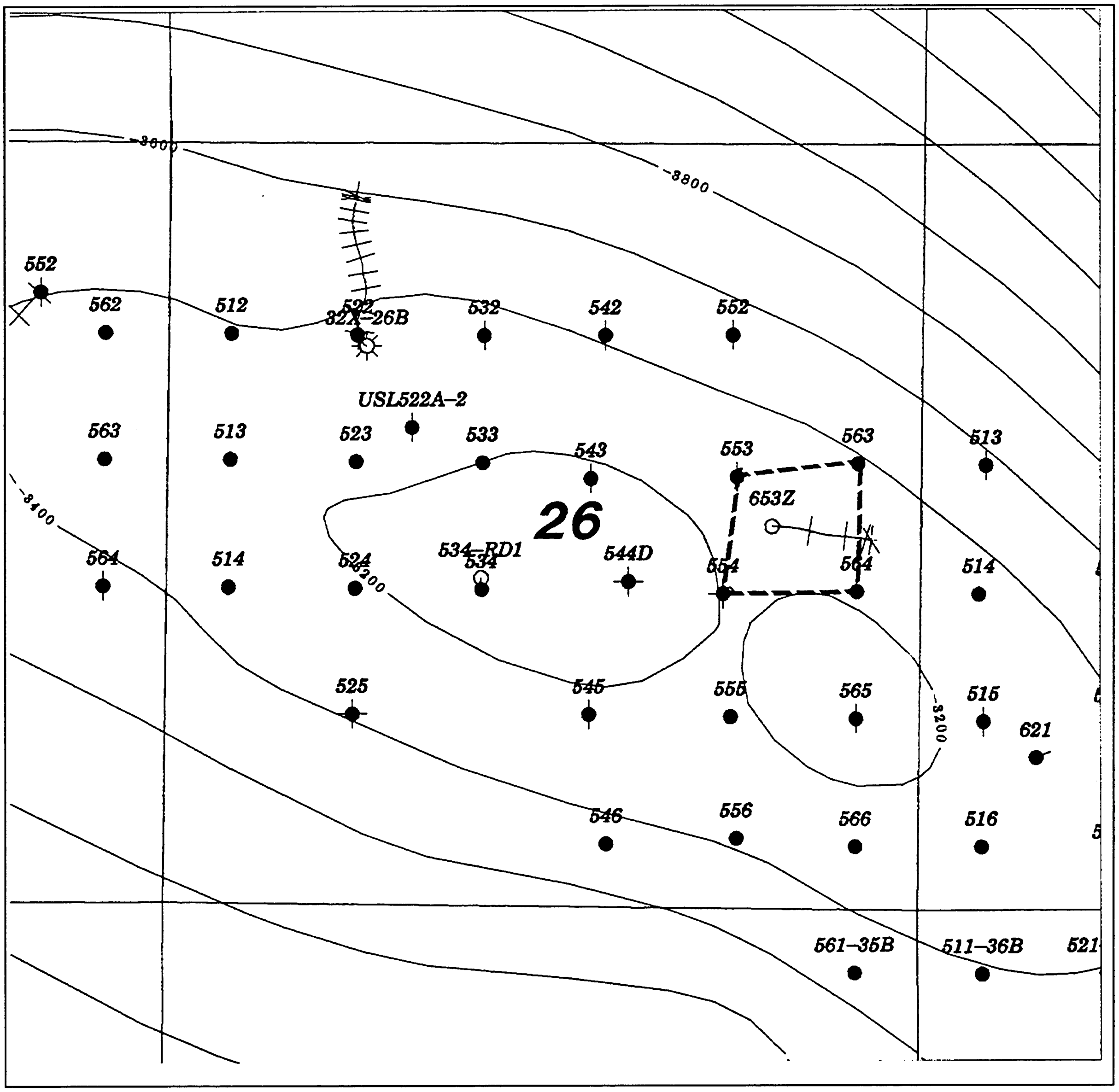

-3600
-3800
-3400
-3200
-3200
552
562
512
522
32X-26B
532
542
552
USL522A-2
563
513
523
533
543
553
563
513
653Z
26
564
514
524
534-RD1
534
544D
554
564
514
525
545
555
565
515
621
546
556
566
516
561-35B
511-36B
521

Figure 1.1-4. Structure contour map on the top of the Antelope Shale (P Point), Section 26B-T31S/R23E, Buena Vista Hills Field, Kern County, California. Pilot area outlined by dashed line.

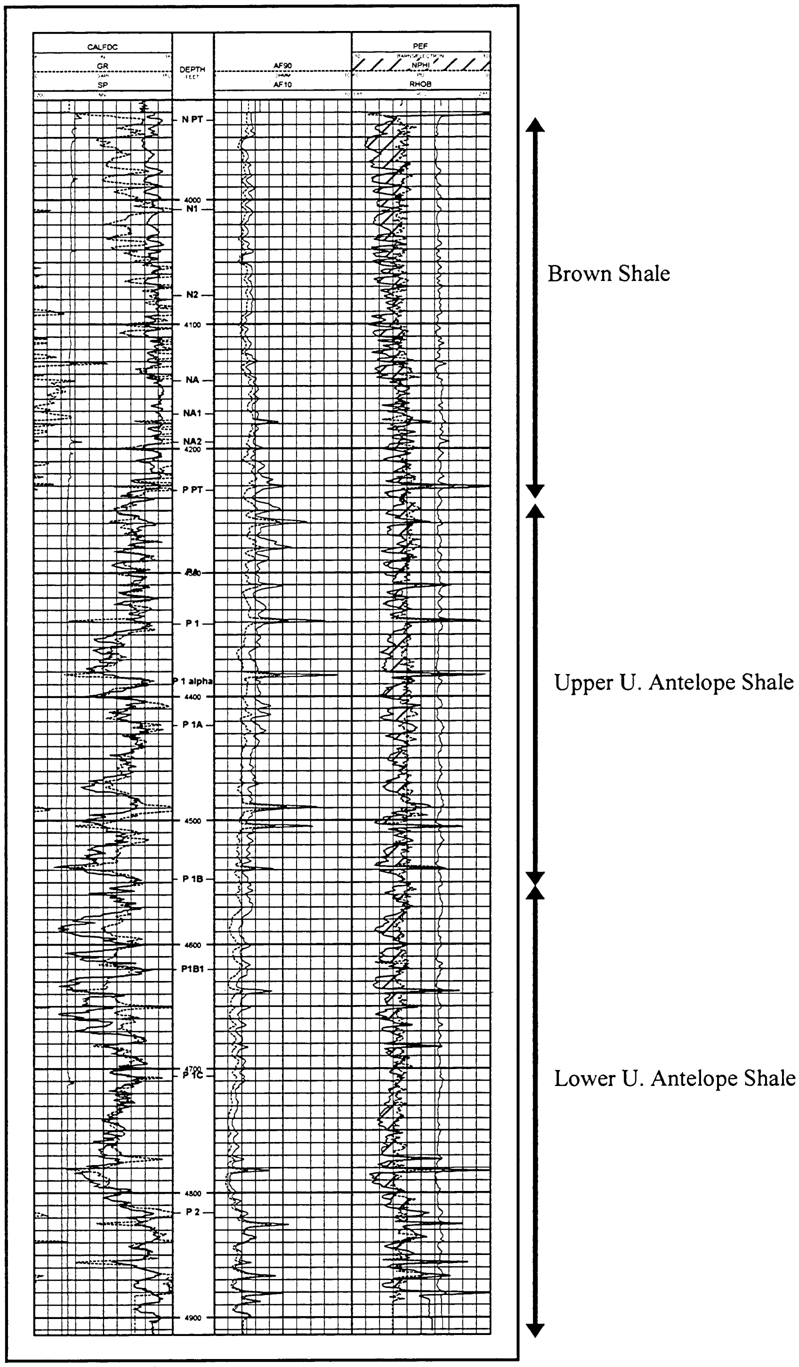

Figure1.1-5. Resistivity/density log of 653Z Well, Section 26-T31S/R23E.

1.2. MINERALOGICAL AND CHEMICALCOMPOSITION OF CHERT, SHALE, AND MUD-FILLED VEINS IN THE ANTELOPE SHALE 653Z-26B WELL

By Alden B. Carpenter, Sharon J. Puckett, and Angela W. Barker
Chevron Petroleum Technology Company

SUMMARY

The work described in this report had three major objectives in support of reservoir characterization in the Buena Vista Hills Field:

1. Determine the average composition of opal-CT in the cored interval and determine if systematic variations in the properties of opal-CT with depth are large enough to warrant consideration in formation evaluation from log measurements.

2. Determine the average composition of mixed-layer illite/smectite in the cored interval and determine if variations in their properties with depth are large enough to warrant consideration in formation evaluation from log measurements.

3. Determine if the clay-filled fractures in the Brown Shale and upper Antelope Shale are a result of soft-sediment deformation or a result of the tectonic deformation of consolidated sediments.

Ten samples of chert and porcelanite, eight samples of "end member" shale, and one sample containing mud-filled veins were analyzed in detail to answer these questions.

The median calculated density of the opal-CT in 10 samples of chert and porcelanite was 2.19 gm/cc. There was a statistically significant reduction in the *d*-spacing of the (101) peak of opal-CT from 4.09 to 4.04 Å in these samples with increasing depth. There was some indication that the density of the opal-CT increases from 2.17 to 2.24 gm/cc with decreasing $d\text{-}_{101}$. However, there is too much scatter in this small data set to justify using a mineral model in which the density of the opal-CT decreases with increasing depth. The relatively high density of the opal-CT in these samples may reflect proximity to the opal-CT/quartz transformation boundary.

The median content of clay and organic matter (43 volume percent) in eight samples of "end member" shale was surprisingly low given the appearance of the samples. The high quartz and feldspar content of these "end member" shale samples precluded collecting new information about the major element chemical composition of the clay fraction in the shale samples. The trace elements contents of the clay/mica fraction were high but were reasonably consistent from sample to sample as follows: Th, 33; B, 500; and Gd, 18 ppm.

The clay-filled fractures in the Brown Shale and upper Antelope Shale of the 653Z-26B Well and other wells are undoubtedly a result of soft-sediment deformation. The mud-filled veins

in a sample of porcelanite from the McKittrick field contain approximately 30% more clay and feldspar (aluminosilicate) than the rock matrix. The veins do not contain significant carbonate cement or more opal-CT than the rock matrix. Consequently, these veins are essentially identical to the clay-filled fractures in shallow, unconsolidated diatomaceous sediments of the east Pacific margins. Fractures produced by tectonic deformation of consolidated sediments should be filled with chemical precipitates such as opal, fibrous quartz, or carbonate rather than detrital clay.

INTRODUCTION

The work described in this report had three major objectives in support of reservoir characterization in the Buena Vista Hills Field:

1. Determine if systematic variations in the properties of opal-CT with depth are large enough to warrant consideration in formation evaluation from log measurements.

2. Determine if variations in the properties of clay minerals with depth are large enough to warrant consideration in formation evaluation from log measurements.

3. Determine if the clay-filled fractures in the Brown Shale and upper Antelope Shale are a result of soft-sediment deformation or a result of the tectonic deformation of consolidated sediments.

The first two objectives provide data for mineral-based formation evaluation. This approach generally provides more accurate estimates of porosity, clay volumes, S_w, permeability, and reservoir facies than earlier approaches such as using cross-plots for estimation of porosity or total gamma ray signal for estimating V_{shale}. These gains result from the mineral-based approach, which makes simultaneous use of all log measurements to determine variations in both mineral and fluid abundances. The accuracy of mineral-based formation evaluation is often lost if interpretations are based on "generic" or "default" values of mineral properties, particularly in the case of clay minerals. In addition, it is important to be certain that properties of the most important minerals do not vary significantly within a logged interval before proceeding with the interpretation of log measurements.

The third objective provides data to help assess possible contributions of microfractures to bulk permeability in the siliceous shale core from the 653Z-26B Well. A microfracture is a small-scale[1] planar discontinuity in a rock due to mechanical failure. Microfractures usually have a significant impact on bulk permeability, which may be either positive or negative depending on their origin (tension vs. shear) and on the presence or absence of fracture filling. Microfractures are common in the more siliceous intervals of the Monterey Formation but there is some controversy over their impact on bulk permeability. It is generally agreed that many fractures occur as en echelon sigmoidal features with regular spacing that occur within clearly defined zones. Seilacher (1969), Williams (1982), and Grimm and Orange (1997) describe these features as mud-filled fractures or veins, which originated from the synsedimentary slumping of diatomaceous sediments. Identical features occur in unconsolidated diatomaceous sediments at sediment depths of less than one meter along the submarine continental slopes off Guatemala and Peru. Mud-filled fractures probably have a significant negative impact on bulk permeability perpendicular to the mud-filled fractures. There is probably little impact on permeability parallel to the mud-filled fractures and no impact on vertical permeability because the fractures are confined to very discrete beds. Aydin (1997) contended that the fractures are of tectonic origin and enhance permeability parallel to the fractures provided that the fractures do not become filled by mineral cement.

---

[1] Commonly less than 10 cm perpendicular to bedding and less than 100 cm parallel to bedding.

These hypotheses can be tested by analysis of the fracture filling. The fractures are undoubtedly synsedimentary if the fractures are filled with material that contains more clay than the rock matrix. We do not expect fractures which formed after the conversion of opal-A to opal-CT to be filled with clay-rich material because clays would be immobilized by opal-CT cement as the rocks become porcelanite. The fractures are undoubtedly tectonic if they are unfilled or filled with a chemical precipitate such as opal-CT or carbonate.

METHODS OF STUDY

Chert and Porcelanite

Ten beds of chert and porcelanite ranging from 1.5 to 2.5 cm in thickness and spaced at approximately 40-meter intervals were analyzed. Samples were selected on the basis of apparent purity as judged by glassy luster, hardness, and light-color. The samples between 3950 and 4500 feet were described as cherts based on their glassy luster and ability to scratch steel. These samples were typically micro laminated and contained numerous clay-filled fractures. Samples from depths greater than 4500 feet were described as porcelanite based on their matte luster and inability to scratch steel. These samples were typically massive and did not contain any fractures. Each bed was sawed from the core and broken into two or three pieces. One of these pieces was broken into coarse fragments to obtain a subsample of highest purity by hand picking under a microscope. Each subsample was ground and analyzed by x-ray fluorescence, x-ray diffraction, and Fourier transform infrared spectroscopy (FTIR). A single piece of rock weighing 6-13 grams was used for the determination of matrix density. A list and description of the chert samples is given in Table 1.2-1.

Shales

Seven beds of "end-member" shale ranging from 2 to 4 mm in thickness and spaced at approximately 40-meter intervals were analyzed. Samples were selected on the basis of their dark brown color, apparent absence of sand grains, and complete lack of fluorescence in the core photographs taken with ultraviolet light. Intervals containing the thin shale beds were cut from the core. The core was then split parallel to bedding to release the shale bed. Fragments of the shale bed were picked under a microscope to obtain a subsample consisting of "end member" shale. Each subsample was ground and analyzed by x-ray fluorescence. The samples from the five shallowest depths were also analyzed by x-ray diffraction. The remaining samples were not analyzed by x-ray diffraction because the chemical analyses indicated that these samples contained excessive amounts of free silica.

Clay-Filled Fractures

Analyses of material from a clay-filled fracture and the enclosing matrix were determined on a sample from a depth of 3299.7 ft. collected from a core from the 342-17Z Well, McKittrick Field. This material was essentially identical in appearance to samples from the 653Z-26B well except that the clay-filled fractures were significantly wider in the sample from the 342-17Z. Chevron geologists familiar with the Antelope Shale believe that the mud-filled veins in the 342-17Z core are genetically the same as those in the 653Z-26B core. The clay-filled fractures in siliceous rocks from the 653Z-26B Well are generally less than 1 mm in width and are nearly impossible to sample for sufficient material for good analyses. The sample from the 342-17Z contained clay-filled fractures up to 3 mm in width.

The sample was very well indurated and the clay-filled fractures were tightly bonded to the enclosing matrix. Consequently, the sample was crushed to approximately 10 mesh and particles containing abundant clay-filling and matrix were separated from each other by hand-picking under a microscope. A portion of the sample was then crushed to obtain a 40-60 mesh size fraction. This material was passed through a Frantz magnetic separator set at 10° cross slope, 15° forward slope, and full field strength. The fracture-filling material was very strongly concentrated in the magnetic fraction and the rock matrix was concentrated in the non-magnetic fraction. Both the hand picked and magnetically picked samples were chemically analyzed and analyzed by x-ray diffraction.

RESULTS

Chert and Porcelanite

The chemical compositions of the chert and porcelanite samples are summarized in Table 1.2-2. X-ray diffraction (XRD) analysis showed that all of the samples contained opal-CT and quartz. Representative XRD patterns are shown in Figures 1.2-1 and 1.2-2. There was a statistically significant reduction in the *d* spacing of the (101) peak of opal-CT with increasing depth as shown in Table 1.2-3. Approximately half of the patterns had very small peaks corresponding to feldspar and pyrite.

The mineralogical compositions of the samples was estimated by chemical inversion of the bulk chemical analyses with input from the X-ray diffraction analyses (ESTMIN method; Carpenter et al., 1993) (Table 1.2-4). The H_2O^+ content of the opal-CT was estimated by dividing the total H_2O^+ content less H_2O^+ in aluminosilicates by the amount of opal. Density of the opal-CT was calculated from the mineral abundances, mineral densities except for opal-CT, and the measured matrix density. The relationship between the water content and density of the opal-CT was in good agreement with values reported by other labs (Carpenter and Barker, 1997). The median calculated density of the opal-CT was 2.19 gm/cc and there is some indication that the density increases to 2.24 as d_{-101} decreases from 4.09 to 4.04 Å. However, there is too much scatter in this small data set to justify using a mineral model in which the density of the opal-CT decreases with increasing depth. The median calculated density of the opal-CT (2.19 gm/cc) was 0.02 gm/cc higher than any other value for the density of opal that we were able to find in the literature. The high density of the opal in these samples may reflect proximity to the opal-CT/quartz transformation boundary.

The mineralogy of the samples was also determined by Fourier transform infrared spectroscopy (FTIR) (Table 1.2-5). The FTIR analyses failed to detect quartz and detected only one-third of the aluminosilicate present. The matrix densities of the samples were calculated from the FTIR mineral abundances and "FTIR" mineral densities. Matrix densities calculated for the samples from FTIR data are too high because the densities used for opal-CT (2.30 gm/cc) and cristobalite (2.32 gm/cc) are higher than apply to nearly all natural opal-CT. Natural opal-CT contains 3-8 weight percent H_2O with interlaminated sheets of HP-tridymite (2.18 gm/cc), M-tridymite (2.25 gm/cc), β-cristobalite (2.205 gm/cc) and α-cristobalite (2.33 gm/cc). The "FTIR" density of cristobalite (2.32 gm/cc) corresponds to the density of nearly pure, anhydrous α-cristobalite which appears to be only a small component of common natural opal-CT. The density of the bulk opal-CT/cristobalite was calculated from the FTIR mineral abundances, "FTIR" mineral densities except for opal-CT or cristobalite, and the measured matrix density. The median calculated density of the opal-CT/cristobalite calculated by this procedure was 2.19 gm/cc, in good agreement with the density of opal-CT calculated from the ESTMIN data and assumptions.

Shales

The chemical compositions of the "end member" shale samples are given in Tables 1.2-6 to 1.2-9. XRD analysis of "random" sample mounts showed that all of the samples contained mixed-layer illite/smectite, discrete illite and/or mica, quartz, plagioclase, K-feldspar, and pyrite. One sample contained an easily detectable amount of clinoptilolite. Opal-CT, kaolinite, and chlorite were not detected in any of the samples. Representative XRD patterns for these samples are shown in Figures 1.2-3 and 1.2-4. The mineralogical compositions of the "end member" shale samples based on the integration of x-ray diffraction and chemical data are shown in Tables 1.2-10 and 1.2-11.

The median content of clay and organic matter (43 volume percent) was surprisingly low given the appearance of the samples. However, the result is consistent with observations in other regions where shales contain less than 50% clay minerals. The result is also consistent with earlier experiences, which showed that it is very difficult to accurately assess the mineralogy of very fine-grained rocks by microscopic examination. The high quartz, feldspar, and organic content of these "end member" shale samples precluded collecting new information about the major element chemical composition of the clay fraction in the shale samples. It is usually very difficult and very expensive to obtain a relatively pure clay-mineral concentrate from a sample with such high silt and organic matter content.

The trace element contents of the clay/mica fraction are high but reasonably consistent from sample to sample as follows: Th, 33; B, 500; and Gd, 18 ppm. (These estimates are based on the assumption that all of the Th, B, and Gd are in the clay fraction.) Most of the uranium in these samples is probably contained in the organic matter and the high uranium content of the samples is probably related to the high content of organic matter.

The accurate determination of "bound water" in some shales is an on-going problem as illustrated by the data in Tables 1.2-6 to 1.2-9. Bound water (H_2O^+) is defined as H_2O

released from minerals during heating in an inert atmosphere (usually pure nitrogen) at 950°C for 1 hour after having been previously dried at 110°C for 1 hour. This procedure works well for samples which do not contain organic matter and minerals which react with organic matter at high temperatures. Samples which contain organic matter and free Fe-Mn oxides (e.g. hematite), Fe-Mn carbonates (e.g. siderite), or sulfates (e.g. anhydrite) present a special problem because of reactions which convert hydrogen in organic matter to H_2O such as:

$$Fe_2O_3 + 3CH_2 + \Rightarrow 2Fe + 3C + 3H_2O. \qquad (1)$$

This situation produces the results shown in Table 1.2-6 in which the analytical totals are unacceptably high and in Table 1.2-7 in which the sum of the individual volatile constituents is much larger than the sample weight loss on ignition at 950°C (LOI).

The best solution to this problem at this time is to estimate the bound water (H_2O^+e) by subtracting all other constituents from 100 percent as shown below:

$$H_2O^+e = 100 - \Sigma \text{ all of other oxides} - .626*(S-.04*Corg) -.774*Cl-1.25*Corg \qquad (2)$$

where .04 and 1.25 are project-specific factors related to the S and C content of the organic matter and .626 and .774 are constants which correct for the "replacement" of O by Cl and S in halite and pyrite respectively. The chemical compositions of the shales with estimated H_2O^+ contents is shown in Table 1.2-8. The agreement between the sum of volatiles and LOI is significantly better when the estimated H_2O^+ is substituted for the reported H_2O^+ (Table 1.2-9). We do not recommend attempting to estimate H_2O^+ by subtracting other volatiles from LOI because the identity and magnitude of some volatiles is not known. Some of the LOI in these shales undoubtedly comes from the loss of O in Fe-oxides as shown in equation 1 above. The amount of O lost from Fe-Mn minerals will be a complex function of the kinds and amounts of Fe-Mn minerals, the H content of the organic matter, and the specifics of the ignition process.

A possible alternative to the present procedure would be to ignite the sample in an oxygen-bearing atmosphere which would quantitatively convert all organic H to H_2O^+. This would give a value for total H reported as H_2O^+ (analogous to total Fe reported as Fe_2O_3). H_2O^+ (mineral) might then be calculated by deducting the H_2O^+ generated by the combustion of the organic matter:

$$H_2O^+(\text{mineral}) = H_2O^+ (\text{total}) - H_2O^+ (\text{from combustion of organic matter}) \qquad (3)$$

This could be done if the H/C ratio of the organic matter is known since the organic carbon content of the samples can be determined quite accurately. Unfortunately, the H/C ratio of organic matter is highly variable and a "generic" H/C probably will not work very well. The H content of the organic matter will have to been known quite accurately since the effect of organic hydrogen on H_2O^+ is very large. (Each unit weight of organic hydrogen produces 8.9 units of H_2O^+.) The difficulty of determining H_2O^+ (mineral) in organic-rich shales is an old problem but we are optimistic that a viable procedure will be developed within the next one or two years.

Mud-Filled Veins

A photograph of the sample used for the separation of the mud-filled veins from the rock matrix is shown in Figure 1.2-5. The chemical composition of the mud-filled veins and rock matrix are given in Table 1.2-12. Sample weights were generally less than 1 gram so there was insufficient material for the determination of FeO, S, and H_2O^+. Representative XRD patterns of the mud-filled veins and rock matrix are shown in Figure 1.2-6.

The chemical and mineralogical compositions of the mud-filled veins and rock matrix were more similar than we expected. The mud-filled veins were approximately 30% higher in Al_2O_3 and higher in Si, total Fe, Mg, Na, and K. The mud-filled veins contained more quartz than the rock matrix. The mud-filled veins had a much larger ratio of quartz to opal-CT based on the differences in total Si and H_2O^+. There was no visible evidence of any significant chemical precipitate in the mud-filled veins.

The mud-filled veins contain approximately 30% more clay and feldspar (aluminosilicate) than the rock matrix and do not contain significant carbonate cement or more opal-CT than the rock matrix. These observations support the hypothesis that the mud-filled veins are synsedimentary.

CONCLUSIONS

1. The median calculated density of the opal-CT in 10 samples of chert and porcelanite was 2.19 gm/cc. There was a statistically significant reduction in the *d*-spacing of the (101) peak of opal-CT from 4.09 to 4.04 in these samples with increasing depth. There was some indication that the density of the opal-CT increases from 2.17 to 2.24 gm/cc as $d\text{-}_{101}$ decreases from 4.09 to 4.04 Å. However, there is too much scatter in this small data set to justify using a mineral model in which the density of the opal-CT decreases with increasing depth. The median calculated density of the opal-CT (2.19 gm/cc) was 0.02 gm/cc higher than any other value for the density of opal that we were able to find in the literature. The high density of the opal in these samples may reflect proximity to the opal-CT/quartz transformation boundary.

2. The median content of clay and organic matter (43 volume percent) in eight samples of “end member” shale was surprisingly low given the appearance of the samples. The high quartz and feldspar content of these “end member” shale samples precluded collecting new information about the major element chemical composition of the clay fraction in the shale samples. The trace elements contents of the clay/mica fraction were high but were reasonably consistent from sample to sample as follows: Th, 33; B, 500; and Gd, 18 ppm.

3. The chemical analyses of the “end-member” shales indicate that accurate determination of bound water (H_2O^+) is difficult for samples, which contain organic matter, and minerals, which react with organic matter at high temperatures. A possible alternative to the present procedure would be to ignite the sample in an oxygen-bearing atmosphere, which would quantitatively release all mineral H_2O^+ and convert all organic H to H_2O^+. This would give a

value for total H reported as H_2O^+. H_2O^+ (mineral) could then be calculated by deducting the H_2O^+ generated by the combustion of the organic matter if the carbon content and H/C ratio of the organic matter are known.

4. The mud-filled veins in a sample of porcelanite from the McKittrick Field contain approximately 30% more clay and feldspar (aluminosilicate) than the rock matrix and do not contain significant carbonate cement or more opal-CT than the rock matrix. These observations support the hypothesis that the mud-filled veins are synsedimentary.

ACKNOWLEDGMENTS

We thank Deborah Lerner, Liz Burton and Eric Daniels, for their careful reviews and constructive suggestions for this memorandum.

REFERENCES

Aydin, A., (1997). Private communication.

Carpenter, A. B., Barker, A. W., (1997). Petroleum in Hemipelagic Deposits ("Siliceous Shales") of the San Joaquin Valley, California. CPTC Technical Memorandum TM97000348, 112 p.

Carpenter, A. B., Barker, A. W., and Hoffmaster, R. L., (1993). Introduction to Mineralogical Analysis by the ESTMIN Procedure, CPTC Technical Memorandum TM93000707, 16 p.

Grimm, K. A. and Orange, D. L., (1997). Synsedimentary fracturing, fluid migration, and subaqueous mass wasting: intrastratal microfractured zones in laminated diatomaceous sediments, Miocene Monterey Formation, California, U.S.A.: Journal of Sedimentary Research 67, 601-613.

Hunt, J. M., (1979). *Petroleum Geochemistry and Geology.* W. H. Freeman, San Francisco, 617 p.

Isaacs, C. M., (1980). *Diagenesis in the Monterey Formation Examined Laterally Along the Coast Near Santa Barbara, California*: Ph.D. Thesis, Stanford University, 329 p.

Seilacher, A., (1969). Fault-graded beds interpreted as seismites: Sedimentology 13, 155-159.

Williams, L. A., (1982). Lithology of the Monterey Formation (Miocene) in the San Joaquin Valley of California: In, Williams, L. A. and Graham, S. A. (editors), *Monterey Formation and Associated Coarse Clastic Rocks, Central San Joaquin Basin, California*, Society of Economic Paleontologists and Mineralogists, Los Angeles, CA, pp. 17-36, 653Z Chert Shale TM. doc., August 5, 1998.

Table 1.2-1. List and descriptions of chert samples selected for detailed study.

Depth (ft)	Hardness	Luster	Bedding	Fractures
3958.2	3-5	Semi glassy	Thin bedded	Abundant Clay-filled Fractures
3984.9	4-6	Semi glassy	Thin bedded	Abundant Clay-filled Fractures
4067.2	4-6	Semi glassy	Thin bedded	Abundant Clay-filled Fractures
4147.2	4-6	Glassy	Thin bedded	Abundant Clay-filled Fractures
4256.5	4-6	Glassy	Thin bedded	Abundant Clay-filled Fractures
4400.4	4-6	Semi glassy	Thin bedded	Sparse Clay-filled Fractures
4505.2	3-4	Matte	Massive	None
4636.0	3-4	Matte	Massive	None
4784.7	3-5	Semi glassy	Thin bedded	None
4879.8	3	Matte	Massive	None

Table 1.2-2. Properties of opal-CT, 653Z 26B Well.

Depth (feet)	***d*-Spacing (101)** (Angstroms)	**H_2O^+ Content of Opal-CT**[1]	**Density of Opal-CT**[2]
3958.2	4.087	4.4	2.19
3984.9	4.084	3.5	2.19
4067.2	4.089	4.1	2.13
4147.2	4.087	3.5	2.19
4256.5	4.083	4.2	2.19
4400.4	4.072	3.9	2.17
4505.2	4.078	5.6	2.25
4636.0	4.043	4.6	2.17
4784.7	4.045	3.4	
4879.8	4.064	4.0	2.24

[1] Calculated H_2O^+ content of opal-CT.

[2] Calculated density of opal-CT

Table 1.2-3. Chemical composition of chert and porcelanite, 653Z-26B Well.

Depth	SiO_2	Al_2O_3	TiO_2	Fe_3D	FeO	MgO	CaO	Na_2O	K_2O	P_2O_5	CO_2	H_2O^+	S	Cl	C(org)	Total
3958.2	89.0	1.87	.082	.38	.3	.15	.59	.62	.27	.10	.23	4.3	.44	.26	2.35	101.2
3984.9	89.4	1.91	.075	.44	.3	.16	.59	.59	.28	.09	.24	3.6	.47	.23	1.89	100.4
4067.2	88.9	2.33	.101	.55	.3	.20	.38	.67	.36	.10	.14	4.1	.58	.19	2.33	101.5
4147.2	90.9	1.80	.080	.31	.3	.08	.23	.58	.28	.08	.06	3.6	.46	.16	1.82	100.9
4256.5	87.5	3.18	.154	1.20	.3	.26	.52	.85	.58	.12	.17	4.2	.92	.22	2.33	102.6
4400.4	88.2	2.12	.093	.41	.5	.14	1.36	.64	.31	.10	.72	3.9	.61	.23	2.21	101.7
4505.2	83.8	3.70	.189	.96	.5	.49	.72	.89	.60	.14	.25	5.2	.85	.26	3.52	102.4
4636.0	85.6	4.09	.198	.92	.4	.36	.59	.97	.70	.11	.16	4.6	.61	.23	2.76	102.6
4784.7	85.1	1.87	.075	.80	.5	1.02	2.54	.60	.29	.06	2.97	3.3	.38	.20	1.68	101.6
4879.5	85.8	3.57	.167	.89	.6	.30	.58	1.05	.73	.11	.22	4.1	.66	.21	2.41	101.6

Explanation of Terms

Fe3D: "Ferric iron by difference". Equal to total iron minus acid-soluble ferrous iron reported as Fe_2O_3.

H_2O^+: Bound water. Water retained by the sample after heating for 1 hour at 110°C.

Total: Sum of all oxides (SiO_2-H_2O^+) + .626*(S-.04*Corg) + .774*Cl + 1.25*Corg.

Table 1.2-4. Mineralogical composition of chert and porcelanite as determined by ESTMIN from chemical analysis and x-ray diffraction (XRD) Data.

Depth	Lithology	Opal-CT	Quartz	Clay	Dolomite	Pyrite	Organic Matter	Meas. Matrix Density
3958.2	Chert	84	4	8	0.5	0.6	3.0	2.20
3984.9	Chert	84	4	8	0.5	0.7	2.4	2.21
4067.2	Chert	81	5	10	0.3	0.8	2.9	2.17
4147.2	Chert	85	4	8	0.1	0.5	2.3	2.21
4256.5	Porcelanite	74	7	14	0.4	1.5	2.9	2.25
4400.4	Chert	81	5	9	1.5	0.6	2.8	2.20
4505.2	Porcelanite	70	8	16	0.5	1.2	4.4	2.28
4636.0	Porcelanite	69	9	18	0.3	0.8	3.5	2.24
4784.7	Porcelanite	79	4	8	6.2	0.5	2.1	2.24e
4879.5	Porcelanite	72	8	16	0.5	1.0	3.0	2.29

Equations and Assumptions

Lithology as defined by mineralogical composition; chert is 80-100% opal-CT, porcelanite is 50-80% opal-CT.

Organic matter = 1.25* organic carbon. (Assumes that the organic matter contains 80% organic carbon. This is intermediate between the typical organic carbon content of kerogen (76%) and asphalt (83%) Hunt (1979).)

Pyrite = 1.87*(S-.05*organic matter) or 1.5*Fe3D whichever is less. (Assumes the organic matter contains 5% S.)

Dolomite = 2.08*CO_2. (Assumes dolomite contains 48% CO_2.)

Clay plus Feldspar = 4.35*Al_2O_3. (Assumes clay plus feldspar contains 23% Al_2O_3. This corresponds to the Al_2O_3 content of oligoclase (Ab80) (23% Al203) and mixed-layer illite/smectite containing 50% expandable layers (23% Al_2O_3). Issacs (1980) reported that the clay plus feldspar fraction of the Monterey Formation along the Santa Barbara Channel contained 24% Al_2O_3.)

Quartz = 2*(clay plus feldspar). (Assumes that one-third of the silicate detritus is detrital quartz. This estimate is consistent with the intensity of the quartz peaks in the x-ray diffraction patterns. Most shales contain at least 35% quartz. Issacs (1980) assumed that one-fourth of the silicate detritus in the Monterey Formation along the Santa Barbara Channel was quartz.)

Opal-CT = 100 – sum of organic matter, pyrite, dolomite, clay plus feldspar, and quartz.

Matrix densities were measured by Core Laboratories, Bakersfield. The matrix density estimated for sample 4784.7 was based on the following mineral densities: opal-CT, 2.19; quartz, 2.65; clay and feldspar, 2.65; dolomite, 2.86; pyrite, 5.02; organic matter, 1.30.

Table 1.2-5. Comparison of ESTMIN and FTIR mineralogical analyses of chert and porcelanite.

Mineralogical composition of chert and porcelanite as determined by ESTMIN (chemical analysis and XRD data)

Depth	Lithology[1]	Opal-CT[2]	Quartz	Clay & Feldspar[3]	Dolomite	Pyrite	Organic Matter	Meas. Matrix Density[4]
3958.2	Chert	84	4	8	0.5	0.6	3.0	2.20
3984.9	Chert	84	4	8	0.5	0.7	2.4	2.21
4067.2	Chert	81	5	10	0.3	0.8	2.9	2.17
4147.2	Chert	85	4	8	0.1	0.5	2.3	2.21
4256.5	Porcelanite	74	7	14	0.4	1.5	2.9	2.25
4400.4	Chert	81	5	9	1.5	0.6	2.8	2.20
4505.2	Porcelanite	70	8	16	0.5	1.2	4.4	2.28
4636.0	Porcelanite	69	9	18	0.3	0.8	3.5	2.24
4784.7	Porcelanite	79	4	8	6.2	0.5	2.1	2.24e
4879.5	Porcelanite	72	8	16	0.5	1.0	3.0	2.29

Mineralogical composition of chert and porcelanite as determined by FTIR analysis

Depth	Lithology[1]	Opal-CT[2]	Quartz	Clay & Feldspar[3]	Dolomite	Pyrite	Organic Matter	Est. Matrix Density[4]
3958.2	Chert	95	0	5	0	0	nd[5]	2.32
3984.9	Chert	95	0	5	0	0	nd	2.31
4067.2	Chert	95	0	4	0	1	nd	2.33
4147.2	Chert	100	0	0	0	0	nd	2.30
4256.5	Chert	90	0	10	0	1	nd	2.35
4400.4	Chert	97	0	3	0	0	nd	2.31
4505.2	Chert	92	0	7	0	1	nd	2.35
4636.0	Chert	86	0	13	0	1	nd	2.36
4784.7	Chert	94	0	0	6	0	nd	2.33
4879.5	Chert	91	0	9	0	0	nd	2.34

Remarks

[1] Lithology as defined by mineralogical composition; chert is 80-100% opal-CT, porcelanite is 50-80% opal-CT.

[2] Opal-CT: includes opal-CT and "cristobalite" as determined by FTIR.

[3] Clay & Feldspar: FTIR analysis indicated that all feldspar was oligoclase and that all clay was chlorite.

[4] Estimated matrix density: The FTIR estimate is based on the following mineral densities: opal-CT, 2.30; cristobalite, 2.32; quartz, 2.65; oligoclase, 2.63; chlorite, 2.78; dolomite, 2.86; pyrite, 5.00.

[5] nd: not determined.

Table 1.2-6. Chemical composition of "end-member" shale beds (raw data, weight percent).

Depth	SiO_2	Al_2O_3	TiO_2	Fe3D	FeO	MnO	MgO	CaO	Na_2O	K_2O	P_2O_5	CO_2	H_2O^+	S	Cl	Corg	Total
3985.0	51.4	14.7	.770	4.83	1.5	.03	1.47	1.46	1.35	2.36	0.33	0.35	12.7	3.07	.03	9.06	106.4
4141.8	51.8	15.0	.740	4.50	1.8	.03	1.36	1.44	1.33	2.46	0.43	0.10	13.0	3.14	.05	9.12	107.2
4270.8	55.6	15.3	.689	4.10	1.6	.03	1.38	2.08	1.65	2.34	0.26	0.42	10.7	2.62	.02	6.47	105.8
4341.0	53.4	16.1	.734	3.96	1.7	.03	1.10	2.02	1.78	2.76	0.36	0.03	10.9	2.32	.02	6.70	104.6
4661.0	53.9	13.0	.687	4.67	nss	.04	1.29	3.25	1.55	2.17	0.29	2.23	nss	3.00	.07	5.97	
4661.2	57.7	13.3	.594	3.55	1.6	.02	1.11	2.63	1.66	1.91	0.22	1.34	9.8	2.66	.10	5.39	103.8
4730.4	60.9	12.1	.591	3.07	1.8	.03	1.22	2.13	1.74	1.84	0.23	1.64	nss	1.87	.10	4.54	
4862.7	72.6	7.60	.375	2.32	1.3	.00	0.68	0.83	1.20	1.44	0.21	0.17	7.6	2.15	.15	4.37	103.2

Explanation of Terms

Fe3D: "Ferric iron by difference". Equal to total iron minus acid-soluble ferrous iron reported as Fe_2O_3.

H_2O^+: Bound water. Water retained by the sample after heating for 1 hour at 110°C.

Total: Sum of all oxides (SiO_2-H_2O^+) + .626*(S-.04*Corg) + .774*Cl + 1.25*Corg.

nss: Not sufficient sample.

Table 1.2-7. Comparison of sum of volatiles with loss on ignition (LOI) (weight percent).

Depth	CO_2	Organic Matter	H_2O^+	"Mineral Sulfur"	Total Volatiles	Loss On Ignition
3985.0	0.35	11.9	12.7	2.59	27.6	18.6
4141.8	0.10	12.0	13.0	2.66	27.8	19.1
4270.8	0.42	8.5	10.7	2.28	21.9	15.0
4341.0	0.03	8.8	10.9	1.97	21.7	14.8
4661.0	2.23	7.9	nss	2.69		15.9
4661.2	1.34	7.1	9.8	2.38	20.6	14.1
4730.4	1.64	6.0	nss	1.63		13.0
4862.7	0.17	5.8	7.6	1.92	15.4	10.1

Explanation of Terms

"Mineral Sulfur": Weight loss due to sulfur in pyrite after deducting a correction for organic sulfur.

Table 1.2-8. Chemical composition of “end-member” shale beds with estimated H_2O^+ and trace elements (weight percent).

Depth	SiO_2	Al_2O_3	TiO_2	Fe3D	FeO	MgO	CaO	Na_2O	K_2O	P_2O_5	CO_2	H_2O^+e	S	Corg	Th	U	B	Gd
3985.0	51.4	14.7	.770	4.83	1.5	1.47	1.46	1.35	2.36	0.33	0.35	6.3	3.07	9.06	12	19	163	7.0
4141.8	51.8	15.0	.740	4.50	1.8	1.36	1.44	1.33	2.46	0.43	0.10	5.7	3.14	9.12			147	5.0
4270.8	55.6	15.3	.689	4.10	1.6	1.38	2.08	1.65	2.34	0.26	0.42	4.9	2.62	6.47	12	16	148	4.0
4341.0	53.4	16.1	.734	3.96	1.7	1.10	2.02	1.78	2.76	0.36	0.03	6.3	2.32	6.70	9.8	14	128	4.0
4661.0	53.9	13.0	.687	4.67	nss	1.29	3.25	1.55	2.17	0.29	2.23	7.6	3.00	5.97			172	5.5
4661.2	57.7	13.3	.594	3.55	1.6	1.11	2.63	1.66	1.91	0.22	1.34	6.0	2.66	5.39			184	9.0
4730.4	60.9	12.1	.591	3.07	1.8	1.22	2.13	1.74	1.84	0.23	1.64	5.8	1.87	4.54			165	5.5
4862.7	72.6	7.6	.375	2.32	1.3	0.68	0.83	1.20	1.44	0.21	0.17	4.4	2.15	4.37	6.6	15	102	5.5

Explanation of Terms

Fe3D: “Ferric iron by difference”. Equal to total iron minus acid-soluble ferrous iron reported as Fe_2O_3.

H_2O^+e: Estimated H_2O^+; equal to 100 – the sum of all other oxides - .626*(S-.04*Corg) - .774*Cl - 1.25*Corg.

nss: Not sufficient sample

Th, U, B, and Gd are reported in ppm.

Table 1.2-9. Comparison of revised sum of volatiles with loss on ignition (LOI) (weight percent).

Depth	CO_2	Organic Matter	H_2O^+e	“Mineral Sulfur”	Total Volatiles	Loss On Ignition
3985.0	0.35	11.9	6.3	2.59	21.2	18.6
4141.8	0.10	12.0	5.7	2.66	20.5	19.1
4270.8	0.42	8.5	4.9	2.28	16.1	15.0
4341.0	0.03	8.8	6.3	1.97	17.1	14.8
4661.0	2.23	7.9	7.6	2.69	20.4	15.9
4661.2	1.34	7.1	6.0	2.38	16.8	14.1
4730.4	1.64	6.0	5.8	1.63	15.1	13.0
4862.7	0.17	5.8	4.4	1.92	12.3	10.1

Explanation of Terms

H_2O^+e: Equal to 100 – the sum of all other oxides - .626*(S-.04*Corg) - .774*Cl - 1.25*Corg.

“Mineral Sulfur”: Weight loss due to sulfur in pyrite after deducting a correction for organic sulfur.

Table 1.2-10. Mineralogy of "end-member" shale samples as determined by ESTMIN analysis (weight percent).

Depth	Quartz	K-Feldspar	Plagioclase	Clay & Mica	Dolomite	Pyrite	Apatite	Organic Matter
3985.0	18	10	21	35	.8	3.5	.4	11.9
4141.8	17	11	22	33	.2	3.6	.7	12.0
4270.8	20	11	28	28	.9	3.3	.3	8.5
4341.0	16	12	26	34	.1	2.7	.5	8.8
4661.0	25	8	20	30	5.0	4.1	.4	7.9
4661.2	27	6	22	31	3.0	3.6	.2	7.1
4730.4	34	6	18	30	3.7	2.4	.2	6.0
4862.7	57	4	9	21	.4	2.9	.3	5.8

Table 1.2-11. Mineralogy of "end-member" shale samples as determined by ESTMIN analysis (volume percent).

Depth	Quartz	K-Feldspar	Plagioclase	Clay & Mica	Dolomite	Pyrite	Apatite	Organic Matter
3985.0	16	9	19	32	0.7	1.7	0.3	22
4141.8	16	10	20	30	0.2	1.7	0.5	22
4270.8	19	11	26	26	0.8	1.6	0.3	16
4341.0	15	11	24	31	0.1	1.3	0.4	17
4661.0	24	7	19	28	4.4	2.1	0.3	15
4661.2	26	6	21	29	2.6	1.8	0.2	14
4730.4	32	6	17	29	3.3	1.2	0.2	12
4862.7	54	4	9	20	0.3	1.5	0.2	11

Table 1.2-12. Chemical composition of mud-filled veins and rock matrix (weight percent).

Method	Color	SiO_2	Al_2O_3	TiO_2	Fe_2O_3	MgO	CaO	Na_2O	K_2O	P_2O_5	H_2O^+e	Corg	Ba
Hand-picked	Light	75.6	4.10	.21	1.96	.44	.40	.90	.70	.09	7.42	6.21	227
Hand-picked	Dark	74.0	4.96	.25	2.31	.52	.52	1.09	.79	.11	9.27	4.69	731
Magnetic Sep.	Light	67.9	4.03	.21	1.97	.45	.40	.55	.67	.10	16.3	5.62	200
Magnetic Sep.	Dark	77.6	5.31	.30	2.80	.59	.49	.70	.88	.14	3.76	5.64	1590

Explanation of Terms

Hand-picked: Hand-picked sample.
Magnetic Sep.: Sample recovered by magnetic separation.
Fe_2O_3: Total Fe reported as Fe_2O_3.
H_2O^+e: Estimated H_2O^+. Equal to 100 minus sum of all other oxides – 1.25*Corg. (The sample size was too small to allow determination of CO_2 and S)
Ba: Ba is reported in ppm

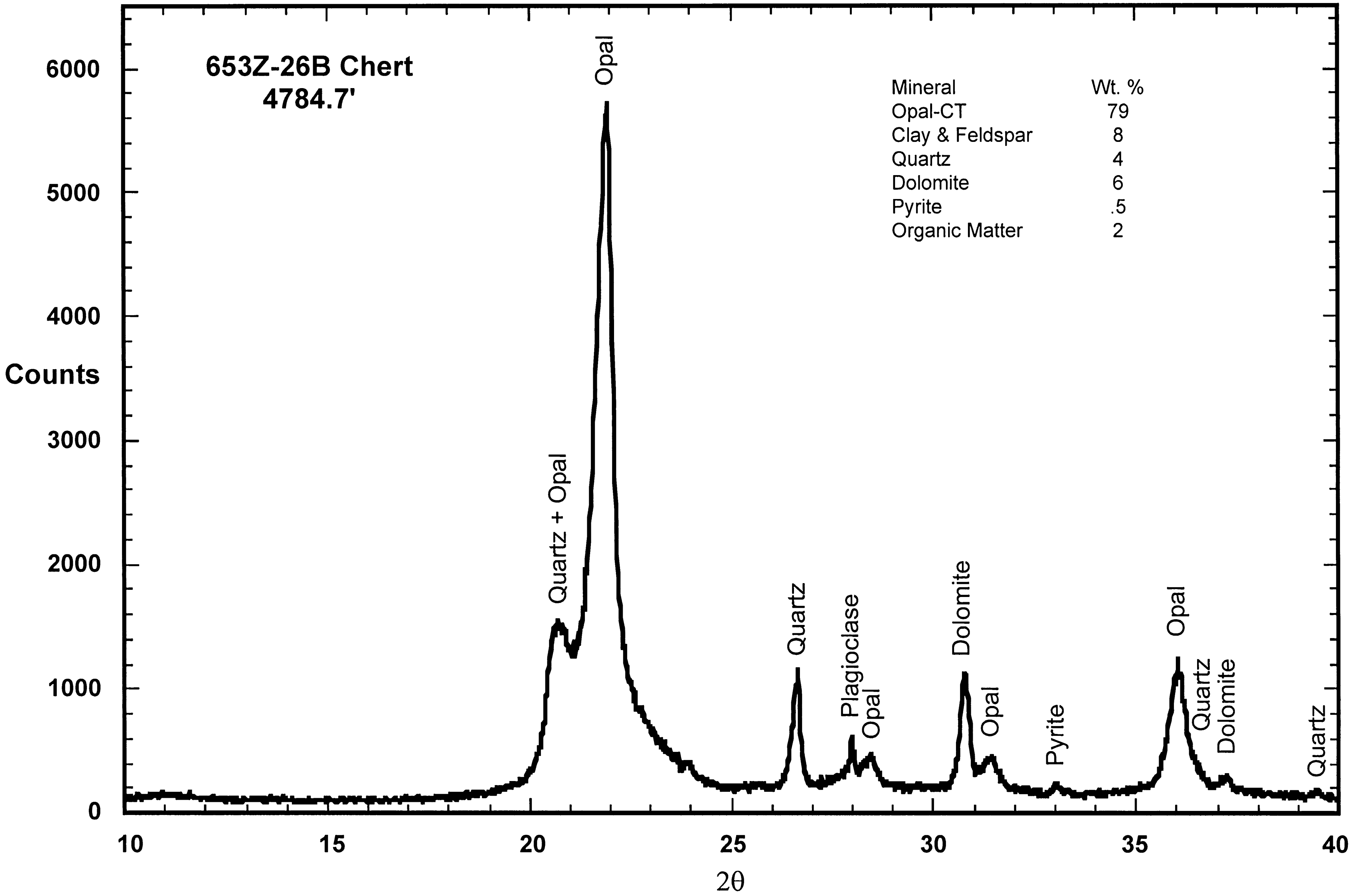

Figure 1.2-1. X-ray diffraction pattern of opal-CT porcelanite, 4784.7 ft.

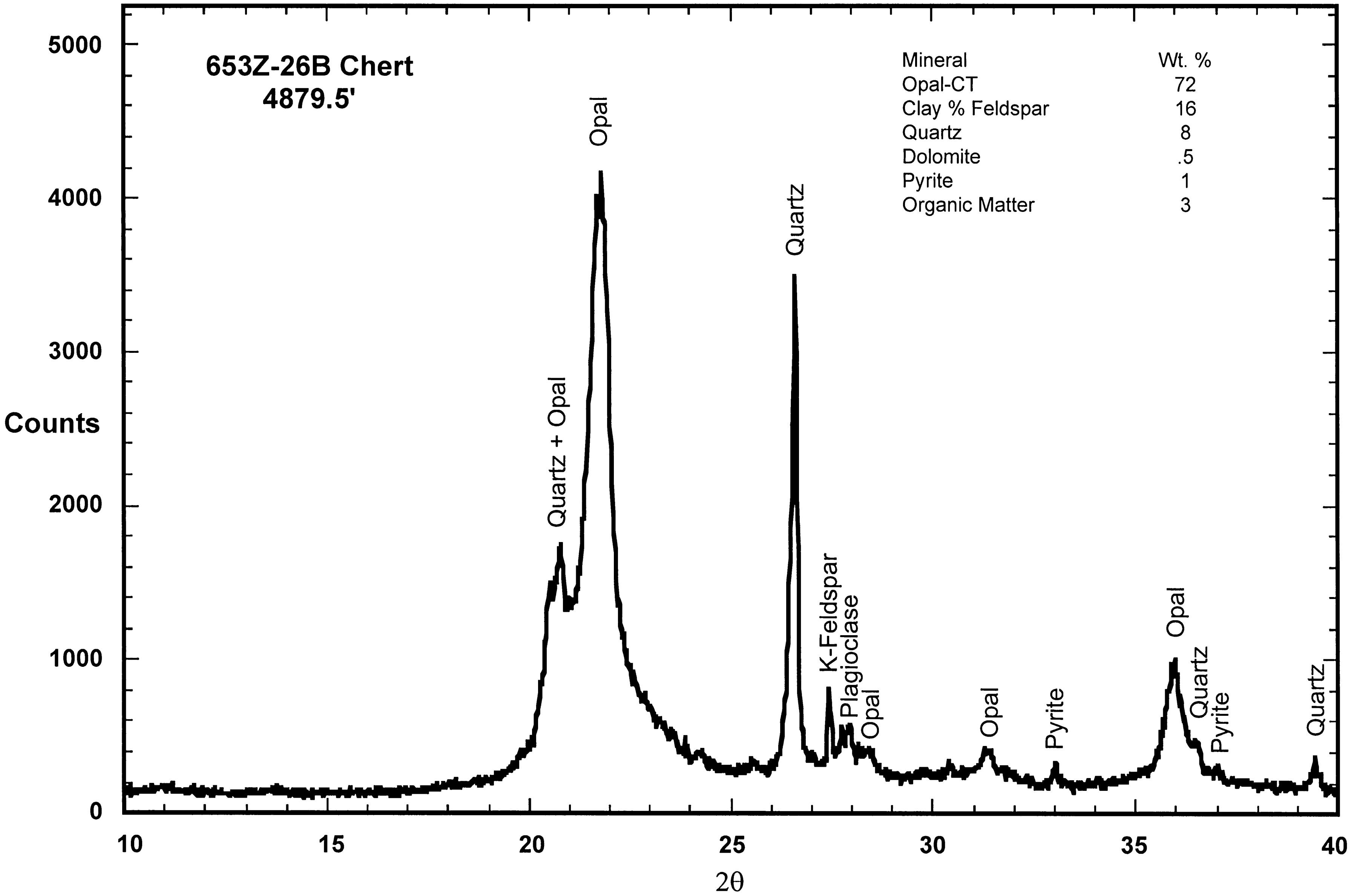

Figure 1.2-2. X-ray diffraction pattern of opal-CT porcelanite, 4879.5 ft.

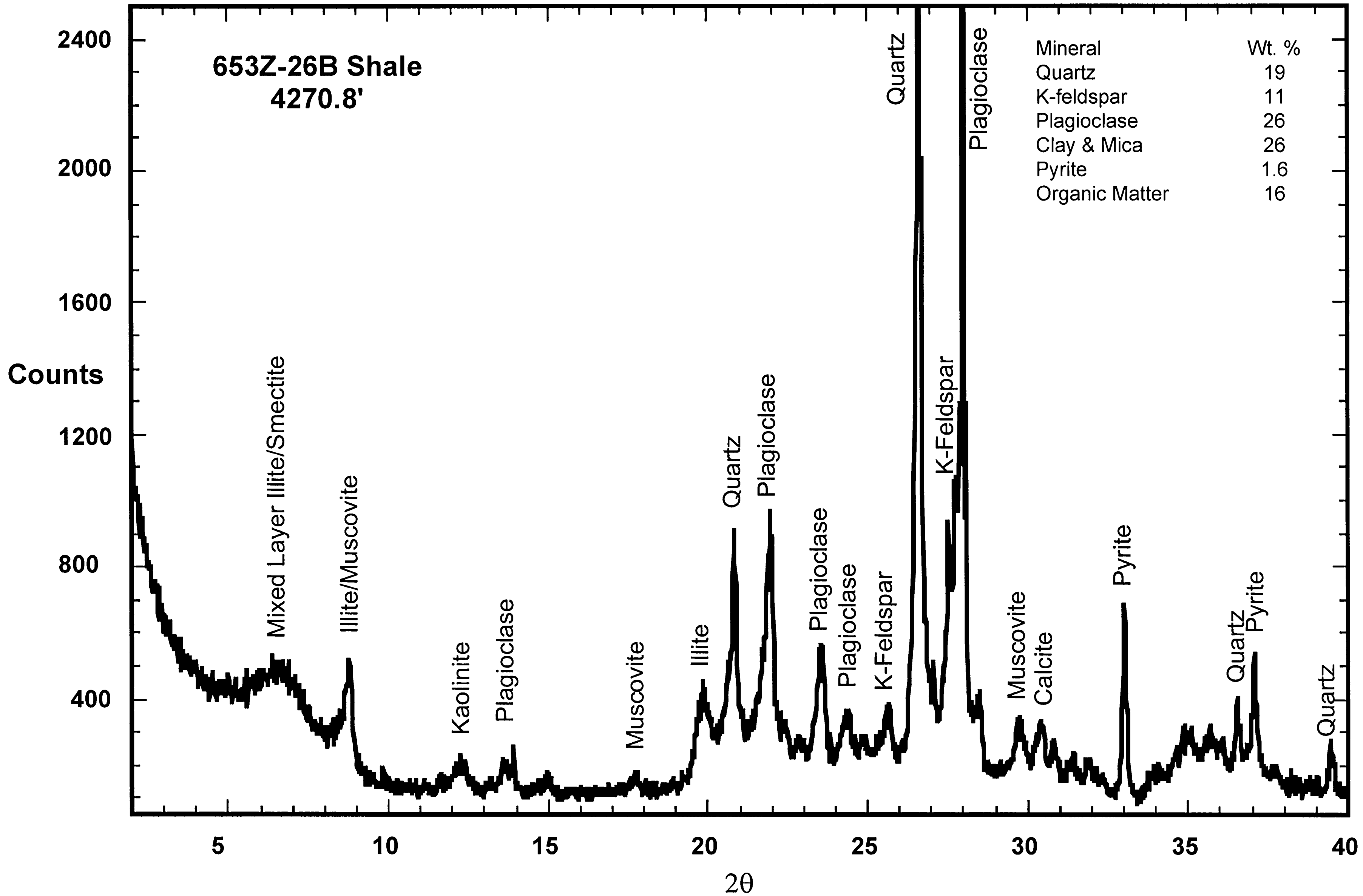

Figure 1.2-3. X-ray diffraction pattern of "end member" shale bed, 4270.8 ft.

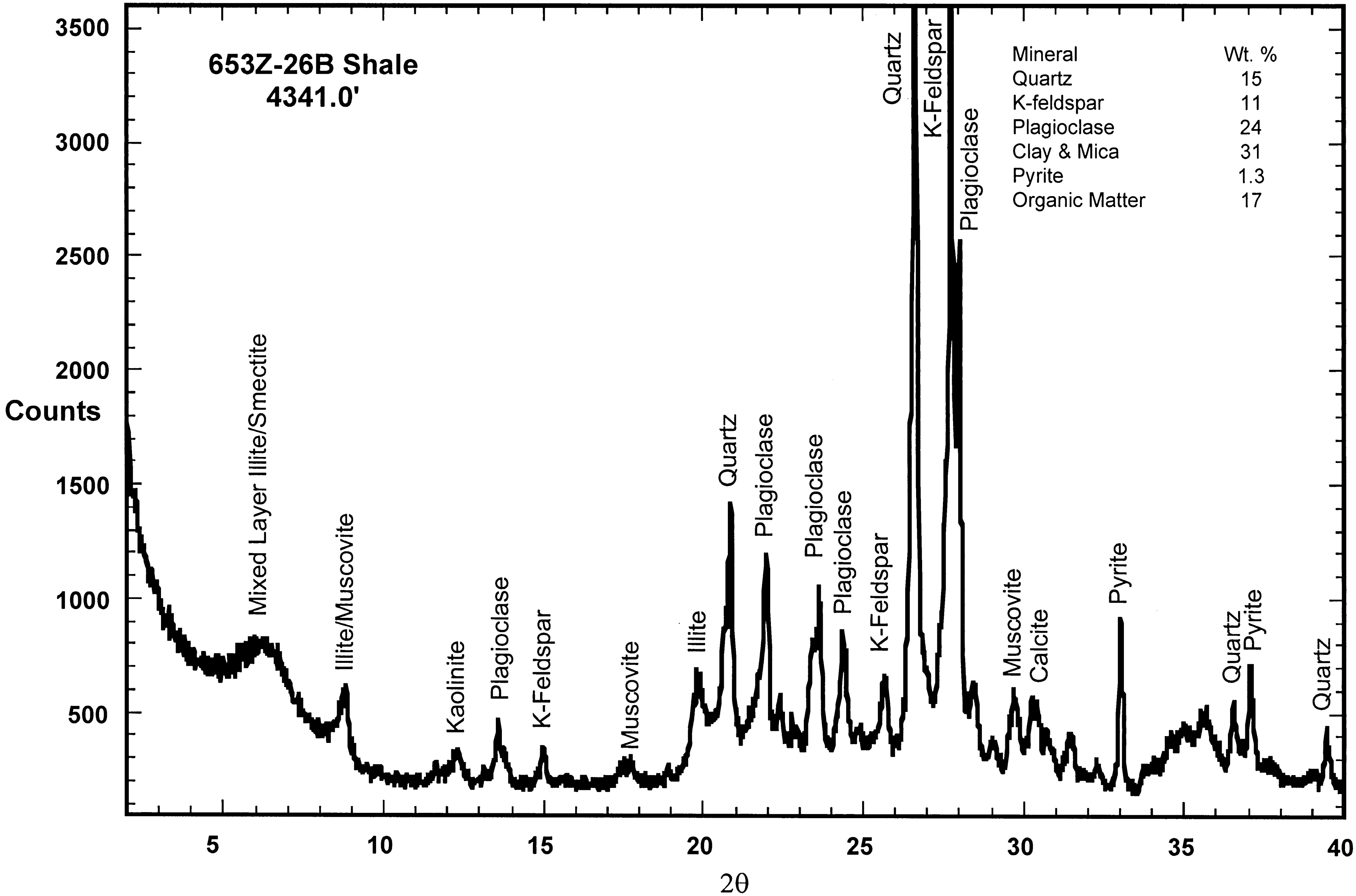

Figure 1.2-4. X-ray diffraction pattern of "end member" shale bed, 4341.0 ft.

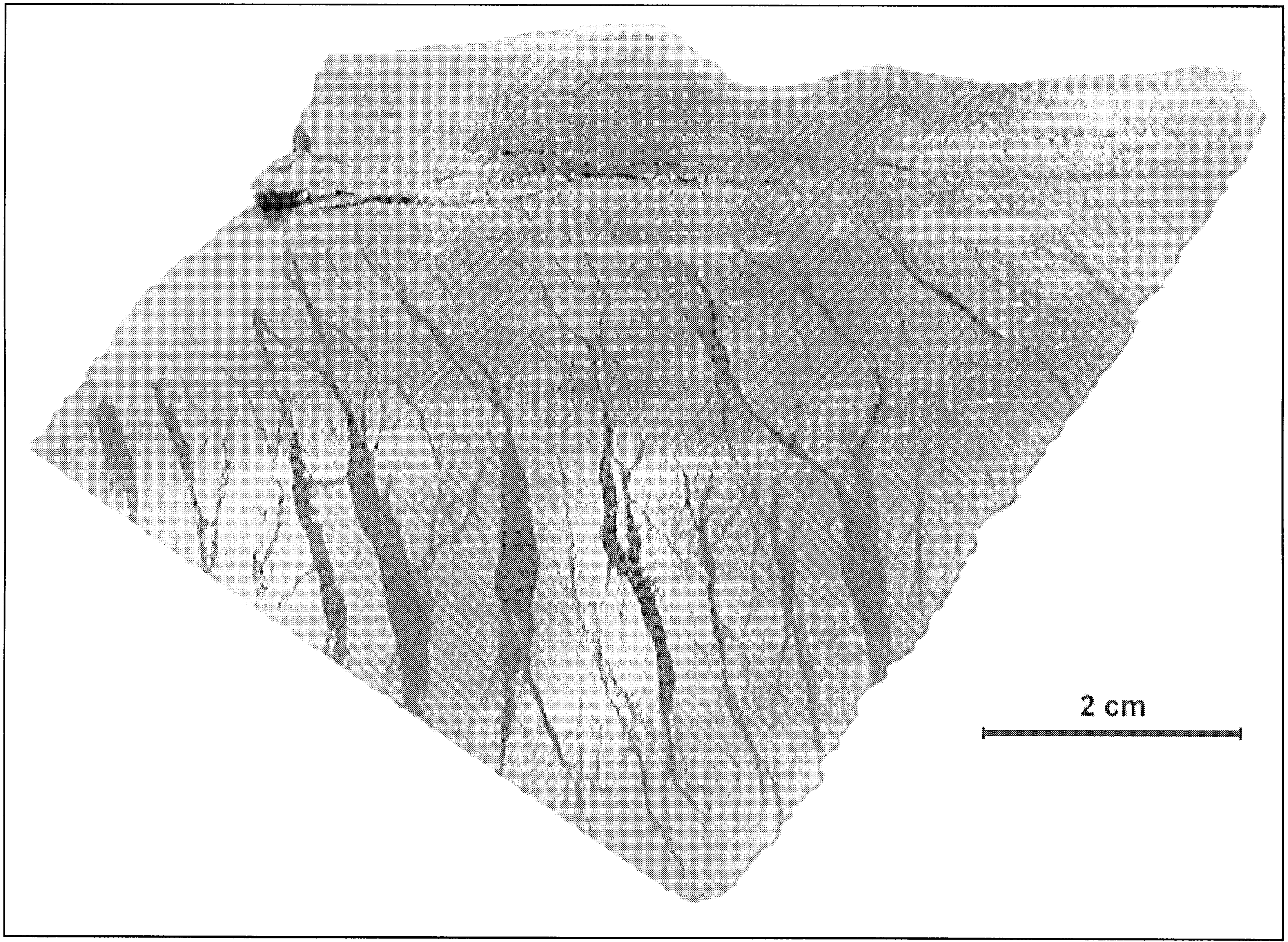

Figure 1.2-5. Photograph of mud-filled veins in porcelanite, 3299.7 ft., 342-17Z well, McKittrick Field. This sample was disaggregated to provide material for the chemical and XRD analyses of the mud-filled veins and rock matrix.

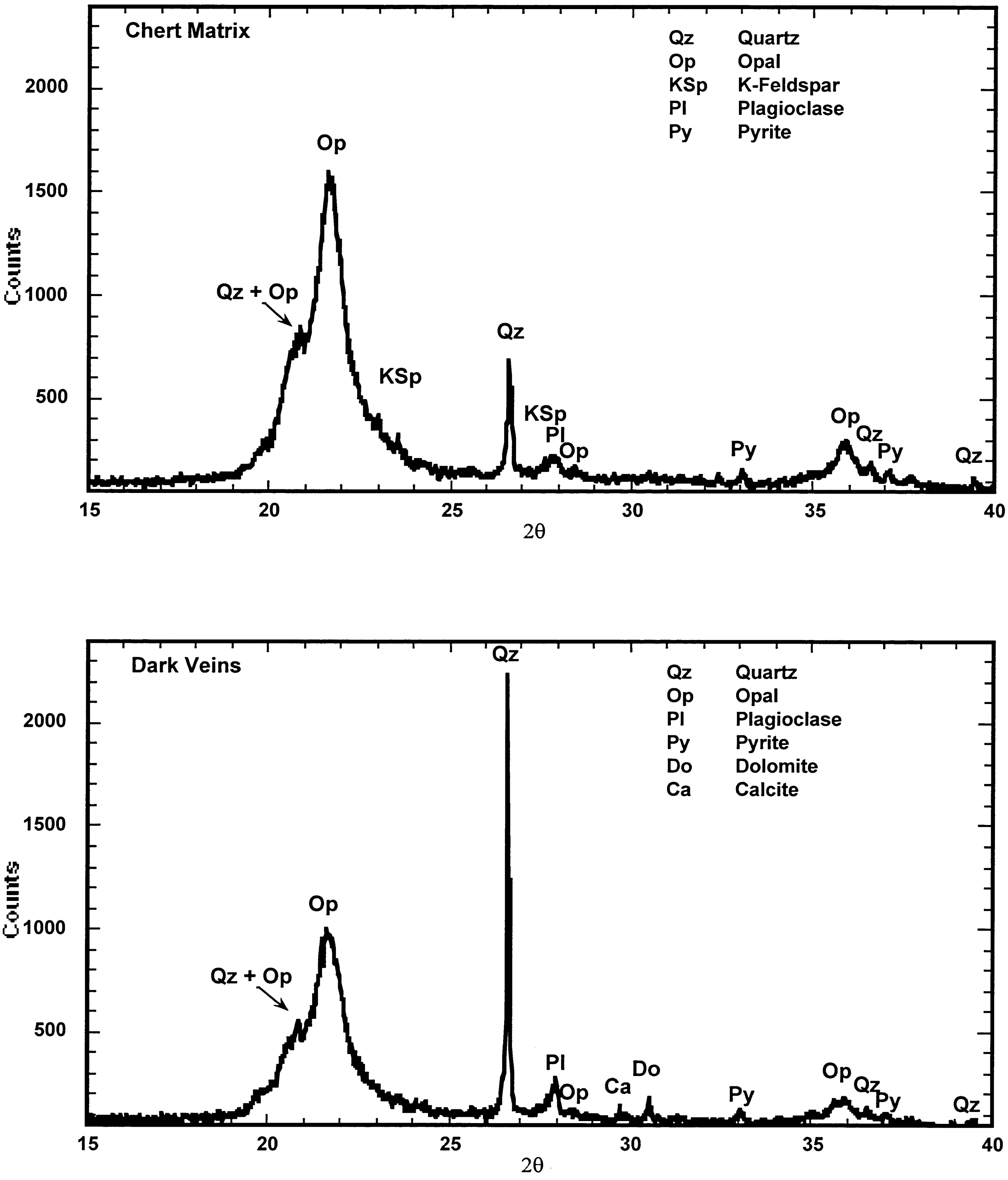

Figure 1.2-6. X-ray diffraction patterns of mud-filled veins and rock matrix. The mud-filled veins have a high ratio of quartz and aluminosilicates to opal-CT than the rock matrix.

1.3. CORE ANALYSES & ROCK PROPERTIES: ESTIMATING INITIAL OIL SATURATION IN THE ANTELOPE SHALE

Ed deZabala
Chevron Petroleum Technology Company

SUMMARY

Available core analysis results for the Antelope Shale in Buena Vista Hills Well 653Z-26B include: routine core analyses, mercury intrusion/extrusion capillary pressure tests, USBM/Amott wettability tests, spontaneous imbibition tests, and water/oil and gas/oil relative permeability tests. The aim of this memorandum is to analyze the available core analysis results in a consistent manner.

When classified by four main rock types, all the core analyses together yield a fairly consistent model for porosity, permeability, and initial and current oil saturations. The four rock types are: 1) opal-CT (porcelanite), 2) opal-CT/siltstone (clayey porcelanite), 3) sandstones (low-clay sandstones) and 4) sandstone/siltstones (sandstones with significant clay/silt content). Together, opal-CT and opal-CT/siltstones comprise most (~80 to 90%) of the rock volume.

Opal-CT has high porosity (> 0.30), low bulk density (RHOB $\leq$ 1.95 g/cc), fairly low permeability ($K_a \leq 0.2$ md) and low oil saturations, S_{oi}. Routine core analysis indicates average current oil saturations of about 0.14. Careful new analysis of mercury intrusion tests and other special core analysis tests indicate that average initial oil saturations were about 0.21. The new analysis also indicates that S_{oi} increases with porosity in opal-CT rocks. Wettability tests indicate that opal-CT tends to be weakly- to moderately water wet, with some mixed wet tendencies. Wettability and spontaneous imbibition tests indicate that oil recovery occurs by spontaneous imbibition of brine, even with low initial oil saturations ($S_{oi} \leq 0.20$). Oil recovery by spontaneous imbibition is effective on core length scales (~1 to 2 in.) in opal-CT, but it is not clear if it has been an effective mechanism in the reservoir.

Opal-CT/siltstones have lower porosity (< 0.30), moderate bulk densities (2.00 g/cc to 2.40 g/cc), low permeability ($K_a \leq 1$ md) and low oil saturations. Routine core analysis indicates average current oil $S_o = 0.13$. Special core analyses indicate average initial So = 0.36. The difference is not significant because only a few (5 samples) of higher-permeability opal-CT/siltstones were analyzed. Opal-CT/siltstones are similar to opal-CT, but with lower porosity.

Sandstones have moderate porosities (0.18 to 0.30), high grain densities (RHOG $\geq$ 2.60 g/cc), high permeability (5 md to 200 md), and high oil saturations. Routine core analyses indicate an average current $S_o = 0.37$ in sandstones. Special core analyses indicate an average initial $S_o = 0.73$ and an average residual saturation, $S_{orw} = 0.31$.

Sandstone/siltstones have lower porosities (0.08 to 0.23), moderate grain densities (2.55 g/cc to 2.63 g/cc), lower permeabilities (0.2 md to 10 md) than sandstones, and moderate oil saturations. Routine core analyses indicate an average current $S_o = 0.21$. Special core analyses indicate an average initial $S_o = 0.47$ and an average residual saturation, $S_{orw} = 0.22$.

Opal-CT, opal-CT/siltstones, and sandstone/siltstones are to be weakly- to moderately water wet with some mixed wet tendencies. Sandstones are moderately to strongly water wet. No evidence was found for oil wet rocks.

Even with the low initial oil saturations, opal-CT and opal-CT/siltstones probably contain a minimum of ~80% of the initial oil volume. The available core analysis data indicate that initial oil saturations in opal-CT and sandstones can be correlated reasonably well using two different linear trends, using either porosity or bulk density as the dependent variable. In both cases, the linear trends overlap only over small ranges of porosity of bulk density. However, oil saturations in the mixed rock types (opal-CT/siltstone and sandstone/siltstone) are not represented very well by the bilinear correlations.

RECOMMENDATIONS & OBSERVATIONS

Core analysis tests indicate that oil recovery from siliceous shales is effective on the scale of a plug sample. Additional work is necessary to determine if it can be effective at larger length scales in the reservoir.

Transition zone effects were not considered in this memorandum. Initial oil saturations correspond to $S_o = 1 - S_{wirr}$, where S_{wirr} is an irreducible water saturation. Additional analysis of the available capillary pressure data would help define the shape of a transition zone.

Carefully designed mercury intrusion and extrusion capillary pressure tests are rapid and relatively inexpensive core analysis tools. Results from this memorandum indicate that mercury intrusion/extrusion tests yield some results comparable to more expensive and time-consuming oil/water tests. The use of mercury intrusion/extrusion tests should be expanded to other siliceous shale rock types and reservoirs.

AVAILABLE CORE ANALYSIS RESULTS

The special core analysis (SCAL) test program included: gas/oil and water/oil relative permeability tests, USBM/Amott wettability tests, spontaneous imbibition recovery tests, and high- and low-pressure mercury intrusion/extrusion tests. All SCAL test procedures were designed at Chevron Petroleum Technology Company (CPTC), La Habra.

Relative permeability tests were conducted by Core Laboratories (Bakersfield, CA) according to detailed written procedures supplied by CPTC. Relative permeability tests were aimed at the more permeable sandstone and siltstone rock types. Conventional relative permeability tests were not conducted using low-permeability (e.g. <0.1 md) siliceous shale samples for two reasons: 1) laboratory results on such samples are difficult to interpret and 2) direct viscous displacement of oil by water is unlikely. Results of 8 unsteady state (USS) gas/oil relative permeability tests and seven (7) USS water/oil relative permeability tests are reported by Core Laboratories[1]. Relative permeability tests were aimed at the more permeable sandstone and siltstone rock types. After one of the gas/oil tests the sample failed, so the subsequent water/oil tests was not conducted. Due to a shortage of appropriate plug samples (e.g., sandstones), gas/oil and water/oil tests were conducted on the same samples. After the gas/oil test was terminated, the plug sample was re-saturated with oil and a water/oil test was conducted. The test order ensures that both displacements begin with the same initial water saturation, Swi.

Three ambient-condition USBM/Amott wettability tests were conducted by Core Laboratories (Bakersfield). The aim of the tests was to gauge the wettability, initial oil saturation, and movable oil saturation in low-permeability siliceous shales (e.g., opal-CT).

Four reservoir-condition (stock tank crude oil at T = 155 °F) spontaneous imbibition recovery tests were conducted at CPTC, La Habra. The aim of the tests was to gauge possible oil recovery from low-permeability siliceous shales by spontaneous imbibition of water. Waterflood oil recovery from low-permeability siliceous shale is more likely to occur by spontaneous imbibition of water from neighboring high-permeability sand bodies (i.e., by countercurrent flow) than by direct viscous displacement by water.

Core Laboratories (Carrollton, TX) conducted 15 high-pressure mercury intrusion tests, using a separate suite of siliceous shale samples. After the spontaneous imbibition tests were terminated, all four (4) samples were subjected to high-pressure mercury intrusion at Chevron Overseas Petroleum's Geosciences Laboratory (San Ramon, CA). After the relative permeability tests were terminated, each plug sample was divided into two nearly equal pieces. One piece was subjected to high-pressure mercury intrusion while the other was subjected to low-pressure mercury intrusion. The high-pressure mercury intrusion tests were designed to measure the entire pore system, including microporosity, for each sample. The low-pressure tests were designed to investigate the behavior of larger pores: those most likely to be invaded by hydrocarbon at reasonable column heights in the reservoir.

In all, 35 mercury intrusion capillary pressure test were performed. In all cases, after intrusion to the maximum specified pressure, the mercury extrusion process (non-wetting liquid mercury expelled from sample as pressure is reduced) was also monitored. For each of the rock types the mercury intrusion/extrusion tests were designed to: 1) measure the distribution of pore sizes, 2) estimate initial oil saturations and permeability, and 3) estimate residual oil saturations. Also, results of mercury intrusion tests were compared to results of oil/water displacement tests.

MERCURY CAPILLARY PRESSURE TEST RESULTS

Results of the mercury intrusion tests are summarized in Table 1.3-1. Details of the test results and procedures are included in Core Laboratories final report[2]. Mercury capillary pressure can be converted to "oil/water" capillary pressure by the ratio of interfacial forces for the two fluid systems. Throughout this report, we assume mercury/mercury vapor interfacial forces {i.e., $\sigma*\cos(\theta)$} equal to 370 dyne/cm and oil/water interfacial forces equal to 30 dyne/cm. Thus, $P_c(O/W) = 30*P_c(Hg)/370 = Pc(Hg)/12.33$. For equating hydrocarbon column heights to capillary pressure, we assume an oil/water gradient of 0.1 psia/foot.

The suite of samples was divided into four main rock types[3]: 1) opal-CT, 2) opal-CT/siltstone, 3) sandstone, and 4) sandstone/siltstone. In Table 1.3-1, sample entries are sorted by rock type, then by depth. In this memorandum, opal-CT refers to porcelanite. Opal-CT/siltstone refers to siliceous shales with significant amounts of both biogenic silica and detrital clay/silt particles. Sandstones refer to clays with only minor amounts of clay and sandstone/siltstones refer to rocks with significant amounts of sand, silt, and clay. Sandstones and sandstone/siltstones contain only minor amounts of biogenic silica.

Typically, opal-CT contains mostly biogenic silica with low grain density (RHOG < 2.40 g/cc), high porosity (0.30 to 0.40), and low permeability ($K_a < 0.2$ md). Figure 1.3-1 illustrates a typical mercury intrusion/extrusion result for opal-CT with a sample from a depth of 3958.05 feet. It has low grain density (RHOG = 2.236 g/cc), high porosity (0.369), and low permeability ($K_a = 0.093$ md). The high mercury entry pressure, $P_e =$ 295 psia, is equivalent to and oil/water entry pressure, $P_e = 23.9$ psia. Even at a mercury $P_c = 10{,}000$ psia, which is equivalent to an oil/water $P_c = 810$ psia, only 30% of the pore space is occupied by non-wetting phase (liquid Hg). At the maximum intrusion pressure of 54700 psia, 99.8% of the pore volume is occupied. Upon reducing the applied pressure back to atmospheric (14.7 psia), about 30% of the pore space is occupied by residual non-wetting phase. With the assumed oil/water gradient, mercury intrusion results indicate that oil would begin entering the opal-CT at column heights of ~240 feet. A column height of more than 8000 feet would be required to achieve an oil saturation of only ~30%! Lower entry pressures and larger oil saturations at smaller column heights could be explained by invoking wettability corrections. However, unless it is assumed to be strongly oil-wet, oil saturations in opal-CT are likely to be significantly less than 30% for reasonable column heights. Results of wettability tests, discussed in a subsequent section, do not indicate that any of the rocks are strongly oil wet.

Opal-CT/siltstone contains mixtures of biogenic silica with significant amounts of clay, silt, and sand particles. Typical opal-CT/siltstones have intermediate grain densities (2.40 g/cc to 2.55 g/cc), somewhat lower porosity (0.15 to 0.30), and low permeability ($K_a \leq 1$ md). Figure 1.3-2 illustrates two mercury intrusion/extrusion results for opal-CT/siltstone samples from a depth of 4512.35 feet. Solid lines trace the P_c-S_w history for the high-pressure (to 49800 psia) test; the dashed lines trace the P_c-S_w history for the low-pressure (to 6980 psia) test. Both samples indicate mercury entry pressure ranging from 75 to 80 psia, which corresponds to oil/water entry pressure ranging from 6.1 to 6.4 psia. Lower entry pressures for opal-CT/siltstones indicate the presence of some larger pores compared to the opal-CT end member. At a mercury capillary pressure of 5000 psia (oil/water P_c ~405 psia), the non-wetting phase saturation ranges from ~30% for the high-pressure test, to ~40% for the low-pressure test. For the high-pressure test, 97.9% of the pore space is occupied by mercury at P_c = 49700 psia. For the low-pressure test, 54.8% of the pore space is occupied by mercury at P_c = 6980 psia. Differences in porosity, permeability, and capillary pressure behavior (See Figure 1.3-2 or Table 1.3-1) for the two samples reflect some core-scale heterogeneity. Nonetheless, both results are fairly similar. While oil may enter it at smaller column heights than opal-CT, opal-CT/siltstones are not likely to contain significantly more oil than opal-CT. Maximum possible oil saturations are likely to be less than 30% to 40% at reasonable hydrocarbon column heights.

Sandstones contain mostly sand and small amounts of silt/clay particles. Typical sandstones have RHOG > 2.60 g/cc, moderate porosity (0.18 to 0.30), and higher permeability (5 md to 200 md). Figure 1.3-3 illustrates typical mercury intrusion/extrusion results for two sandstone samples from a depth of 4432.65 feet. Measured porosity, permeability, and RHOG for both samples are almost the same indicating a very low level of core-scale heterogeneity. This sample was one of best sandstone samples recovered in the 653Z-26B well. Both P_c-S_w curves are very similar. Solid lines trace the P_c-S_w history for the high-pressure (to 49800 psia) test; the dashed lines trace the P_c-S_w history for the low-pressure (to 198 psia) test. The high- and low-pressure tests indicate mercury entry pressures of 7.8 and 11.5 psia, respectively. For the oil/water system, the equivalent entry pressures are 0.63 and 0.93 psia respectively. For the high-pressure test, 96.5% of the pore space is occupied by mercury at P_c = 49800 psia. For the low-pressure test, 75.2% of the pore space is occupied by mercury at P_c = 198 psia (equivalent oil/water P_c ~ 16 psia or an oil column of ~ 160 feet). Oil will enter the high-permeability sandstones at small column heights (< 10 feet). At reasonable hydrocarbon column heights, Sandstones are likely to contain initial oil saturations of 70% to 85%.

Sandstone/siltstones contain significant amounts of silt and clay with some larger sand grains but very little biogenic silica. Typical sandstone/siltstones have moderate grain density (2.55 g/cc to 2.63 g/cc), lower porosity (0.08 to 0.23), and lower permeability (K_a < 5 md) than sandstones. A small minority of samples classified as sandstone/siltstones may contain some carbonate cementation so that RHOG > 2.65 g/cc. Figure 1.3-4 illustrates typical mercury intrusion/ extrusion results for two sandstone/siltstone samples from a depth of 4518.55 feet. Measured porosity, permeability, and RHOG for both samples are almost the same, indicating a very low level of core-scale heterogeneity. The high and low-pressure curves follow exactly the same P_c-S_w history during the intrusion cycle. Both tests indicate mercury entry pressure of ~95 psia, which corresponds to an oil/water entry pressure of 7.7 psia. For the high-pressure test, 95.4% of the total pore space is occupied by mercury at the maximum P_c = 49900 psia. For the low-pressure test, 54.2% of the pore space is occupied at the maximum P_c = 3980 psia. At similar column heights, Sandstone/siltstones will contain somewhat higher oil saturations than opal-CT/siltstones. At reasonable hydrocarbon column heights, sandstone/siltstones likely contain oil saturations ranging from 40% to 50%.

Permeability & Entry Pressure from Mercury Intrusion Tests

For samples listed in Table 1.3-1, pore volume, grain volume, and porosity were measured using helium Boyle's Law expansion. Air permeability was measured using a conventional air permeameter. To check the measured air permeability, the mercury intrusion results were used to calculate the air permeability using Swanson's method, as outlined by Kamath[4]. For a large database of Chevron mercury intrusion samples, including a large number from siliceous shales from Point Arguello, Kamath found:

$$K_a\,(\mathrm{md}) = 347*(\phi*R)^{1.6},$$

where ϕ is given as a fraction and R is the maximum value of the quantity $\{S_{nw}/P_c\}$ (in units of %/psia). S_{nw} is the non-wetting phase saturation. For most of the samples, measured and calculated permeabilities are very close. For a few samples, mostly opal-CT/siltstones, the measured permeabilities are two- to three orders of magnitude greater than that estimated from the mercury intrusion tests. For those samples, we conclude that the measured permeabilities are too high due to fractures in the plug sample. The fractures are not natural, they probably occurred during core handling. For the case of fractured samples, we use the calculated permeability rather than the measured permeability. Where the measured and calculated permeabilities are in reasonable agreement, we calculate a new permeability, reported as K_a "Best", which is the geometric mean of the two results. We use K_a "Best" as better measure of the true permeability (See Table 1.3-1) for all correlations. Figure 1.3-5 plots K_a "Best" versus porosity for all mercury intrusion samples. With a large degree of scatter, Figure 1.3-5 suggests a decreasing trend of permeability with porosity. Figure 1.3-5 actually contains several porosity-permeability trends as a function of rock type. Sandstones and sandstone/siltstones indicate an increasing trend of permeability with porosity, with porosity ranging from 0.08 to 0.30. Opal-CT samples appear to have nearly constant permeability with porosity ranging from 0.30 to ~0.45. Opal-CT/siltstones appear to extend the opal-CT permeability trend to lower porosity values (0.15 to 0.30). The porosity-permeability trends reflect expected trends due to grain size and sorting.

Figure 1.3-6 plots Ka "Best" versus RHOB (bulk density) for all samples. We select RHOB to correlate with permeability because RHOB may be easier to extract from older log suites than porosity. In Figure 1.3-6, sandstones and some siltstones form a decreasing trend of permeability with RHOB that reflects mostly decreases in porosity. The sandstone trend appears to be valid for RHOB > 2.16 g/cc. For all opal-CT samples and some opal-CT/siltstones, a separate trend appears to be valid for RHOB < 2.16 g/cc. However, for opal-CT/siltstones and sandstone/ siltstones with RHOB > 2.16 g/cc, the simple RHOB-permeability trends are not appropriate.

Figure 1.3-7 plots oil/water entry pressure (estimated from mercury intrusion results) versus K_a "Best" for all samples. Entry pressure is negatively correlated with permeability. The correlation appears to be nearly linear on a log-log scale. For Sandstones with K_a ranging from 5 md to 200 md, entry pressure ranges from ~1 psia to

~4 psia. Oil will begin to enter sandstones at fairly small column heights (i.e., 10 to 40 feet above a free water level). For sandstone/siltstones and some opal-CT/siltstones with K_a ranging from ~0.1 md to 5 md, entry pressure ranges from ~4 psia to ~10 psia. At moderate hydrocarbon column heights (i.e., 40 to 100 feet), oil will begin entering sandstone/siltstones and some opal-CT/siltstones. For low-permeability opal-CT, entry pressure ranges from ~30 psia up to 300 psia. Hydrocarbon column heights ranging from ~300 feet up to ~3000 feet may be necessary for oil to enter opal-CT intervals. Smaller column heights might be sufficient for oil entry if opal-CT rocks prove to be less water wet than our initial assumption (i.e., $\sigma^*\cos\theta$ significantly less 30 dyne/cm). Subsequent analyses in this memorandum suggest that oil/water interfacial forces should be closer to ~10 dyne/cm rather than 30 dyne/cm. With that correction, oil column heights ranging from ~100 feet up to 1000 feet would be sufficient for oil to enter opal-CT rocks.

Wettability, important consideration particularly for opal-CT rocks, is discussed in detail in the next section.

WETTABILITY & SPONTANEOUS IMBIBITION RECOVERY TEST RESULTS

USBM/Amott Tests

Core Laboratories conducted USBM/Amott wettability tests using three plug samples. Sample properties and test results are summarized in Table 1.3-2. Two of the samples, from depths of 3989.20 feet and 4355.95 are opal-CT, whereas, the sample from a depth of 4315.60 feet is a sandstone/siltstone. Basic sample properties (ϕ, K_a, and RHOG) for each sample are typical for the assigned rock types. After mild miscible cleaning with toluene/methanol at ambient temperature, methanol was miscibly replaced by brine. The mild miscible extraction process is not expected to alter wettability. The brine-saturated samples were drained to S_{wi} at oil/water capillary pressures of ~190 psia (equivalent to mercury intrusion P_c ~ 2340 psia). Samples were drained in a centrifuge with stock tank crude oil as the non-wetting phase. For the two opal-CT samples, Swi values are fairly large and appear to be in agreement with mercury intrusion results on similar samples. For the Sandstone/siltstone sample, Swi of ~0.40 is also in good agreement with mercury intrusion results.

Figure 1.3-8 plots the P_c-S_w history for the wettability test on the opal-CT sample #1 from a depth of 3989.20 feet. Despite the large initial water saturation, $S_{wi} = 0.682$, spontaneous imbibition (i.e., at $P_c = 0$) of brine recovered much of the oil, leaving $S_w = 0.907$. Spontaneous brine imbibition recovered 70.7% of the initial oil saturation. Subsequent forced imbibition in the centrifuge recovered only a small amount of additional oil, $S_{w,max} = 0.939$, even with an imposed capillary pressure of –186 psia. Subsequently, the sample was removed from the centrifuge and allowed to spontaneously imbibe oil. A negligible amount of oil imbibition was observed ($\Delta S_w = -0.007$). Subsequent forced drainage with oil yielded $S_w = 0.860$ at $P_c = +187.6$ psia, indicating a large amount of water-trapping during secondary drainage. The large amount of oil recovery by spontaneous imbibition and the negligible amount oil imbibition indicate that the opal-CT sample is moderately- to strongly-water wet, which is reflected by the value of the water-oil Amott index (+0.78). The lower value of the USBM index (+0.33) suggests that the sample is weakly water wet with no mixed-wet behavior. The USBM index is determined by comparing the areas under the P_c-S_w curves. The large degree of water-trapping during secondary imbibition skewed the USBM results. The Amott wettability index is a better indication of wettability for sample #1.

Figure 1.3-9 plots the P_c-S_w history for the wettability test on the sandstone/siltstone sample #5 from a depth of 4315.60 feet. From $S_{wi} = 0.393$ spontaneous brine imbibition (i.e., at $P_c = 0$) recovered 49.7% of the initial oil ($S_w = 0.695$). Subsequent forced imbibition recovered 43.5 % more oil, yielding $S_w = 0.959$ at $P_c = -201.7$ psia. After removal from the centrifuge, sample #5 spontaneously imbibed some oil ($\Delta S_w = -0.068$), reducing S_w to 0.891. Forced drainage with oil yielded $S_w = 0.549$ at $P_c = +197.9$ psia. Overall, sample #5 is weakly water wet with mixed-wet behavior. That behavior is reflected by the water-oil Amott index (+0.37). The USBM index (-0.08) indicates a slight oil-wet tendency. The Amott index is a better indication of wettability than the USBM index. Spontaneous imbibition of both oil and water occurred, but water imbibition was much stronger. Mixed-wet behavior is exemplified by the large amount of additional oil recovery (43.5% initial oil) by forced imbibition and the very low final oil saturation ($S_{or} = 0.041$?). Much of the oil recovered by forced imbibition was re-mobilized oil due to the application of large centrifugal forces in the centrifuge. That displacement process does not represent reservoir behavior. It is likely that the oil saturation established by spontaneous imbibition alone is close to the waterflood residual oil saturation in the reservoir (i.e., $S_{orw} = 0.305$) for sample #5.

Figure 1.3-10 plots the P_c-S_w history for the wettability test on opal-CT sample #6 from a depth of 4355.95 feet. Even with a large initial water saturation, $S_{wi} = 0.790$, spontaneous brine imbibition recovered 49% of the initial oil, leaving $S_w = 0.894$. Very little additional recovery occurred by forced imbibition of water. At $P_c = -180$ psia, $S_w = 0.902$. Spontaneous imbibition of oil recovered some water ($\Delta S_w = -0.046$). Overall, opal-CT sample #6 is moderately water wet with some mixed wet tendencies. That is reflected by the water-oil Amott index (+0.68). The USBM index (+0.90) suggests that sample #6 is strongly-water wet. Again, the Amott index is a better indication of wettability than the USBM index.

The wettability tests indicate that opal-CT and sandstone/siltstone samples show some mixed wet tendencies with overall wettability ranging from weakly to moderately water wet. At initial water saturations similar to those in the reservoir, all samples strongly imbibed brine. For the two opal-CT samples, oil recovery by spontaneous imbibition ranged from 0.104 PV to 0.225 PV (49% and 70% of the initial oil in place, respectively). Surprisingly, the Sandstone/siltstone sample exhibited the weakest water wet behavior, yet 0.302 PV oil was recovered by spontaneous imbibition (43.5% recovery of initial oil).

Spontaneous Imbibition Tests

Four reservoir-condition spontaneous imbibition tests were conducted at CPTC. Sample properties are summarized in Table 1.3-3. All samples were 1.5" diameter by ~2.0 " long. All four samples fall into the broad classification of opal-CT. Initially, the four samples were selected based on visual observations[6]. One sample is a "thickly laminated" shale (thin beds with ~0.5 cm thickness), one sample is a "thinly laminated" shale (thin beds with sub-millimeter thickness), and two samples are termed "water-sucking" shales[6] (no visible bedding features but slabbed core surface strongly imbibed water). Plug samples were taken "as is" with no solvent extraction. Stock tank crude oil was injected at a pressure of 1000 psia to saturate the samples. Imbibition tests were conducted by immersing the oil-saturated samples in synthetic Buena Vista Hills brine in specially-designed[7] imbibition cells at T = 155 °F and observing oil production into a graduated pipette.

Figure 1.3-11 plots oil recovery versus imbibition time for all four samples. After two days (~3000 minutes) of imbibition, the thickly-laminated shale (#26A) produced 0.048 PV oil, about 55.2% of the initial oil. Over the same time frame, the thinly-laminated shale (#24) produced 0.087 PV oil, about 21.2 % of the initial oil. Both tests were terminated due to equipment problems before the imbibition process was complete (See Figure 11.3-1). For subsequent tests on samples #27 and #29, experiments were conducted for more than 5 days. Samples #27 and #29, both "water-sucking" shales, recovered 0.063 and 0.089 PV oil, respectively. That corresponds to recoveries of 48% and 38.2% of the initial oil.

Despite fairly low initial oil saturations in opal-CT rocks, spontaneous imbibition of brine can recover a significant fraction of the initial oil, at least on the scale of a core plug (1.5 inch diameter by 2.0 inch long). Wettability and imbibition tests indicate that spontaneous imbibition recovery ranged from 20% to 70% of the oil in place, with an average of ~40%.

Figure 1.3-11 indicates that half of the total oil recovered by spontaneous imbibition occurred at after about 600 to 800 minutes (~10 to 13 hours) in the small plug samples. In the plug samples, the maximum length from any core surface is ~1 inch. All surfaces of the plug were available for flow. The long imbibition times for relatively short lengths in the opal-CT samples indicates that oil recovery by spontaneous imbibition is a slow process. In the reservoir, oil recovery by counter-current flow from opal-CT by spontaneous imbibition of brine from neighboring sandstones will depend on the available contact area between the two rock types. Spontaneous imbibition may be effective only for short distances (several feet at most?) into opal-CT from neighboring sand bodies. Moreover, oil recovery by spontaneous imbibition begins only as the sandstone Sw increases to high levels. Thus, it is likely that most of the oil recovery from opal-CT by spontaneous imbibition would be observed at the tail end of a waterflood process.

Additional Wettability Information

Qualitative wellsite wettability tests[8] were conducted by Horizon Well Logging on chip samples from the bottom of each core section (~2 samples per 30 feet of core) within 2 hours of the core reaching the surface. Qualitative tests did not indicate strong wettability in either direction. Thin sandstone beds tended to be water wet. Samples below a depth of 4570 feet were consistently water wet.

INITIAL OIL SATURATION

Initial oil saturation in the Antelope Shale at Buena Vista Hills is an important concern. High initial oil saturations (>70%) are likely in Sandstones and moderate initial oil saturations (~40 to 50%) are likely in the Sandstone/siltstones. Oil saturations in the lower-permeability opal-CT and opal-CT/siltstone rock types are probably much lower. Even with much lower oil saturations, there is likely to be a large volume of initial oil in opal-CT and opal-CT/siltstones: opal-CT porosity tends to be higher than sandstone porosity and thin sandstones and siltstones typically comprise less than 10% of the Antelope Shale.

Table 1.3-4 summarizes average properties by rock type from routine core analyses over the depth range of 3955.5 to 4907.4 feet in Well 653Z-26B. Samples were "binned" into rock types using simple cutoffs for porosity, bulk density, and permeability. Core properties were measured on 926 plug samples (~1 per foot).

Although some of the very thin (<0.5 inch thickness) sandstones and siltstones were missed by sampling process, Table 4 indicates that opal-CT and opal-CT/siltstones comprise almost 92% of the interval, sandstones only 2%. Routine core analyses indicate that the current average oil saturation in the opal-CT is 0.141. Current average oil saturation in the opal-CT/siltstones is 0.132. Total fluid saturations in the tested plug samples (i.e., So +Sw) were close to unity. Because the Antelope Shale is pressure depleted, there isn't much solution gas to drive mobile fluids from the core as it is tripped to the surface. Also, it is unlikely that spontaneous imbibition of water has reduced oil saturations very much in opal-CT and opal-CT/siltstones, either during the reservoir's production history or during the coring process. Thus, for opal-CT rocks, oil saturations from routine core analysis, once corrected for shrinkage, accurately reflects initial oil saturations. Conversely, for routine core analyses of sandstone and sandstone/siltstone intervals, total fluid saturations are often much less than unity. That probably reflects significant current gas saturations in depleted zones. Thus, routine core oil saturations in Sandstone and Sandstone/siltstone intervals probably reflects waterflood residual oil saturations. Given the results in Table 1.3-4, that corresponds to S_{orw} ~ 0.37 in Sandstones and S_{orw} ~0.21 in Sandstone/siltstones. Both values are consistent with relative permeability results presented in the next section.

Table 1.3-4 gives a good indication of relative volumes of oil in each lithology in the cored interval. We assume average initial oil saturations of ~0.80 and ~0.50 in sandstones and sandstone/ siltstone rock types. For opal-CT and opal-CT siltstones, we assume average initial oil saturations of 0.141 and 0.132, respectively (directly from routine core analysis averages). We may be overestimating oil content in sandstones and underestimating oil content in opal-CT, but the estimates remain useful for gauging relative amounts of oil. Using the estimated initial oil saturations, the average porosity and the frequency of occurrence of each rock type, we can calculate relative oil volumes in each rock type. We find that opal-CT contains 44% of the initial oil, opal-CT/siltstone contains 35% of the initial oil, and sandstone/siltstones contain 13.6% of the initial oil. Sandstones contain only ~7.4% of the initial oil. The simple calculation indicates that the low-permeability Opal-CT and Opal-CT/siltstones contain a minimum of ~79% of the initial oil volume.

The estimate that opal-CT and opal-CT/siltstone rock types contain ~79% of the initial oil volume may be somewhat conservative if we have underestimated oil saturations in those rock types. Moreover, we may have overestimated S_{oi} in sandstones. Results of the wettability tests, spontaneous imbibition tests, relative permeability tests, and mercury intrusion/extrusion tests can be combined to provide improved estimates for initial oil saturation. Tables 1.3-5 and 1.3-6 summarize our modeling efforts to estimate initial oil saturation in the different rock types. Table 1.3-5 summarizes the results of the analysis of mercury intrusion/extrusion tests. Table 1.3-6 summarizes results for the other special core analysis tests.

For the mercury intrusion tests, a capillary pressure of 1600 psia (~130 psia in an oil/water system) was selected initially as an appropriate cutoff to gauge potential oil saturations in all rock types. The P_c cutoff corresponds to capillary pressure equilibrium at an oil column height of ~1300 feet (0.1 psi/ft). As a Base Case, we assumed that the non-wetting phase saturation from the mercury intrusion tests at $P_c = 1600$ psia is equal to S_{oi} ($=1-S_{wi}$). For the other special core tests, we simply use the reported values of S_{oi}.

Figure 1.3-12 plots estimated initial oil saturation, S_{oi}, versus RHOB (g/cc) for all available test results. The results fall into several different populations. For RHOB $\geq$ 2.24 g/cc, comprised mostly of Sandstones and Sandstone/siltstones, S_{oi} ranges from 0.40 to more than 0.80. Sandstone/siltstones have maximum Soi ~ 0.60. For RHOB < 2.00 g/cc, comprised entirely of opal-CT, S_{oi} ranges from close to zero to ~0.20 (See circular red points with yellow fill in Figure 1.3-12). Opal-CT samples with lower RHOB (higher ϕ) tend to contain higher S_{oi}.

Oil/water test results on opal-CT samples tend to exhibit higher S_{oi} than those estimated from mercury intrusion tests. We found it necessary to re-determine S_{oi} estimates from the mercury intrusion tests. We took the following approach to revising estimates of S_{oi} from mercury intrusion tests for opal-CT samples:

1) Find routine core analysis results that are close depth neighbors to mercury intrusion samples.
2) If porosity, permeability, and grain density are very close for both samples, we select the measured oil saturation (no correction) as a "minimum" S_{oi} estimate. For a "maximum" value, we use $S_{oi} = 1 - S_w$. Because total fluid saturations were close to unity, there are only small differences between "minimum" and "maximum" S_{oi} values.
3) Using the "minimum" and "maximum" S_{oi} values from routine core analysis, we go back to the mercury intrusion curve and select new capillary pressure cutoff values corresponding to the "minimum" and "maximum" S_{oi} values.

4) We look for consistency in the new "minimum" and "maximum" cutoff values for mercury P_c.
5) Use the new "minimum" and "maximum" mercury P_c cutoff values to get new estimates of S_{oi} from mercury intrusion results for all samples.

For the mercury intrusion tests, "minimum" P_c cutoff values ranged from 2000 to 5000 psia, with an average of 3600 psia. "Maximum" P_c cutoff values ranged from 4500 to 6000 psia, with an average of about 5200 psia. We selected the "maximum" P_c cutoff value for revising estimates of S_{oi}. As shown in Figure 1.3-12, revised estimates for S_{oi} in opal-CT are somewhat larger, but typical S_{oi} is 0.30 or less. The upward revision of S_{oi} estimates for the mercury intrusion tests is consistent with S_{oi} observed in oil/water tests (e.g., wettability and spontaneous imbibition tests).

In Tables 1.3-5 and 1.3-6, S_{oi} values for the "Adjusted Base Case" are highlighted with a yellow background. The "Adjusted Base Case" best represents initial reservoir conditions.

The new estimates of S_{oi} in opal-CT use an average P_c cutoff of 5200 psia instead of the initial estimate of 1600 psia. Using conventional estimates for interfacial forces (e.g., $\sigma*\cos\theta$), that corresponds to oil/water capillary pressures of 420 psia and 130 psia, respectively. Those values correspond to oil column heights of ~4200 feet and ~1300 feet, respectively. An effective oil column height of more than 4000 feet is not likely. It is more likely that the ratio of interfacial forces for the two fluid systems has been underestimated. Initially, we assumed IFT force values of 370 dyne/cm and 30 dyne/cm for mercury/mercury vapor and oil/water, respectively. IFT forces for the mercury system are fairly well defined. To increase the ratio of IFT forces between the two fluid systems, oil/water IFT forces must decrease. Lowering the IFT or increasing the contact angle (i.e., less water wet) will lower oil/water IFT forces. The initial and revised P_c cutoff values, indicate that oil/water IFT forces must be reduced by a factor of 3.25 (=5200/1600) to about 10 dyne/cm. That requires opal-CT to be weakly- to moderately water wet rather than strongly water wet, which is consistent with the wettability results.

For Point Arguello porcelanites (i.e., same rock type as opal-CT in this memorandum), Kamath et al.[9], invoked "wettability" factors ranging from 2.4 to 5.8 (3.8 average) necessary to correct mercury intrusion results.

For opal-CT, Figure 1.3-12 indicates that S_{oi} increases as RHOB decreases. For opal-CT/siltstones, S_{oi} increases as RHOB increases, but there aren't enough points to define a good trend. For sandstones and sandstone/siltstones, S_{oi} tends to decrease as RHOB increases, but the trend is not well defined. Maximum S_{oi} in sandstones is ~0.80. Maximum S_{oi} in sandstone/siltstones is ~0.60.

Figure 1.3-13 re-plots Figure 1.3-12 as S_{oi} versus porosity. Plotted versus porosity, several trends in S_{oi} are apparent. For porosities ranging from 0.10 to 0.28, S_{oi} increases linearly with porosity for Sandstones and some Sandstone/siltstones. For porosities ranging from 0.28 to 0.43, S_{oi} increases linearly for most opal-CT samples. Some lower-permeability sandstones, sandstone/ siltstones, and opal-CT/siltstones, with porosity ranging from 0.18 to 0.25, fall on an intermediate trend with Soi ~0.40 to 0.50.

A few high-porosity opal-CT samples in Figure 1.3-13 follow a much lower S_{oi} trend. Our first assumption is that they might be "cherts" rather than "porcelanites." However, cherts are not likely to have porosities greater than 0.35. Further examination of those samples revealed that they are all from deeper in the core interval (> 4740 feet). The lower S_{oi} values reflect corrected S_o values from routine core analyses that are consistent with mercury intrusion results. Rather than a change in rock type, the lower oil saturations may simply reflect the fact that those samples are lower in a transition zone (i.e., lower effective P_c).

The simple linear trends of S_{oi} with porosity for sandstone and opal-CT in Figure 1.3-13 may be useful for estimating initial oil in place in the Antelope Shale at Buena Vista Hills. The trends only overlap over a small range of porosity (0.25 to 0.28). However, over an intermediate range of porosity (0.18 to 0.25), the simple linear trends would be overestimating S_{oi} in sandstone/ siltstones and some lower-permeability sandstones.

Figure 11.3-4 illustrates the trend in S_{oi} versus air permeability for all rock types. With some scatter all samples follow the expected trend of S_{oi} increasing with permeability.

For wettability, relative permeability and spontaneous imbibition tests, both S_{oi} and the residual oil saturation, S_{orw}, are determined by direct measurement. For mercury P_c tests, S_{orw} can be estimated from the extrusion curve. However, for high-pressure (50,000 psia) mercury tests, liquid mercury typically fills 95% or more of the total pore volume, including microporosity. After extrusion to low pressure, the volume of trapped "non-wetting" phase (e.g., liquid Hg) corresponds to a maximum value for S_{orw}. For given rock types, Land[10] found that S_{orw} could be correlated to S_{oi} by:

$$S_{orw} = S_{oi}/(1 + C^*S_{oi}),$$

or

$$C = 1/S_{orw} - 1/S_{oi},$$

where C is Land's trapping constant. Land's constant is valid for water wet rocks. Land found C to be a constant that reflects the pore structure of a rock. For typical sandstones, C ranges from 1.5 to ~5. To calculate S_{orw} as a function of S_{oi}, we must assume that C values derived from high-pressure mercury intrusion/extrusion tests are applicable to the reservoir, where maximum non-wetting phase saturations are much lower.

To test that hypothesis, we divided some of the test samples into two pieces. One piece was subjected to high-pressure mercury testing, its companion was subjected to low-pressure testing. The maximum mercury P_c in the low-pressure tests was selected to attain maximum non-wetting phase saturation close to initial oil saturations in the reservoir. Maximum intrusion pressures (See Table 1.3-1) for the low-pressure tests ranged from 100 psia to 6980 psia. Land's C values from low- and high-pressure mercury intrusion/extrusion tests are in very good agreement, as shown in Figure 1.3-15. The small amount of scatter is probably due to core-scale heterogeneity. Thus, we conclude that Land's trapping constants derived from high-pressure mercury intrusion/extrusion tests are valid.

Using the observed recovery behavior and calculated values for Land's C, we determined S_{orw} as a function of S_{oi} for all samples. The difference between S_{oi} and S_{orw} represents a movable oil saturation, assuming that waterflooding (including spontaneous imbibition) contacts the entire (See Tables 1.3-5 and 1.3-6). Figure 1.3-16 plots movable oil saturation ($S_{oi} - S_{orw}$) versus permeability. For sandstones, movable oil saturations are more than 0.40 PV. For opal-CT, movable oil saturations tend to be less than 0.10 PV. Table 1.3-7 summarizes average rock properties and initial oil saturations by rock type for the tested samples. For each rock type, the average rock properties (e.g., ϕ, K_a, and RHOG) are similar to the average properties reported in Table 1.3-4 from the routine core analysis report.

For opal-CT, average $S_{oi} = 0.218$, which is significantly higher than the average (S_o = 0.141) from routine core analysis. The routine core analysis values are probably too low (no correction for shrinkage), while the higher average S_o value from the current analysis is too high because it ignores transition zone effects (all samples at $S_{oi} = 1 - S_{wirr}$). Both analyses provide use bounds for minimum and maximum oil saturations in opal-CT. For opal-CT, average movable oil saturation is ~0.087 PV, which is in good agreement with wettability and spontaneous imbibition test results.

For opal-CT/siltstones, average $S_{oi} = 0.357$, which much higher than the average (S_o = 0.132) from routine core analysis. Only five opal-CT/siltstone samples are included in the current analysis, so the comparison is not statistically valid. Some of the tested samples behaved more like sandstone/siltstones than opal-CT/siltstones. Part of the difficulty in may be due to how rock type was assigned to each sample. Also, the few opal-CT/siltstone samples that were tested had much higher permeabilities than the average from routine core analysis.

For sandstones, average rock properties (ϕ, K_a, and RHOG) for the tested samples are very close to those from routine core analysis. Average sandstone $S_{oi} = 0.734$ and average movable oil saturation is 0.421 PV. That corresponds to an average $S_{orw} \sim 0.313$. Routine core analysis indicated average $S_o = 0.375$ in sandstones. The larger S_o values from routine analysis may reflect higher S_o in unswept sandstone intervals.

For sandstone/siltstones, average rock properties (ϕ, K_a, and RHOG) for the tested samples are very close to those from routine core analysis. Average $S_{oi} = 0.468$ and average movable oil saturation is 0.251 PV, for an average $S_{orw} = 0.217$. That corresponds closely to the average $S_o = 0.211$ from routine core analysis.

When viewed together, routine core analyses and special core analyses yield a consistent picture of rock properties and fluid saturations for important rock types in the Antelope Shale in the Buena Vista Hills Field.

Transition Zone Effects?

Transition zone effects were not considered in this memorandum. Reported initial oil saturations correspond to $S_o = 1 - S_{wirr}$, where S_{wirr} is irreducible water saturation. Additional analysis of the available capillary pressure data would help define the shape of a transition zone.

Some of the available mercury intrusion results were fit to the Brooks-Corey capillary pressure model, which is given by:

$$P_c = P_e{}^*(S_w{}^*)^{-(1/\lambda)} .$$

P_e is the entry pressure (See Figure 1.3-8), λ is a pore-size distribution parameter, and $S_w{}^*$ is the effective wetting phase saturation, given by:

$$S_w{}^* = (S_w - S_{wirr})/(1 - S_{wirr}).$$

Typical values for λ ranged from 0.5 to 0.7, with no apparent trends by lithology. Values for λ less than unity indicate a broad distribution of pore sizes.

If values for P_e, S_{wirr}, and λ are selected as a function of depth and/or lithology, the variation of S_w with height above a free water level ($P_c = 0$) can be determined. That exercise was considered to be beyond the scope of this memorandum.

RELATIVE PERMEABILITY TEST RESULTS

Table 1.3-8 summarizes the results of gas/oil and water/oil relative permeability tests reported by Core Laboratories. Eight (8) samples, mostly sandstones with a few sandstone/siltstones, were selected for testing. One sample (#15 at 4512.35 feet) was identified as an opal-CT/siltstone, but it failed during testing.

Initially, two unsteady-state (USS) water/oil relative permeability tests (#2A and #11A) were conducted at reservoir conditions (155 °F) with stock tank crude oil. Due to the low viscosity (2.3 cp) of the stock tank oil, "piston-like" displacement occurred and, except for the endpoints, relative permeability curves could not be determined. Relative permeability curves can be determined only for saturations larger than the average injected phase saturation at breakthrough. All subsequent relative permeability tests were conducted at ambient temperature with more viscous (10 cp) synthetic oil.

For each sample, after drainage with oil to S_{wi}, a constant-pressure, USS gas/oil relative permeability test was conducted first. The sample was re-saturated with oil and a constant-rate USS water/oil relative permeability test was conducted. Thus both tests were conducted with the same initial water saturation.

The gas/oil relative permeability test results were dominated by early breakthrough. Many of the tests were terminated with significant mobile oil remaining in place (i.e., $k_{ro} \neq 0$). Significant additional analysis would be required to understand the gas/oil results. That objective was considered beyond the scope of this memorandum.

The water/oil relative permeability tests are consistent with the quantitative and qualitative wettability test results and the analysis of the mercury intrusion tests.

Higher permeability sandstones ($K_a > 50$ md) have S_{oi} ranging from 0.70 to 0.80 and S_{orw} ranging from 0.25 to 0.31. Water/oil displacements in high-permeability sandstones recover more than half of the movable oil before breakthrough and endpoint water relative permeability is fairly low ($k_{rw}@S_{orw} < 0.10$). Both observations indicate that high-permeability sandstones are moderately- to strongly water wet.

Lower-permeability sandstones and sandstone/siltstones ($K_a \leq 10$ md) have S_{oi} ranging from 0.40 to 0.50 and S_{orw} ranging from 0.04 to 0.24. For the lower-permeability sandstones and siltstones, oil recovery at breakthrough is typically less than 40% of the movable oil and endpoint water relative permeability ranges from 0.20 to 0.55. Both observations indicate that lower-permeability sandstones and sandstone/siltstones are weakly- to moderately water wet.

Previous wettability test results, for a sandstone/siltstone sample (4315.60 feet, See Table 1.3-2), indicated a mixed-wet condition. For several of the low-permeability sandstones and siltstones, waterflood tests left behind very low residual saturations ($S_{orw} = 0.04$ to 0.06). Those results should be used with caution; the tests were conducted at such high flow rates and pressure drops (i.e., capillary number too high) that discontinuous oil may have been mobilized. The low S_{orw} values do not represent reservoir behavior. Significant additional analysis would be required to analyze the results and determine correct values that represent reservoir flow behavior. That analysis is beyond the scope of this memorandum.

REFERENCES

Advanced Rock Properties Study, Well 653Z-26B, Buena Vista Hills field, Kern County, California, Relative Permeability Final Report, to M. Morea (Chevron USA, Bakersfield, CA) from F. Ene (Core Laboratories Bakersfield, CA), November 7, 1997.

Advanced Rock Properties Study, Well No. 653Z-26B, Buena Vista Field, Kern County, California, Final Report – Mercury Intrusion Tests, to E. F. deZabala (CPTC, La Habra, CA) from F. Ene (Core Laboratories Bakersfield, CA), September 29, 1997.

Personal communication, Alden Carpenter (CPTC, LA Habra, CA), October 21, 1997.

Kamath, J: "Evaluation of the Accuracy of Estimating Air Permeability From Mercury Injection Data," SPEFE (December 1992).

Advanced Rock Properties Study, Well 653Z-26B, Buena Vista Hills field, Kern County, California, Modified USBM/Amott Wettability Data, to M. Morea (Chevron USA, Bakersfield, CA) from F. Ene (Core Laboratories Bakersfield, CA), August 22, 1997.

Personal communication, Alden Carpenter (CPTC, La Habra, CA), October 21, 1997.

Personal communication, R. E. Boyer (CPTC, La Habra, CA), August 22, 1997.

Wellsite Wettability Tests – Buena Vista Hills Field, Well 653Z-26B, B.J. Bilodeau to S.C. Smith (both Chevron USA, Bakersfield, CA), July 25, 1996.

CPTC Technical Memorandum TM94000816, by J. Kamath, E.F. deZabala, R.E. Boyer, R.F. Meyer, and F.M. Nakagawa: "Laboratory Study of Spontaneous Imbibition Potential – Point Arguello Field, Well OCS-P-316 B12," November, 1994.

Land, C.S.: "Comparison of Calculated with Experimental Imbibition Relative Permeability," SPE Paper #3360, presented at the 1971 SPE Rocky Mountain Regional Meeting, Billings, Montana, June 2-4, 1971.

Table 1.3-1. Mercury intrusion/extrusion test results.

Sample I.D.	Depth	ϕ	RHOG	RHOB	Kair, meas.	Kair, Swanson Hg est.	K "Best"	Pc (Hg) max	Snw (Hg) max	Snwr (Hg) max	Pe (Hg), psia	Pe (O/W), psia	Land's "C"	LITHOLOGY
(-)	(feet)	(fraction)	(g/cc)	(g/cc)	(md)	(md)	(md)	(psia)	(fraction)	(fraction)			(-)	
3958	3958.00	0.373	2.236	1.775	0.093	0.042	0.062	54700	0.998	0.294	295	23.9	2.40	Opal CT
3959	3959.00	0.419	2.261	1.733	0.399	0.100	0.20	54700	0.998	0.242	410	33.2	3.13	Opal CT
#26A	4255.70	0.308	2.328	1.919		0.05	0.05	59800	1.000	0.359	*2510*	*203.5*	1.79	Opal CT
4271	4271.65	0.316	2.269	1.868	0.112	0.019	0.046	54800	0.965	0.361	310	25.1	1.73	Opal CT
4369	4369.80	0.377	2.314	1.819	0.071	0.056	0.063	54900	0.997	0.282	710	57.6	2.54	Opal CT
4370	4370.00	0.369	2.318	1.832	0.044	0.037	0.040	54900	0.995	0.270	980	79.5	2.70	Opal CT
#24	4399.70	0.326	2.257	1.847		0.07	0.07	59800	1.000	0.412	*2399*	*194.5*	1.43	Opal CT
4744	4744.25	0.332	2.424	1.951	*3.89**	0.026	0.026	54800	0.993	0.209	4800	389.2	3.78	Opal CT
4747	4747.95	0.461	2.318	1.710	0.564	0.054	0.054	54800	0.997	0.203	3500	283.8	3.92	Opal CT
#29	4795.65	0.378	2.399	1.870		0.043	0.043	59790	1.000	0.237	*3162*	*256.4*	3.22	Opal CT
#27	4796.00	0.359	2.440	1.923		0.040	0.040	59790	1.000	0.275	*3548*	*287.7*	2.64	Opal CT
4200	4200.05	0.240	2.483	2.127	*86**	0.020	0.020	54800	0.953	0.364	*3000*	*243.2*	1.70	Opal-CT/siltstone
15A	4512.35	0.271	2.466	2.069	*85.2**	0.28	0.28	49800	0.979	0.280	79.4	6.4	2.55	Opal-CT/siltstone
15B	4512.35	0.226	2.492	2.155	*36.5**	0.39	0.39	6980	0.548	0.247	75	6.1	2.22	Opal-CT/siltstone
4866	4866.00	0.145	2.551	2.326	1.73	1.68	1.70	54800	0.951	0.451	39.0	3.2	1.17	Opal-CT/siltstone
4432	4432.50	0.297	2.650	2.160	202	142	169	54800	0.987	0.367	12.0	1.0	1.71	Sandstone
11A	4432.65	0.267	2.583	2.160	248	142	188	49800	0.965	0.357	7.8	0.63	1.76	Sandstone
11B	4432.65	0.266	2.588	2.166	253	145	192	198	0.752	0.347	11.5	0.93	1.55	Sandstone
2A	4490.85	0.240	2.630	2.239	85.5	8.9	27.6	49900	0.941	0.305	31.6	2.6	2.22	Sandstone
2B	4490.85	0.230	2.690	2.301	8.3	4.3	6.0	609	0.653	0.274	28.5	2.3	2.12	Sandstone
4A	4491.05	0.205	2.683	2.338	16	2.0	5.7	49900	0.950	0.307	64.6	5.2	2.20	Sandstone
4B	4491.05	0.230	2.671	2.287	7.5	2.4	4.2	279	0.471	0.218	56	4.5	2.46	Sandstone
7A	4493.20	0.215	2.596	2.253	4.2	3.5	3.8	49800	0.989	0.439	46.8	3.8	1.27	Sandstone
7B	4493.20	0.216	2.600	2.254	4.65	4.6	4.6	199	0.494	0.291	39	3.2	1.41	Sandstone
9A	4499.55	0.168	2.589	2.322	24.4	14.3	18.7	49800	0.985	0.487	30.9	2.5	1.04	Sandstone
9B	4499.55	0.178	2.587	2.305	10.8	14	12.3	100	0.561	0.382	12.5	1.0	0.84	Sandstone
4668	4668.85	0.222	2.631	2.269	69	43	54.5	54800	0.932	0.435	11.8	1.0	1.23	Sandstone
4836	4836.90	0.222	2.657	2.289	38.4	22.7	29.5	54800	0.961	0.416	22.5	1.8	1.36	Sandstone
4869	4869.30	0.176	2.652	2.361	2.05	2.26	2.15	54800	0.953	0.487	31.5	2.6	1.00	Sandstone
21A	4291.30	0.238	2.593	2.214	7	1.79	3.5	49900	0.939	0.267	42.7	3.5	2.68	Sandstone/siltstone
21B	4291.30	0.231	2.602	2.232	6.3	1.3	2.9	359	0.305	0.144	40.5	3.3	3.67	Sandstone/siltstone
17A	4518.55	0.231	2.597	2.228	1.05	0.73	0.88	49900	0.954	0.291	95.5	7.7	2.39	Sandstone/siltstone
17B	4518.55	0.233	2.623	2.245	0.96	0.75	0.85	3980	0.542	0.235	94	7.6	2.41	Sandstone/siltstone
4838	4838.85	0.084	2.631	2.494	0.046	0.11	0.071	54800	0.932	0.510	73	5.9	0.89	Sandstone/siltstone
4640	4640.10	0.182	2.752	2.433	0.076	2.26	0.41	54800	0.967	0.419	31	2.5	1.35	Sandstone/siltstone

**** - Measured permeability too high, fractured sample***

Table 1.3-2. Results of USBM/Amott wettability tests.

I.D.	***Depth***	***Rock Type***	ϕ	K_a	***RHOG***	Swi	**Amott Index Water-Oil**	**USBM Index**
(-)	(feet)	(-)	(fraction)	(md)	(g/cc)	(fraction)	(-)	(-)
#1	3989.20	Opal-CT	0.305	0.025	1.81	0.682	+0.78	+0.33
#5	4315.60	Sandstone / siltstone	0.139	0.091	2.64	0.393	+0.37	-0.08
#6	4355.95	Opal-CT	0.293	*3.7**	1.88	0.790	+0.68	+0.90

** possible fractured sample- permeability much larger than expected.*

Table 1.3-3. Results of spontaneous imbibition tests.

I.D.	Depth	ϕ	RHOG	Swi	Swf	% Recovery
(-)	(feet)	(fraction)	(g/cc)	(fraction)	(fraction)	
#26A-*	4255.70	0.281	1.898	0.913	0.961	55.2%
#24-**	4399.70	0.307	1.841	0.588	0.675	21.2%
#29-♦	4795.65	0.352	1.868	0.768	0.857	38.2%
#27 -♦	4796.60	0.360	1.846	0.869	0.932	48.0%

*-thickly laminated siliceous shale, ** -thinly laminated siliceous shale

♦ - "water sucking" siliceous shale

Table 1.3-4. Average properties from routine core analysis by rock type.

Rock Type	**# samples**	**Avg. ϕ**	**Avg. RHOG**	**Avg. K_a**	**Median K_a**	**Avg. S_O (current)**	**% of interval**
(-)	(-)	(fraction)	(g/cc)	(md)	(md)	(fraction)	(%)
Opal-CT	399	0.338	2.31	0.22	0.10	0.141	43.1
Opal-CT/ siltstones	451	0.257	2.36	0.69	0.07	0.132	48.7
Sandstone	19	0.211	2.62	34.	6.3	0.375	2.0
Sand/ siltstones	57	0.208	2.57	7.	0.16	0.211	6.2

Table 1.3-5. Initial & movable oil saturations estimated from mercury intrusion/extrusion results.

Sample I.D.	Depth	ϕ	RHOG	K "Best"	So max. PK&S	So, min PK&S	Pc(Hg) max	Pc(Hg) min	Soi Base Case	Soi Adjusted	Movable Oil - Base Case	Movable Oil - Adjusted	LITHOLOGY
(-)	(feet)	(fraction)	(g/cc)	(md)	(fraction)	(fraction)	(psia)	(psia)	(fraction)	(fraction)	(frac. PV)	(frac. PV)	
3958	3958.00	0.373	2.236	0.062	0.283	0.219	6000	3400	0.148	0.283	0.039	0.114	Opal CT
3959	3959.00	0.419	2.261	0.20	0.369	0.309	6000	3400	0.221	0.369	0.090	0.198	Opal CT
#26A	4255.70	0.308	2.328	0.05	0.181	0.116	5000	3600	0.022	0.181	0.001	0.044	Opal CT
4271	4271.65	0.316	2.269	0.046	0.231	0.147	4490	2250	0.110	0.231	0.018	0.066	Opal CT
4369	4369.80	0.377	2.314	0.063	0.297	0.181	4500	1600	0.181	0.297	0.057	0.128	Opal CT
4370	4370.00	0.369	2.318	0.040	0.264	0.167	4500	2100	0.120	0.264	0.029	0.110	Opal CT
#24	4399.70	0.326	2.257	0.070	0.245	0.159	6600	4200	0.058	0.159	0.004	0.029	Opal CT
4744	4744.25	0.332	2.424	0.026	0.144	0.104	5500	5200	0.009	0.144	0.000	0.051	Opal CT
4747	4747.95	0.461	2.318	0.054	0.162	0.117	4550	4200	0.023	0.162	0.002	0.063	Opal CT
#29	4795.65	0.378	2.399	0.043	0.102	0.086	5100	4900	0.018	0.086	0.001	0.019	Opal CT
#27	4796.00	0.359	2.440	0.040	0.098	0.092	5100	5000	0.012	0.092	0.000	0.018	Opal CT
4200	4200.05	0.240	2.483	0.020	0.015	0.013	N/A	N/A	0.045	0.045	0.003	0.003	Opal-CT/siltstone
15A	4512.35	0.271	2.466	0.28	0.321	N/A	4500	N/A	0.225	0.321	0.082	0.144	Opal-CT/siltstone
15B	4512.35	0.226	2.492	0.39	0.435	N/A	4500	N/A	0.322	0.435	0.134	0.214	Opal-CT/siltstone
4866	4866.00	0.145	2.551	1.70	0.700	N/A	4500	N/A	0.623	0.700	0.262	0.315	Opal-CT/siltstone
4432	4432.50	0.297	2.650	169	N/A	0.411	N/A	N/A	0.863	0.863	0.515	0.515	Sandstone
11A	4432.65	0.267	2.583	188	0.887	0.411	4500	N/A	0.864	0.887	0.522	0.541	Sandstone
11B	4432.65	0.266	2.588	192									Sandstone
2A	4490.85	0.240	2.630	27.6	0.836	N/A	4500	N/A	0.762	0.836	0.479	0.543	Sandstone
2B	4490.85	0.230	2.690	6.0									Sandstone
4A	4491.05	0.205	2.683	5.7	0.826	N/A	4500	N/A	0.740	0.826	0.459	0.533	Sandstone
4B	4491.05	0.230	2.671	4.2									Sandstone
7A	4493.20	0.215	2.596	3.8	0.884	0.434	4500	N/A	0.796	0.884	0.400	0.467	Sandstone
7B	4493.20	0.216	2.600	4.6									Sandstone
9A	4499.55	0.168	2.589	18.7	0.862	N/A	4500	N/A	0.827	0.862	0.382	0.407	Sandstone
9B	4499.55	0.178	2.587	12.3									Sandstone
4668	4668.85	0.222	2.631	54.5	0.832	N/A	4500	N/A	0.800	0.832	0.396	0.420	Sandstone
4836	4836.90	0.222	2.657	29.5	0.846	N/A	4500	N/A	0.797	0.846	0.415	0.453	Sandstone
4869	4869.30	0.176	2.652	2.15	0.762	N/A	4500	N/A	0.688	0.762	0.281	0.330	Sandstone
21A	4291.30	0.238	2.593	3.5	0.612	N/A	4500	N/A	0.496	0.612	0.283	0.380	Sandstone/siltstone
21B	4291.30	0.231	2.602	2.9									Sandstone/siltstone
17A	4518.55	0.231	2.597	0.88	0.557	0.414	4500	N/A	0.451	0.557	0.234	0.318	Sandstone/siltstone
17B	4518.55	0.233	2.623	0.85	0.542	N/A	3980	N/A	0.450	0.542	0.234	0.307	Sandstone/siltstone
4838	4838.85	0.084	2.631	0.071	0.612	N/A	4500	N/A	0.507	0.612	0.157	0.215	Sandstone/siltstone
4640	4640.10	0.182	2.752	0.41	0.472	N/A	4500	N/A	0.426	0.472	0.156	0.184	Sandstone/siltstone

Table 1.3-6. Initial and movable oil saturations estimated from other special core analysis tests.

Sample I.D.	Depth	ϕ	RHOG	K "Best"	So max. PK&S	So, min PK&S	Pc(Hg) max	Pc(Hg) min	Soi Base Case	Soi Adjusted	Movable Oil - Base Case	Movable Oil - Adjusted	LITHOLOGY
(-)	(feet)	(fraction)	(g/cc)	(md)	(fraction)	(fraction)	(psia)	(psia)	(fraction)	(fraction)	(frac. PV)	(frac. PV)	
USBM Wettability Tests:													
[redacted]	[redacted]	[redacted]	[redacted]	[redacted]					[redacted]	0.318	[redacted]	0.225	Opal CT
[redacted]	[redacted]	[redacted]	[redacted]	[redacted]					[redacted]	0.254	[redacted]	0.126	Opal CT
[redacted]	[redacted]	[redacted]	[redacted]	[redacted]					0.607	[redacted]	0.302	[redacted]	Sandstone/siltstone
Relative Permeability Tests:													
4512GO	4512.35	0.212	2.48	0.28					0.439		0.217		Opal-CT/siltstone
4432WO	4432.65	0.241	2.61	168					0.777		0.466		Sandstone
4490WO	4490.85	0.200	2.65	13.3					0.687		0.448		Sandstone
4491WO	4491.05	0.203	2.69	2.6					0.457		0.420		Sandstone
4493WO	4493.20	0.201	2.61	3.1					0.480		0.417		Sandstone
4499WO	4499.55	0.169	2.60	62.5					0.595		0.294		Sandstone
4291WO	4291.30	0.202	2.61	0.90					0.337		0.291		Sandstone/siltstone
4518WO	4518.55	0.213	2.60	0.33					0.531		0.351		Sandstone/siltstone
Spontaneous Imbibition Tests:													
#26A	4255.70	0.281	2.249	0.05					0.087		0.048		Opal CT
#24	4399.70	0.307	2.212	0.07					0.412		0.087		Opal CT
#29	4795.65	0.352	2.341	0.043					0.232		0.089		Opal CT
#27	4796.60	0.360	2.323	0.04					0.131		0.063		Opal CT

Table 1.3-7. Average rock properties and initial saturations for tested samples.

Rock Type	# samples	Avg. ϕ	Avg. RHOG	Median K_a	Avg. K_a	Avg. S_o	Avg. S_o*	Movable Oil
(-)	(-)	(fraction)	(g/cc)	(md)	(md)	(fraction)	(fraction)	fraction PV
Opal-CT	17	0.348	2.30	0.05	0.07	0.218	**0.218**	**0.087**
Opal-CT/ siltstone	5	0.219	2.49	0.28	0.53	0.388	**0.357**	**0.179**
Sandstone	19	0.218	2.63	13	51	0.724	**0.734**	**0.421**
Sandstone / siltstone	9	0.195	2.62	0.80	1.1	0.476	**0.468**	**0.251**

* - Porosity-weighted average oil saturation.

Table 1.3-8. Results of relative permeability.

Sample	Depth	Rock Type	ϕ	Ka	Swi	Ko(Swi)	"Sorg"	krg(Sorg)	Sw@BT	Sorw	krw(Sorw)	Land's trapping constant, "C"	Fraction oil recovered at B.T.
(-)	(feet)	(-)	(fraction)	(md)	(fraction)	(md)	(fraction)	(fraction)	(fraction)	(fraction)	(fraction)	(-)	(fraction)
2	4490.85	Sandstone	0.200	13.3	0.313	8.2	0.329	0.881	0.432	0.239	0.545	2.73	0.266
2A	4490.85	Sandstone	0.200	13.3	0.217	5.4	*no gas/oil test*		0.449	0.323	0.257	1.82	0.504
11	4432.65	Sandstone	0.241	168	0.223	166	0.239	0.487	0.615	0.311	0.086	1.93	0.841
11A	4432.65	Sandstone	0.241	168	0.241	104	*no gas/oil test*		0.527	0.473	0.061	0.80	1.000
4	4491.05	Sandstone	0.203	2.6	0.543	1.2	0.068	0.537	0.706	0.037	0.347	*24.8*	0.388
7	4493.20	Sandstone	0.201	3.1	0.520	1.8	0.112	0.480	0.666	0.063	0.362	*13.8*	0.350
9	4499.55	Sandstone	0.169	62.5	0.405	53.9	0.165	0.577	0.587	0.301	0.081	1.64	0.619
15	4512.35	Opal-CT/ siltstone	0.212	0.28	0.561	*0.018*	0.305	0.523	********** *no water/oil test - sample failed* **********				
17	4518.55	Sandstone/ siltstone	0.213	0.33	0.469	0.112	0.318	0.683	0.592	0.180	0.217	3.67	0.350
21	4291.30	Sandstone/ siltstone	0.202	0.90	0.663	0.236	0.111	0.590	0.755	0.046	0.549	*18.8*	0.316

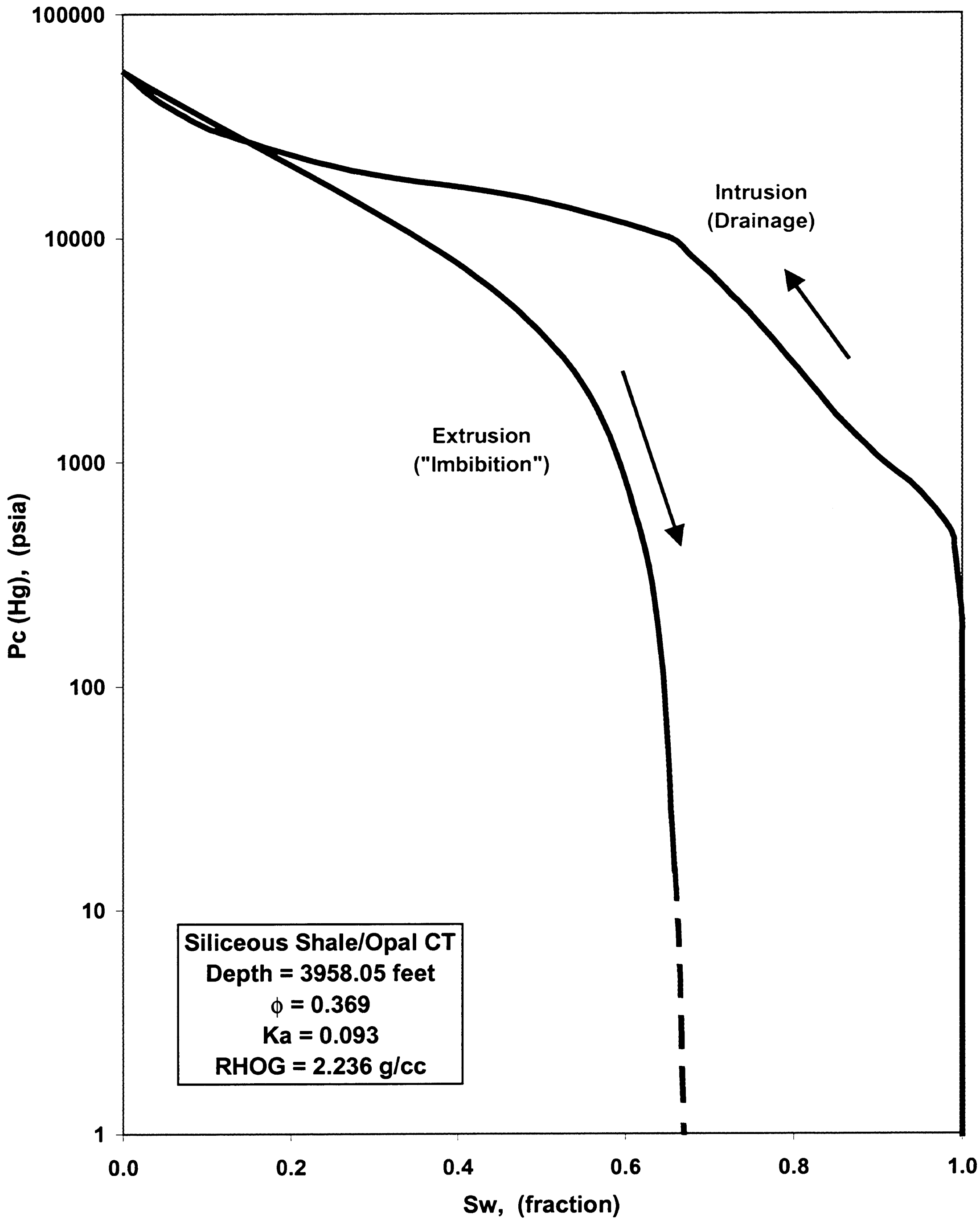

Figure 1.3-1. Typical mercury intrusion/extrusion capillary pressure curve for opal-CT.

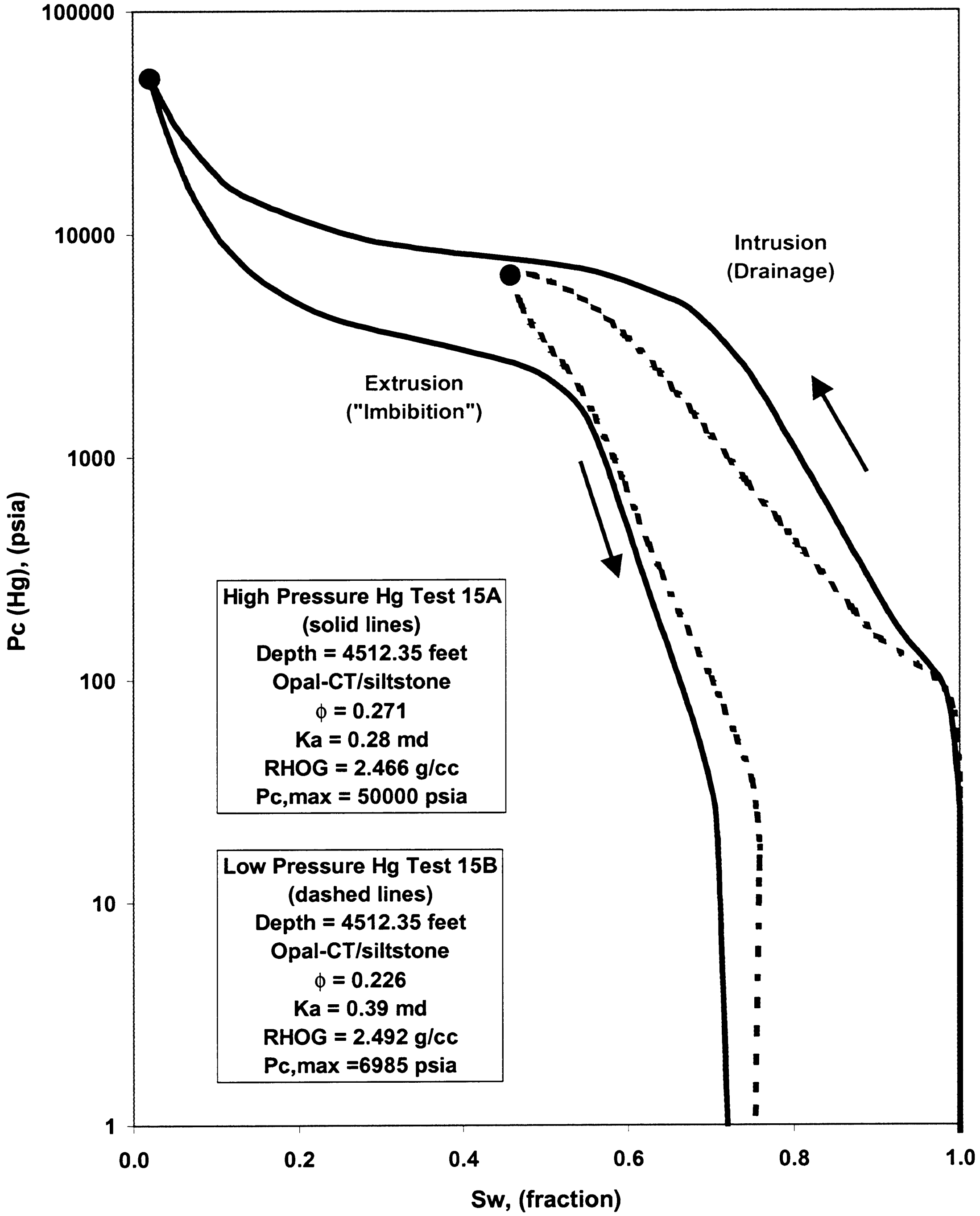

Figure 1.3-2. Typical mercury intrusion /extrusion capillary pressure curves for opal-CT/siltstone.

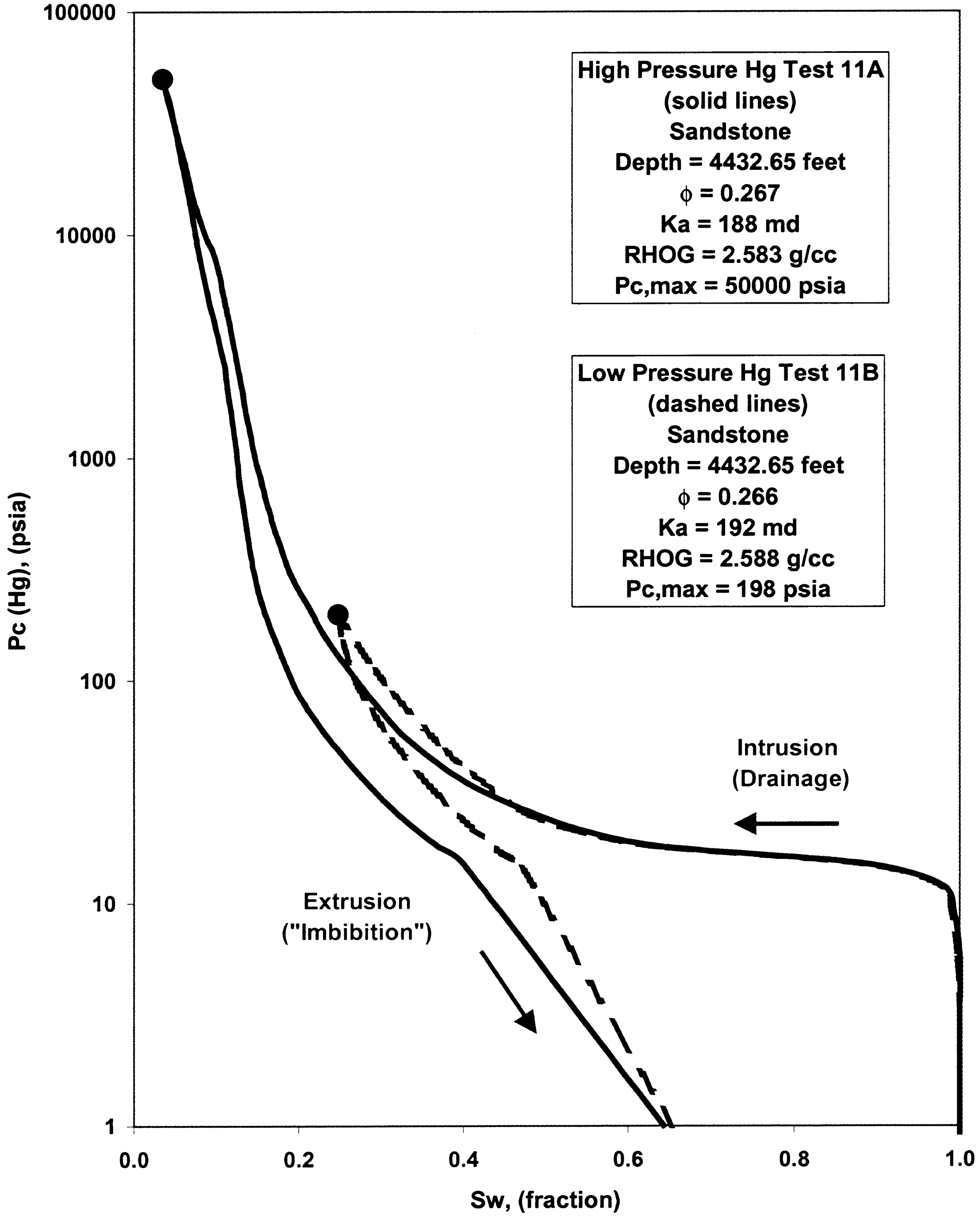

Figure 1.3-3. Typical mercury intrusion/extrusion capillary pressure curves for sandstone.

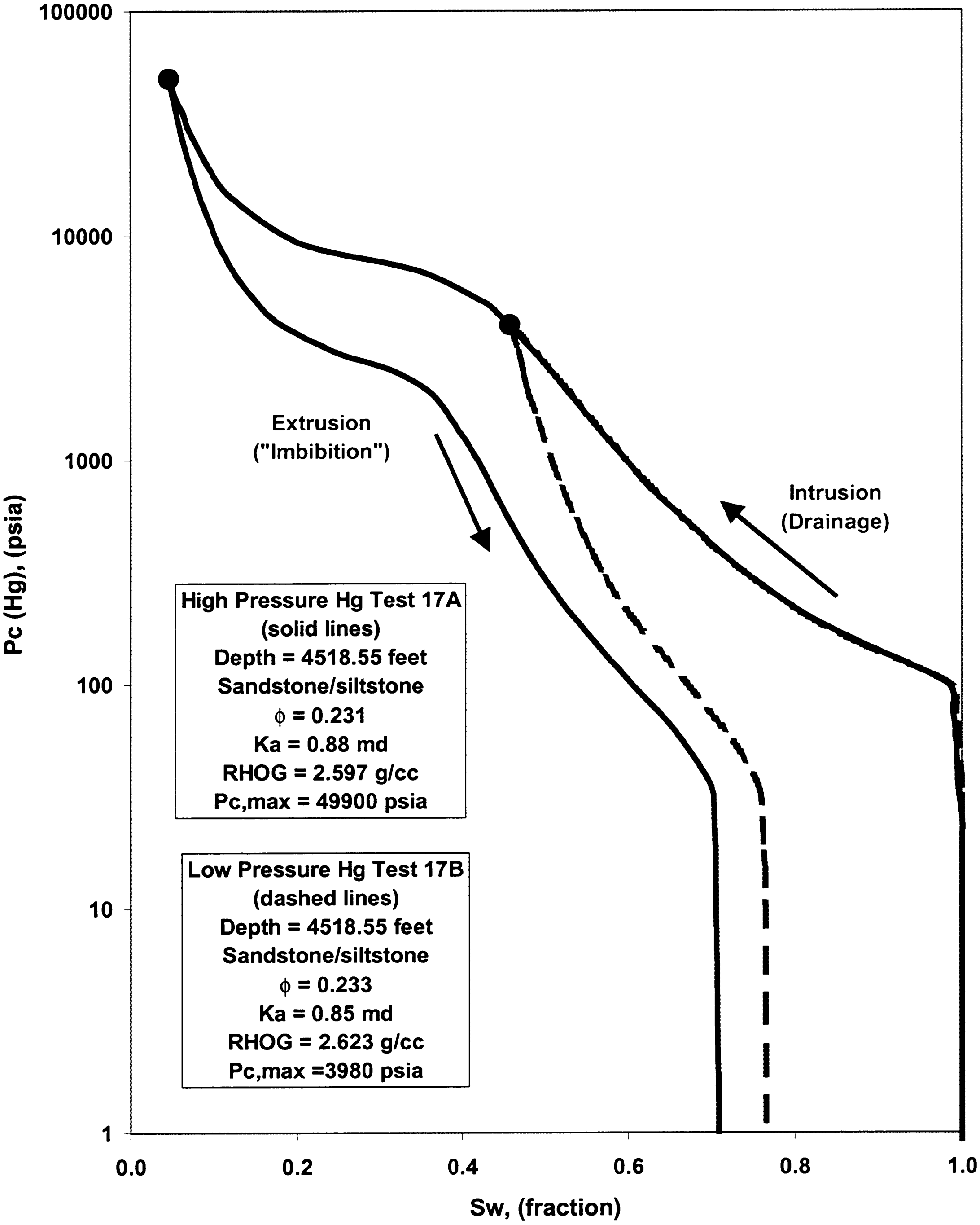

Figure 1.3-4. Typical mercury intrusion/extrusion capillary pressure curves for sandstone/siltstone.

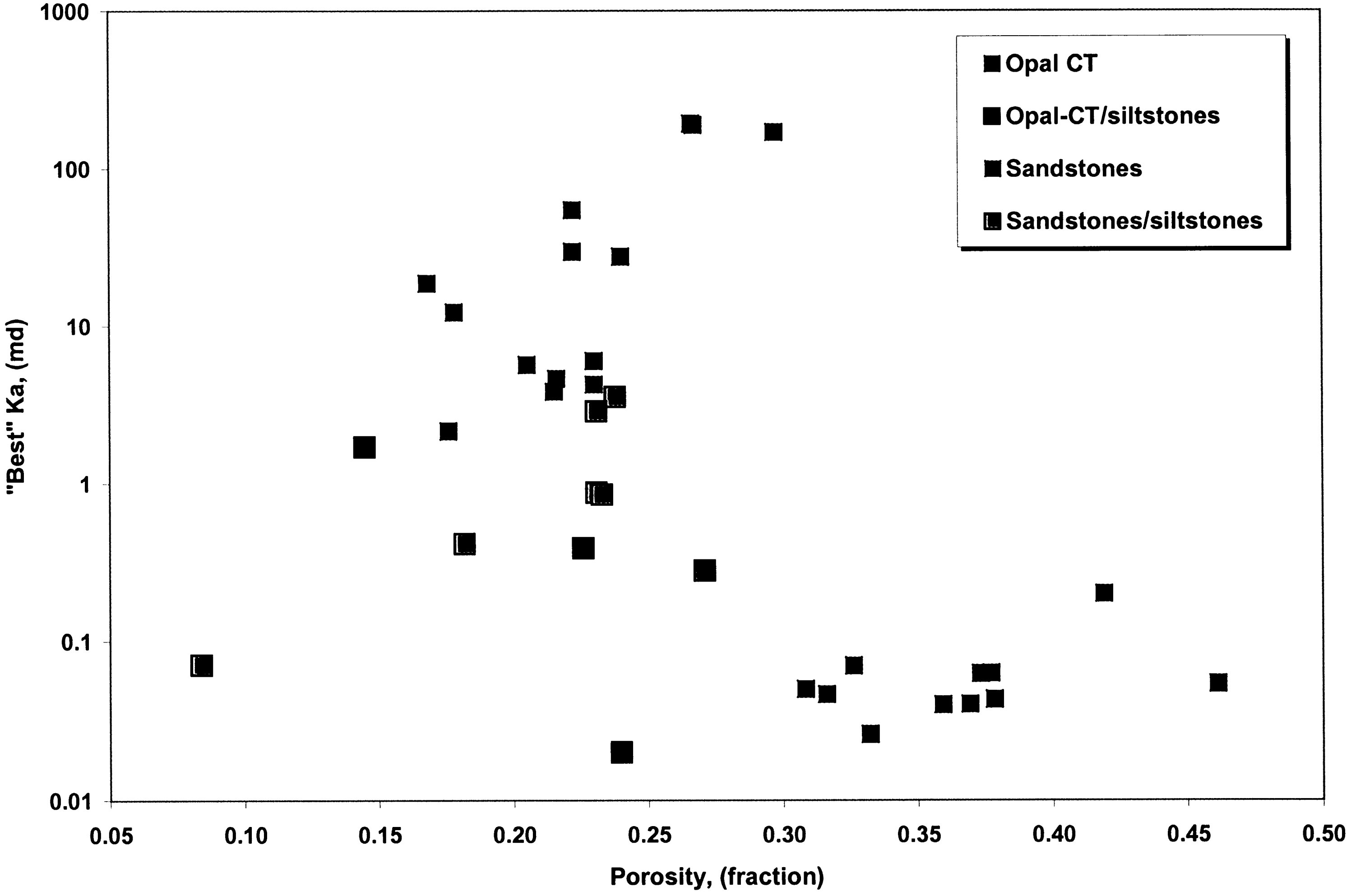

Figure 1.3-5. Permeability versus porosity for all mercury intrusion test samples.

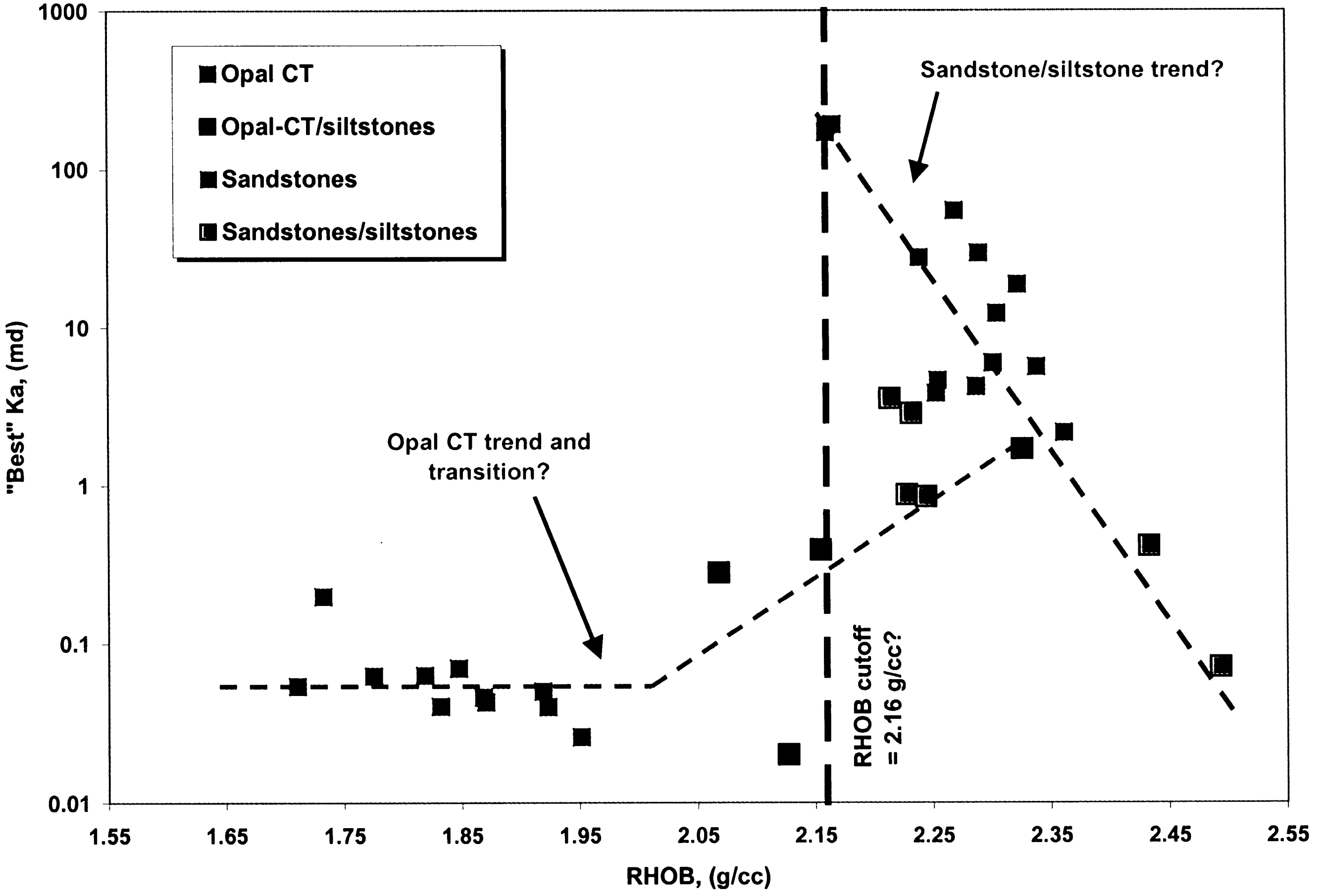

Figure 1.3-6. Permeability versus bulk density (RHOB) for all mercury intrusion test samples.

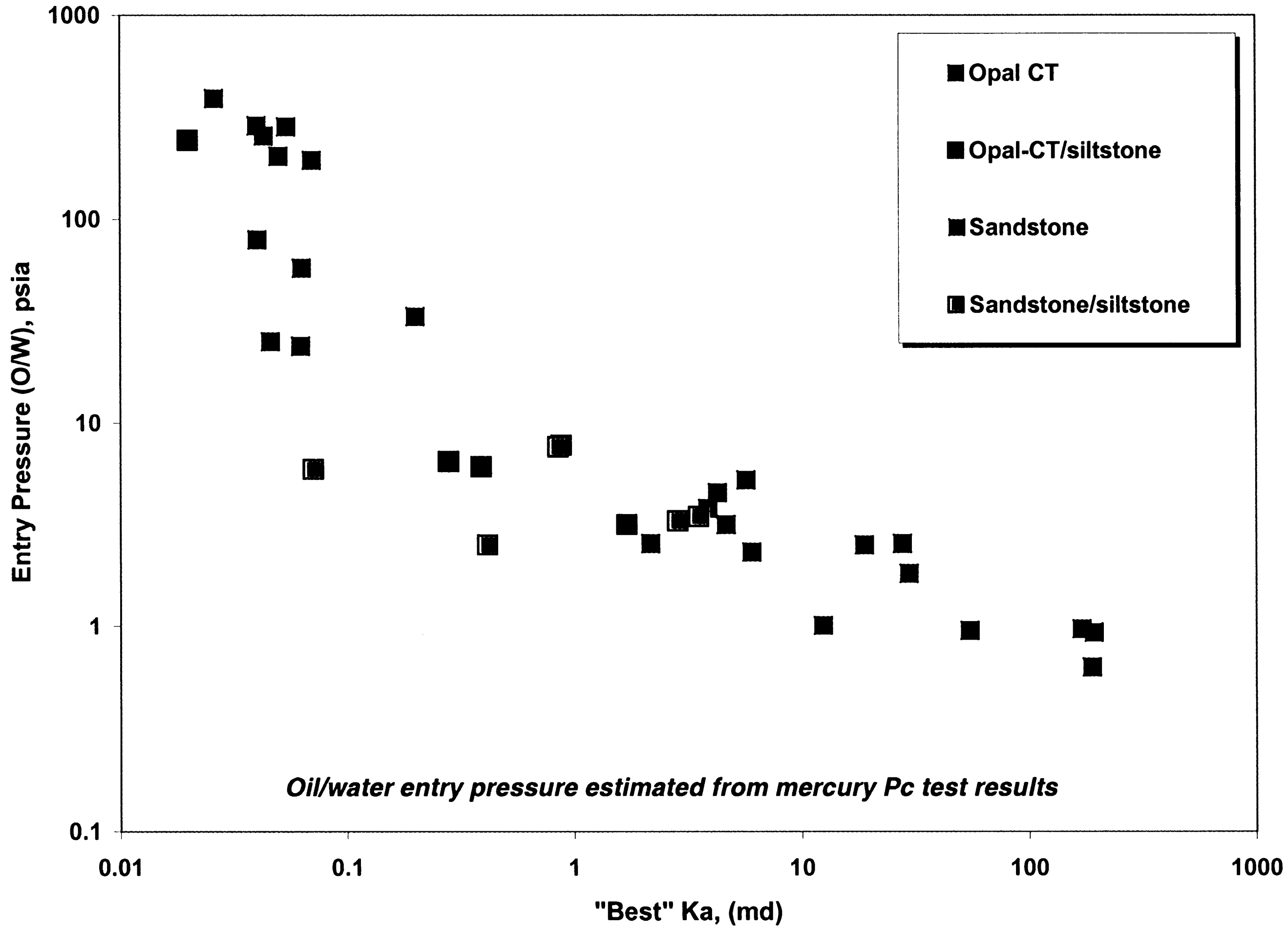

Figure 1.3-7. Oil/water entry pressure versus permeability, estimated from mercury intrusion tests.

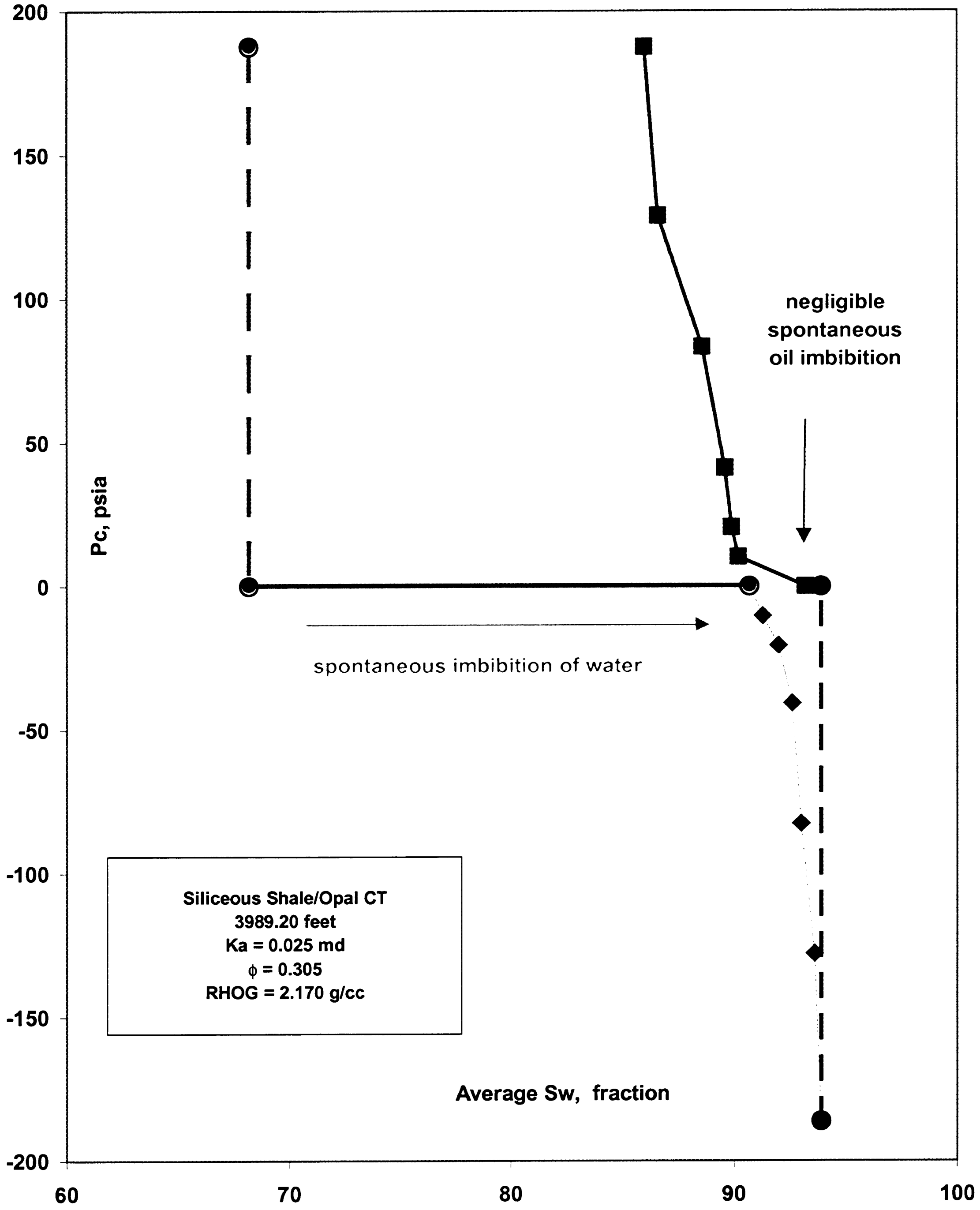

Figure 1.3-8. USBM/Amott wettability test results for opal-CT sample from 3989.20 feet.

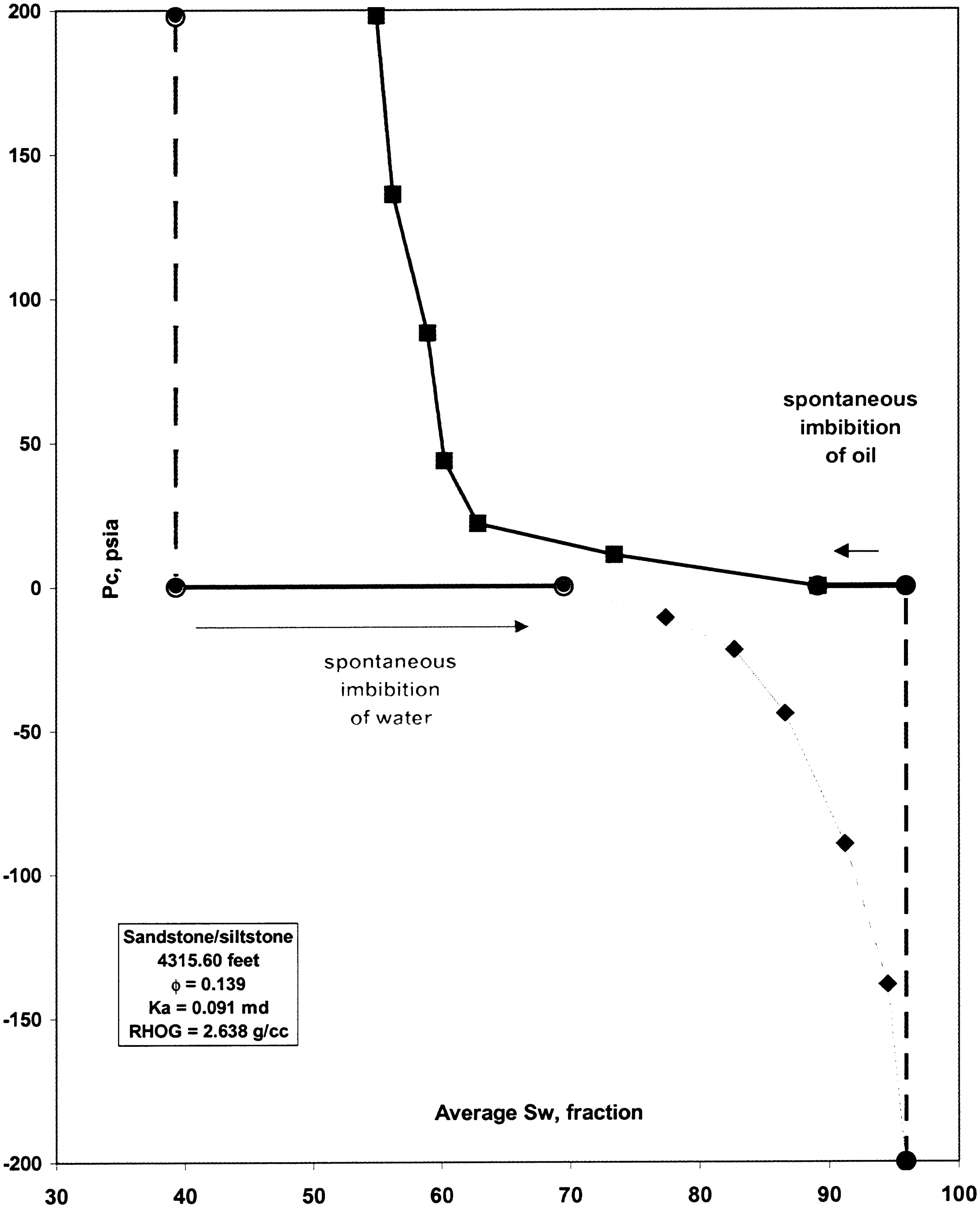

Figure 1.3-9. USBM/Amott wettability test results for sandstone/siltstone sample from 4315.60 feet.

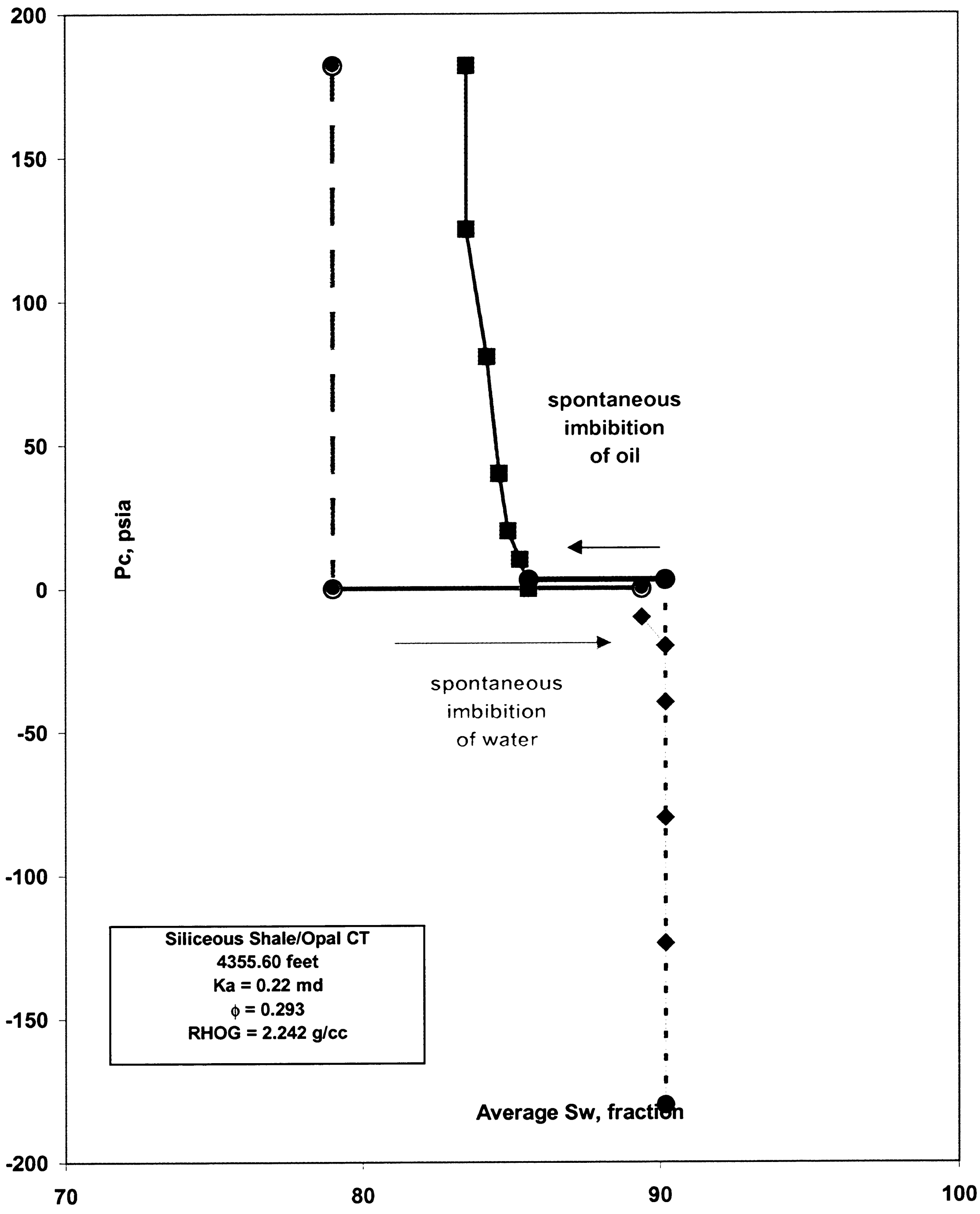

Figure 1.3-10. USBM/Amott wettability test results for opal-CT sample from 4355.95 feet.

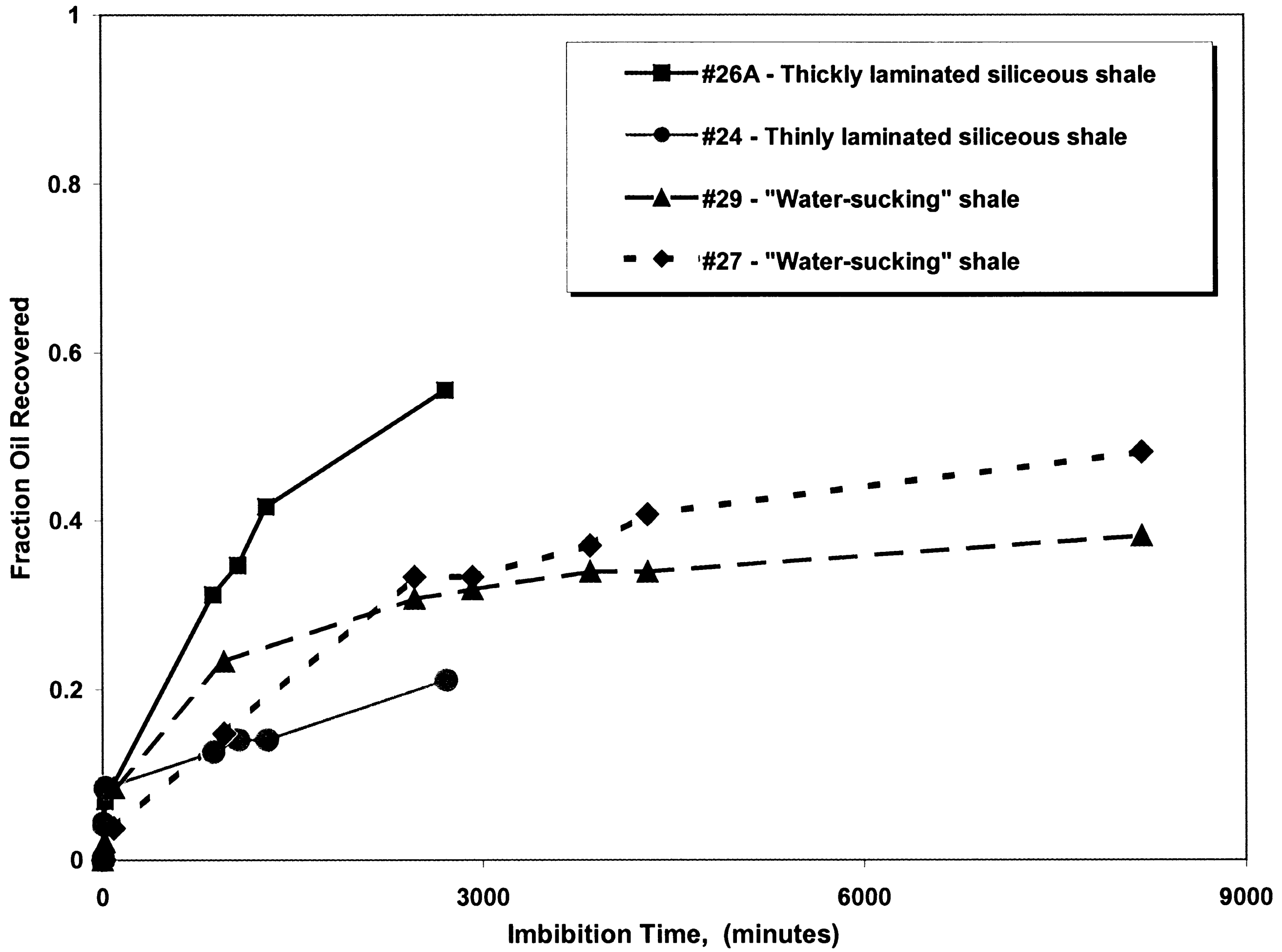

Figure 1.3-11. Oil recovery by spontaneous imbibition at reservoir temperature (opal-CT samples).

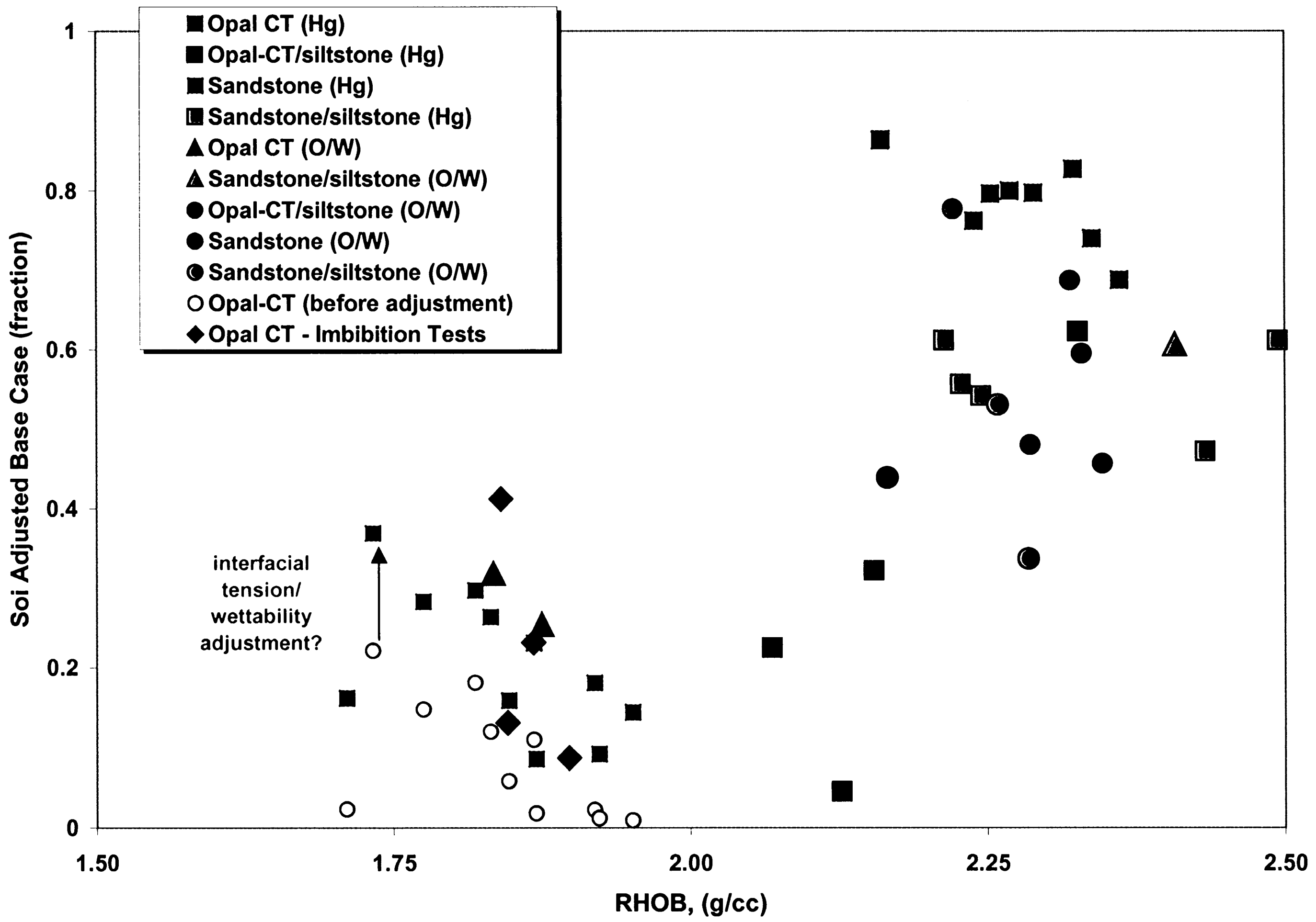

Figure 1.3-12. Estimated initial oil saturation versus bulk density (RHOB).

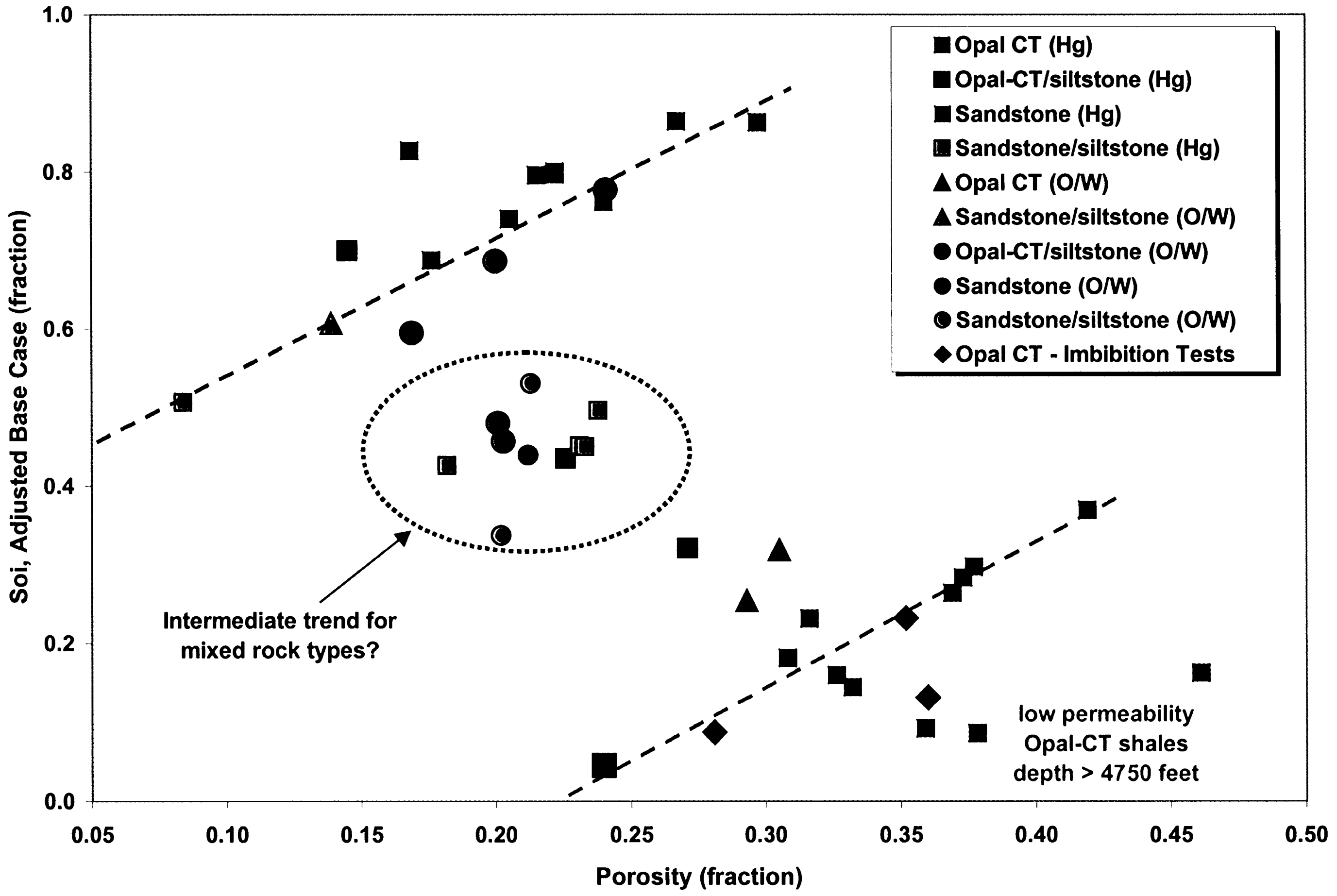

Figure 1.3-13. Initial oil saturation versus porosity. Notice different trends by rock type.

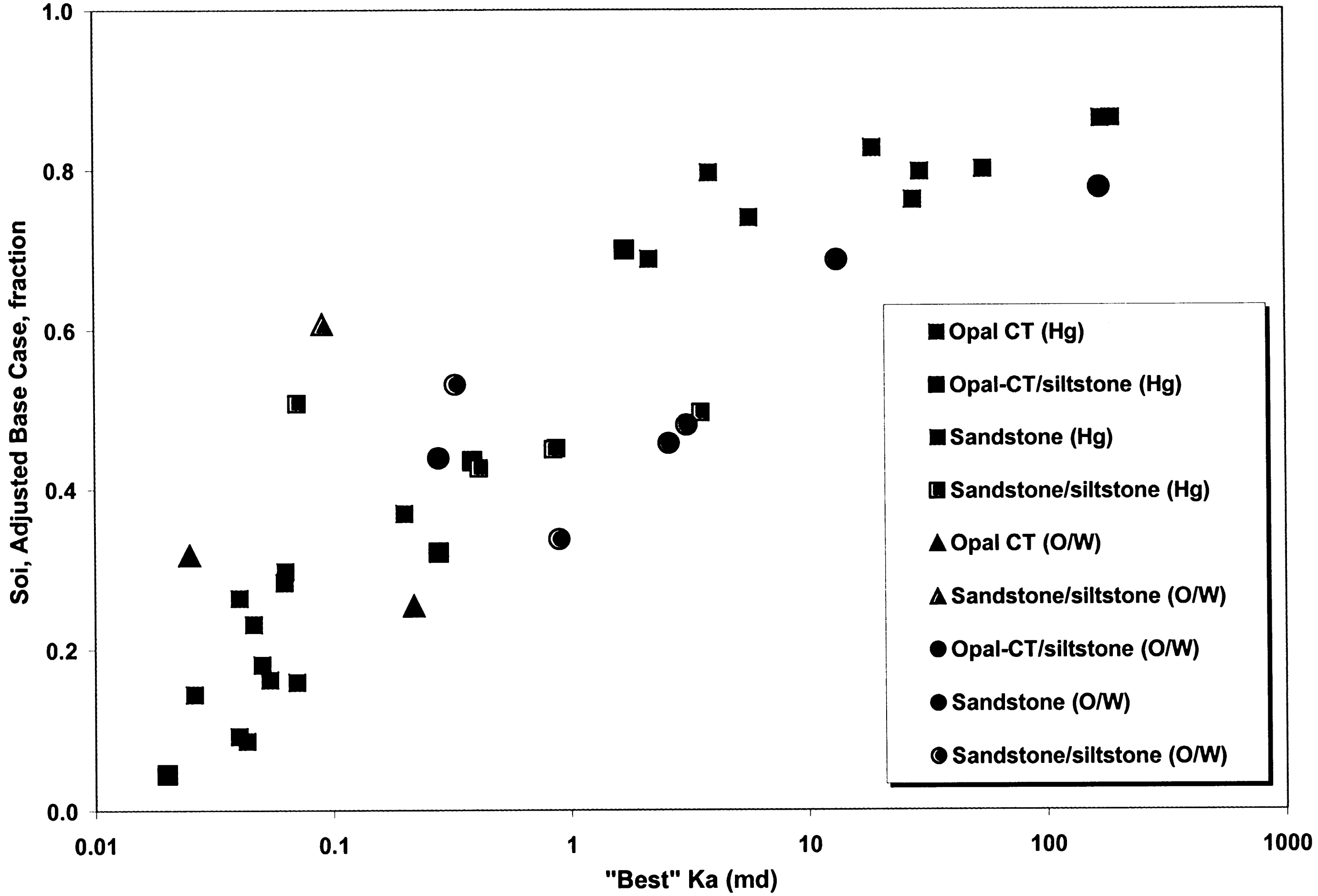

Figure 1.3-14. Initial oil saturation versus air permeability. Notice trend in permeability with rock type.

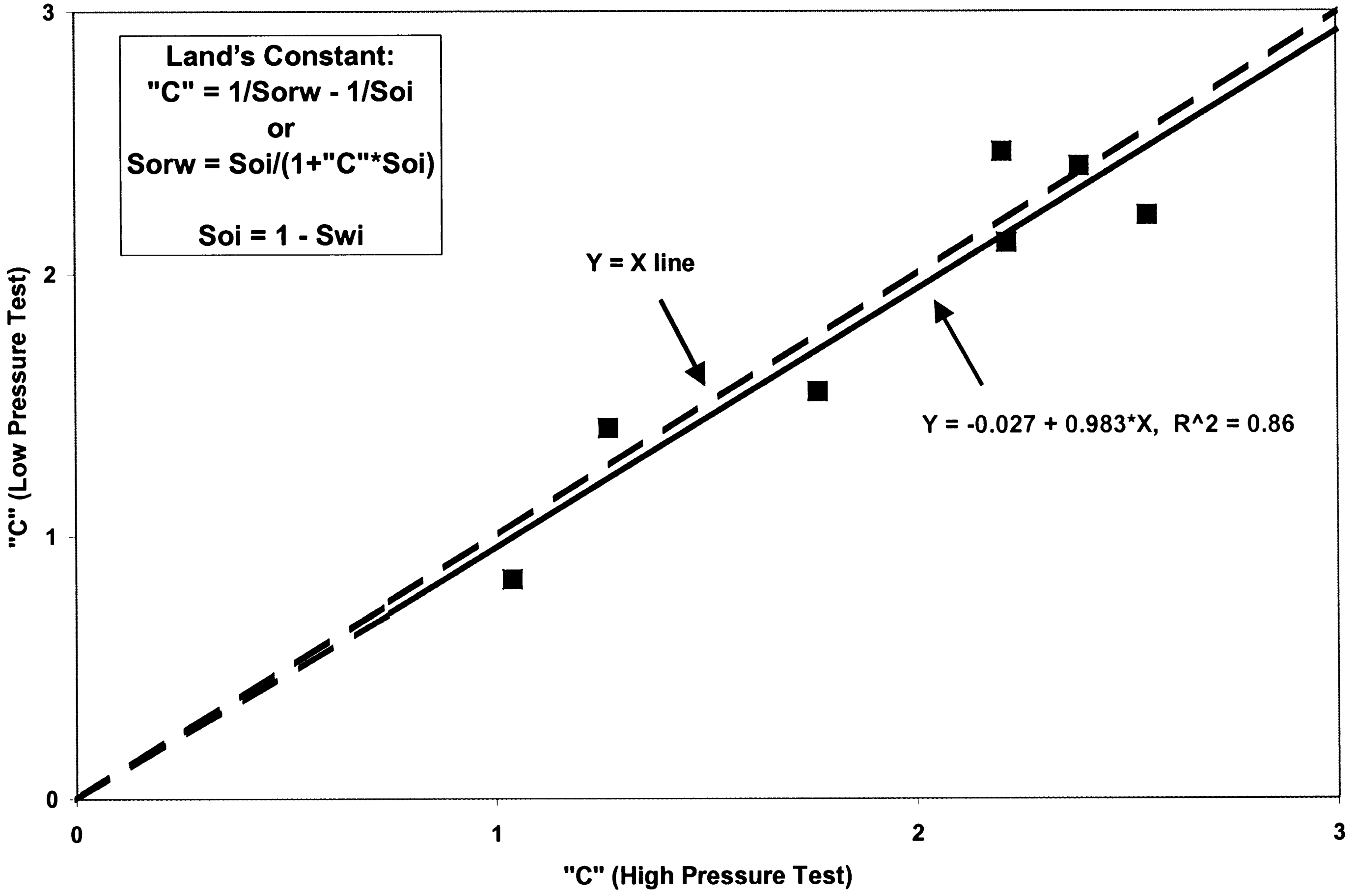

Figure 1.3-15. Land’s trapping constants for high-pressure mercury tests correlate well with low-pressure tests.

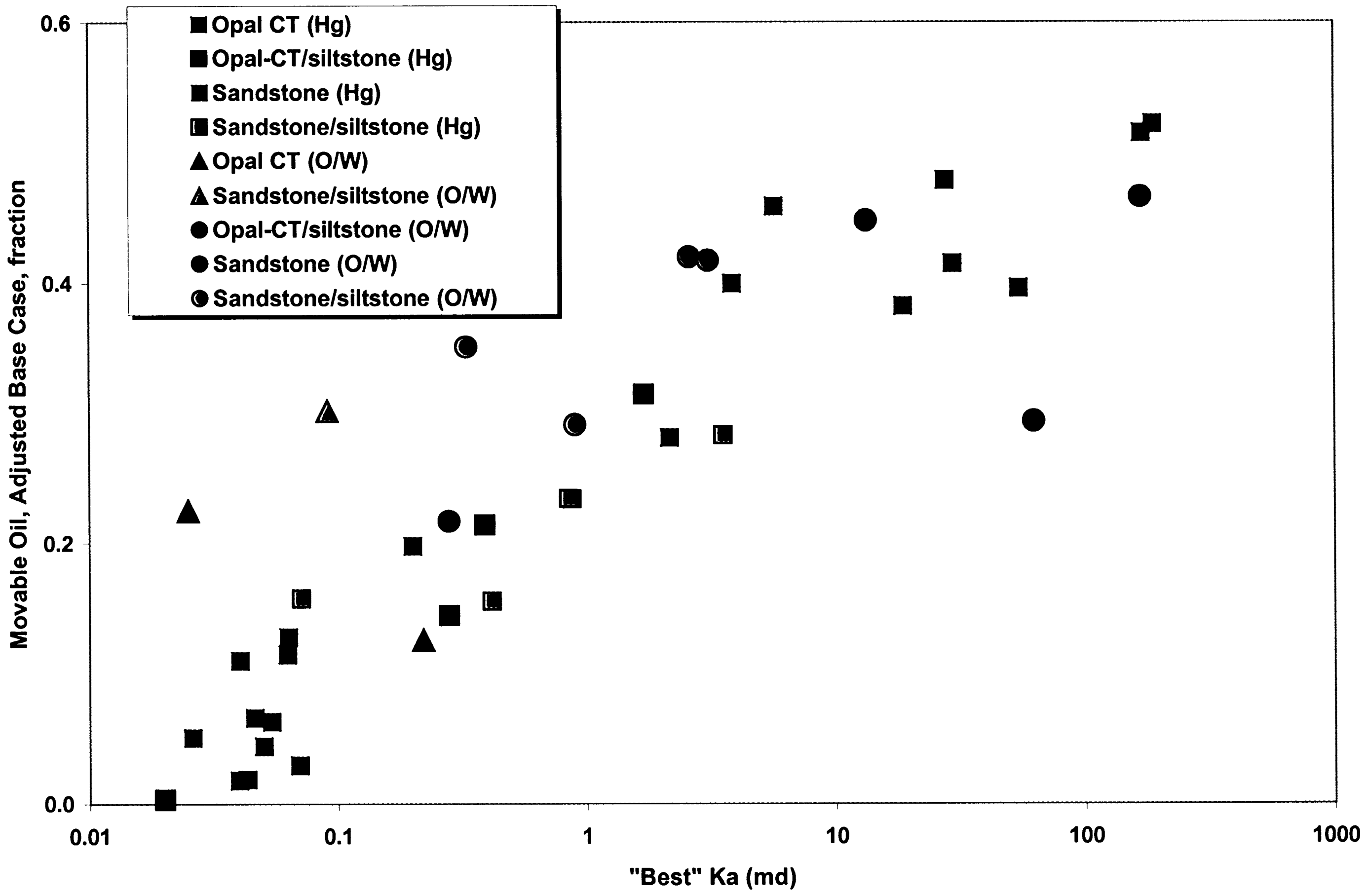

Figure 1.3-16. Movable oil saturation (Soi – Sorw) versus air permeability.

1.4. WELL LOGGING SUMMARY

Tom Zalan

Chevron USA Production Company

INTRODUCTION

As part of the evaluation of the Chevron/DOE Buena Vista Hills Field well 653Z-26B, Schlumberger was commissioned to run the following services:

Array Induction Tool	AIT
Spontaneous Potential	SP
Three Detector Density Tool	TDD
Compensated Neutron Log	CNL
Array Porosity Sonde	APS
Natural Gamma Ray Spectroscopy	NGS
Micro Cylindrically Focused Log	MCFL
Electro Magnetic Propagation Tool	EPT-G
Micro Log	ML
Combinable Magnetic Resonance	CMR
Formation Micro Imager	FMI
Dipole Shear Sonic Imager	DSI
Environmental Capture Sonde	ECS
Modular Dynamics Tester	MDT
Reservoir Saturation Tool	RST
Ultra Sonic Imager	USI
Cement Bond Tool	CBT

GENERAL FINDINGS

The siliceous shale of Buena Vista Hills Field challenges standard traditional wireline log interpretations. The formation matrix density (Figure 1.4-1) is lower than that normally encountered in sands, which skews the porosity derived from logs when the matrix density is set to 2.65 g/cc, a standard for sandstone environments.

The higher formation porosity also causes challenges for compensated neutron log porosity algorithms. The neutron porosity reads lower than true porosity. The fact that the siliceous shale is a siliciclastic rock makes it tough for traditional analysis since "quartz type sandstone" will not traditionally have this high porosity with low permeability simultaneously.

Because of the complex lithology, i.e., the higher porosity siliceous shale has much lower permeability than the sands; thus standard open hole log empirically-based porosity/permeability transforms hold little basis in reality on these rocks.

The low permeability of the rock leads to an initial conclusion that unless open fractures are present, the primary transfer of fluids from the formation to the wellbore is due to water imbibition. The overall resistivity of the rocks is what might be considered "nondescript" when traditional water saturation equations are used.

Buena Vista Hills Antelope Shale appears to have less acoustic attenuation than many other areas of siliceous shale seen in the region. The compressional wave slowness data was successfully acquired and measurable. Shear wave slowness in this rock is moderate, ranging from 180 - 280 microseconds per ft. Many areas in this region might show comparable slowness in excess of 350 microseconds per foot.

Magnetic resonance of the formation appears to be a valuable tool for indication of rock parameters such as porosity, bound fluid, hydrocarbon typing, permeability, and residual oil saturation. These measurements used in conjunction with the other open hole data give a good analysis through zones of varying lithology and lamination thickness. Looking at the CMR log and tying in the station logs from the CMR, we can see what appears to be a relatively laminated oil column of viscosity ranging from 2 - 10 cp throughout the Antelope Shale.

.

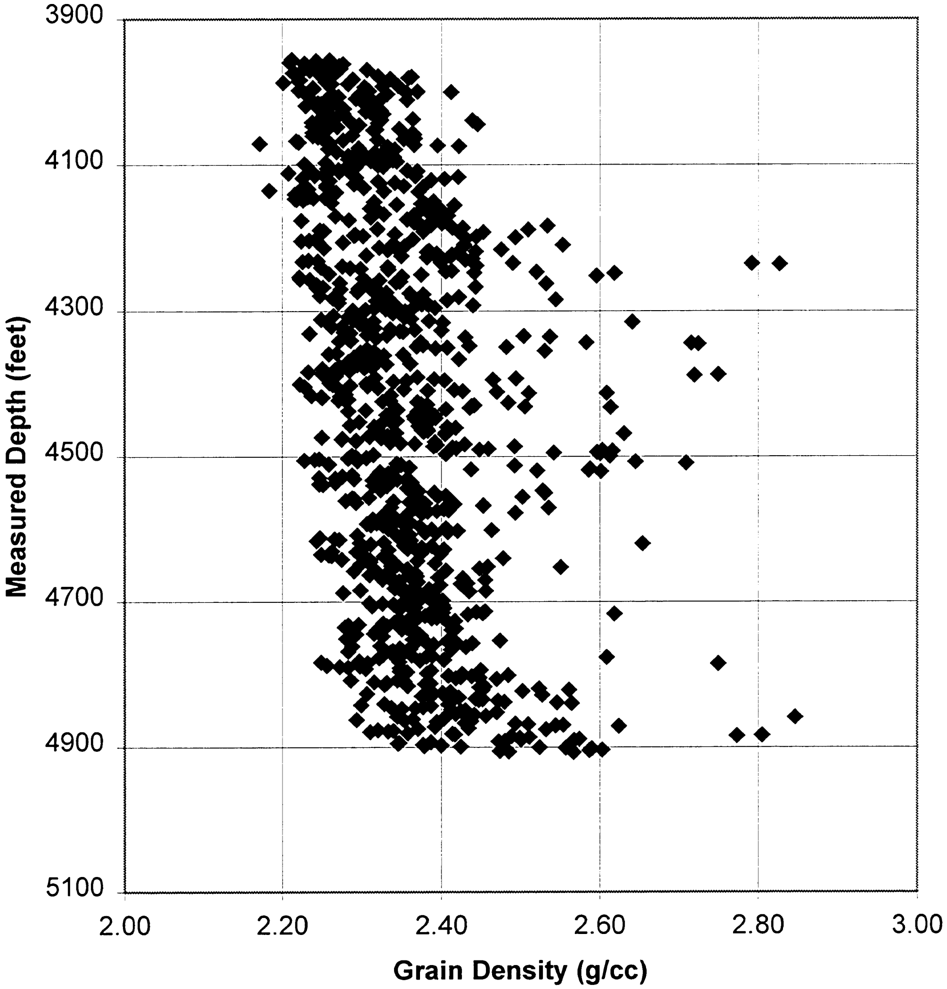

Figure 1.4-1. Matrix density from core variation with depth, Well 653Z-26B.

MINERAL MODELING

Effective reservoir characterization using a mineral-based formation evaluation strategy requires special types of mineralogical analysis. The approach requires accurate knowledge of the average compositions and related properties of individual minerals within the reservoir. The approach also requires that the validity of mineral models be verified by comparing mineralogical estimates from logs with accurate mineralogical analyses of corresponding core.

Stan Denoo of Schlumberger Wireline Services, Denver has created three mineral models from logging suite combinations: model 1) Platform Express triple combo / Combinable Magnetic Resonance (CMR) / Elemental Capture Sonde (ECS); model 2) Platform Express triple combo / CMR; and model 3) Platform Express triple combo only. Each suite gives the same outputs, but more and more local constraints are applied as the logging suite gets smaller. This makes model 1 almost universally applicable but model 3 primarily locally defined.

The models consist primarily of five mineral components: *clay, potassium feldspar, detrital quartz, carbonate,* and *opal-CT phase biogenic silica***.**

The volume of *clay* is equal to the ECS clay volume taken directly from the log. When the ECS is not in the suite, the clay volume can be computed from the *t2* logarithmic mean of the CMR or from the photoelectric factor of the Platform Express.

The volume of *potassium feldspar* is from the Natural Gamma Tool potassium channel as a linear function. When the Natural Gamma Tool is absent from the logging suite, the feldspar volume is estimated as twenty-five percent of the clay volume.

The volume of *detrital quartz* is defined as a linear percentage of the clay and feldspar.

The volumes of *limestone and dolomite* are computed based on an estimated formation grain density. The grain density of the formation is computed from the bulk density and the porosity. When the CMR is part of the logging program, the CMR total porosity may be used to compute the grain density **rhogr = (rhob - phi) / (1-phi)**. If the CMR is not present, the initial porosity is the average of the neutron and density porosity. The grain density computed by a neutron-density average porosity was found to be high by 0.19 gm/cc. The corrected matrix value is then used to compute the new porosity **phi = (rhogr -rhob) / (rhogr-1)**. Grain densities between 2.66 gm/cc and 2.73 gm/cc are defined as limestones, and greater than 2.73 gm/cc are dolomites.

The volume of *opal-CT biogenic silica* is determined by clay correcting end point grain densities for pure opal-CT (2.10 gm/cc) and pure detrital quartz (2.65 gm/cc), and then dividing the computed total quartz volume into detrital and biogenic parts.

Mineral model 2 using the Platform Express triple combo and the CMR agrees best with mineralogical analyses of core. In wireline log track 3 of Figure 1.4-2, volume fractions of mineral components from bulk foot core mineralogical analyses (solid lines) are plotted against mineral model results (dash lines). From the right limit of log track 3 to the right set of solid and dash lines is the volume of quartz+feldspar. From the right set of solid and dash lines to the left set of solid and dash lines is the volume of clay+pyrite+organic matter. From the left set of solid and dash lines to the left limit of log track 3 is the volume of opal-CT. Figures 1.4-3 - 5 are crossplots for the interval - 4300 feet of the mineral model and core volume fractions of, respectively, quartz+feldspar, clay+pyrite+organic matter, and opal-CT. It is evident from these plots that the mineral model fairly accurately represents the actual (core) mineralogy.

Mineral model 3 using the Platform Express triple combo agrees second best. Mineral model 1, including the Elemental Capture Sonde, agrees worst. We believe adding the Elemental Capture Sonde to the mix degrades the agreement to core because it contributes mineralogical information that conflicts with either the Platform Express triple combo and/or the CMR. These differences in the model results are still being investigated.

Another byproduct of the Schlumberger modeling effort was the derivation of permeability from the shallow resistivity log, Rxo. Track 4 of Figure 1.4-2 shows Rxo-based permeability agrees in character and magnitude with core permeabilities, as opposed to CMR-derived permeabilities, which are off from core by one to two orders of magnitude.

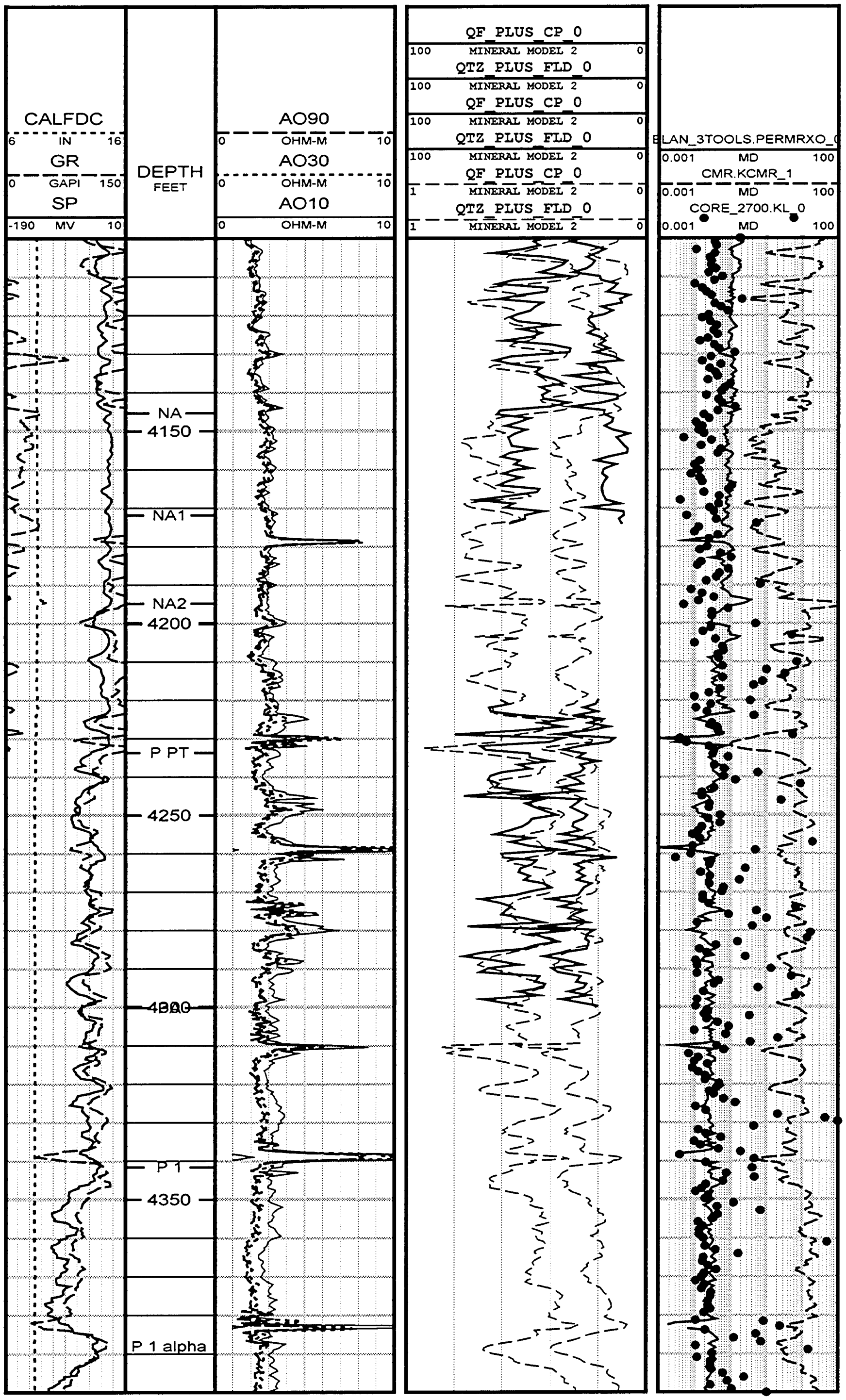

Figure 1.4-2. Schlumberger ELAN mineral model from logs (dashed lines in wireline log track 3) agrees with Chevron core ESTMIN mineralogy (solid lines in track 3). Permeability from shallow resistivity log agrees with core permeability (track 4).

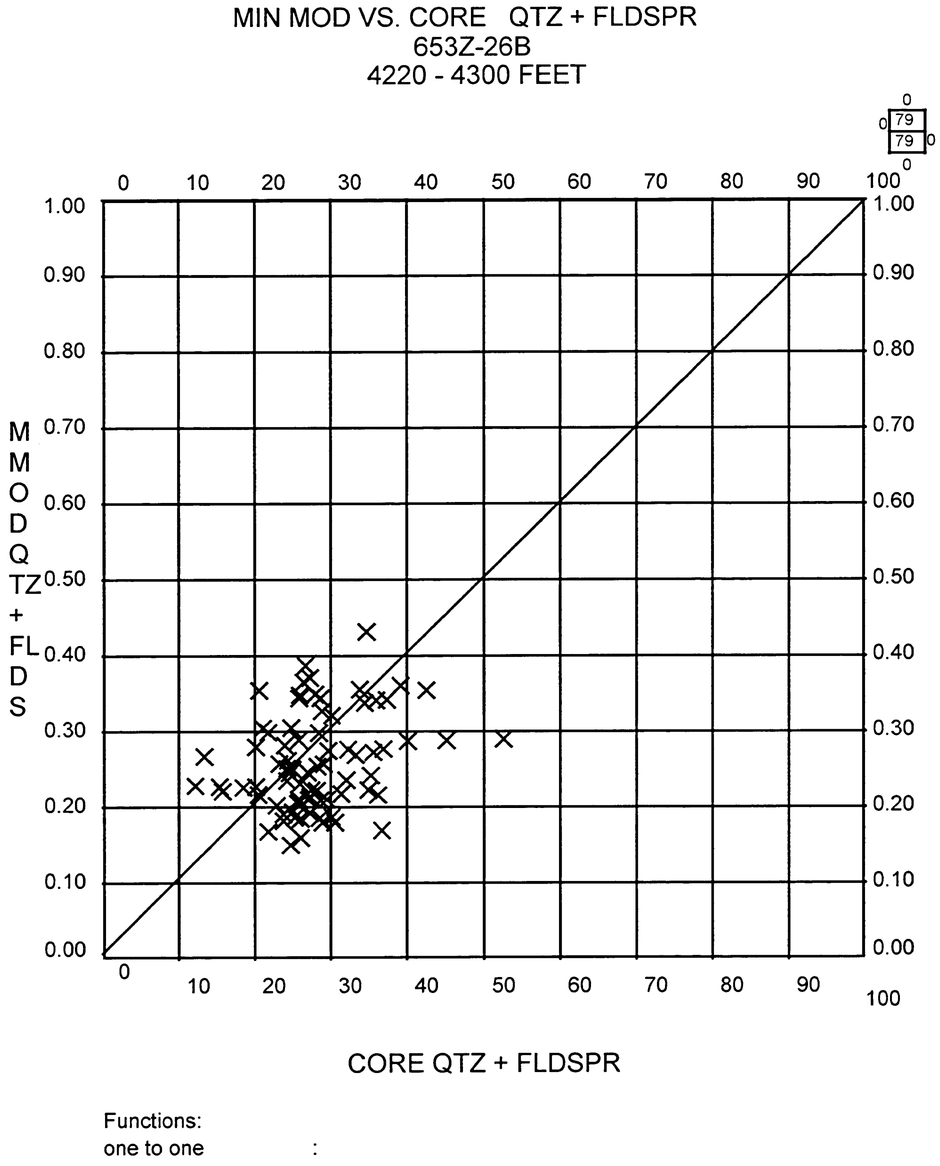

Figure 1.4-3. Cross plot of volume of Quartz+Feldspar — Schlumberger ELAN mineral model versus Chevron core ESTMIN.

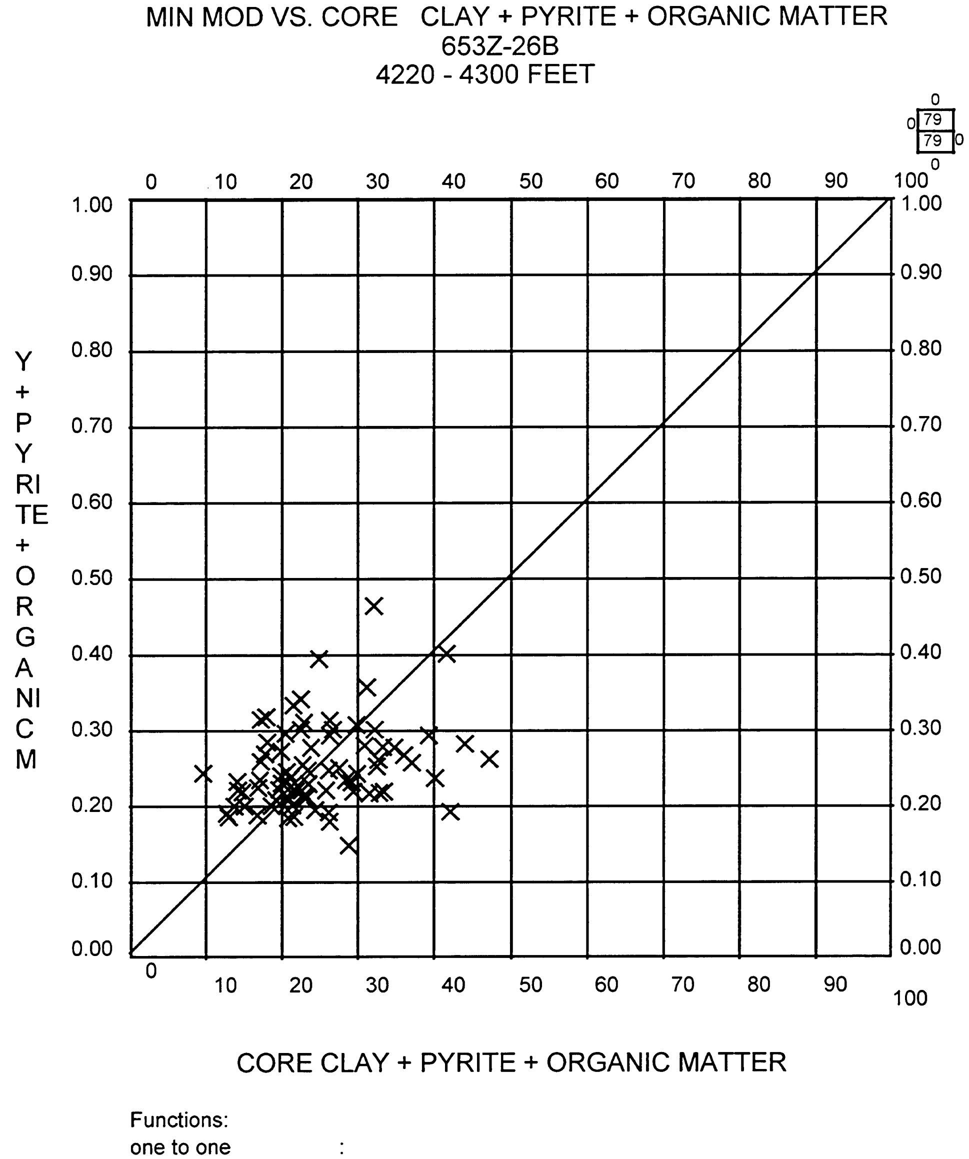

Figure 1.4-4. Cross plot of volume of Clay+Pyrite+Organic Matter — Schlumberger ELAN mineral model versus Chevron core ESTMIN.

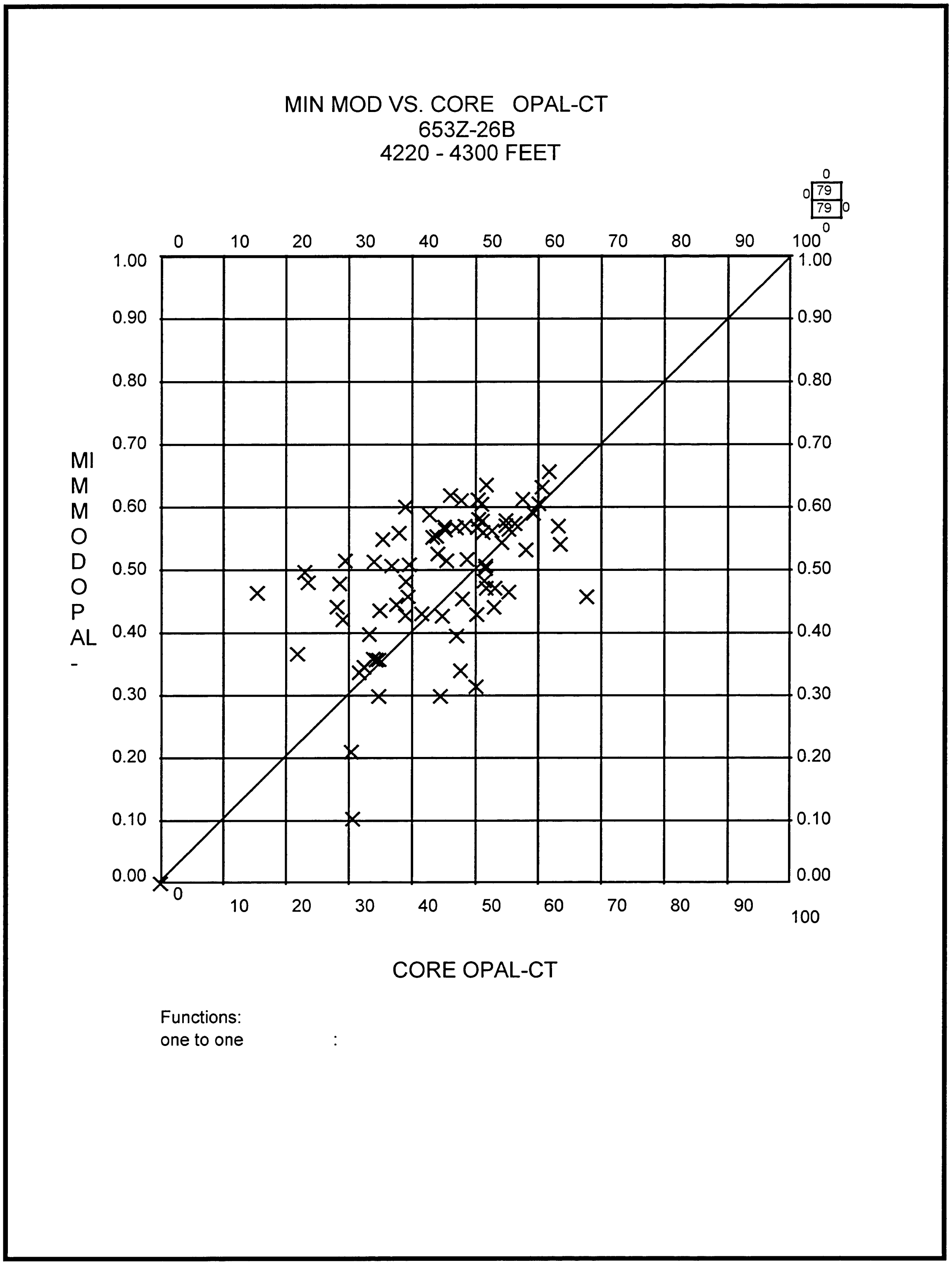

Figure 1.4-5. Cross plot of volume of Opal-CT — Schlumberger ELAN mineral model versus Chevron core ESTMIN.

BOREHOLE IMAGE ANALYSIS

Schlumberger completed an analysis of the FMI data from well 653Z in 1996. Figure 1.4-6b shows a typical FMI image from the lower Upper Antelope with bedding resolved down to 0.1 ft. Also shown in the figure are examples of a fault and a fracture and the matching core. Figure 1.4-7 shows an upper hemisphere equal area net of all the planar features that were identified on the FMI over the interval 3952 ft to 4902 ft. The poles to bedding planes in Figure 1.4-7 (green squares) show a tight clustering of dips that average 10.9° with an average dip azimuth of N34°E. The red, dark blue and light blue squares show fractures of different qualities ("A" being of highest quality and "C" being of lowest quality). Figure 1.4-8 shows an azimuth histogram for these fractures. While there are numerous azimuths represented in Figure 1.4-8, the most abundant are in the S40°E to S45°E direction. Figure 1.4-9 shows a dip histogram for the same set of fractures and shows that dips range from 10° to 90°, but that the most common occurrence is between 80° and 90°.

The orange squares, pink squares, and pink X's in Figure 1.4-10 show an azimuth histogram for faults, microfaults, and healed fractures respectively. Like those of the fractures already discussed, there are numerous azimuths represented in Figure 1.4-10 but the most abundant are in the S40°E to S45°E direction. Figure 11 shows a dip magnitude histogram for the faults, microfaults, and healed fractures and shows that dips range from 10° to 80° with only a slight preference for the 50° to 70° degree dip range.

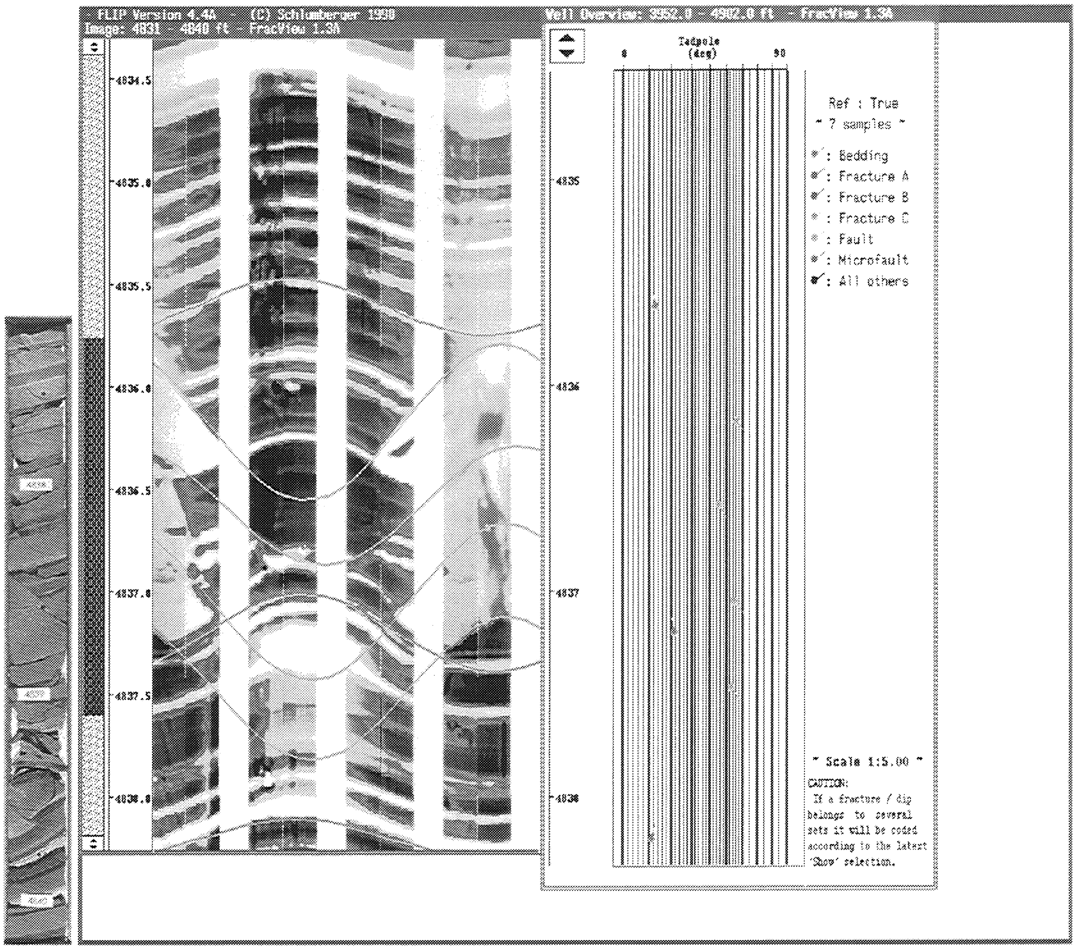
- FLIP Version 4.4A - (C) Schlumberger 1998
Image: 4831 - 4840 ft - FracView 1.3A
4834.5
4835.0
4835.5
4836.0
4836.5
4837.0
4837.5
4838.0
Well Overview: 3552.0 - 4902.0 ft - FracView 1.3A
Tadpole (deg)
0
90
4835
4836
4837
4838
Ref : True
~ 7 samples ~
: Bedding
: Fracture A
: Fracture B
: Fracture C
: Fault
: Microfault
: All others
~ Scale 1:5.00 ~

CAUTION:
If a fracture / dip belongs to several sets it will be coded according to the latest 'Show' selection.

(a) (b)

Figure 1.4-6. (a) Core photo in white light of equivalent depth interval in (b). (b) Formation MicroImager microresistivity image of lower Upper Antelope Shale.

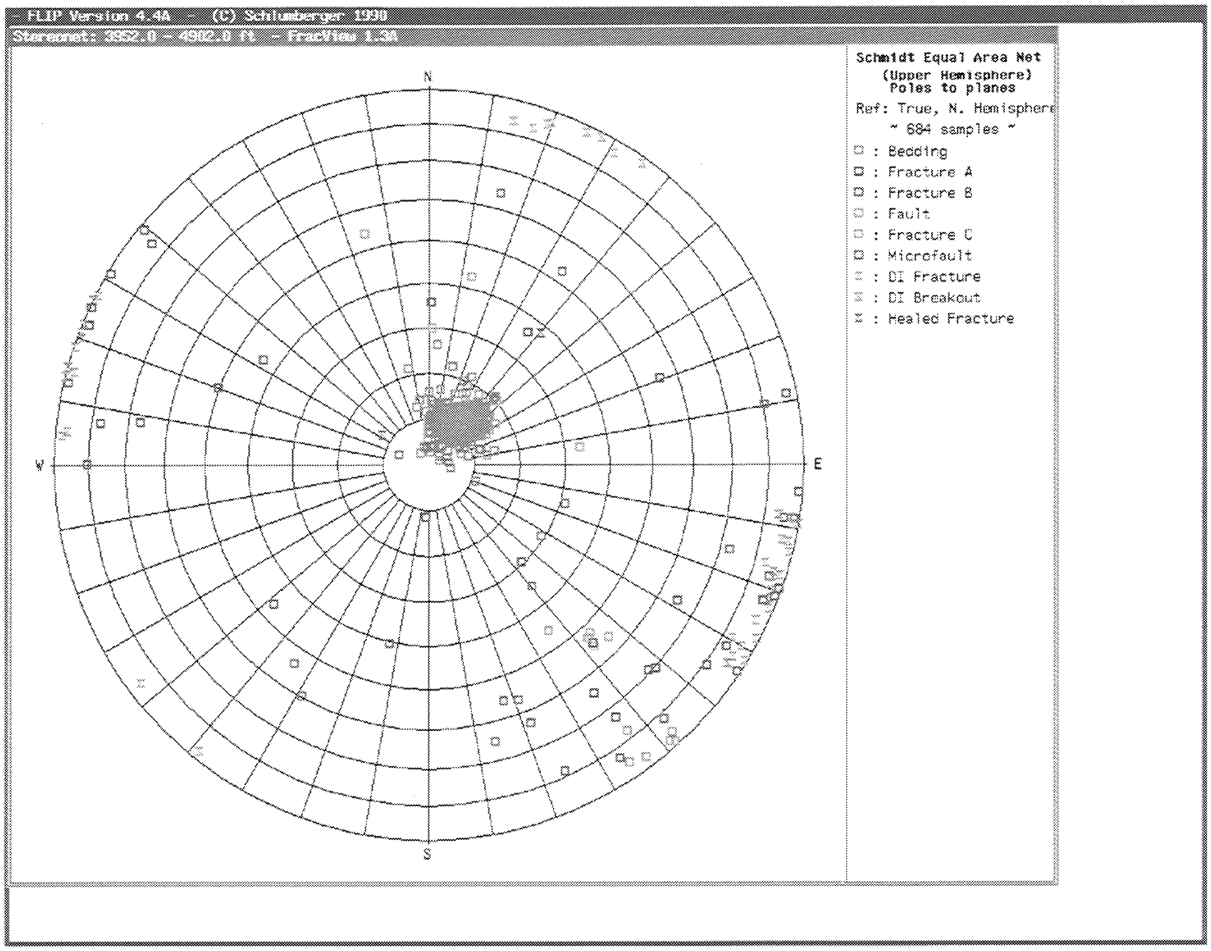

Figure 1.4-7. Upper hemisphere polar equal area net of poles to planes of bedding, faults, and fractures.

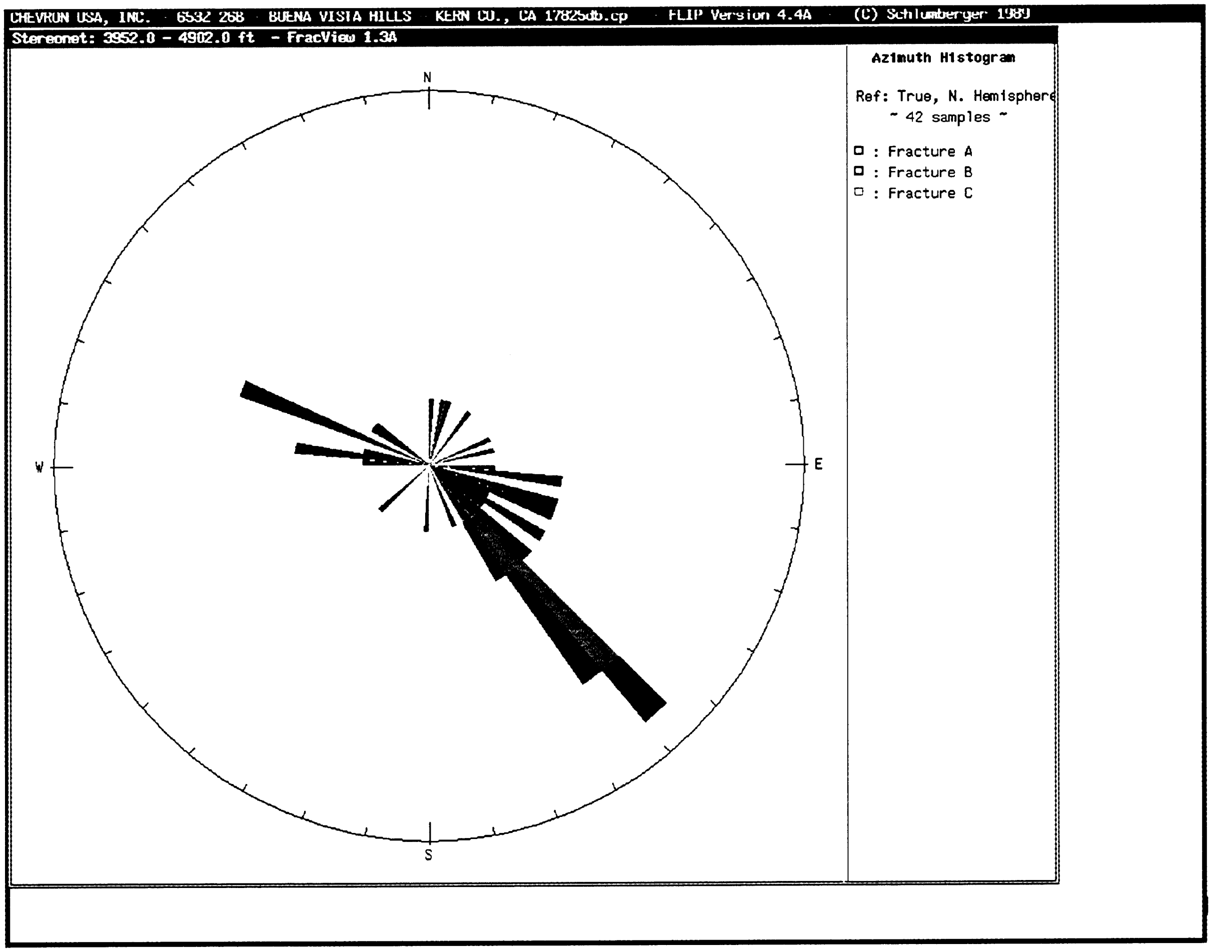

Figure 1.4-8. Histogram (rose diagram) of fracture dip azimuths interpreted from FMI.

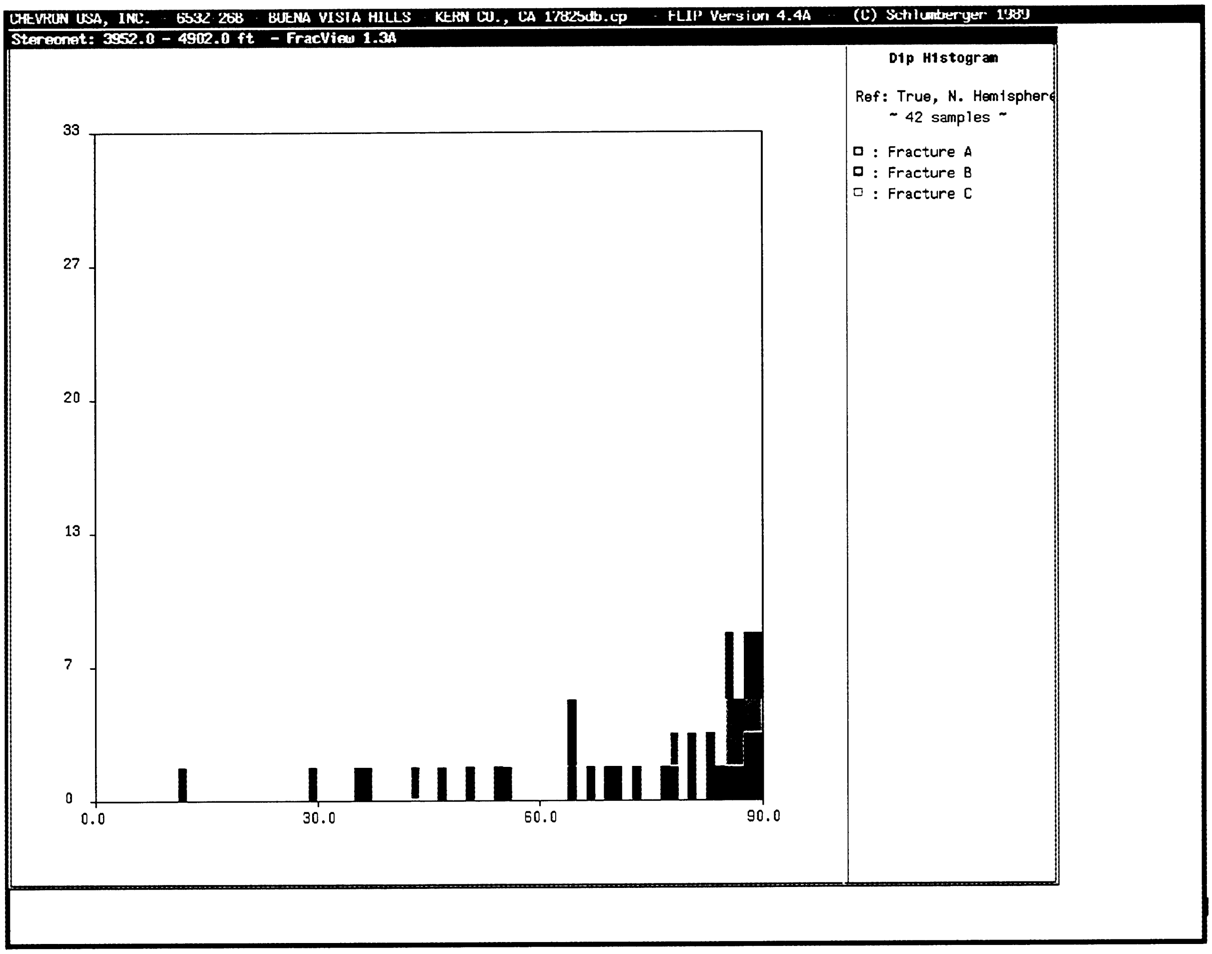

Figure 1.4-9. Histogram of dip magnitudes interpreted from FMI.

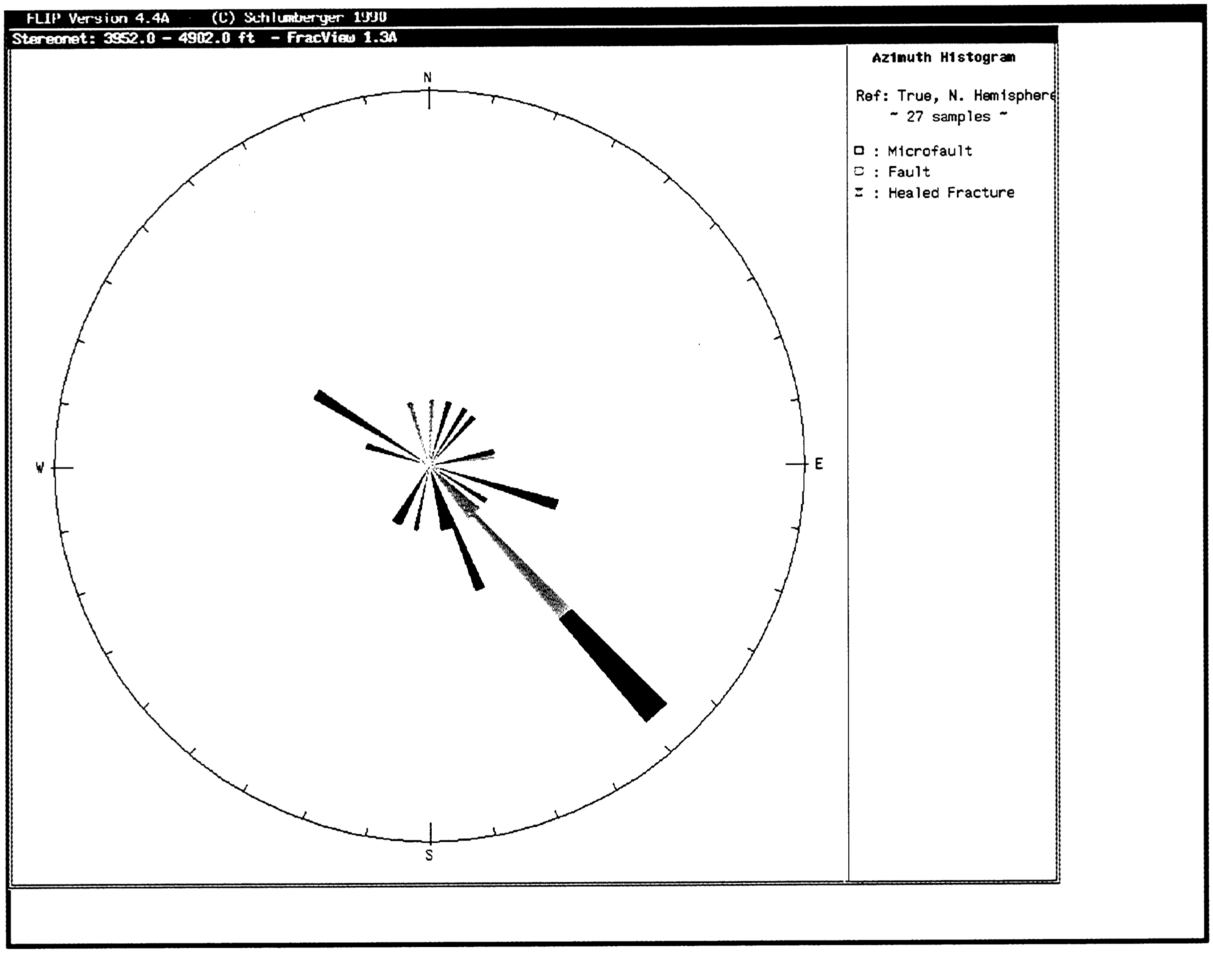

```
FLIP Version 4.4A     (C) Schlumberger 1990
Stereonet: 3952.0 - 4902.0 ft  - FracView 1.3A

Azimuth Histogram

Ref: True, N. Hemisphere
    ~ 27 samples ~

□ : Microfault
□ : Fault
⧗ : Healed Fracture
```

Figure 1.4-10. Histogram (rose diagram) of fault and healed fracture azimuths interpreted from FMI.

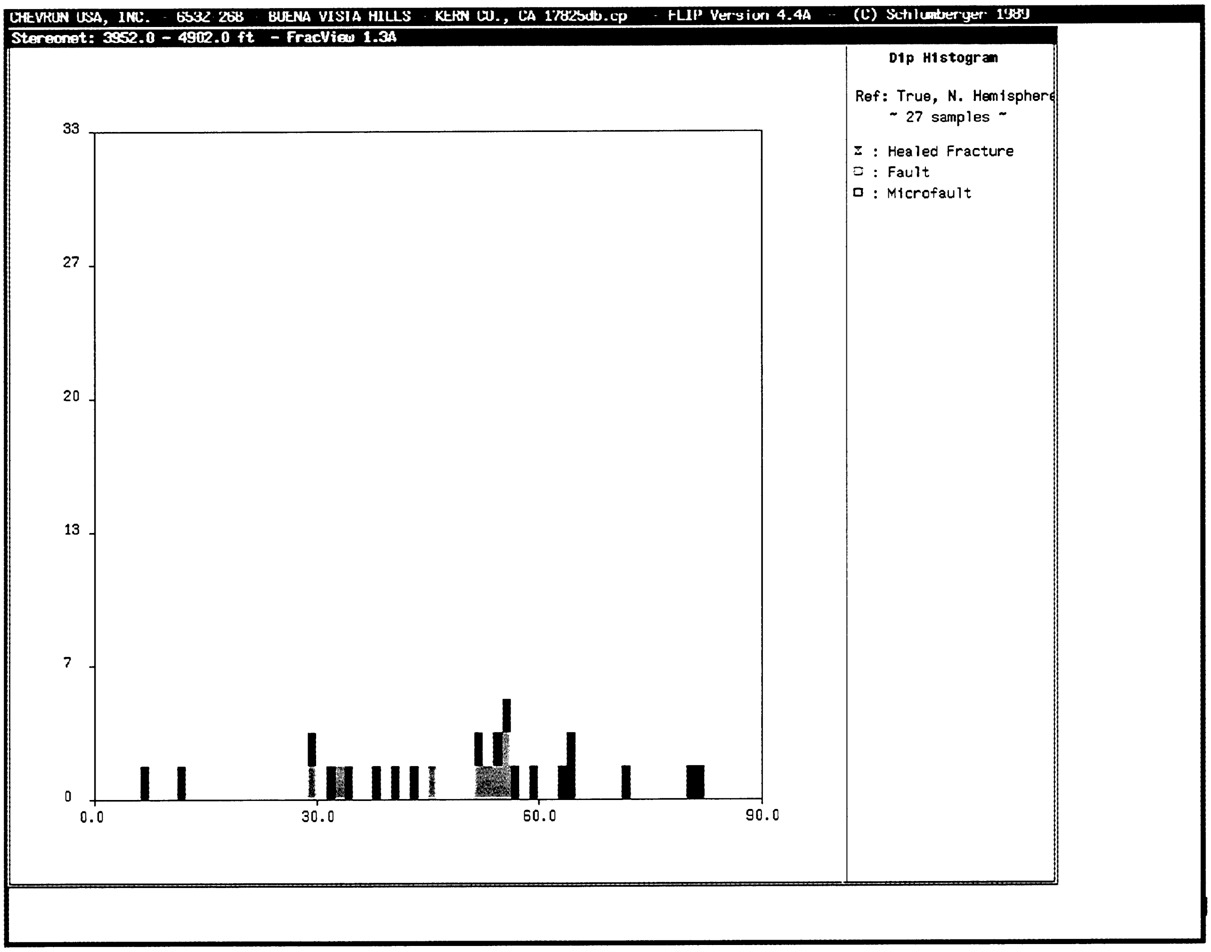

Figure 1.4-11. Histogram of dip magnitudes of faults and healed fractures interpreted from FMI.

NMR SCAN OF CORE PLUGS

Nuclear magnetic resonance (NMR) measurements were made by Core Laboratories, Houston on fifteen rock plug samples using a Core Spectrometer. NMR measurements were performed before and after fluid extraction from the specific permeability core plugs in order to compare NMR log and core responses.

All fifteen samples were supplied in native state (fresh condition). NMR data were acquired with a 0.5 ms echo time spacing with delay and train settings to achieve the best possible signal-to-noise (S/N) ratio.

After NMR measurements on the native state plug samples, the plugs were cleaned, resaturated with synthetic brine, and loaded into the calibrated (using 100% water samples) Core Spectrometer. The NMR measurements were made with a 0.5 ms echo time spacing with the delay and train settings to again achieve the best possible S/N ratio.

Porosity was calculated from the NMR measurement on each fully brine saturated sample using a multi-exponential fit computer program. Fully saturated and native state NMR measurements are compared in Table 1.4-1. The median values of the NMR transverse relaxation times, T2, are also compared in Table 1.4-1. The difference in porosity between the fully brine saturated and native state measurements defines the level of liquid saturation in the rock. The measured porosity and NMR transverse relaxation times are significantly lower in the native state plug samples due to gaseous phase being present.

The geometric mean of the NMR transverse relaxation times, T2, match closely with the NMR log, but NMR core plug porosity does not match routine core porosity or NMR log porosity. This porosity discrepancy is not yet understood.

Table 1.4-1. Comparison of fully saturated and native state NMR measurements.

		FULLY SATURATED STATE		**NATIVE STATE**	
Sample #	**Depth, FT**	**Porosity (%)**	**T_2 (ms)***	**Porosity (%)**	**T_2 (ms)***
S1	**4432.50**	**19.11**	**119.11**	**10.76**	**23.08**
S2	**4640.10**	**10.59**	**19.85**	**10.02**	**9.99**
S3	**4668.85**	**16.58**	**125.33**	**9.26**	**12.46**
S4	**4836.90**	**12.02**	**59.64**	**11.38**	**37.48**
S5	**4838.85**	**4.53**	**7.60**	**4.08**	**2.42**
S6	**4866.00**	**8.99**	**25.64**	**6.90**	**6.14**
S7	**4869.30**	**9.40**	**30.06**	**9.16**	**15.45**
SS1	**4369.80**	**35.52**	**7.66**	**30.79**	**7.26**
SS2	**4370.00**	**32.42**	**7.38**	**30.67**	**8.59**
SS3	**4271.65**	**27.00**	**6.08**	**26.39**	**4.61**
SS4	**4744.25**	**31.44**	**6.86**	**29.11**	**5.65**
SS5	**4200.05**	**21.83**	**1.46**	**19.44**	**1.28**
SS6	**4747.95**	**38.76**	**9.81**	**38.66**	**9.75**
SS7	**3958.05**	**34.79**	**6.08**	**32.44**	**5.33**
SS8	**3959.00**	**34.59**	**6.17**	**33.87**	**5.30**

*** - T_2 is the median value (50 Percentile).**

NEW PRODUCTION LOGGING TECHNOLOGY

Downhole Video Camera (DHV International & Halliburton): The downhole video camera has been extensively used in the evaluation of producing wells throughout Chevron's worldwide operations. Wells have been logged under static and dynamic conditions, some of which have production rates comparable to Buena Vista Hills wells. The downhole video camera has been found to be most effective when wellbore fluid clarity exists, flow rates are not turbulent, water is the continuous phase, gas rates are low, segregated flow exists, and scale is present (scale enhances light reflectivity off casing inner wall). Lastly, the camera must be deployed in such a way as to be able to log under typical producing conditions. Chevron's experience has been positive when using the downhole video camera to view wellbore fluids under shut-in conditions; however, downhole video has limited utility when wells are actually logged under dynamic flowing conditions. Fluid clarity is the key to effective camera application.

Downhole video logs were run in Wells 554-26B and 553-26B (Section 26-T31S/R23E) in October 1995 in order to determine exactly where oil, gas, and water are produced from the Antelope Shale. Downhole video logs were used to determine fluid entry because the wells are produced on pump and there was not enough room to run conventional production logs in the annulus between tubing and the slotted liner.

Oil and water entry were observed in 554-26B in the air-filled part of the borehole during both shut-in and flowing periods. Gas entry was observed in the air-filled part of the borehole during flowing conditions only and in the fluid filled part of the borehole during both shut-in and flowing conditions. Oil entry was concentrated in a 25 ft thick zone just below P point, although evidence for oil entry near the bottom of the well was observed. The shut-in fluid level was found at mid perf level and was static. Gas bubbles and suspended solids obscured vision in the fluid-filled part of the borehole. This evidence suggests that significant crossflow occurs during shut-in. Gas apparently flows out of deeper parts of the reservoir and into lower pressure zones and water flows from shallower and maybe deeper parts of the reservoir and into lower pressure zones. Gas and fluid exit points into the formation are unknown.

The fluid level in the 553-26B was above the slotted liner, so effective reservoir fluid entry could not be observed. A shallow casing leak with water entry and several holes in the casing were observed, which probably accounts for the high fluid level.

Video logs were run in wells 563-26B and 564-26B (Section 26-T31S/R23E) in March 1997. The principal objective of these surveys was to identify gas and oil entry into the wellbore. A secondary objective was to identify possible holes or leaks in the casing that warrant remedial attention.

The 563-26B Well was producing 1/5/20 O/W/G prior to shutting in to prepare for video logging. This well held only 10 psi wellhead pressure after having been shut-in for two weeks. The fluid level in the well was at 3052 feet; above the top of the slotted liner at 3938 feet. Gas bubbling was moderate to strong above 4318 feet (in the P interval) and disappeared below 4318 feet. No oil entry was observed in the well. A water shutoff hole or leak was observed in the 8 5/8" casing at 1054 feet. Leaks were also observed at the top of the 6 5/8" slotted liner at 3897 feet.

The 564-26B Well was producing 3/60/10 O/W/G prior to shutting in to prepare for video logging. This well held no wellhead pressure after having been shut-in for two weeks. The fluid level in the well was at 3264 feet; above the top of the slotted liner at 3845 feet. Gas bubbling was observed to be moderate to strong as deep as the video logging tool could be lowered, down to a scale obstruction at 4566 feet (in the P1B interval). Very light oil entry and oil-stained slots were observed at 3986 - 3991feet (in the N interval).

Four water shutoff holes were observed in the 6 5/8" protective string at 3015 feet. A possible hole or crack was observed in the 6 5/8" slotted liner at 4555 feet.

Chuck Magnani of Chevron Petroleum Technology Company (CPTC) evaluated the feasibility of using two additional new production logging tools/sensors in Buena Vista Hills, the *PANEX Torque-Capacitance Memory Flowmeter* and the *Halliburton Gas Holdup Tool (GHT)*. The following conclusions were reached:

PANEX Torque-Capacitance Memory Flowmeter: The PANEX torque-capacitance memory flowmeter was evaluated in a controlled field-trial in West Texas. The primary objective of this test was to generally characterize the PANEX flowmeter under controlled single phase conditions to verify instrument performance relative to PANEX specifications. A second goal was to determine the flowmeter's resolution for measuring low flowrates. Key conclusions from this study were: (1) The flowmeter has potential application in single phase, high rate environments such as injection wells; (2) Problems were encountered related to sensor hysteresis, thermal stability, time constants and resolution (PANEX is currently working on these problems); (3) Under controlled conditions, the flowmeter exhibited a linear response when rates exceeded 300 BWPD; however, below 300 BWPD, the instrument was unreliable; (4) The PANEX Torque-Capacitance flowmeter design is not robust and prone to downhole plugging; i.e., the shroud surrounding the spinner acts as a vena contracta causing debris to collect in the spinner metering chamber causing subsequent instrument malfunctions. The flowmeter shows potential; however, additional lab work is required to eliminate observed field problems. At this time the flowmeter is not recommended for multiphase flow evaluation in producing wells at the Buena Vista Field.

Halliburton Gas Holdup Tool (GHT): Chevron conducted the first field trial of the Halliburton Gas Holdup Tool (GHT) at the East Painter Field on well 13-18A in Wyoming. The GHT was tested in a gas well producing with three phase flow. Although flow rates for East Painter Field well 13-18A were higher than those at the Buena Vista Hills Field, the nature of the flow problem is analogous to producing conditions at Buena Vista Hills. Under controlled field trial conditions, the GHT did not function properly. The GHT identically replicated the response of a backup, center-sample nuclear densitometer. Although both tools utilize nuclear sources, they operate on entirely different nuclear principles. The GHT did not maintain calibration from the beginning to the end of the survey. Halliburton could not explain or reconcile these discrepancies. Since the prototype field test, Halliburton has reported to have improved the GHT sensor performance; however, at this time, the tool has not been characterized under dynamic flow conditions to be credibly integrated in a combinable production logging tool stack to help improve downhole flow rate measurement. Given the overall remaining effort to characterize and reevaluate the GHT, the sensor is not recommended for application at the Buena Vista Hills Field.

CARBON/OXYGEN LOGGING

A Carbon/Oxygen log was run in the 653Z well in May 1997 for the purpose of measuring oil saturation. Two logging passes of the Schlumberger Reservoir Saturation Tool (RST) were run at a speed of 170 ft/hr to ensure a repeatability of five saturation units (87% certainty level). We attempted to run the log to TD (4907 feet MD), but repeatedly encountered an obstruction at 4700 feet MD. Therefore the C/O data was acquired from 3700 to 4700 feet.

Schlumberger utilized alpha processing to compute oil saturation. For assisting in choosing a completion interval for the 653Z-26B well, Carbon/Oxygen log results were analyzed to high-grade our choice of interval to complete. RST and core oil saturations are plotted in wireline log track 6 of Figure 1.4-12. Plotted in wireline log tracks 2 and 3 of Figure 1.4-12 are, respectively, high core fluorescence and core fluorescence, based on image analysis of digital core photography. In wireline log track 2, high core fluorescence is indicative of sandstones/siltstones (with minor carbonates), and/or higher oil saturations. Whereas wireline log track 3, the core fluorescence track, indicates the presence of siliceous shales, sandstones and minor carbonates. Based in great part on relatively higher RST oil saturations (20 - 40%) in select intervals above and below P Point (top Antelope shale), we selected the interval P Point ± 100′ (4130 - 4350 feet) to complete. We believe in the six months that lapsed between casing/cementing the well and running the Carbon/Oxygen log, fluids from the undisturbed region in the formation have moved back in the vicinity of the wellbore. Thus, the Carbon/Oxygen log may more accurately reflect actual oil saturations than that measured in core (which is subject to flushing by mud filtrate).

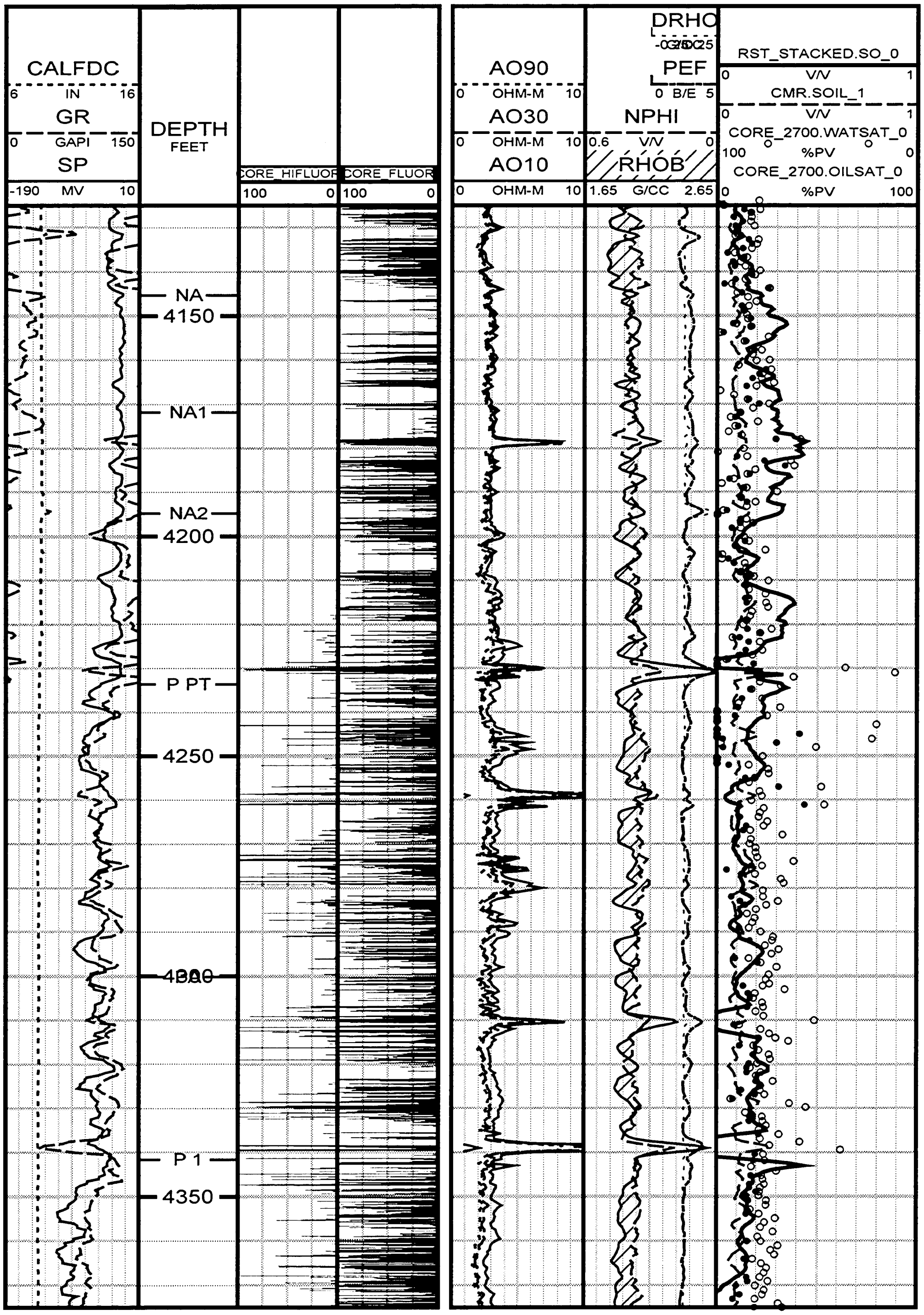

Figure 1.4-12. Carbon/Oxygen log shows higher oil saturations than core.

1.5. 3D EARTH MODELING

Dale Julander and Tom Zalan
Chevron USA Production Company
Dale Beeson, Julian Thorne and Ed deZabala
Chevron Petroleum Technology Company

This section describes the procedure used to estimate the four main reservoir properties modeled at Buena Vista Hills as part of this study: 1) Porosity, 2) Permeability, 3) Oil Saturation, and 4) Lithofacies (sandiness). During late 1997 and early 1998, a significant effort was directed at cleaning, modifying, and quality checking borehole data to prepare them for use in deriving the four reservoir properties. More than 95% of the wells in the Buena Vista Hills Field have limited open-hole log data [usually 1950's - 1960's vintage electric logs with spontaneous potential (SP) only]. Accordingly, most of our modeling efforts focused on establishing a relationship between these logs - - particularly SP - - and reservoir properties. After considerable effort, reasonable transforms for these properties were derived for wells having SP curve data.

These log-derived property data were then spatially simulated within stratigraphic grids (Sgrids) for the Brown Shale and Antelope units. FaciesFinder (an advanced, proprietary, facies-based, reservoir characterization UNIX application developed at Chevron) and GOCAD UNIX computer applications were used to simulate, or "characterize", these properties spatially for two different models: (1) a United Anticline "regional" Sgrid and (2) a smaller "quarter-pattern" Sgrid that contained just one producer and one injector (the 653Z Well). The regional grid provided a conceptually reasonable framework into which to place the quarter-pattern Sgrid for fluid flow simulation. The general workflow for the reservoir characterization process included generating the 1D property realizations at the wells, extending this to 2D via automated facies analysis, populating the 3D volume with property simulations, and visualizing the final product using GOCAD (Figure 1.5-1).

POROSITY

The method for deriving porosity curves for each of the wells at BV Hills involved normalizing the SP log as a shale-volume indicator (Vsh_SP) and subsequently transforming the Vsh_SP to porosity. The best-fit transform (Figure 1.5-2), with a correlation coefficient R = 0.649, is a third-order polynomial that relates porosity to Vsh_SP as follows:

$$\text{POROSITY} = -0.3602(\text{Vsh\_SP})^3 + 0.5412(\text{Vsh\_SP})^2 - 0.3136(\text{Vsh\_SP}) + 0.365$$

This relationship establishes upper and lower porosity bounds of 37% and 23%, respectively, which captures the majority of the measured values in the field.

This transform was applied to all of the Buena Vista Hills wells during the third quarter of 1997. Subsequently, quality control methods were used to detect anomalous data that required additional attention. Several wells were identified as having anomalously high porosities compared to surrounding wells. Further review indicated that most of these wells required reprocessing due to a variety of reasons (e.g., correction of SP data due to baseline drift and fine-tuning the parameters used to normalize the SP) while one well was eliminated because of unresolved issues related to an overly complicated drilling and logging history. New porosity curves were generated for the problematic wells.

PERMEABILITY

We were unsuccessful in our attempts to derive a direct correlation between core permeability and SP. However, a permeability transform was generated following a lengthy process that included an evaluation of old drill stem test (DST) data from the field. The data set consisted of more than 400 DSTs in the Brown Shale and Antelope, though Chuck Magnani of CPTC determined early on that the majority were of too short a duration to provide useful information about formation permeability. Through a process of elimination, Chuck Magnani determined that only eleven DSTs contained *some* formation permeability information. Seven of these were determined to have adequate duration to allow complete estimation of formation permeabilities; estimates for these tests (labeled "valid" tests for discussion purposes) ranged from 0.01 - 1.8 millidarcies (md). The remaining four DSTs were short enough duration to have been somewhat influenced by borehole storage and transition effects but long enough duration to also allow formation permeabilities to be estimated. Estimates for these four tests (labeled "transition & storage" tests for discussion purposes) ranged from 0.023 - 5.0 md.

After trying to establish a correlation between DST permeability and Vsh_SP in many ways (e.g., valid DSTs only, valid DSTs + transition & storage tests, first/second/third order polynomials, logarithmic, exponential), a best-fit match (Figure 1.5-3) was obtained for the exponential case for valid DSTs only (correlation coefficient R = 0.841):

PERMEABILITY = 4.0827 * e**(- 2.5084 * Vsh_SP)

where permeability is in millidarcies. The actual data used to derive this relationship covered a permeability range from 0.34 to 1.8 md and a Vsh_SP range from 0.274 to 0.839. However, the predicted endpoint values of K = 4.08 md for Vsh_SP = 0 (coarsest grained case) and K = 0.33 md for Vsh_SP = 1 (finest grained case) did not adequately capture the full range of permeabilities known to exist within the reservoir based on modern core data from well 653Z. A modification of the DST-based permeability transform was, therefore, made to more accurately capture low (shale) and high (sandstone) permeability endpoints. The transform, above, was used for Vsh_SP values that fell between 0.274 and 0.839 (the valid range of DST data) while linear functions were used to extend the ends of the transform to Vsh_SP values of 0 and 1, respectively. The permeability endpoints for the linear relationships were estimated from a liquid permeability vs. cumulative probability plot (based on core data from the 653Z Well) and represent the 1% (0.009 md) and 99% (31.009 md) cumulative probability permeability values. The final transform equations are as follows:

If (Vsh_SP < 0.274), then PERMEABILITY = 31.009 - 105.679 * Vsh_SP

If $(0.274 <= Vsh\_SP <= 0.839)$, then PERMEABILITY $= 4.0827 * e**(- 2.5084 * Vsh\_SP)$

If $(Vsh\_SP > 0.839)$, then PERMEABILITY $= 3.046 - 3.037 * Vsh\_SP$

Permeability curves have subsequently been calculated for each of the wells in the field and have been checked for quality based on consistency comparisons with surrounding wells. Curves that appeared unusually high or low throughout the vertical extent of the model were reviewed and reprocessed as needed.

As we continued in our efforts to characterize the Buena Vista Hills reservoirs, we came to the realization that the most significant lithologic units, in terms of saturation and producibility, were thin turbidite sandstones. Because of this, we found that even the three permeability equations, above, didn't adequately capture the extreme permeability end values necessary to model these thin, but very permeable, sandstones. To accomplish this, we applied a neural net transform process to the 653Z Well using FaciesFinder (Figure 1.5-4). This method used SP and deep and shallow resistivity logs to predict permeability at the 653Z Well with a correlation coefficient $R = 0.82$ (using 90% of the data to correct for error in due to sample blocking). These predictions provided us with a permeability range of 0.005 md to 187.8 md which almost exactly matched the core-measured range for the 653Z Well of 0.002 md to 187.8 md. Neural net training, optimized to the 653Z Well, was then applied to predict permeability in other wells on the United Anticline that had SP, deep and shallow resistivity logs. In this case, the resistivity logs were only used for relative shape "textural" information in the neural net training since their variable vintages make their direct value comparisons between wells suspect.

OIL SATURATION

Efforts to derive a best-fit, log-based, relationship between porosity and irreducible water saturation (Swi) based on capillary pressure measurements from the 653Z well core plugs were completed in early 1998 (Figure 1.5-5). These analyses suggested that separate relationships were necessary for sandstones versus siliceous shales. (Sandstones had low Swi values while siliceous shales had high Swi values relative to porosity.) Initial oil saturations (Soi) were then estimated from the Swi using the relationship: $Soi = 1 - Swi$. Ed deZabala of CPTC derived the following equations for Soi:

FOR SANDSTONES: $Soi = 0.55 + Phi$ (for $0.10 < Phi < 0.30$)
FOR SILCEOUS SHALE: $Soi = -0.229 + 1.3158*Phi$ (for $0.25 < Phi < 0.44$)

Upon further review, this laboratory-derived method for estimating Soi appeared to adequately represent the sandstone saturations but to over-estimate the saturations in the shaly lithology based on the core data from the 653Z Well. The siliceous shale equation was subsequently simplified, resulting in the following final Soi relationships:

FOR SANDSTONES: $Soi = 0.55 + Phi$ (for $0.0001 < Phi < 0.30$), else $= 0.85$
FOR SILICEOUS SHALE: $Soi = 0.14$

Successful implementation of these equations hinged on being able to estimate the percentage of each lithofacies type in every cell in the 3D geologic model so that the proper ratio of high and low Soi could be assigned. The following section describes the procedure used to determine lithofacies.

LITHOFACIES (SANDINESS)

Estimates of lithofacies (sandiness) were completed for each of the wells in the United Anticline using the following methodology. As a starting point, core lithology data were blocked over 2 foot intervals into percent "sandstone/siltstone" and "shale" for the 12 wells in the field that have Brown and Antelope shale core descriptions. With the exception of the 653Z Well, most of the cores used in this analysis date from the 1950's and 1960's and have subsequently been destroyed. Consequently, the only available lithologic information for these cores comes from the written descriptions stored in our well files. The 2-foot core blocking was designed to represent the lithologic data at about the same level of resolution available in most of the field log data. Table 1.5-1 shows a list of these 12 core wells.

Lithologic variation across the field was modeled using the neural net analysis capabilities in FaciesFinder and relating the 2 foot blocked core data to log curves. Only those wells shown in red in Table 1.5-1 were ultimately used in the neural net analysis. (The remaining wells were not used because they either: 1) lacked detail in their respective core descriptions which resulted in over-generalized lithologic descriptions or 2) the cores were too short to be of much use.) These wells contained a large enough number of samples to be representative of the two lithology types and did not excessively over-generalize the lithologic variability.

In the neural net analysis, fifty percent of the core data from the 5 useable wells comprise the 'training" set, and the Vsh_SP log curves were used to predict the fraction of sand, or sandiness. (Note: Though other open-hole logs were available to us, e.g., deep and shallow resistivity, we decided to use only the normalized raw SP curve to avoid differences associated with multiple vintages of other log types). In order to deal with occasional occurrences of over-generalized core descriptions that led to thicker than 2 foot blocking, we: 1) allowed exclusion of a percentage of the extreme data in the crossplot between predicted and observed sandiness under the assumption that many of these points were the result of the exaggerated blocking, and 2) allowed a minimal depth shift between predicted and observed sandiness to account for depth generalization due to blocking.

After many iterations, a best fit sandiness prediction between core data and Vsh_SP was achieved based on the following parameters and specifications: 1) 90% of the data were used for the correlation; 2) textural analysis was applied to the SP using a 4 foot sliding "window"; and 3) a +/- 2 foot shift in observation location was allowed due to blocking generalization.

These basic parameters applied to the five training wells produced a gross average sandiness value of 7.6% for the Brown and Antelope shales in the United Anticline. With 10% of the data eliminated as outliers due to the blocking method applied, the correlation coefficient for the best-fit prediction was R = 0.92. (Figure 1.5-6). This method was recently used to derive sandiness estimates for all wells in the United Anticline.

Table 1.5-1. Buena Vista Hills Field cored wells.

Well Name	# of 2ft samples	Sample interval	Location*
(523-9D)	191	3632' -5248'	HA
(653Z-26B)**	451	3953' - 4903'**	UA
(USL522A-2-26B)**	125	4036' - 5284' **	UA
(552-27B)	163	4005' - 7000'	UA
563-27B	29	5482' - 5538'	UA
425-36B***	62	4096' - 4498'	HA
532-1C	20	4360' - 4398'	HA
524-6D	6	4739' - 4749'	HA
552-8D	754	3700' - 5542'	HA
502-9D	27	3712' - 4170'	HA
533-9D	30	4680' - 5629'	HA
(555-9D)	430	3917' - 4778'	HA

* UA=United Anticline; HA=Honolulu Anticline
**W. Narr fracture analysis
***Later removed from database due to bad SP log

FACIES ANALYSIS

The purpose for doing facies analysis was to provide a means for conditionally simulating property distribution in the earth model. Semi-automated facies analysis was accomplished using FaciesFinder, which relates reservoir property data to "facies" based on well log pattern recognition. Strengths in using this method included: 1) incorporation of deterministic geological concepts into a probabilistic framework, 2) ability to constrain facies boundary and related rock property uncertainty via multiple 2D realizations, and 3) ability to use cross-validation techniques to increase confidence in results.

Initially, marker-controlled structural surfaces were generated to provide a stratigraphic framework. Sixteen structure surfaces (TMC down to, and including, P2) gridded in Z-Map+ were quality controlled in GOCAD for conformity. These structure surfaces were interpolated between well marker control. The structure surfaces provided both the facies analysis framework as well as the boundary constraints for the stratigraphic grids generated in the 3D-property simulation process. Eight stratigraphic intervals were defined within this framework as relatively distinct and appropriate for facies analysis and property simulation. Marker-defined intervals analyzed in the Brown Shale section included: TMC-N1, N1-NA, NA-NA2, and NA2-PPT. Marker-defined intervals analyzed in the Antelope section included: PPT-P1alpha, P1alpha-P1B, P1B-P1C, and P1C-P2. Table 1.5-2 provides information on interval thicknesses for the area of the United Anticline and also indicates which wells were excluded from facies analysis. Wells were excluded from facies analysis because, 1) they had too little log data for a given interval for effective pattern recognition, and/or 2) uncorrectable errors existed in the data for a given interval.

Table 1.5-2. Buena Vista Hills United Anticline marker intervals used in 2D facies analysis and 3D reservoir property simulation.

United Anticline Regional Sgrid: 50 x 100 x 267 Cells*

Brown Shale Section Markers	Average Thickness	Maximum Thickness	# of Layers
TMC-N1	142.9'	230'	36
N1-NA	165.6'	373'	42
NA-NA2	79.8'	313'	20
NA2-PPT	58.9'	133'	15
Antelope Section			
PPT-P1alpha	160.2'	291'	40
P1alpha-P1B	167.2'	270'	42
P1B-P1C	164.9'	215'	42
P1C-P2	116.6'	144'	30

* Wells excluded from facies analysis included: QG81580 & QG85470 for TMC-N1; QG85500 for PPT-P1alpha & P1alpha-P1B; QG84440, QG81610 & QG82120 for P1B-P1C; IR85850 for P1C-P2

Normalized, unclipped, SP logs (VSH_RAWSP) were used in the facies analysis process. Reservoir properties were related to log-pattern-derived facies. Distinct facies vs. property relationship provided a means of determining the value of a given algorithm-based facies interpretation strategy. Reservoir properties used included: permeability (using the methodology described above), porosity, Vsh_ SP, Sandiness, air permeability in log scale (derived from neural net analysis of SP, deep & shallow resistivity), and air permeability in linear scale (a transform of air perm in log scale). These property data were averaged across a given interval and then related to facies assemblages based on log shapes (Figure 1.5-7). Once an optimal facies interpretation strategy was found, multiple facies map realizations were generated for a given interval. These multiple non-unique realizations provided a means for quantifying the uncertainty associated with the spatial distribution of the associated property data.

The most successful log pattern interpretation strategies for the Brown Shale and Antelope Shale in the United Anticline included: (1) a method that "looks" for sedimentary cyclic symmetry or asymmetry from the analyzed interval scale down to one foot thickness (e.g., upward fining or coarsening sequences), and (2) a method that characterizes the vertical clustering of log highs and lows to distinguish between high vs. low energy depositional environments (e.g., as for turbidites). Facies assemblages based on these interpretation strategies proved effective for providing reasonable spatial control of reservoir properties during the 3D conditional simulation process.

RESERVOIR PROPERTY DISTRIBUTIONS

FaciesFinder was used for conditionally simulating reservoir property distributions during construction of the 2 Sgrids used in this study. The following summary describes details associated with each of the Sgrids:

(1) The United Anticline "regional" Sgrid was simulated in order to provide a necessary regional connectivity to the property distribution patterns. The entire TMC – P2 interval was represented in this model. Surface corner points were defined as follows:

lower left : X = 1563000.25, Y = 617000.125
lower right: X = 1566000.0, Y = 621000.0
upper right: X = 1557999.75, Y = 626999.875
upper left: X = 1555000.0, Y = 623000.0 (Table 1.5-2)

This provided a grid area extending from NW to SE along the axis of the anticline with 50 "X" and 100 "Y" cells 100 feet on a side. The TMC – P2 interval was subdivided by two hundred and sixty seven layers averaging 4 feet thick each. Interval-based facies interpretations along with local log correlation were then integrated within FaciesFinder to populate the Sgrid with property distributions (Figure 1.5-8).

(2) The "quarter-pattern" Sgrid was essentially a smaller volume cut out of the larger United Anticline model. It contained just one producer (553) and one injector (653Z) and was specifically designed for fluid flow production simulations between the two wells.

For this localized grid, surface corner points were defined as follows:

lower left: X = 1561165.0, Y = 622640.0
lower right: X = 1561605.0, Y = 622640.0
upper right: X = 1561605.0, Y = 623080.0
upper left: X = 1561165.0, Y = 623080.0 (Table 1.5-3)

This grid was divided into 11 "X" and 11 "Y" cells 40 feet on a side. Only the PPT – P2 interval was simulated (because it was agreed that this was the most likely interval to be considered for CO2 flooding). This interval was subdivided by one thousand one hundred and fifty two layers averaging 0.5 feet thick each to provide additional resolution in the fluid flow production test (Figure 1.5-9). A Chevron scale-up application was subsequently used to reduce the number of layers from 1152 to 300 in order to make the fluid flow production simulation less computer-time intensive (Figure 1.5-10). A comparison flow simulation test of both the scaled-up and scaled-down earth models indicated that the scale-up process was robust in retaining the important flow-related property distribution characteristics.

Table 1.5-3. Buena Vista Hills quarter-pattern marker intervals used in 3D reservoir property simulation to generate earth model used in fluid flow production simulation.

Antelope Section Markers	Boreholes 653Z to 553 Quarter-Pattern Local Sgrid: 11 x 11 x 1152 Cells*		
	Average Thickness	Maximum Thickness	# of Layers
PPT-P1alpha	147.1'	175'	294
P1alpha-P1B	156.8'	178'	314
P1B-P1C	158.2'	163'	316
P1C-P2	113.9'	125'	228

Finally, GOCAD was used to visualize and mathematically manipulate the FaciesFinder-distributed property data across the Buena Vista Hills Field. An overview of this process is illustrated graphically in Figure 1.5-1.

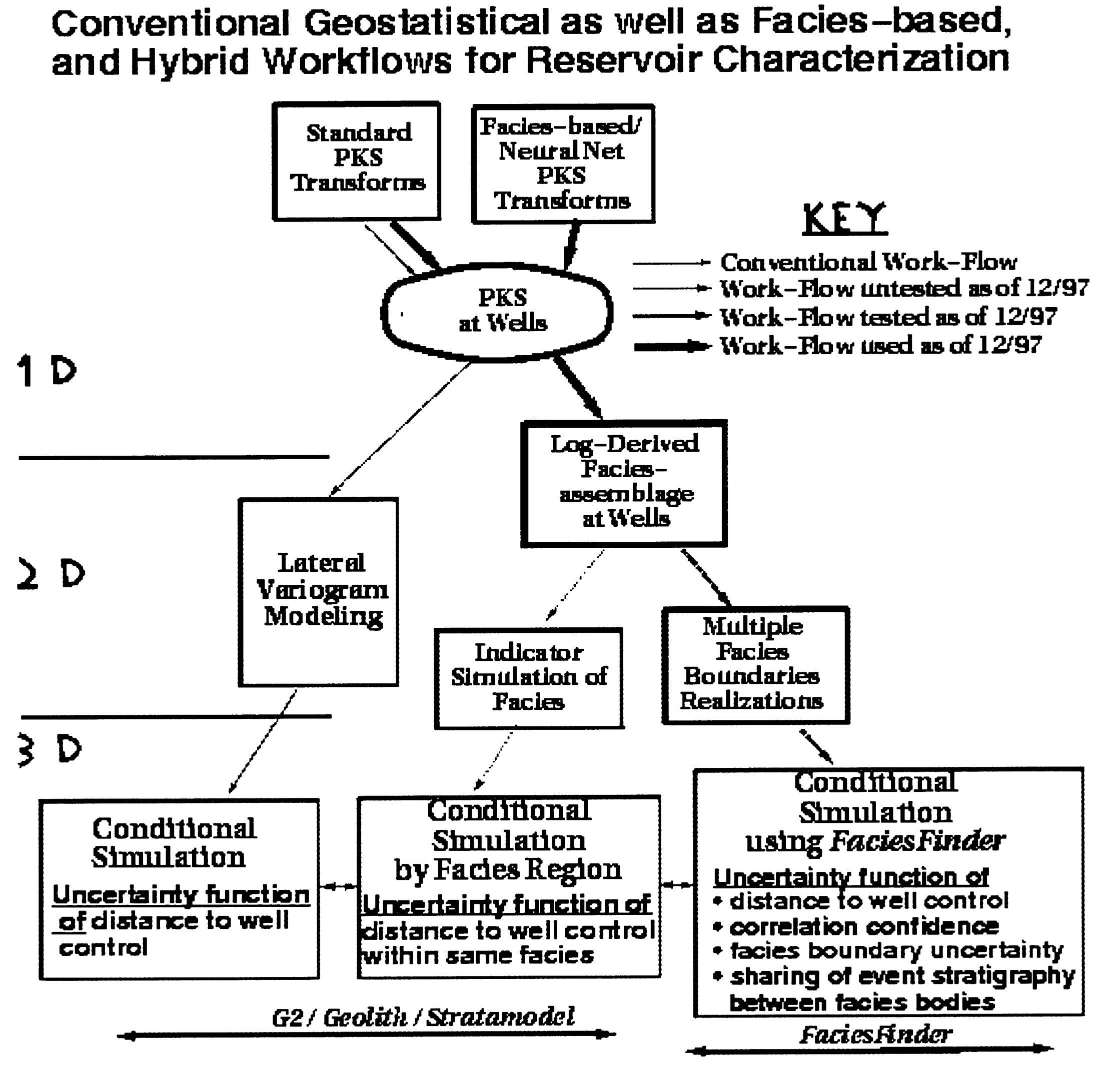
Conventional Geostatistical as well as Facies-based, and Hybrid Workflows for Reservoir Characterization
Standard PKS Transforms
Facies-based/ Neural Net PKS Transforms
KEY
Conventional Work-Flow
Work-Flow untested as of 12/97
Work-Flow tested as of 12/97
Work-Flow used as of 12/97
PKS at Wells
1 D
2 D
3 D
Log-Derived Facies-assemblage at Wells
Lateral Variogram Modeling
Indicator Simulation of Facies
Multiple Facies Boundaries Realizations
Conditional Simulation
Uncertainty function of distance to well control
Conditional Simulation by Facies Region
Uncertainty function of distance to well control within same facies
Conditional Simulation using FaciesFinder
Uncertainty function of
• distance to well control
• correlation confidence
• facies boundary uncertainty
• sharing of event stratigraphy between facies bodies
G2 / Geolith / Stratamodel
FaciesFinder

Figure 1.5-1. Reservoir characterization workflows. Method applied at Buena Vista Hills shown by dark arrows. Future steps will include multiple facies boundaries realizations and conditional simulation using FaciesFinder.

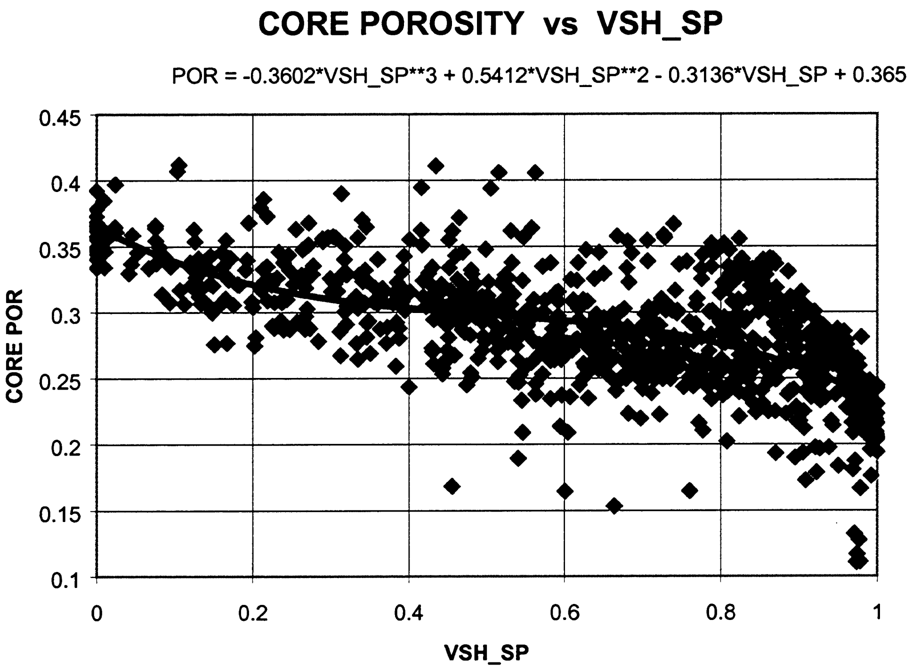

Figure 1.5-2. Cross plot of core porosity versus Vsh_SP (correlation coefficient = 0.649).

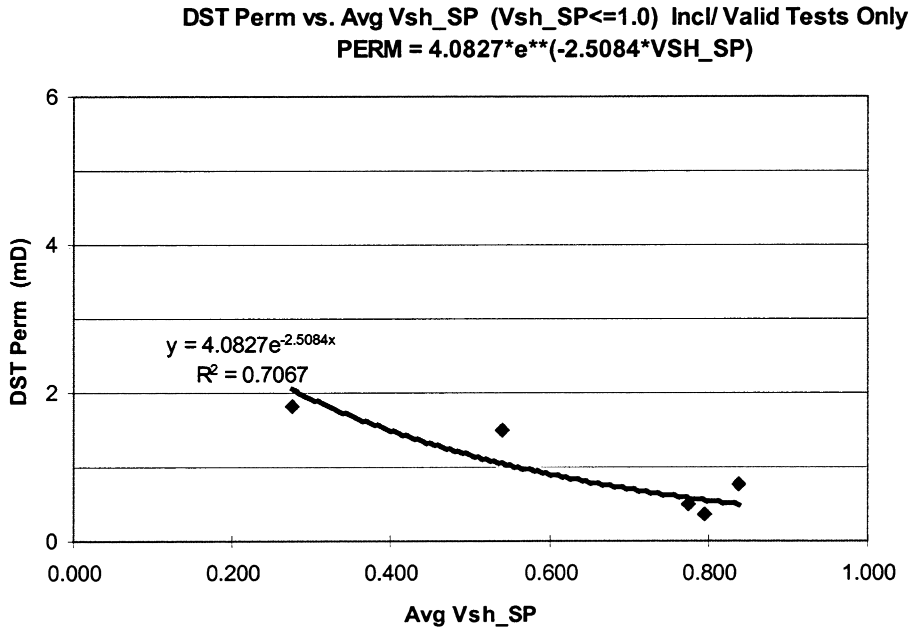

Figure 1.5-3. Cross plot of drill stem test permeability versus average Vsh_SP (within the tested interval) (correlation coefficient = 0.841).

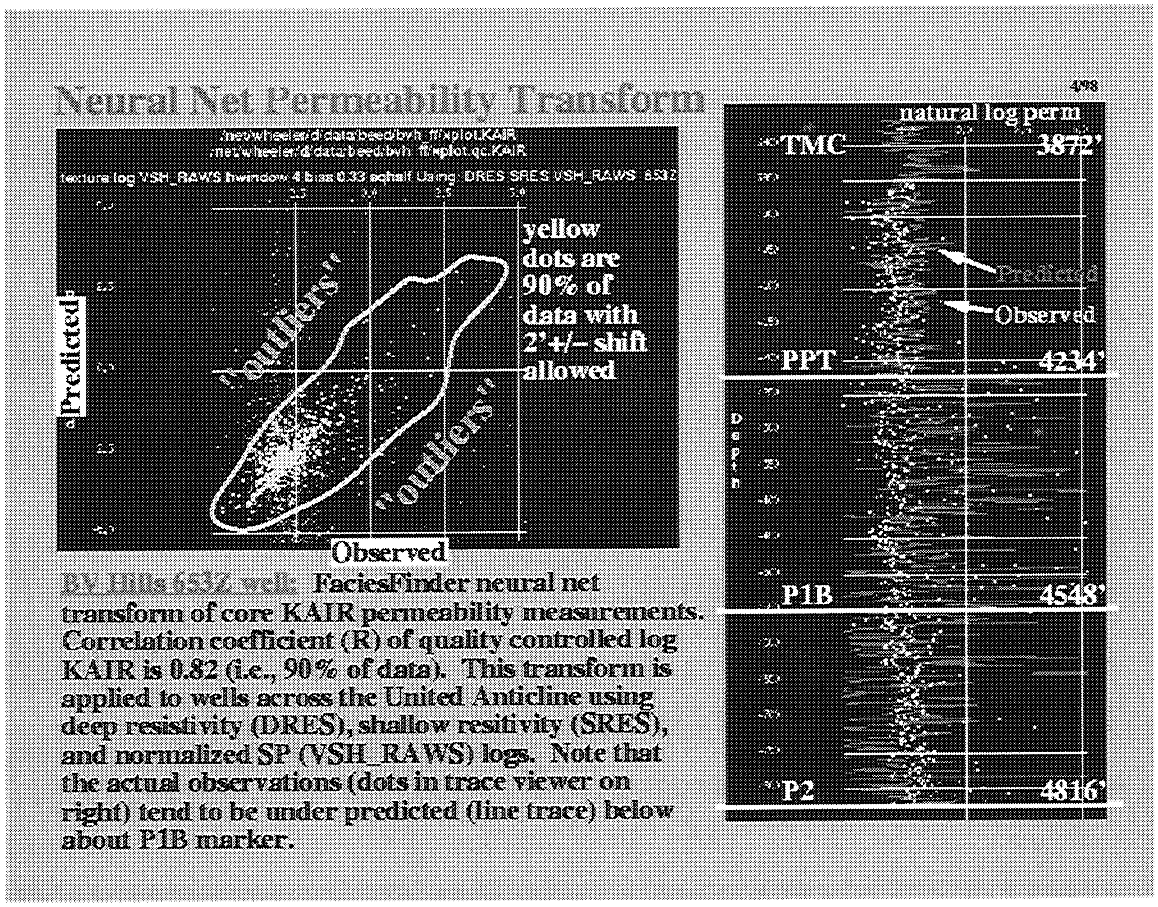

Neural Net Permeability Transform

4/98

:net/wheeler/d/data/beed/bvh_ff/xplot.KAIR
:net/wheeler/d/data/beed/bvh_ff/xplot.qc.KAIR
texture log VSH_RAWS hwindow 4 bias 0.33 sqhalf Using: DRES SRES VSH_RAWS 653Z

yellow dots are 90% of data with 2'+/- shift allowed

BV Hills 653Z well: FaciesFinder neural net transform of core KAIR permeability measurements. Correlation coefficient (R) of quality controlled log KAIR is 0.82 (i.e., 90% of data). This transform is applied to wells across the United Anticline using deep resistivity (DRES), shallow resitivity (SRES), and normalized SP (VSH_RAWS) logs. Note that the actual observations (dots in trace viewer on right) tend to be under predicted (line trace) below about P1B marker.

Figure 1.5-4. Neural net permeability transform using FaciesFinder. A transform of KAIR permeability referenced to the 653Z Well was derived from logs in common for wells across the United Anticline. In this way, representative high and low permeabilities were predicted for other wells within the Brown Shale / Antelope Shale section.

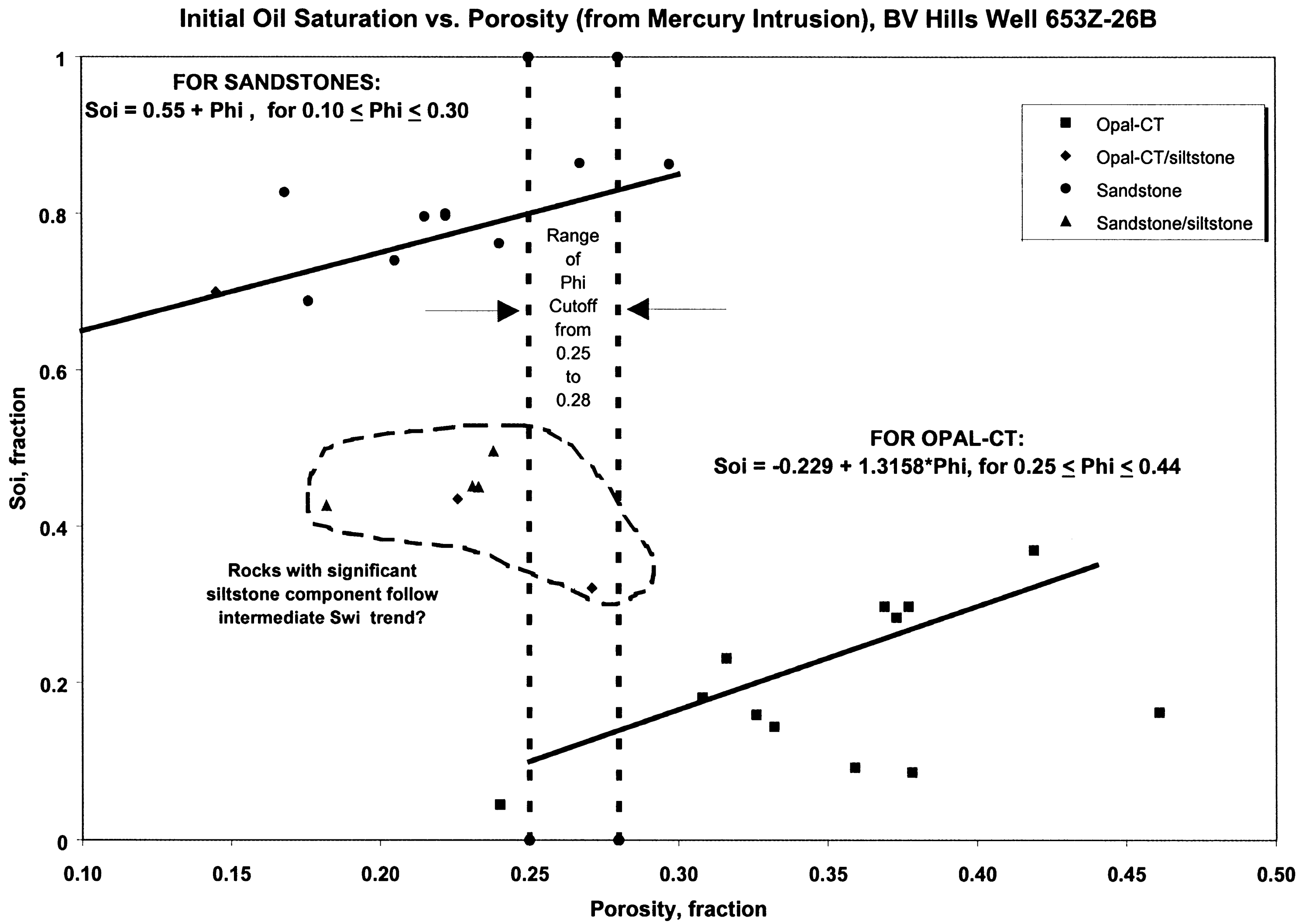

Figure 1.5-5. Cross plot of initial oil saturation (as measured by mercury intrusion) versus porosity, calculated using the correlation in Figure 1.5-1.

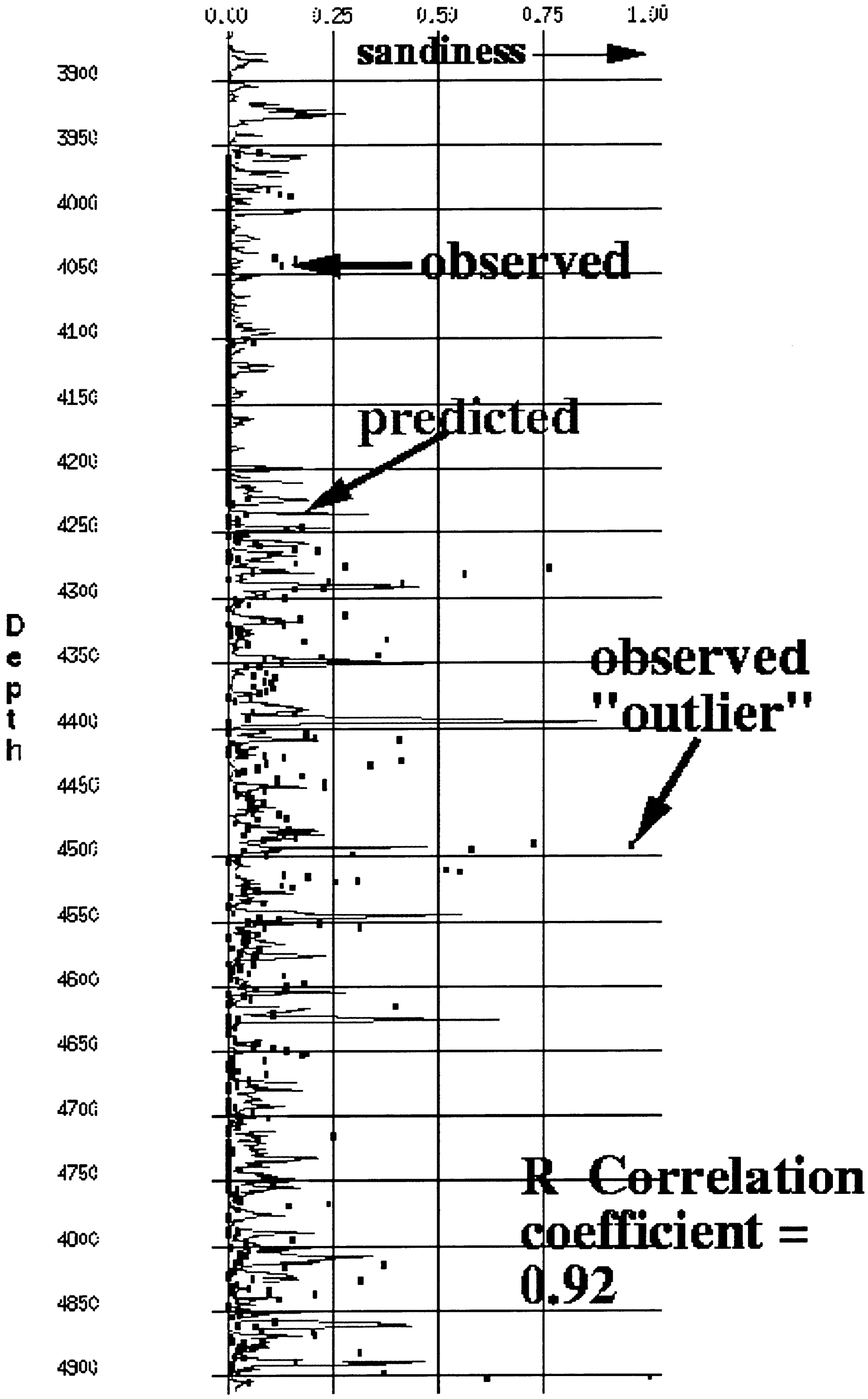

Figure 1.5-6. 1D neural net analysis using FaciesFinder. Best-fit prediction of sandiness based on matching core descriptions to openhole log data.

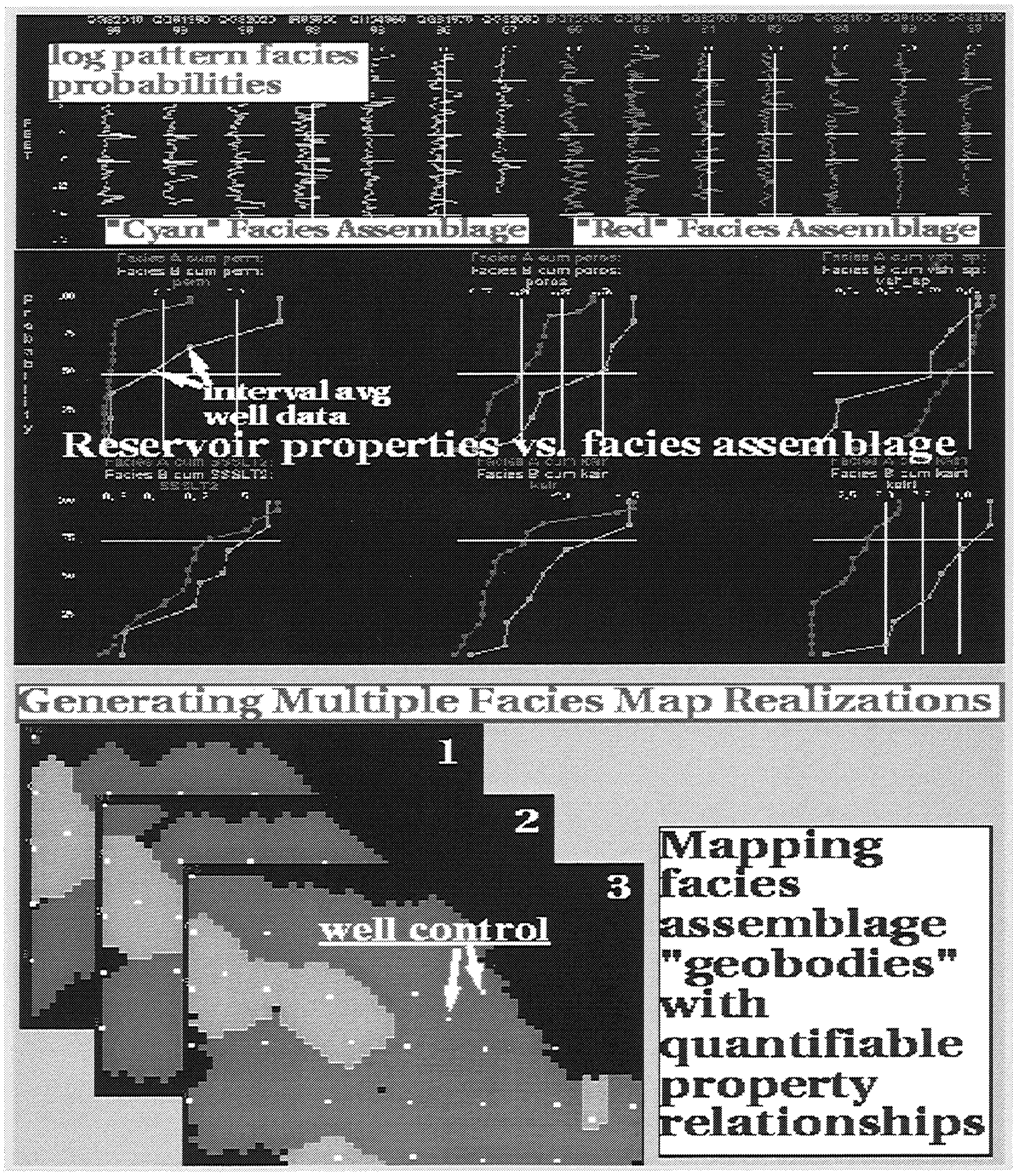
log pattern facies probabilities
"Cyan" Facies Assemblage
"Red" Facies Assemblage
interval avg well data
Reservoir properties vs. facies assemblage
Generating Multiple Facies Map Realizations
1
2
3
well control
Mapping facies assemblage "geobodies" with quantifiable property relationships

Figure 1.5-7. 2D facies analysis using FaciesFinder. Shape and trend patterns are recognized in log data and related to interval-average reservoir properties in each well. Multiple map realizations are generated for distinct facies to quantify the uncertainty associated with the spatial distribution of the associated property data.

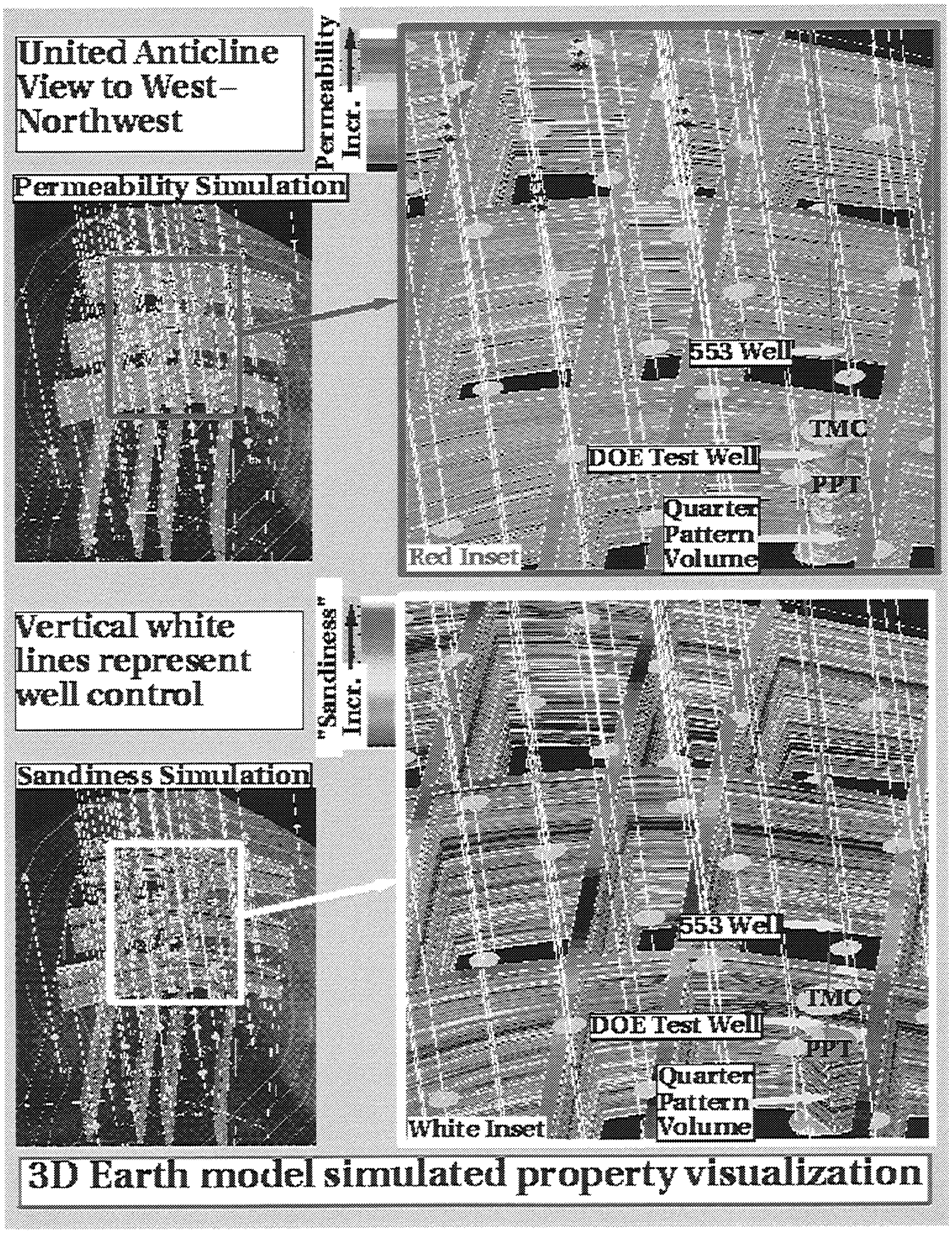
United Anticline View to West-Northwest
Permeability Incr.
Permeability Simulation
553 Well
TMC
DOE Test Well
PPT
Quarter Pattern Volume
Red Inset
Vertical white lines represent well control
"Sandiness" Incr.
Sandiness Simulation
553 Well
TMC
DOE Test Well
PPT
Quarter Pattern Volume
White Inset
3D Earth model simulated property visualization

Figure 1.5-8. Reservoir property simulation for the United Anticline. The alternating "layered" look to the permeability and sandiness trends conforms to the geological concept of a turbidite depositional setting. In addition, a trend to more abundant coarser clastics to the SW side of the anticline agrees with other evidence for a sediment source to the SW.

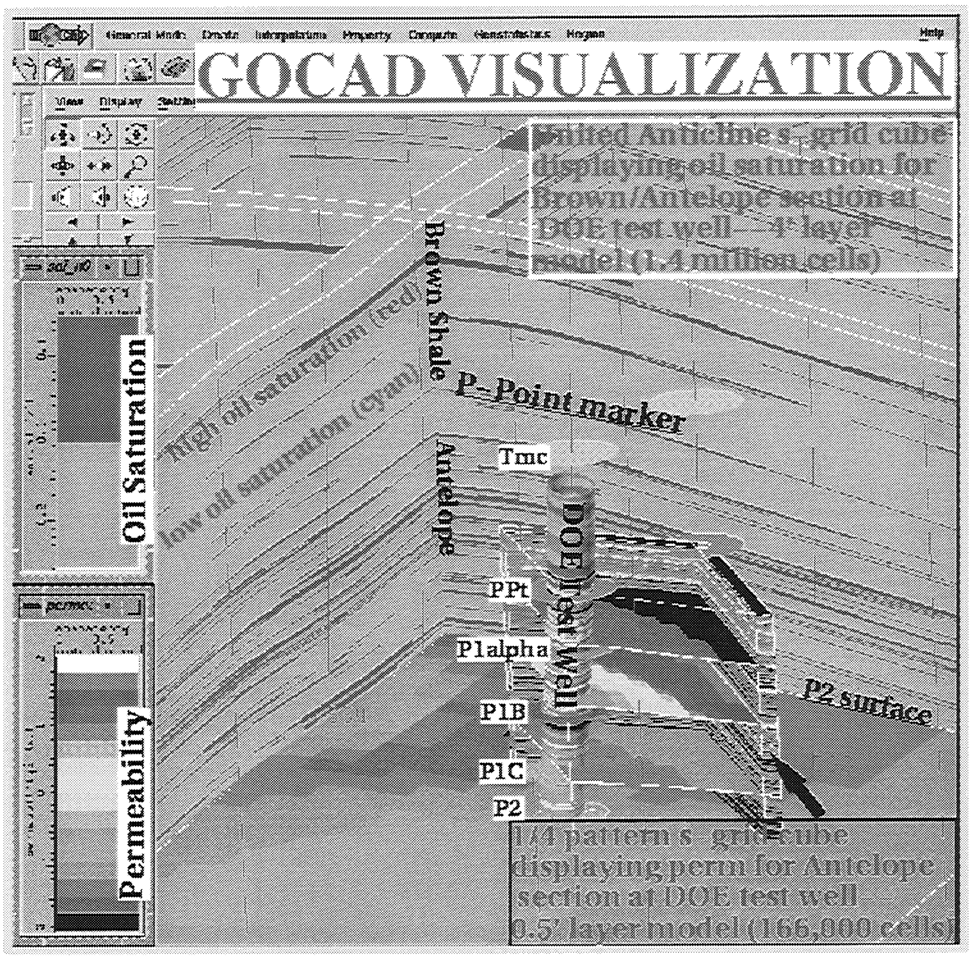
GOCAD VISUALIZATION
United Anticline s-grid cube displaying oil saturation for Brown/Antelope section at DOE test well—4' layer model (1.4 million cells)
Brown Shale
P-Point marker
High oil saturation (red)
low oil saturation (cyan)
Oil Saturation
Permeability
Antelope
Tmc
DOE Test Well
PPt
P1alpha
P1B
P1C
P2
P2 surface
1/4 pattern s-grid cube displaying perm for Antelope section at DOE test well 0.5' layer model (166,000 cells)

Figure 1.5-9. Reservoir property simulation and visualization for the United Anticline "geologic" model and the ¼ pattern "production simulation" model. Note the distribution of oil saturation (red) which highlights the relatively thin and laterally continuous flow zones, especially in the Antelope section.

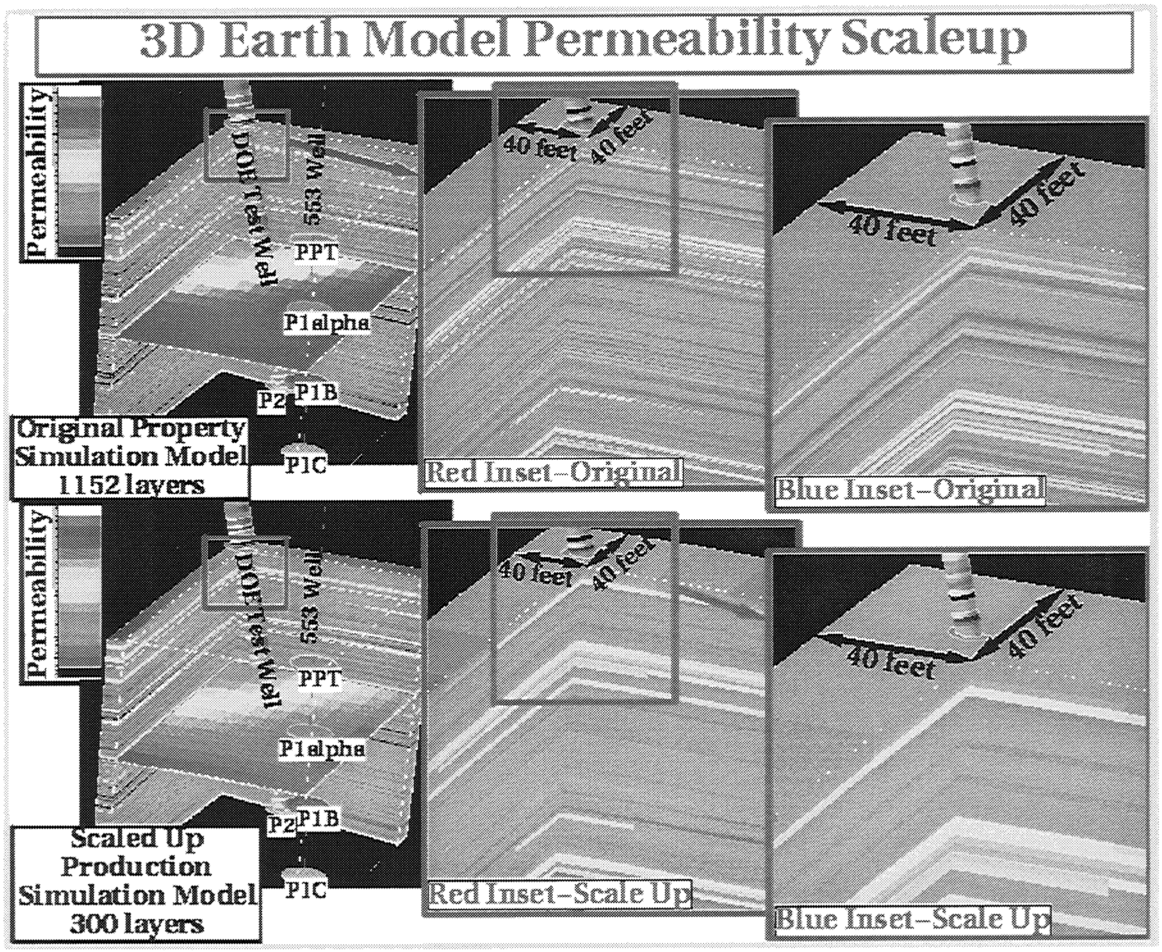
3D Earth Model Permeability Scaleup
Permeability
DOE Test Well
553 Well
PPT
P1alpha
P2
P1B
P1C
Original Property Simulation Model 1152 layers
40 feet
40 feet
Red Inset-Original
Blue Inset-Original
Permeability
DOE Test Well
553 Well
PPT
P1alpha
P2
P1B
P1C
Scaled Up Production Simulation Model 300 layers
40 feet
40 feet
Red Inset-Scale Up
Blue Inset-Scale Up

Figure 1.5-10. Scale-up of the production simulation earth model. This illustration shows how permeability distributions in 0.5-foot layers in the original model were scaled up by a factor of 4 while still retaining model integrity.

1.6. FLUID CHARACTERIZATION AND LABORATORY DISPLACEMENTS

Dengen Zhou and Ray Tang
Chevron Petroleum Technology Company

Laboratory experiments reported in the literature suggest that crossflow driven by diffusion, capillary and gravity forces can recover oil efficiently from heterogeneous reservoirs in a gas injection process. The published experiments were generally conducted on high permeability systems (> 100mD). Cores from Buena Vista Hills Field show mixed lithology, with high permeability sandstone layers and low permeability siliceous shales (< 1mD). Can we use the crossflow mechanisms to recovery oil from the siliceous shale if CO_2 is injected into the reservoir? This project was designed to investigate oil recovery potentials from CO_2 crossflow in the Buena Vista Hills reservoir. If results are promising, then the data can be used to design a CO_2 injection project for the Buena Vista Hills.

The Buena Vista Hills reservoir mainly consists of siliceous shale with very low permeability (< 1 mD). However, thin high permeability sandstone layers exist throughout the reservoir. If these sandstone layers are connected, they can serve as a distribution network when CO_2 is injected into the reservoir. In this case, the injected CO_2 initially spreads through the sandstone network, then contacts oil in the shale by diffusion and/or by crossflow driven by capillary and gravity forces. To investigate the potential of these mechanisms, we designed and completed two sets of experiments: (1) waterflood and tertiary CO_2 displacement on a composite sandstone core (composite core); and (2) CO_2 displacement on a mixed lithology core. The first set of experiments evaluated CO_2 recovery efficiency in the sandstone layers, and the second set quantified oil recovery by crossflow mechanisms.

DISPLACEMENT ON THE COMPOSITE CORE

The Buena Vista Hills reservoir temperature is about 160 F, significantly higher than that of West Texas reservoirs. The MMP (minimum miscibility pressure) for CO_2 injection into the Buena Vista Hills oil reservoir is estimated at about 4000 psi, which is significantly high than the initial reservoir pressure (2500 psi). If CO_2 is injected into this reservoir, CO_2 displacement of oil is an immiscible process. How efficient is this process in comparison of miscible displacements? The Buena Vista Hills reservoir has been waterflood with very poor recovery. Because of the relative high permeability, it is very likely that the sandstone layers have been waterflooded. When CO_2 is injected, CO_2 injection in the sandstone layers is a tertiary process. To simulate the reservoir situation, we first waterflooded the sandstone core, then performed CO_2 injection.

10 plugs were put together to form a 51.6 cm long composite core with a pore volume of 95.45 cc. The diameters of the plugs were 1.5 inches. The sandstone plus were cut from whole cores from Chevron 653Z-26B (from -4491.15 ft to -4413.10 ft). The composite core was initially cleaned by alternatively pumping toluene and methanol, then fully saturated with reservoir brine. Initial water saturation (0.457 pv) was obtained by pumping stock tank oil at relatively high rates (4 to 12 cc/hr). Finally, the core was saturated with the recombined oil by injecting recombined oil to displace the stock tank oil. The waterflood experiment was conducted at 4cc/hr. The final recovery from waterflood was about 51% OOIP (residual oil saturation of 26% pv). The

waterflood experiment stopped after about 2.4 HCPV water injection. CO_2 injection was then started at an injection rate of 1 cc/hr. Abut 2 HCPV CO_2 was injected before the end of the experiment. During both the waterflood and the CO_2 injection experiments, the down stream BPR (Back Pressure Regulator) was set to 2600 psig, and the core was situated in an oven at a constant temperature of 160 F.

Figure 1.6-1 shows the measured production from the waterflood and tertiary CO_2 displacements. Waterflood recovered about 50% of original oil in place, and additional 30% of OOIP was recovered by CO_2. The recovery behavior of the CO_2 displacement is consistent with that of typical immiscible displacement processes. There was substantial recovery after breakthrough. We also conducted 1-d simulations of the experiments. Compositional simulations indicate that the residual oil to CO_2 is about 17% OOIP. The residual oil consists of the heavy components of the oil.

The simulations were conducted by tuning the water/oil relative permeability curves to match the waterflood production and pressure drops. Figure 1.6-2 shows the comparison of the measured and simulated pressure drops. The waterflood pressure drops had the characteristics of waterflood in strongly water-wet media, suggesting the sandstone core was strongly water-wet. The pressure increases just before water breakthrough suggest a strong capillary end effect. In the simulations we did not consider capillary effects. Therefore, the simulated pressure drops are higher than the measurements before water breakthrough. The relative permeability curves used in the simulations are given in Figure 1.6-3 and Figure 1.6-4. The shapes the oil/water relative permeability curves are consistent with that of strongly water-wet media. The relative permeability curves for gas and oil are close to straight lines. Notice that the relative permeability curves may change if capillary pressure is included.

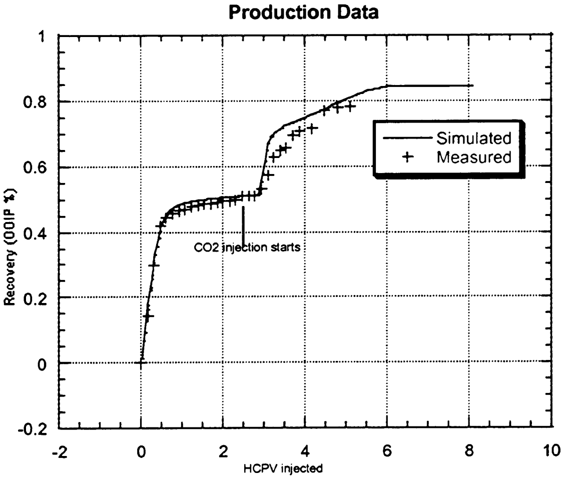

Figure 1.6-1. Oil productions from waterflood and tertiary CO_2 injection.

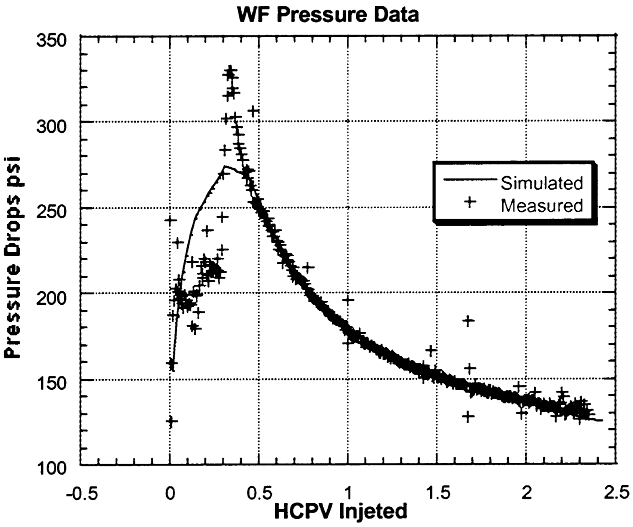

Figure 1.6-2. Pressure drops from the waterflood experiment.

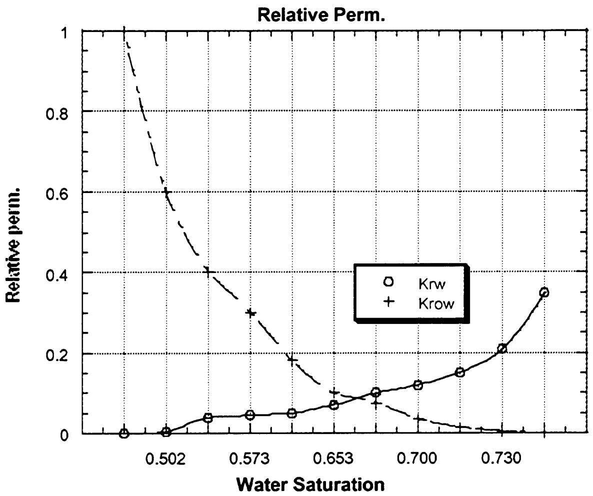

Figure 1.6-3. Oil/water relative permeability curves used in simulating the waterflood experiment.

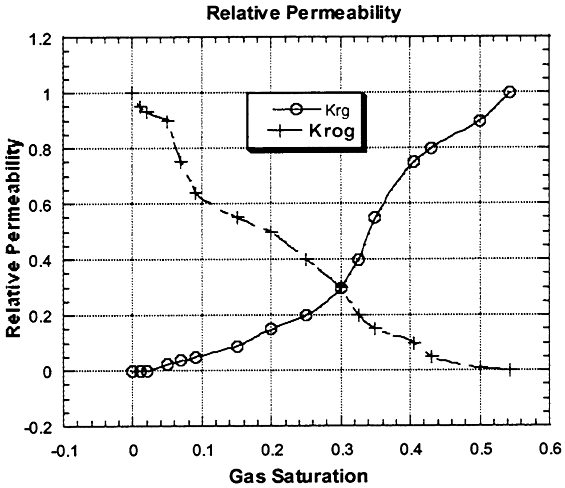

Figure 1.6-4. Gas/Oil relative permeability curves used in the simulating the CO_2 flood.

The experimental and simulation results indicate that although CO_2 injection at 2600 psig is a immiscible displacement process, the recovery efficiency is still very attractive, due to the strong extraction effect of CO_2.

DISPLACEMENT ON THE MIXED LITHOLOGY CORE

The second set of the experiments were designed to evaluate the potential of crossflow between the high permeability sandstone layers and the siliceous shale in which most of the filed OOIP resides. We prepared the "mixed lithology" core, which consists of two parts: a sandstone slab and an whole-core siliceous shale slab from the Buena Vista Hills Well 653Z. Because the sandstone layers in the reservoir are very thin, it was hard to get a whole core that was large enough to construct the mixed lithology core. We used a Berea sandstone slab to construct the mixed lithology core. Using a Berea sandstone should not affect the experimental results, because crossflow depends mainly on the existence of permeability contrast.

Special care was taken to ensure good communication between the sandstone and the shale slabs. A Viton gasket was used to reduce the flow of gas in the gap between the two slabs and to keep sufficient area for crossflow between the two zones (Figure 1.6-5). The contact surface of the sandstone and the shale is placed vertically to encourage gravity driven co-current crossflow (Figure 1.6-6).

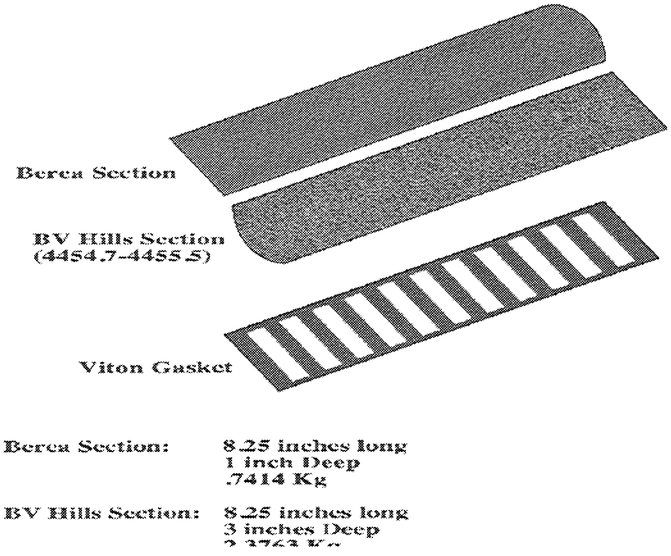
Berea Section
BV Hills Section
(4454.7-4455.5)
Viton Gasket
Berea Section:
8.25 inches long
1 inch Deep
.7414 Kg
BV Hills Section:
8.25 inches long
3 inches Deep

Figure 1.6-5. A schematic of the mixed lithology core elements: slabs of sandstone and Buena Vista Hills Shale and a Viton gasket. The gasket is designed to reduce gas flow in the gas between the two slabs in the same time allowing crossflow occur.

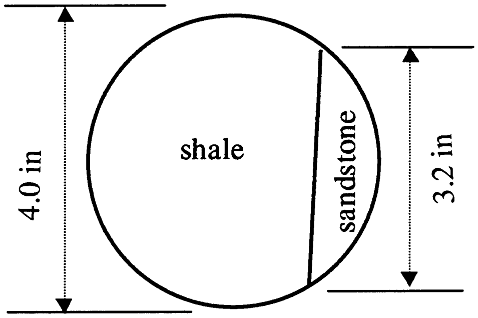
4.0 in
shale
sandstone
3.2 in

Figure 1.6-6. Cross sectional view of the mixed lithology core.

The relative sizes of the sandstone and siliceous shale are illustrated in Figure 1.6-6. The rock volumes of the sandstone and the siliceous shale are 241.6 cc and 1456.4 cc, respectively. The porosity and the air permeability of the sandstone are 12% and 55 mD. Because of the low permeability of the siliceous shale, we did not clean the shale slab and kept it in the native status. The sandstone slab was vacuumed for more than two days. After the core was placed in the core holder, the core was then saturated with stock tank oil by slowly injecting stock tank oil at pressures up to 600 psi. A total of 71.85 cc of oil was injected into the system over a period of two weeks. No water is involved in the experiments to reduce the complexity of the experiments.

Figure 1.6-7 is a schematic of the displacement equipment unit. The core is situated in an oven at reservoir temperature (160 F). The core was initially saturated with Buena Vista Hills stock tank oil. CO_2 is then injected at a constant rate of 1.0 cc/hr, which corresponds to a rate of 1 ft/d if the injected CO_2 flows through the sandstone portion of the core only. In the first phase of the experiment, we kept the core pressure at about 600 psi by using a back pressure regulator connected to the outlet of the core. The BPR pressure was raised to 2500 psi in the second phase of the experiments. The produced gas and oil were flashed to room conditions (68 F), and the production of gas and oil were recorded automatically. The system can also automatically monitor the inlet and outlet pressures, from which pressure drop can be calculated. The produced gas is collected into an evacuated gas tank. Cumulative gas production is monitored by pressure change in a 100 liter gas cylinder that was initially evacuated.

The Buena Vista Hills reservoir pressure is currently about 600 psi, and the initial reservoir pressure was about 2500 psi. The efficiency of CO_2 extraction increases with the increase in pressure. However, re-energizing the reservoir would require injecting a large volume of water, and most importantly, it delay CO_2 injection by months or years. Thus, we designed this set of experiments to evaluate the oil recovery potentials at both 600 psi and 2500 psi. First we injected CO_2 at 600 psi; after oil production ceased at 600psi, we injected CO_2 at 2500 psi.

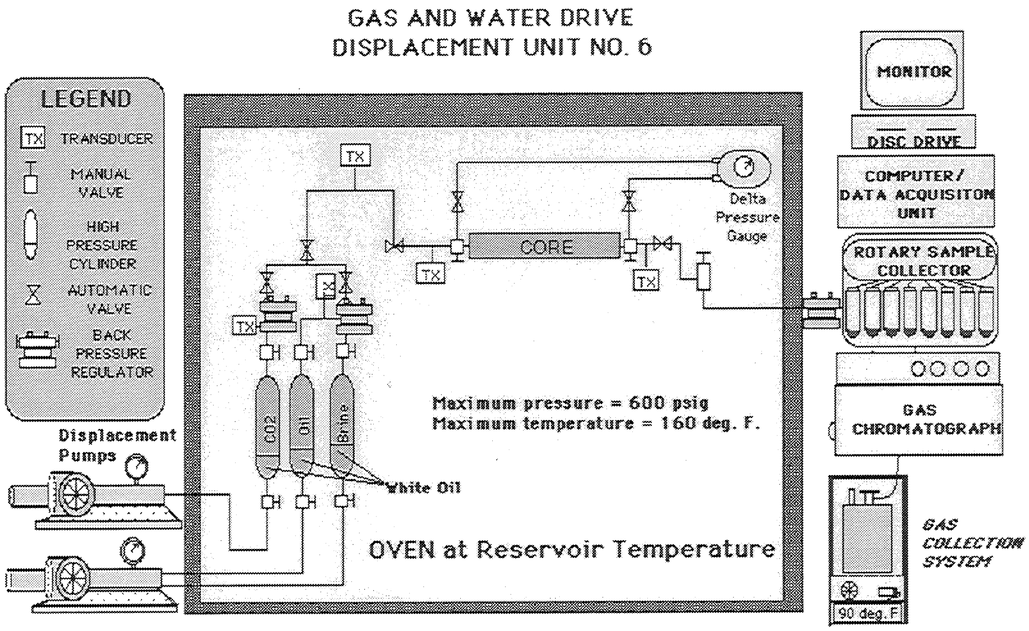
GAS AND WATER DRIVE
DISPLACEMENT UNIT NO. 6
LEGEND
TX TRANSDUCER
MANUAL VALVE
HIGH PRESSURE CYLINDER
AUTOMATIC VALVE
BACK PRESSURE REGULATOR
Displacement Pumps
TX
CORE
Delta Pressure Gauge
CO2
Oil
Brine
White Oil
Maximum pressure = 600 psig
Maximum temperature = 160 deg. F.
OVEN at Reservoir Temperature
MONITOR
DISC DRIVE
COMPUTER/ DATA ACQUISITON UNIT
ROTARY SAMPLE COLLECTOR
GAS CHROMATOGRAPH
GAS COLLECTION SYSTEM
90 deg. F

Figure 1.6-7. A flow diagram of the displacement rig. The rig is automated to conduct displacements at reservoir temperature and pressure.

RECOVERY RESULTS AT 600 PSI

The oil production data at 600 psi suggest only a small contribution from crossflow. Figure 8 shows the oil production from this phase of the experiment. The overall production is low (about 17% of OOIP). However, it is interesting to note that some additional oil was produced after the 6th day of injection. This small increase in production after two days without oil production indicates the contribution of crossflow from diffusion and/or gravity. It shall be noted at about

600 psi, CO_2 is not a very efficient solvent to the crude oil. One would expect that crossflow driven by diffusion and gravity increases as system pressure increases, which is investigated in the second phase of the experiment.

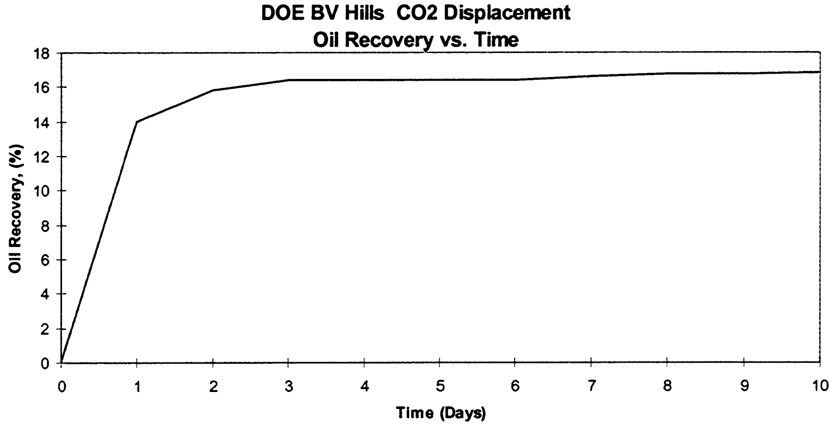

Figure 1.6-8. Oil Production from CO_2 injection.

RECOVERY RESULTS AT 2500 PSI

After oil production ceased at 600 psi, the system pressure was raised to 2500 psi. Significant oil production was observed at 2500 psi. Figure 1.6-9 shows the oil production as a function of time. At 2500 psi and 160 F, CO_2 has a density of about 0.5 g/cc, however, the pressure is still significantly lower than the minimum miscibility pressure (MMP). The volume of the produced oil is estimated from the weight of the produced oil and the density of the produced oil. At the end of the experiment, about 16 HCPV of CO_2 has been recycled at a constant rate of 1 cc/hr. The oil production rate had varied from 1 cc/day at the early time of the experiment to 0.3 cc/day at the end of the project. We also observed that the produced oil was significantly lighter than the original oil in the core (stock tank oil). Notice that the final oil production was slightly more than what we have injected into the core, suggesting that we had contacted and recovered some of the original oil in the shale.

To identify the oil components that CO_2 can recover from the reservoir, we measured the density and compositions of the produced oil samples. GC analysis of the oil samples showed that CO_2 recovered most components lighter than the C25+ fraction. The original oil density (stock tank oil) at 60 F was 0.886 g/cc, while the densities of the produced oil were in the range of 0.82 to 0.86 g/cc. The stock tank oil consists of about 19% (mol %) of C25+ fraction corresponding about 45% (weight %) of the oil mass. There were less than 3 % (or 7% by weight) of C25+ in the produced oil samples. These composition data suggest that a natural distillation process was taking place.

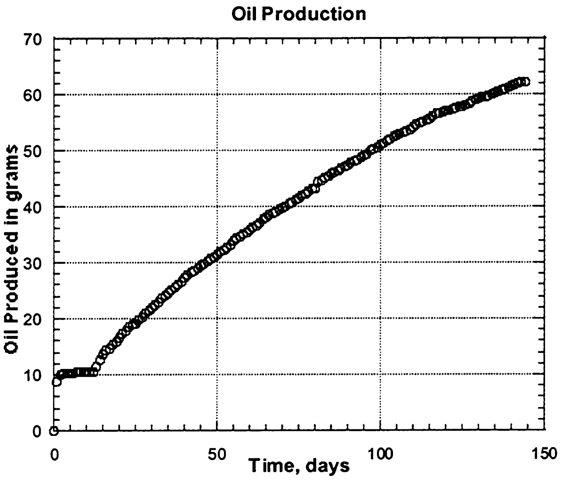

Figure 1.6-9. Total oil production from the high pressure (2500 psi) CO_2 flood. The volume of the produced oil is estimated using the density of the produced oil.

DISCUSSION

Material balance calculations on the sandstone slab suggest that about 60% to 65% (by weight) of the oil was recovered by CO_2 injection. To obtain a material balance for the sandstone slab, we measured the weights of the sandstone slab before (before it was saturated with oil) and after the experiment to estimate the amount of oil left in the slab. The difference of the weights (9.6g = 750.8g (after) – 741.4 g (before)) should be the amount of oil left in the sandstone slab. If the sandstone slab was completely saturated with oil, it contained about 29 cc (or 25.7 g) of oil. Because we did not clean the shale slab, the total oil in the shale should be more than 43 cc. Thus, we recovered about 16 grams (or 63% by weight) of oil from the sandstone. Notice that a small amount of epoxy was applied on the sandstone slab in the process of mounting the core into the core holder, which may make the value of oil left in the sandstone slightly higher.

Calculations from the compositions of the produced oil also suggests that about 65% (weight %) of were recovered. In the stock tank oil, C25+ fraction is about 45% (by weight) of the oil mass, while it contributes less than 7% in the produced oil. If CO_2 can recover all the components lighter than C25+ and a small fraction of C25+, about 62% of total oil mass can be recovered, which is consistent with the material balance calculations on the sandstone slab.

The objective of the experiments was to evaluate the potential of oil recovery by crossflow. The question is then: how much oil was recovered from the shale in this experiment? Total oil recovered from the mixed lithology core was 62.3 grams (10.59 g at 600psi and 51.67 g at 2500 psi). We saturated the core with 63.7 g of stock tank oil. The amount of stock tank oil injected into the core would account, at maximum, about 40 g of the produced oil. This calculation indicates that the original oil in the shale slab contributed about 22 cc of oil produced. It also suggests that crossflow can recover not only oil restored in the shale slab but also some of the original oil in the shale. It is important to point out that these calculations were based on the compositions of the stock tank oil and the produced oil. The amount of C25+ fraction recovered was a rough estimate

In constructing the mixed lithology core, a key challenge was to keep crossflow between the two slabs and to reduce CO_2 flow through the slab contact along the core. To check the sealing along the core, we measured the permeability of the mixed lithology core at the end of the experiment. The measured permeability for the entire assembly was 2.1 mD. The permeability of the sandstone at the end of the experiment was about 3 mD (measured with a permeameter). These numbers suggest that the slab contact contributed about half of the total core permeability. The CO_2 channeling in the reservoir can be significantly less that that in the experiments. Thus the amount of CO_2 injected to recover the same amount of oil would be significantly less than the experiments suggested. Detailed numerical simulations are needed to scale the experimental data to the field situation

CONCLUSIONS

We have completed two sets of displacement experiments on a composite sandstone core and a mixed lithology core to evaluate the oil recovery potential of crossflow in siliceous shale reservoir. The experimental data demonstrated that crossflow mechanisms can recover significant amount oil from very low permeability siliceous shale at 2500 psi. Very little oil was recovered at 600 psi. Analysis of the experimental data indicates that CO_2 crossflow not only recovered restored oil from the shale, but also recovered some of the original oil in the shale.

1.7. FLOW SIMULATION

Ray Tang and Dengen Zhou
Chevron Petroleum Technology Company

SUMMARY

With the completion of the 3D earth model in spring 1998, we proceeded to investigate the flow characteristics of the reservoir. We used 3D streamlines and finite-difference formulations to investigate sweep and recovery performance of a quarter-pattern element model representative of the geology near Well 653Z. The results suggest rapid breakthrough, poor sweep and poor recovery performance for Buena Vista Hills Antelope Shale.

DISCUSSION

The 3D earth modeling results were used to generate a quarter element model of a 5-spot pattern with Well 653Z in the southeast corner and Well 553 in the northwest corner. Figure 1.7-1 shows the 3D permeability distribution of the element model. The model contains 12x12x300 cells, which was scaled up from the 3D earth model, which was created, on a higher resolution of 12x12x1152. Scale-up was performed with Chevron's SCP program. In effect, the scale-up process preserves the high permeability layers while averaging and combining the low permeability layers. A comparison of simulations using the high resolution grid and scaled-up grid is presented below.

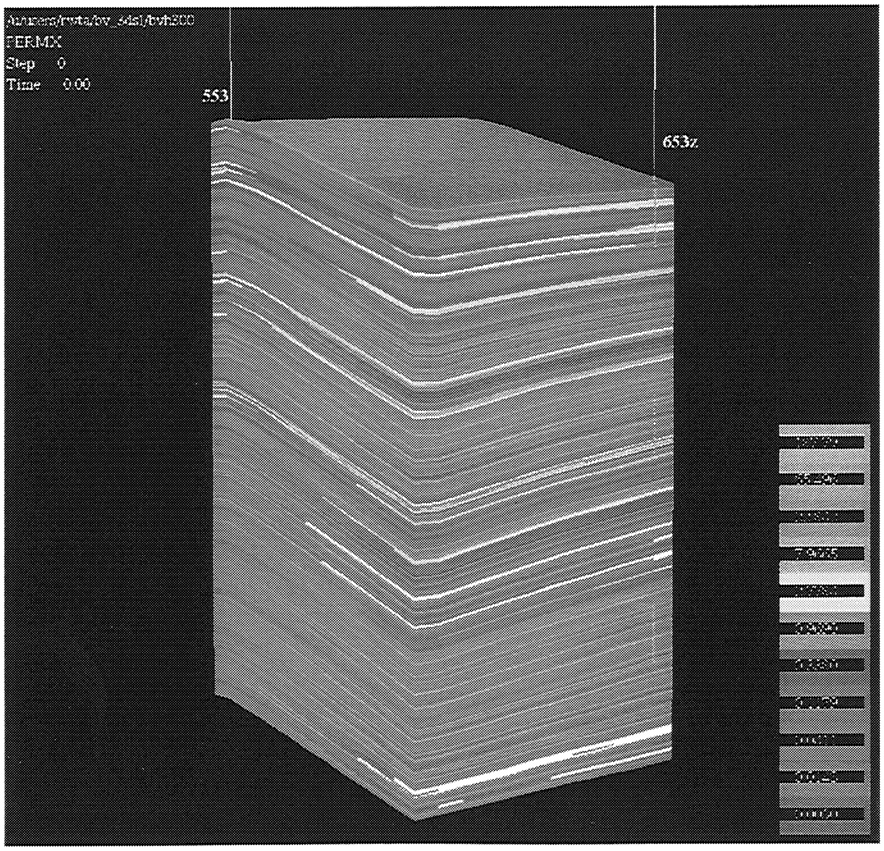

Figure 1.7-1. Buena Vista Hills permeability distribution near Well 653Z.

Figure 1.7-2 show water injection sweep through the 12x12x300 model with Well 653Z injecting and Well 553 producing. Constant initial oil saturation was assumed to illustrate more clearly the sweep performance. Breakthrough occurs after only small portion of the reservoir, containing sandy layers, is swept. Continued injection improves sweep marginally.

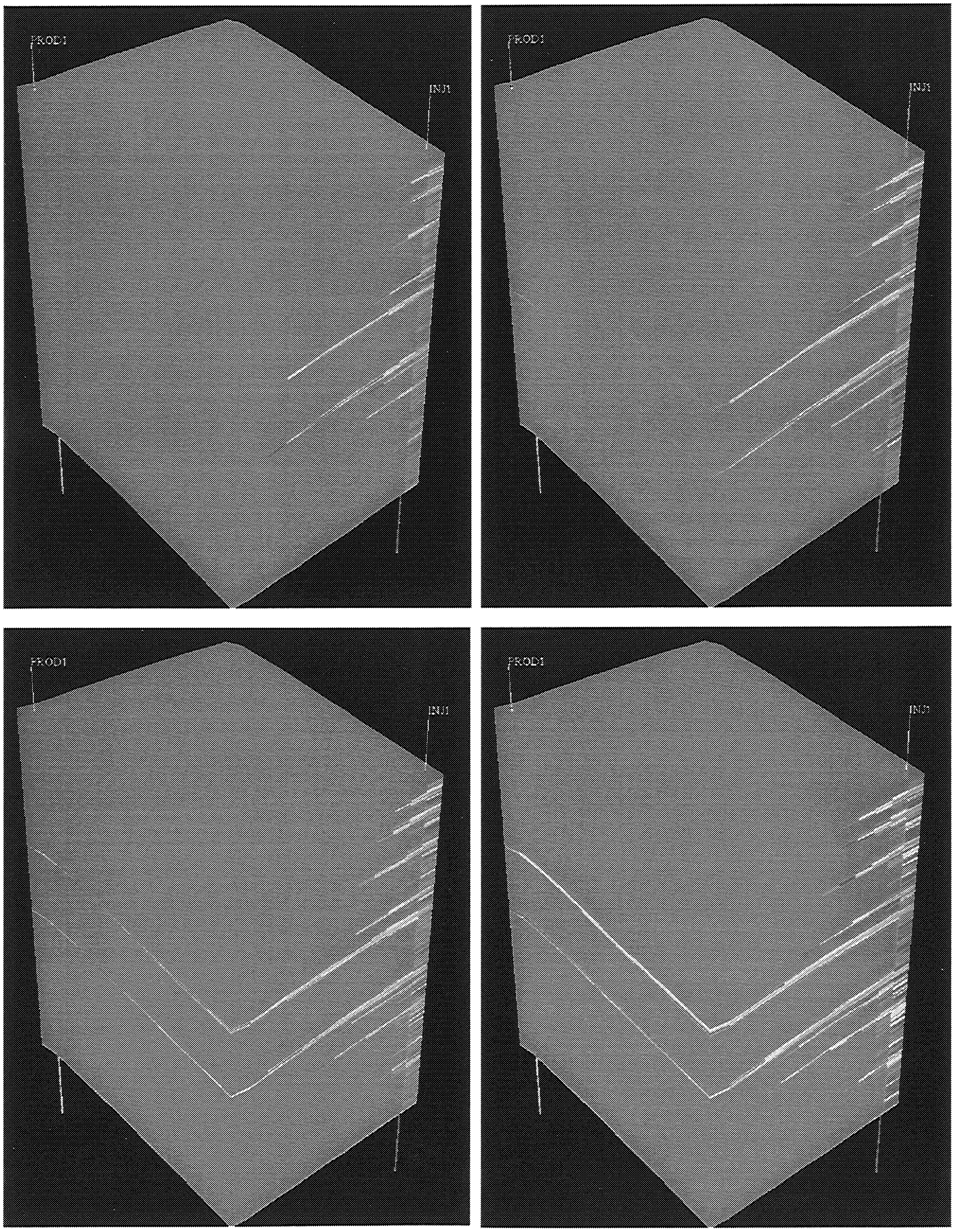

Figure 1.7-2. 3D streamline model water saturation distribution at different times.

Figure 1.7-3 shows water injection sweep on the 12x12x1152 grid corresponding to the same time as the last display in Figure 1.7-2. The difference between the scaled up model and the high resolution model is apparent in that one "thief" zone dominates sweep in the high resolution model compared to two thief zones in the scaled up model. However, Table 1.7-1 shows that the key feature of rapid breakthrough, poor sweep and recovery characteristics were reasonably captured despite the differences.

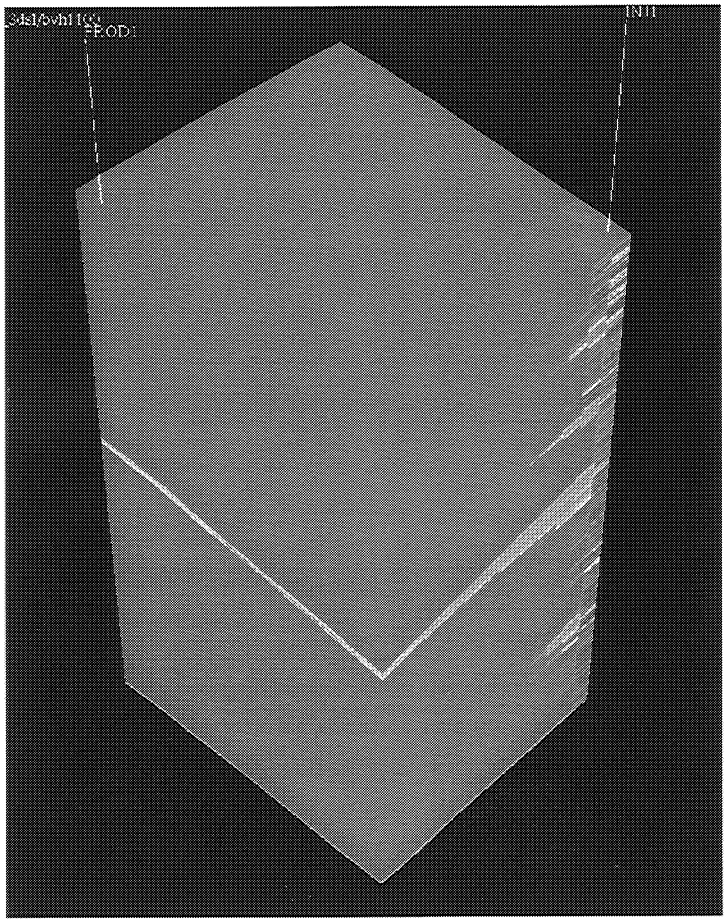

Figure 1.7-3. 3D streamline model water distribution in original high vertical resolution model (12x12x1152) at 608.3 days, same time as last picture in Figure 1.7-2.

Table 1.7-1. 3D streamline recovery and fractional flow at the end of the run, 1825 days.

At 1825.0 days	Recovery % OOIP	Oil Production Rate STB/D	Water Production Rate B/D
High Resolution Model	2.17	83.4	30.2
Scaled Up Model	2.03	80.0	31.3

Evaluation of depletion, water injection and CO_2 injection performance was conducted using the scaled up model with Chevron's CHEARS program. A compositional formulation was required to capture the interaction of CO_2 and reservoir oil. CHEARS uses the Peng-Robinson equation-of-state (PREOS) to model the fluid phase behavior. Tuning of PREOS parameters to the PVT and oil-CO_2 mixture measurements were performed by the Phase Behavior group at Chevron as part of this project. Table 1.7-2 presents the equation-of-state parameters used in simulations and Table 1.7-3 provides the initial compositions at a saturation pressure of 600 psi (estimated current reservoir pressure) and 160°F. The concentrations listed in Table 1.7-3 are in the same order as the component listing in Table 1.7-2.

Table 1.7-2. PREOS parameters.

```
COMPONENTS
*     NAME          MOL WT
      CO2           44.0100
      METHANE       16.0430
      C2-3          37.3790
      C4-6          70.5684
      C12          165.7252
      C35          484.2636
*
OILVISC    LBC    0.0233640    0.0585330   -0.0407580    0.0081600
GASVISC    LBC    0.0233640    0.0585330   -0.0407580    0.0093324
*
PARACHOR
        49.0    71.0   134.7   239.1   552.8 1575.3
*
EOSPARMS
*     NAME      PC(PSIA)     TC(F)    VC(CUFT/LBMOL)    W          SC
OMEGAA     OMEGAB
      CO2        1070.6036    87.8720      1.5058     0.2276     0.2463
0.457240   0.077800
      METHANE    667.8010  -116.6260      1.5899     0.0108    -0.1540
0.457240   0.077800
      C2-3       660.1129   150.4960      2.8286     0.1266    -0.1551
0.457240   0.077800
      C4-6       521.2758   376.8779      4.9312     0.2248    -0.1115
0.457240   0.077800
      C12        329.8484   764.3803     12.2270     0.4814     0.0707
0.457240   0.077800
      C35        157.7655  1212.5504     34.9235     1.1300     0.1143
0.457240   0.077800
*
BININTCOEF
 0.1000
 0.1250  0.0100
 0.1250  0.0210  0.0000
 0.1250  0.0440  0.0100  0.0000
 0.1250  0.0590  0.0100  0.0000  0.0000
```

Table 1.7-3. Initial oil composition at estimated current conditions.

```
*              DEPTH   PRESS     WOC
*
EQUILIBRIUM     3200.   600.     #
*
*
COMPINIT           BUBBLE       600.
 EQUILCMP
       0.00071  0.111  0.11826  0.15745  0.45415  0.15940
```

The simulated reservoir conditions were constrained by producing well limits that were set at 500 reservoir barrels of gross withdrawals and 50 psi bottom hole pressure. Injection pressure was constrained at 2250 psi which correspond to the estimated fracture pressure. Water injection, CO_2 injection and water-alternating-CO_2 (WAG) processes were simulated.

Figure 1.7-4 shows the oil saturation distribution initially in the CHEARS model. Oil saturation range from a minimum of 0.14 to a maximum of 0.75, with a mean of 0.23, a median of 0.19 and a standard deviation of 0.09. Oil saturation is low except in thin sandy stringers. Although the movement of injected fluid is obscure by the initial saturation distribution, displaying CO_2 concentration in the oil phase as a function of time as in Figure 1.7-5 confirms that sweep performance is consistent with 3D streamline results. After a long period of injection and CO_2 cycling, mixing of CO_2 and oil occurs because of gravity driven crossflow from the high permeability layers to the low permeability layers. However, the oil saturation in the Antelope Shale is so low that mixing has negligible benefit on recovery as the comparison shows in Table 1.7-4. Sweep and recovery is poor for all processes simulated, water, gas and WAG injection. Table 1.7-4 provides a summary of the recoveries after 10 years of injection.

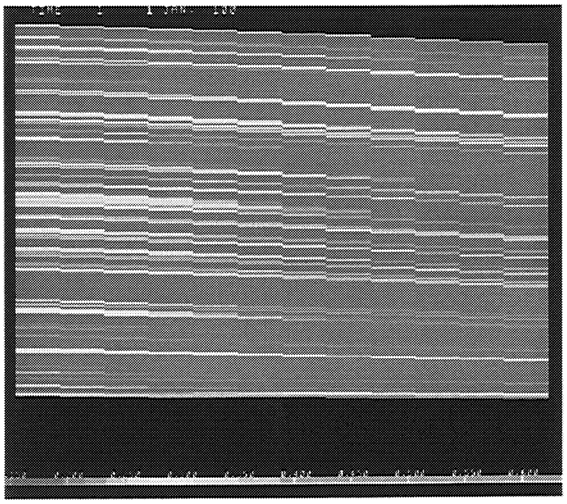

Figure 1.7-4. Oil saturation distribution along the south face of the CHEARS model.

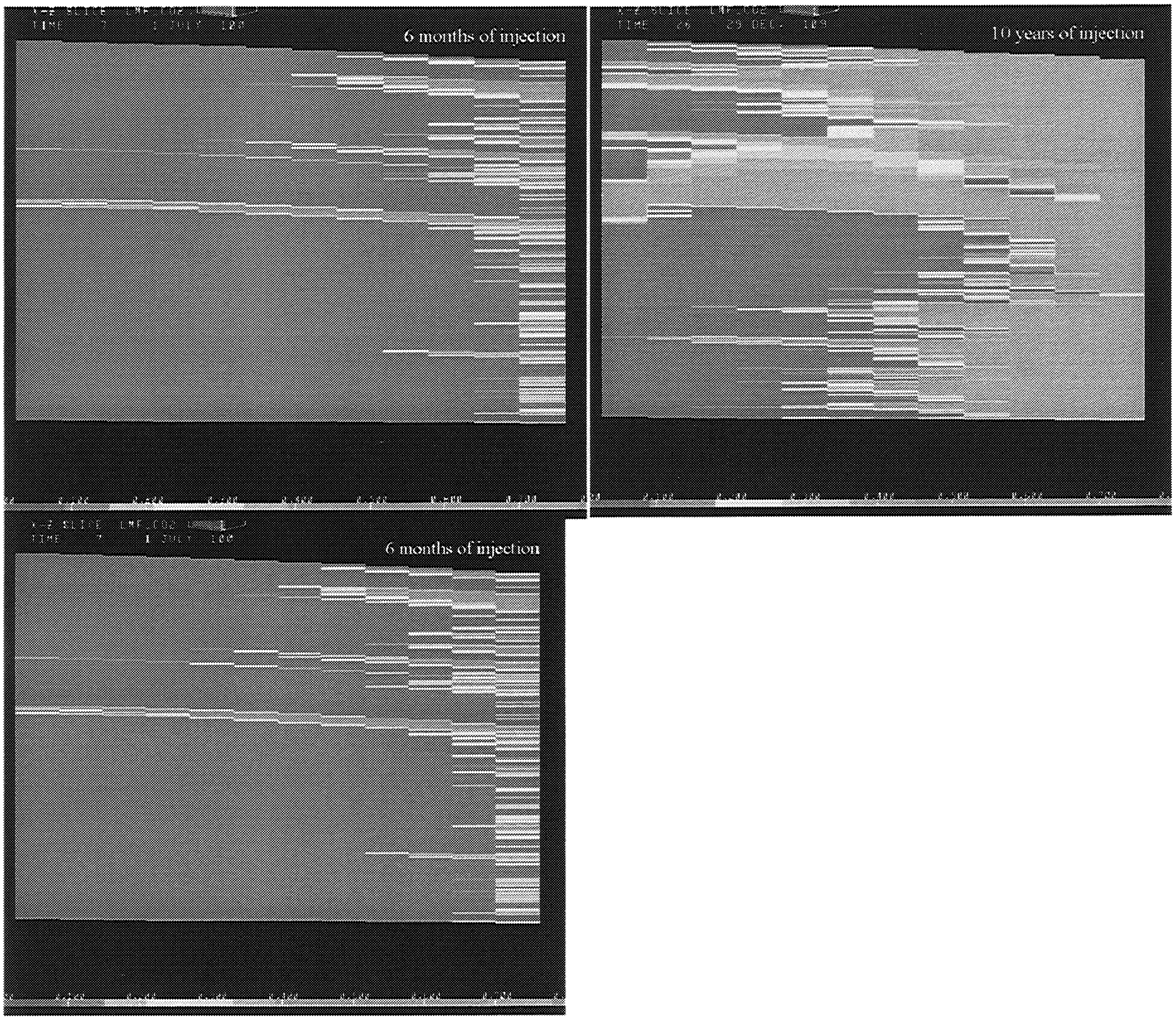

Figure 1.7-5. CO_2 fraction in reservoir oil along the south face of the CHEARS model, 1:1 WAG.

Table 1.7-4. Comparison of total recovery after 10 years of injection.

At 3650 days	Recovery % OOIP	Oil Production Rate STB/D	Gas Production Rate MCF/D	Water Production Rate B/D
Water Injection	7.1	21.2	3.3	61.1
WAG Injection	7.4	80.0	109	31.3
Gas Injection	3.3	15.1	526.	0.

CONCLUDING REMARKS

The principal objective of the Phase 1 period tasks was determining the potential of CO_2 EOR at Buena Vista Hills conditions; if potential exist, simulate the recovery performance for a pilot project and for the full field. The simulation results presented above do not warrant further effort in estimating pilot or full field potential. The primary factors impairing CO_2 potential at Buena Vista Hills are low oil saturation and poor conformance caused by very adverse heterogeneity.

We are continuing some modeling effort in attempting to better understand the mix-lithology core flooding results. In a parallel effort, Chevron identified more significantly favorable CO_2 EOR conditions at the Lost Hills field, which contains less heterogeneous siliceous shale formations with higher oil saturation relative to Buena Vista Hills.

1.8. 653Z-26B HYDRAULIC FRACTURING

Mark Emanuele

Chevron USA Production Company

STAGE #1

Hydraulic propped fracture treatments were attempted in two different Upper Antelope Shale intervals. The first attempt was made at a depth of 4200'- 4210' MD (4145'-4154' TVD). This 10 ft interval was selected, based upon its favorable hydrocarbon saturation and in-situ stress profile. The stress profile was constructed from dipole sonic log, (shear and compressional wave data), processed utilizing Chevron's proprietary Rock Mechanics Algorithm (RMA). The goal of the first hydraulic fracture was to cover both the Lower Brown Shale and the Upper Antelope Shale in a single treatment.

The stress profile generated by RMA indicated the minimum horizontal stress across the perforated interval was approximately 0.5 psi/ft or 2050 psi. Although this horizontal stress seemed low, reservoir pressure in this interval is accordingly low, approximately 700-800 psi. A series of diagnostic injections was pumped prior to the main treatment to determine the closure stress, the magnitude of near wellbore friction (or fracture tortuosity) as well as the number of effective perforations accepting fluid. This data is contained in Table 1.8-1 below. During these injections, both surface and downhole tiltmeter arrays were employed, allowing the fracture azimuth, dip and height to be measured.

Table 1.8-1. 653Z Stage #1 frac pressure data.

Diagnostic Injection #	Fluid Type	Surface ISIP (psi)	ISIP Gradient (psi/ft)	BH Closure Stress (psi)	Closure Pressure Gradient (psi/ft)	Near Wellbore Friction (psi)	Effective Perfs Open (40 shot)
1	2% KCL	2145	0.95	3295	0.79	2100	7
2	25lb linear gel	1951	0.90	3244	0.78	1086	11
3 (XL-Minifrac)	Crosslinked Gel 3 ppg prop. Slug	2547	1.04	3485	0.84	1840	16

From the diagnostics injections pumped during Stage #1, the real-time downhole tiltmeter array indicated that there was excessive fracture height growth exceeding the top tiltmeter at 3950 ft. Little to no downward fracture growth was indicated by the downhole tiltmeter array. The cause of this excessive height grow is thought to be the induced fracture propagating into a poorly cement bonded interval, 20 ft above the perforations. Based on the fact that height growth was excessive, (the fracture was not going to cover the intended target interval of the upper Antelope Shale), and the near wellbore fracture complexities resulted in elevated ISIP and closure pressure gradients, it was decided to forego this interval and re-perforate lower in the Antelope Shale.

Elevated ISIP's (Instantaneous Shut-In Pressures) and closure pressure gradients, exceeded overburden gradients, indicated a horizontal or highly dipping fracture component was likely created. Figure 1.8-1 is a plot of the lithostatic overburden gradient derived from the openhole density log. It can be seen that the all 3 ISIP's from Sage #1 exceeded the overburden gradient.

Surface tiltmeters results (see Section 1.9) indicate that there was consistent no fracture azimuth from one injection to the next, and that there was a significant dipping (non-vertical) component to each fracture created. These multi-component fractures are most likely the cause of the high near wellbore friction (tortuosity). Surface tiltmeter data corroborates well with the fracture pressure data. The surface tiltmeter data large volume multi-component fractures, both vertical and dipping, with no specific azimuth. This lack of a preferred fracture azimuth is an indication that the deviatoric stresses are fairly close in magnitude.

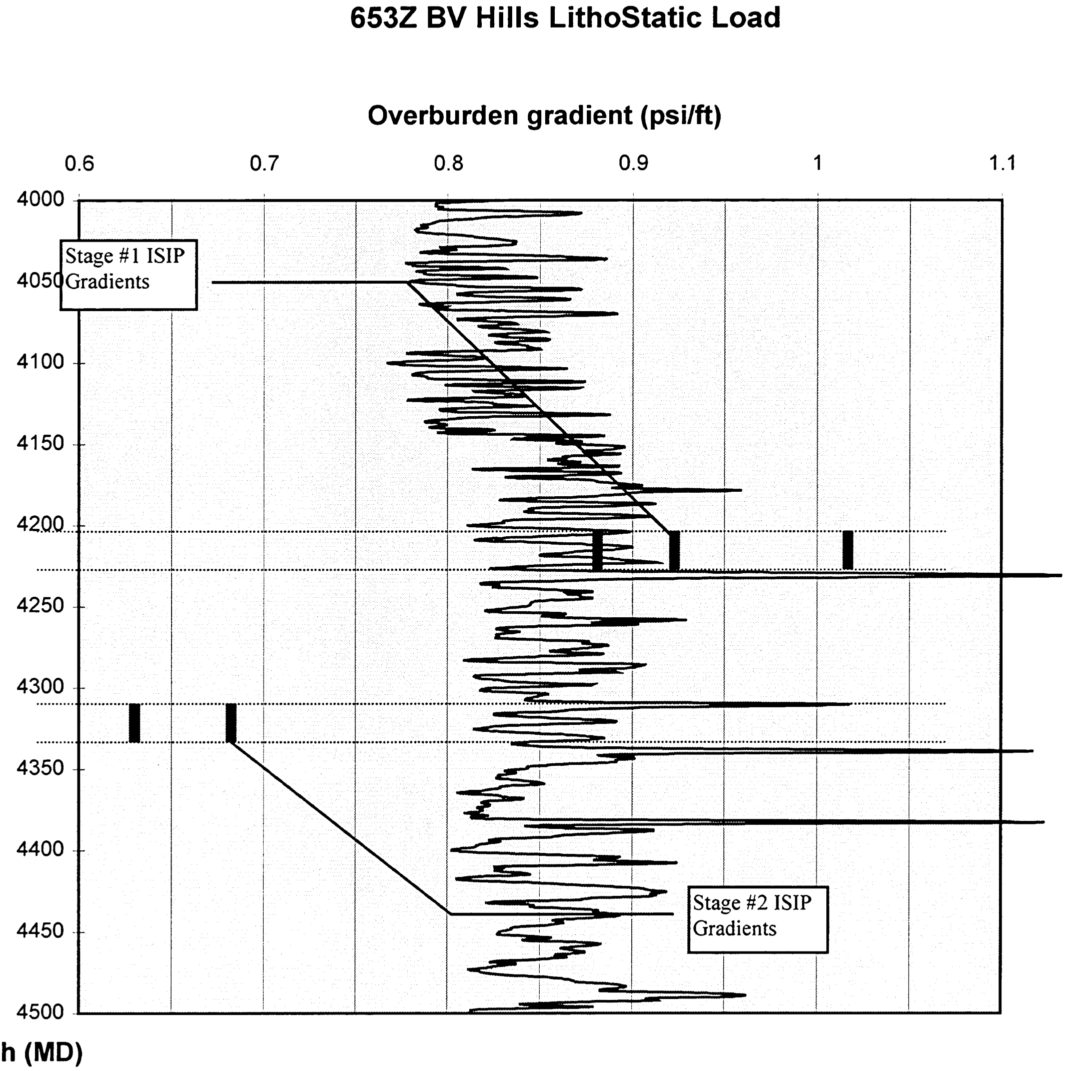

Figure 1.8-1. Lithostatic load.

STAGE #2

New perforations were added from 4305'- 4315' MD (4244'- 4253' TVD) and the previous perforations were isolated utilizing a packer. Similar diagnostic injections were employed for Stage #2. The results are listed in the Table 1.8-2 below:

Table 1.8-2. 653Z Stage #2 frac pressure data.

Diagnostic Injection #	Fluid Type	Surface ISIP (psi)	ISIP Gradient (psi/ft)	BH Closure Stress (psi)	Closure Pressure Gradient (psi/ft)	Near Wellbore Friction (psi)	Effective Perfs Open (40 shot)
1a	15% HCl	N/A	N/A	N/A	N/A	N/A	N/A
1b	2% KCL	N/A	N/A	N/A	N/A	N/A	N/A
2	30lb Linear Gel	938	0.66	1877	0.45	450	20
3 (Minifrac)	Crosslinked Gel 3 ppg prop. slug	1215	0.72	2677	0.63	600	10
4 (Minifrac)	Crosslinked Gel 2 ppg prop. slug	Screenout Treatment Terminated	Screenout, Treatment Terminated	Screenout Treatment Terminated	Screenout Treatment Terminated	Screenout Treatment Terminated	Screenout Treatment Terminated

Predicted stress values from the sonic log data were within 10% of the measured stress after diagnostic Injection #2. Subsequent injections only seemed to complicate near wellbore fracture complexities, as can be seen by the increase in ISIP, closure stress and near wellbore friction (tortuosity). Injection #4, which was a repeat of the crosslinked minifrac (Injection #3), met with injection pressures higher than the wellbore tubulars were rated. Further attempts to hydraulic prop fracture Stage #2 were aborted.

CONCLUSION

Based on the pressure analysis and tiltmeter results (See Section 1.9), the conclusion can be drawn that a complex system of multiple fractures (vertical and non-vertical) were created during diagnostic injections for both Stages 1 and 2. It is currently unknown what causes the propagation of multiple fractures, but it may be related to the finely laminated siliceous shale/sand sequences in the Antelope Shale. These micro-thin beds may delaminate at a given pressure after injection begins, thus severely limiting vertical fracture growth. The limited width of these non-vertical fractures thus causes a severe pressure increase during proppant placement, resulting in premature treatment termination.

1.9. SURFACE AND DOWNHOLE TILTMETER FRACTURE MAPPING, WELL 653Z-26B

Eric Davis
Pinnacle Technologies

INTRODUCTION

This reports provides results of Pinnacle Technologies' surface and downhole tiltmeter fracture mapping of Well 653Z-26B in Buena Vista Field, CA. The treatments were conducted in the period of February 19 to 23, 1998. Target zones for the two attempted fracture treatments were at depths ranging from 4100'– 4290' within the Lower Brown Shale/Upper Antelope Shale and 4244'– 4253' within the Antelope Shale. Although repeated attempts were made to break down the formation, including reperforating, a complete treatment was never attempted due to high pressures and screenouts encountered when proppant slugs were added to the diagnostic fractures. Eight downhole tiltmeters were installed in nearby Well 564 to characterize fracture height growth, though it was not discovered until after the treatment that the tiltmeters were in a slotted liner which did not have solid contact with the well casing. This situation prevented the acquisition of useful downhole tiltmeter data and the subsequent analysis of that data for fracture height. Surface tiltmeter data, however, did allow the determination of fracture azimuth, dip, and horizontal fracture volume component of the diagnostic treatments. The results of that analysis are presented in this report.

METHOLOGY

Tiltmeter Fracture Mapping

Creation of a hydraulic fracture, by definition, involves parting of the rock and displacing the fracture faces to create fracture width. The principle of tiltmeter fracture mapping is simply to infer hydraulic fracture geometry by measuring this fracture-induced rock deformation. The induced deformation field radiates in all directions and can be measured either downhole with wireline-conveyed tiltmeter arrays or with a surface array of tiltmeters. Figure 1.9-1 shows a schematic diagram of the induced deformation field from a vertical fracture as seen both downhole and at the surface. As shown, measuring the deformation field at the surface with a two-dimensional array gives a very different view of the deformation field than a one-dimensional (line) array downhole in an offset wellbore.

At the surface, the induced deformation magnitudes are so small – typically of order one ten-thousandth of an inch – that they are impossible to measure. Fortunately, measuring the gradient of the displacement field, or the tilt field, is far easier. The induced deformation field at the surface is primarily a function of fracture azimuth, dip, depth to fracture center, and total fracture volume (Figure 1.9-2). The induced deformation field is almost completely independent of reservoir mechanical properties and in-situ stress state. For example, a north-south growing vertical hydraulic fracture of a given size yields the same surface deformation pattern whether the fracture is in low modulus diatomite, extremely hard carbonate, or even unconsolidated sandstone. The deformation pattern is simply a north-south trending trough surrounded by symmetrical ridges (the ridges are asymmetrical if the fracture is dipping) whose magnitude depends on the created fracture volume and whose separation depends on the depth-to-fracture-center.

The simplicity of the concept allows robust and unambiguous determination of a few primary fracture parameters like fracture azimuth and dip and, with somewhat less precision, created fracture volume, depth-to-fracture-center and fracture offset due to asymmetric growth. The characteristic shape and orientation of the tilt field is not altered with increasing fracture depth. The magnitude of the tilt is, of course, attenuated with increasing fracture depth, which serves to limit the practical surface mapping depth.

The greatest limitation of surface tilt mapping is that some critical details, like individual fracture dimensions, cannot be resolved at fracture depths far greater than the created fracture dimensions. This is because at greater depth not only do the induced surface tilts get smaller, but there is also an inherent blurring of the fracture source "edges" as the measurement distance gets large compared to the separation of the fracture edges (i.e. fracture dimensions). Downhole tiltmeter mapping was developed to get around the fracture dimension resolution limitation by bringing the measurement distance down to the same order of magnitude as the created fracture dimensions.

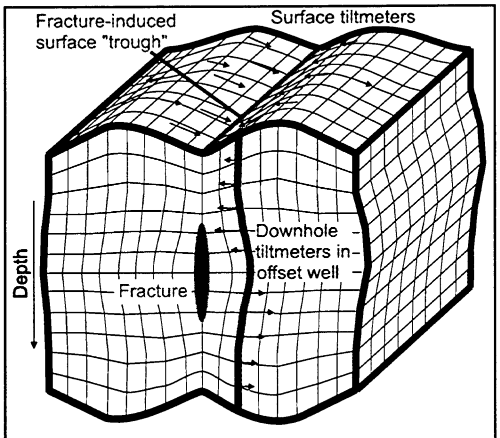
Fracture-induced surface "trough"
Surface tiltmeters
Downhole tiltmeters in offset well
Fracture
Depth

Figure 1.9-1. Principles of tiltmeter fracture mapping.

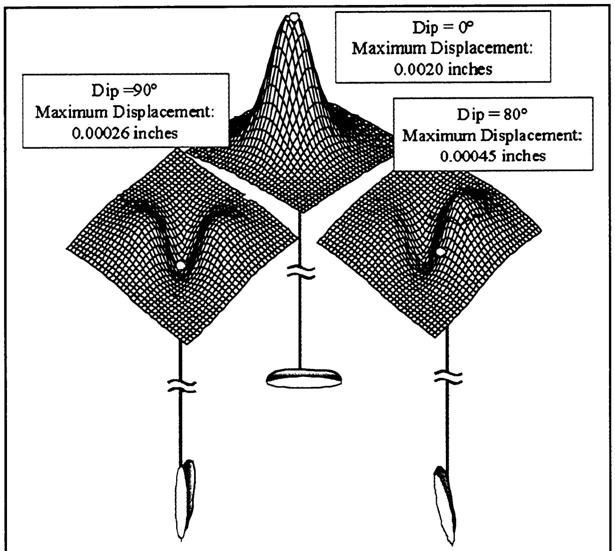
Dip = 0°
Maximum Displacement:
0.0020 inches
Dip =90°
Maximum Displacement:
0.00026 inches
Dip = 80°
Maximum Displacement:
0.00045 inches

Figure 1.9-2. Surface deformation for hydraulic fractures of different orientations at 3000 ft depth.

How surface tilt mapping works

Surface tiltmeter mapping involves measuring the fracture-induced tilt at many points above a hydraulic fracture, and then solving the geophysical inverse problem to determine the fracture parameters that must have been created in order to produce the observed deformation field. While the concept is simple, the magnitudes of the induced surface deformations are quite small and require highly sensitive measurement. A typical hydraulic fracture treatment at a 7,000 foot depth results in induced surface tilts of only about 10 nanoradians – or about 10 parts in a billion.

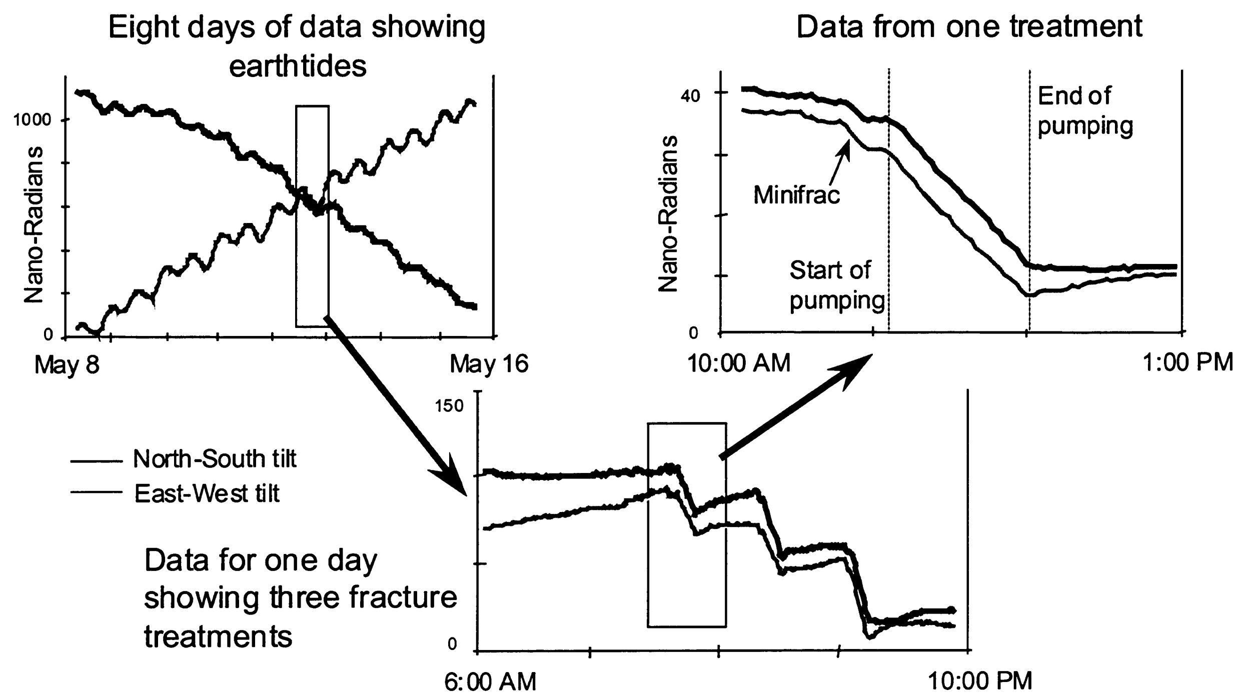

Figure 1.9-3. Three pictures of raw tiltmeter data on different time scales, ranging from one week with clear eartides to a few hours artound a fracture treatment.

These minute tilts are measured with highly sensitive tiltmeters that operate on the same principle as a carpenter's level. Tiltmeters are metal cylinders roughly 30 inches long and 2 inches in diameter, which measure their own tilt on two orthogonal axes. As the instrument tilts, a gas bubble contained within a conductive-liquid-filled glass casing moves to maintain its alignment with the local gravity vector. Precision electronics detect changes in resistivity between electrodes mounted on the glass sensor that are caused by motion of the gas bubble. The latest generation of high-resolution tiltmeters, developed jointly by Pinnacle Technologies and Lawrence Livermore National Laboratory, were awarded a prestigious *R & D 100 Award* in 1997 and can detect tilts of less than one nanoradian.

For fracture mapping purposes, an array of 12 to over 24 tiltmeters are placed around the well to be fractured at radial distances from 15% to 75% of the fracture depth, as this is the region of maximum induced surface tilt. Fortunately, the exact layout of the monitoring array is not critical. Fracture mapping resolution is primarily dependent on the number of tiltmeter sites employed and the signal-to-noise ratio of the measurements. Resolution of fracture orientation is typically better than +/- 5 degrees at depths less than 5,000 ft, and can drop to +/- 10 degrees as depth approaches 10,000 ft. Resolution of fracture center location ranges from 20 to 200 feet for fractures shallower than 3,000 ft, and drops to many hundreds of feet for fractures approaching 10,000 ft.

Each tiltmeter site has an instrument surrounded by sand within PVC pipe (3" to 9" diameter) that is cemented in a relatively shallow (10 to 40 ft. deep) borehole. Figure 1.9-3 shows a sample record of tilt data versus time on many different time scales. The first view shows the daily swings of the tilt data in response to the solid earth tides caused by the earth's rotation with respect to the sun and moon, and a long-term drift due to surface subsidence. The next zoom-in shows an 18-hour time period when three hydraulic fracture treatment stages (seen clearly in the data) were pumped in the well being monitored. The final zoom-in shows a two-hour time period that clearly shows the recording of fracture-induced tilt from one of the propped fracture treatments. The three fracture treatments shown were in a relatively shallow depth range of approximately 3,000 ft. and hence yielded induced tilts of order 100 nanoradians. The fracture-induced tilt is then extracted at each instrument site to yield an array of observed surface tilt vectors.

The observed tilt data is inverted to find the hydraulic fracture parameters that yield the best fit to the observed data, and a Monte-Carlo technique is employed to estimate parameter uncertainty. The top side of Figure 1.9-4 compares the observed and theoretical fracture-induced tilt vectors from a best-fit fracture solution and shows a tabular listing of the mapped fracture orientation and depth. Note how a careful visual inspection of the observed tilt vectors alone reveals a trough that runs roughly northeast-southwest (fracture azimuth of N 45° E) and that both ridges are of roughly equal magnitude implying a fracture dip that is almost perfectly vertical (90 degrees). In simple single-plane-fracturing cases like this, visual inspection alone reveals the essential results.

The lower side of Figure 1.9-4 shows another overlay of observed and theoretical tilt vectors for the case of a horizontal fracture. Note the dramatic difference in the induced surface tilt patterns. Curiously, the mapped horizontal hydraulic fracture is in the same field as the vertical frac shown, and the horizontal fracture is created in a structurally deeper part of the reservoir.

As the fracture-induced tilt is measured as a function of time, fracture mapping can be performed throughout the course of the treatment (and soon, in real-time). In some cases fractures may initiate in one plane and then twist into another orientation, or initiate secondary fracture growth in another plane at some point in time during a treatment. Other parameters like depth-to-fracture-center may also change significantly during a treatment if, for example, the fracture breaks through a barrier and begins rapid upward (or downward) height growth.

DISCUSSION

Surface Tiltmeter Analysis

It is highly unusual to find as many fracture orientations in one well as we found in Well 653Z. Table 1.9-1 summarizes the results from all seven mini fracs, showing multiple components for each. For the first mini frac on 2/23/98, there was a clear break in the data, so we analyzed this frac in two pieces (1a and 1b). When we refer to fracs as vertical and horizontal in this table, we mean within 30° of perfectly vertical for a vertical frac (a perfectly vertical frac has a dip of 90°), and within 30° of perfectly horizontal for a horizontal frac (a perfectly horizontal frac has a dip of 0°). Fracs that are neither vertical nor horizontal are referred to as "dipping".

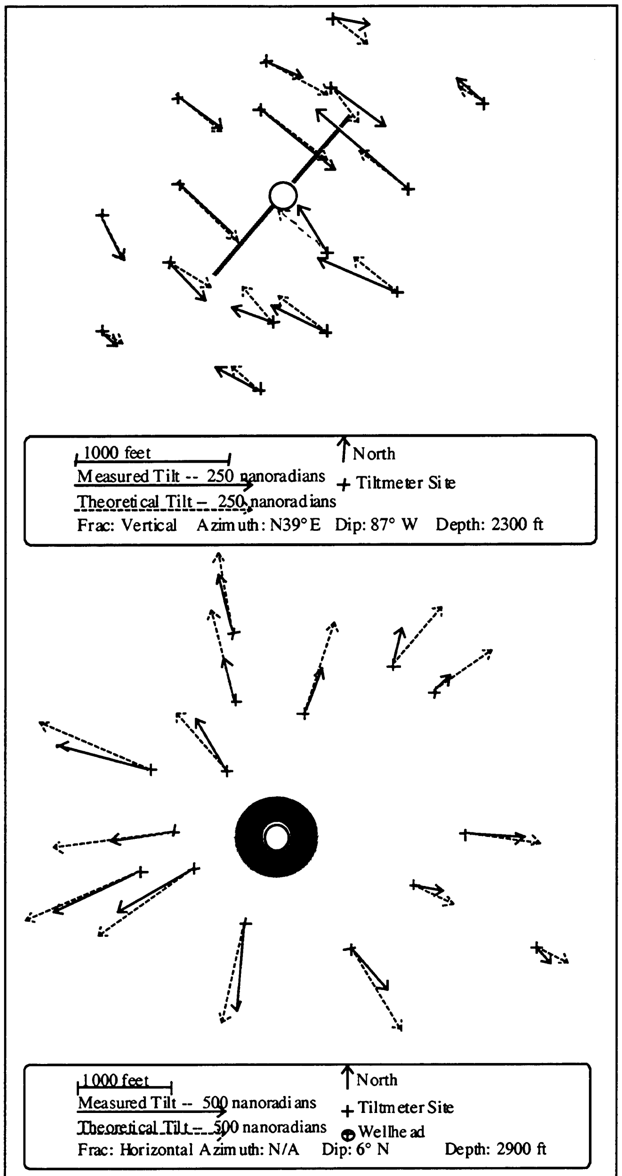
1000 feet
North
Measured Tilt -- 250 nanoradians
Tiltmeter Site
Theoretical Tilt -- 250 nanoradians
Frac: Vertical Azimuth: N39°E Dip: 87° W Depth: 2300 ft
1000 feet
North
Measured Tilt -- 500 nanoradians
Tiltmeter Site
Theoretical Tilt -- 500 nanoradians
Wellhead
Frac: Horizontal Azimuth: N/A Dip: 6° N Depth: 2900 ft

Figure 1.9-4. Observed and theoretical fracture-induced tilt vectors for a vertical (top) and horizontal (bottom) fracture. Curiously, the mapped horizontal fracture is in the same field as the vertical fracture shown, and the horizontal fracture is created in a structurally deeper part of the reservoir.

Table 1.9-1. Surface tiltmeter mapping results for the seven mini fracs performed on Well 653Z.

Date	Stage	Slurry Volume (BBL)	Pump Times	Fracture Type	Fracture Azimuth	Fracture Dip	Frac-System Volume %
2/19/98	1	123	12:17–12:25	Vertical	N 57° W ±8	61° W ±8	76%
2/19/98	1	123	12:17–12:25	Dipping	N 12° E ±8	40° W ±8	24%
2/19/98	2	95	12:55–13:01	Vertical	N 29° E ±8	67° W ±8	58%
2/19/98	2	95	12:55–13:01	Dipping	N 86° E ±25	48° S ±25	42%
2/19/98	3	181	13:38–13:46	Vertical	N 86° E ±12	67° S ±10	57%
2/19/98	3	181	13:38–13:46	Dipping	N 15° E ±12	25° W ±8	43%
2/23/98	1a	21	12:17–12:27	Vertical	N 1° E ±12	72° E ±10	65%
2/23/98	1a	21	12:17–12:27	Dipping	N 66° W ±12	48° N ±8	35%
2/23/98	1b	9	12:27–12:31	Vertical	N 84° W ±9	73° S ±8	85%
2/23/98	1b	9	12:27–12:31	Dipping	N 11° E ±16	43° W ±15	15%
2/23/98	2	100	13:06–13:10	Vertical	N 4° E ±20	76° E ±15	81%
2/23/98	2	100	13:06–13:10	Dipping	N 58° E ±25	32° N ±20	19%
2/23/98	3	150	13:44–13:50	Vertical	N 79° E ±13	80° S ±8	69%
2/23/98	3	150	13:44–13:50	Dipping	N 5° W ±8	43° W ±8	31%
2/23/98	4	150	14:39–14:44	Vertical	N 60° E ±17	86° S ±8	51%
2/23/98	4	150	14:39–14:44	Dipping	N 39° W ±15	47° W ±14	49%

Normally we put the surface tiltmeters on a one minute sample rate, which gives us an overkill of data points for the targeted main frac job. Unfortunately, this sample rate gave us only a few data points to look at for most of the mini fracs, making the analysis more difficult and resulting in higher than normal uncertainties. Nevertheless, it is clear that many different fracture orientations were created during the course of these treatments.

The most plausible explanation we can devise for this behavior is that the formation near the perforations never broke down. Instead, the fluid ran up along the wellbore until it encountered a region of low enough breakdown pressure or stress to create a fracture. Upon introduction of a proppant slug, the new fracture immediately screened out. During subsequent mini-fracs, the fluid passed the original fracture and continued up the wellbore until it encountered another relatively weak or low stress region.

Downhole Tiltmeter Analysis

The downhole tiltmeter array produced virtually no signal in response to the hydraulic fracture treatment at Well 653Z (Figures 1.9-5, 6, and 7). Many possible reasons the downhole tools might have been unable to map the fracture were considered, including:

- *Were the tiltmeters close enough to the treatment well to capture a signal?* Since we had performed tiltmeter mapping from smaller treatments further away, signal size should not have been an issue.
- *Was the noise level in the observation well too high to resolve the signal?* Although the observation wellbore was quite noisy due to continued gas production while the downhole tools were installed, the noise level was still a factor of 10 smaller than the expected signal.
- *Were the tools at the correct depth?* All calculations showed the target depth was correct. Line tension clearly showed the tools had not stuck in the wellbore on the way down, as the loss of the sinker bar is unmistakable. Temperature readings from the tools also matched the expected temperature at the target depth.
- *Were the tool centralizers in good contact with the casing?* Since centralizer drag is significant compared to the weight of the tools, there would be a substantial change in line tension if even a few tools lost solid contact with the casing. Since NO tool detected a fracture-induced signal, it seemed implausible that poor casing contact was the problem. Furthermore, line tension was significantly higher than normal when the tools were removed from the well. In fact, as we discovered later, one centralizer arm had become lodged in a slot in the slotted liner and required a workover rig to free the tool.
- *Did the formation fracture so far up the wellbore that the tools did not detect it?* In order to produce a signal of less than 1μR at the top tool, modeling indicated the center of the fracture had to be *at least* 300 ft above or below the perforations. This possibility was presented to Chevron, however unlikely it may seem.

Following a discussion with Chevron representatives, it was determined that a free hanging slotted casing was present in Well 653Z which prevented adequate mechanical coupling of the downhole tiltmeter array with the surrounding country rock. This condition prevented the transmission of fracture-induced material deformation to the tiltmeter casing so little to no tilt occurred on the devices. This condition prevented the use of the downhole tiltmeter array to determine fracture height and depth.

RESULTS AND CONCLUSIONS

Monitoring of fracture orientation is of key importance to understand well / pattern production behavior. Chevron intended to utilize this data to make decisions regarding the infill drilling location of new wells as they began to exploit the Lower Brown Shale/Upper Antelope Shale in Buena Vista Hills Field.

Fracture Azimuth, Dip and Horizontal Component of the Created Fracture

An unusual combination of small, vertical, and steeply dipping fractures were created, all varying widely in orientation and dip. Table 1.9-1 summarizes the results from all seven mini fracs, showing multiple components for each. For the first mini frac on 2/23/98, there was a clear break in the tilt responses, so we analyzed this frac in two pieces (1a and 1b).

Figure 1.9-8 provides a map view of the fracture azimuths and their spatial relation to the wellheads and the wellbore. Surface tiltmeter fracture mapping substantiates the following conclusions:

- Most hydraulic fracture treatments result in a nearly vertical fracture, often accompanied by one or more nearly horizontal fracture components. Rarely do we encounter fractures defined as "steeply dipping", i.e. with a dip between 30° and 60° off horizontal. However, all seven diagnostic fracture treatments in Well 653Z-26B resulted in a nearly vertical fracture, with an unpredictable azimuth, accompanied by a steeply dipping fracture.
- Average azimuth for the vertical fracture components of each stage is N 15° E with a range of N 84° W to N 79° E, which covers nearly all possible fracture azimuths. Average azimuth for the dipping fracture components is N 9° W also with a large range of N 86° E to N 66° W.
- Six of the seven vertical fracture components dip around 74° down to the South, with a range of 61° to 86° down to the South. The seventh (Mini 2 on 2/19/98) dips the opposite direction, 67° down to the North.
    - Dipping fractures constitute an unusually high average of 32% of the total fracture system volume for each of the 8 stages mapped here, (range of 15%-49%).

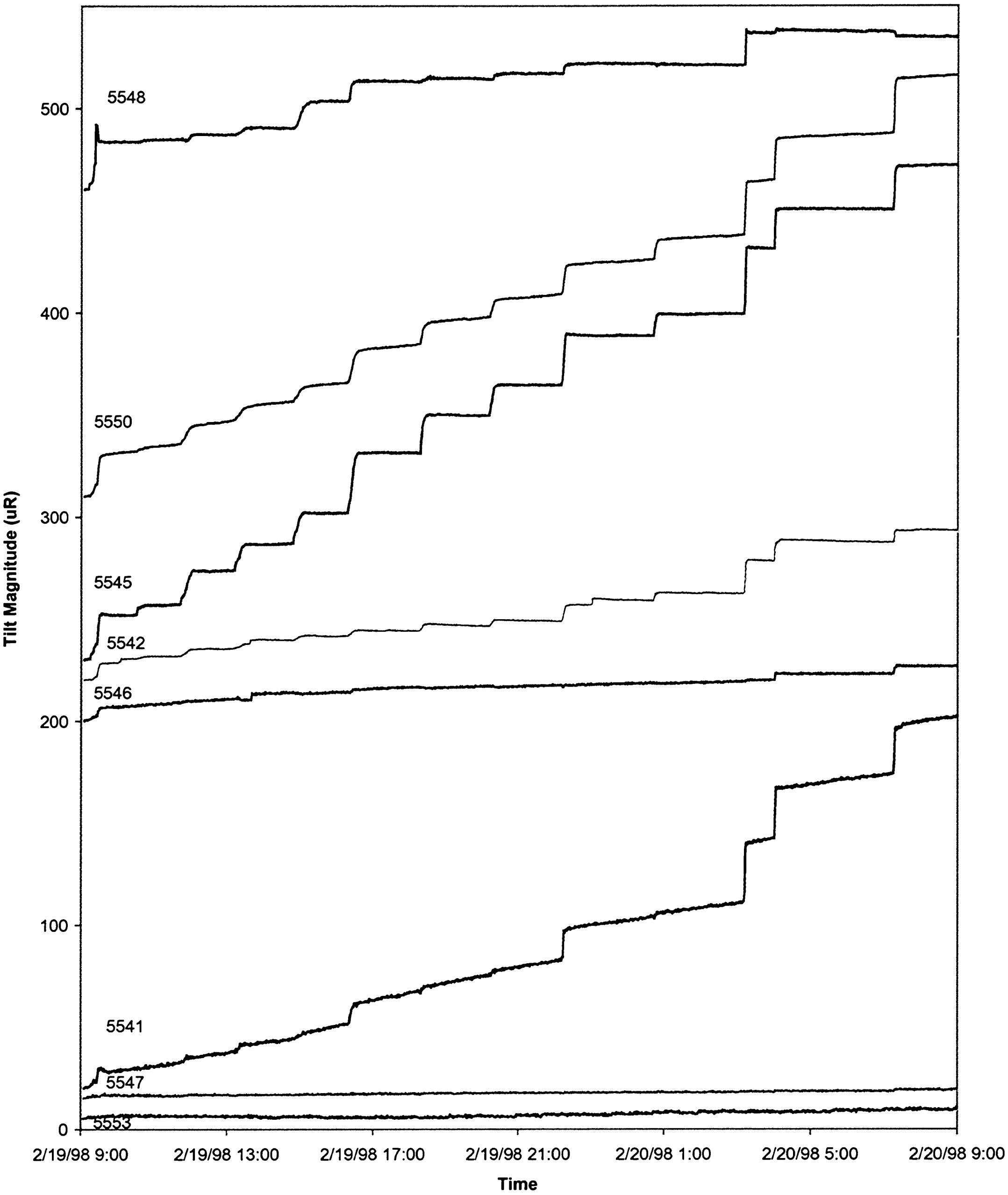

Figure 1.9-5. Tilt signals from all downhole tiltmeters for the 24 hour period from 2/19 at 9:00 am to 2/20 at 9:00 am. The top line shows the top tiltmeter (#5548), then next shows the next tiltmeter down (#5550), etc. Periodic jumps by most tiltmeters in the array, several of which correlate with pumping times, are presumed to be a result of gas production in the well.

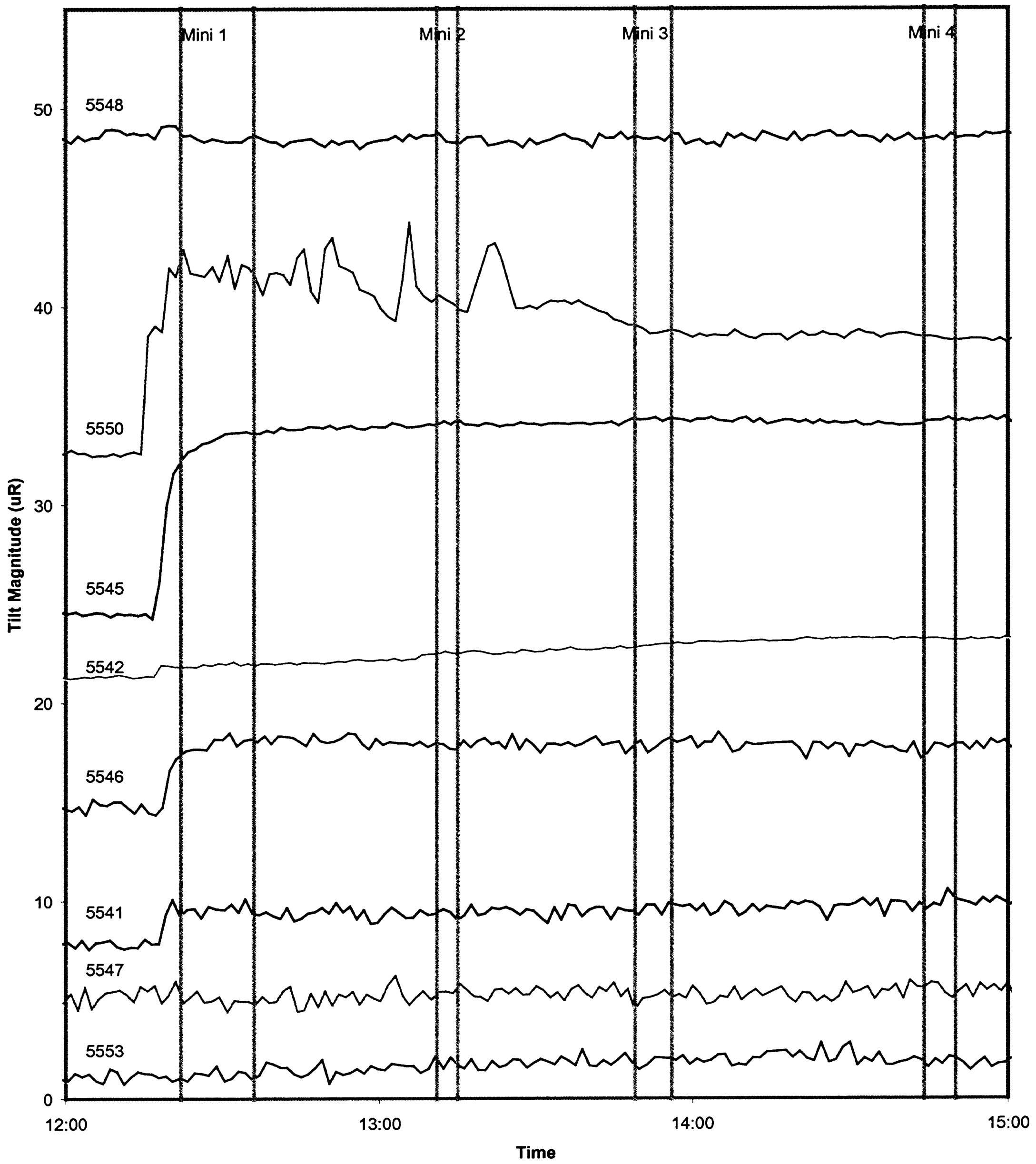

Figure 1.9-6. Tilt signals from all downhole tiltmeters for the 3 hour period from 2/23 at 12:00 pm to 3:00 pm. The top line shows the top tiltmeter (#5548), then next shows the next tiltmeter down (#5550), etc. Signal just prior to the first mini-frac is now presumed to be a result of gas production, not associated with the fracture treatment.

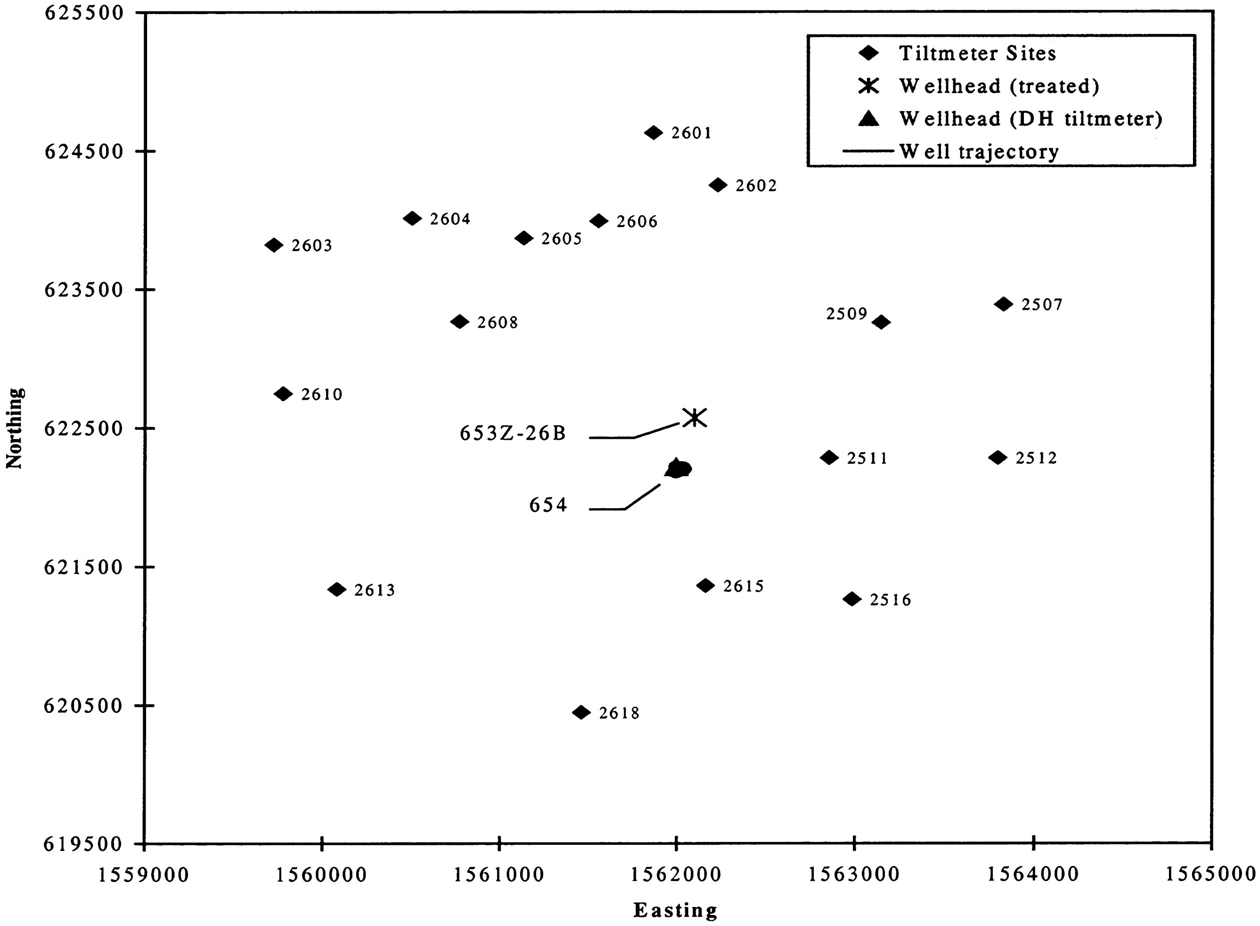
625500
624500
623500
622500
621500
620500
619500
Northing
1559000
1560000
1561000
1562000
1563000
1564000
1565000
Easting
◆ Tiltmeter Sites
✱ Wellhead (treated)
▲ Wellhead (DH tiltmeter)
—— Well trajectory
2601
2602
2603
2604
2605
2606
2608
2509
2507
2610
653Z-26B
654
2511
2512
2613
2615
2516
2618

Figure 1.9-7. Map view of surface tiltmeter sites in relation to wellhead locations for the treated well and the observation well for the downhole tiltmeter array.

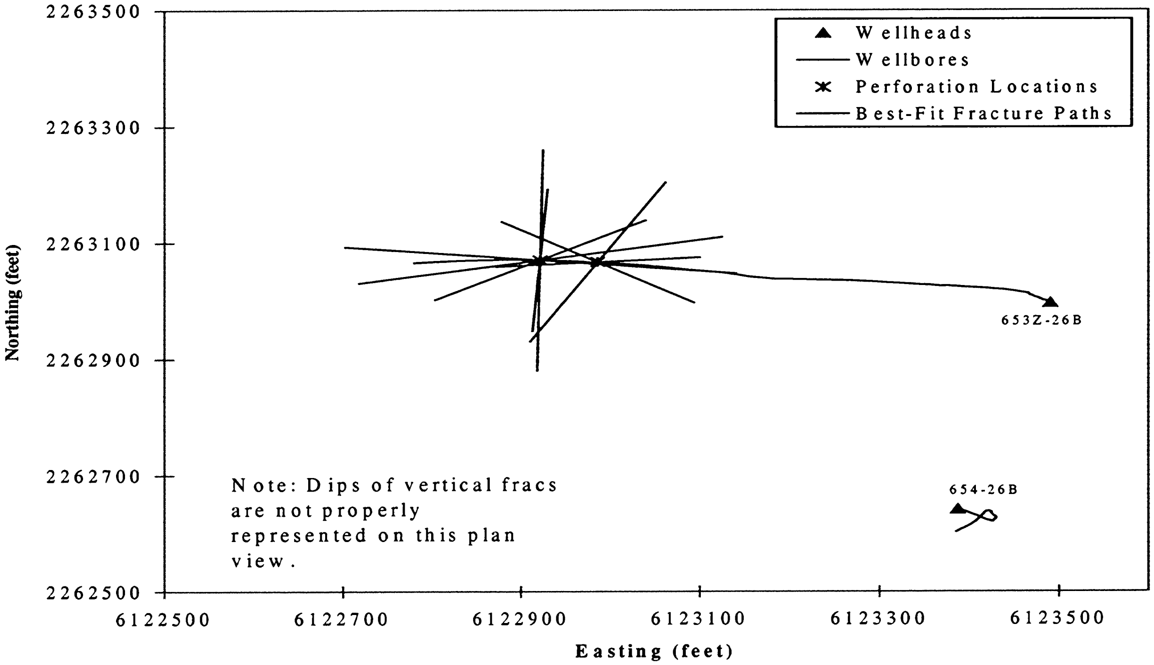

Figure 1.9-8. Plan view of fractures created during treatment of Well 653Z.

SECTION 2.

LOST HILLS TECHNICAL PROGRESS

2.1. GEOLOGIC OVERVIEW OF LOST HILLS FIELD

Lost Hills Field is located 40 miles northwest of Bakersfield, CA (Figure 2.1-1). The field was discovered in 1910. Productive intervals include Middle to Upper Miocene siliceous shales and diatomite, and Plio-Pleistocene sands.

The field is situated along a northwest-southeast trending series of structural highs that begins with the Coalinga Anticline to the northwest and culminates with the Lost Hills Anticline to the southeast. This series of highs roughly parallels folds of similar age on the westside of the San Joaquin Valley. These folds are oriented nearly parallel to the trend of the San Andreas Fault to the west and approximately perpendicular to the direction of regional compression.

Lost Hills oil is trapped at the crest and along the southeast plunge of the anticline (Figure 2.1-2 and 2.1-3). In this portion of the field where the pilot will be located (Figure 2.1-4), the structural plunge varies from 2 to 6 degrees toward the southeast. Dips along the northeast flank average around 30 degrees while those on the southwest flank average around 15 to 20 degrees. This asymmetry in dips in the NE_SW direction is consistent with a fault-bend folding model. This model predicts that structural growth of the Lost Hills Anticline was initiated during latest Miocene time and that the resulting anticline is perched above a ramp thrust that is located around 1300 feet below the surface. Numerous northeast-southwest trending normal faults with throws rarely exceeding 40 feet cut the Lost Hills structure. These faults do not appear to effect production.

The stratigraphy at Lost Hills is shown in Figures 2.1-5 and 2.1-6. The Monterey Formation is comprised of the Devilwater Shale, McLure Shale and Reef Ridge members. The Devilwater consists of shales and siliceous shales. It is slightly phosphatic. The McLure is subdivided into the McDonald Shale and the Antelope Shale. The McDonald consists of interbedded porcelanites and siliceous shales. It is also slightly phosphatic. The Antelope is comprised of finely laminated cherts and porcelanites. The uppermost member of the Monterey Formation is the Reef Ridge and it is subdivided into the Brown Shale and Belridge Diatomite. The Brown Shale is made up of interbedded siliceous shales, shales and silts. The Belridge Diatomite consists of interbedded diatomaceous mudstones, and fine-grained, argillaceous sandstones/siltstones.

Based on studies of late Miocene paleogeography and paleobathymetry, the rocks of the Monterey Formation were deposited in a deep marine environment. In the San Joaquin Basin, the late Miocene environment was such that: water depths were bathyal (between 600 and 3000 feet), cool water temperatures and upwelling in the upper 200 feet supported large diatom populations, and the deeper basin waters were oxygen poor. Two primary sedimentation processes were active in the basin at that time. First, hemipelagic sedimentation: the settling of diatom frustules and clay-sized particles onto the basin floor from the overlying water column. And second, turbidite sedimentation: the deposition of sand, silt, and clay-sized particles carried into the basin by density currents (usually originating along the basin margins).

This combination of environmental conditions and sedimentation processes led to the accumulation of thick deposits of organic-rich, laminated, diatomaceous sediments which occasionally are interrupted by thin-bedded, clastic-rich turbidite deposits. However, compared to the southwestern San Joaquin Basin, sandy turbidites at Lost Hills are not common. (The Monterey Formation in the San Joaquin Basin differs from the coastal and offshore Monterey in that it is much more clastic rich.)

The composition of the Monterey rocks can be described in terms of three primary components: 1) biogenic silica, 2) clay, and 3) silt/sand. As shown in Table 2.1-1, there is a fair amount of vertical compositional variation within the stratigraphic column at Lost Hills. The Devilwater contains 27% biogenic silica, 50% clay, and 23% silt/sand. The McDonald is slightly richer in biogenic silica, roughly comparable in clay, and a bit lower in silt/sand. The Antelope is very rich in biogenic silica, poor in clay, and poor in silt/sand. The Brown Shale is clay rich. The Belridge Diatomite has roughly equal amounts of biogenic silica, clay and silt/sand. The overlying Etchegoin Formation is rich in silt/sand and clay, and almost totally lacking in silica.

Table 2.1-1. Average rock compositions from Well 166, Section 32, T26S/R21E.

Rock Unit	**Average. % Biogenic Silica**	**Average % Clay**	**Average % Silt/Sand**	**Number of Samples**
Etchegoin	4	38	58	8
Belridge Diatomite	33	36	31	19
Brown Shale	26	47	27	28
Antelope Shale	61	18	21	14
McDonald Shale	34	47	19	24
Devilwater Shale	27	50	23	8

As hemipelagic and turbidite deposits built up in the Lost Hills area and were further buried by Etchegoin and Tulare sediments, the diatomaceous sediments of the Monterey Formation gradually lithified into the highly porous (50-60% or more) but impermeable (0.1-10.0 millidarcy) rock termed diatomite. As discussed above, anywhere from 26% to 61% of this diatomite was composed of diatom frustules. Diatom frustules consist of a form of silica called opal-A, which is an unstructured mineral (essentially a solidified gel) usually containing 3-10% water. As this diatomite is buried deeper and reaches greater temperatures (40-50 degrees C), the opal-A material in the diatom frustule becomes unstable and undergoes a phase transition to opal-CT (Figures 2.1-7 to 2.1-9). This form of silica is more structured than opal-A and has released much of its water. Porosity is reduced to ~40%. At still greater depths and higher temperatures (80-90 degrees C), the opal-CT undergoes a final phase transition to a form of quartz with only a trace of water left. The Monterey Formation at Lost Hills is presently comprised of opal-A rocks at shallow depths (± 2300 feet or shallower), opal-CT rocks at intermediate depths (±2300 to ± 4300 feet), and quartz phase rocks below ± 4300 feet.

The exact temperatures at which the opal-A to opal-CT and opal-CT to quartz phase changes occur is governed by the amount of biogenic silica (diatoms) in the rock. Opal-A rocks rich in biogenic silica convert to opal-CT at lower temperatures (and therefore shallower depths) than those poor in biogenic silica. Conversely, opal-CT rocks rich in biogenic silica convert to quartz phase at higher temperatures (and greater depths) than those poor in biogenic silica. For this reason, an interval of rocks whose laminations vary in their biogenic silica content create a transition zone of laminated phases near the phase transition temperature. The laminated phases in these transition zones (particularly where the laminae are thin) may be especially susceptible to natural fracturing, thereby enhancing system permeability. Also, volume reduction and water release associated with the phase changes probably adds to the fracturing in these zones. In general, hydrocarbons are found in all three (opal-A, opal-CT, and quartz) phases. Also production is enhanced in the opal-A to opal-CT and, in particular, the opal-CT to quartz phase transition zones.

Geochemical analyses have demonstrated that Monterey Formation rocks in Lost Hills are typically composed of 1% to 6% total organics, making them fair to good hydrocarbon source rocks. Studies of kerogen maturation have shown that the Monterey rocks are immature (i.e. they have not been buried deep enough to generate oil) within the confines of the Lost Hills Field. However, studies of samples taken from down-flank wells indicate that these rocks are mostly mature in the syncline to the east of Lost Hills and possibly below the ramp thrust immediately beneath the Lost Hills Anticline. Because the Monterey Formation kerogens and the produced oils at Lost Hills have similar isotopic compositions, and because they contain similar concentrations of sulfur, it is believed that Lost Hills oil was sourced from the Monterey Formation itself.

Hydrocarbons migrated into the low permeability Monterey rocks at Lost Hills by way of faults, fractures and thin sands. Also the opal-A to opal-CT and opal-CT to quartz phase transition zones with their higher fracture density probably served as pathways for hydrocarbons to migrate from source beds down-structure to their ultimate resting place in the crest of the anticline.

In the McDonald Shale and Lower Brown Shale/Antelope Shale pools, hydrocarbons are confined fairly well within or immediately below the fractured opal-CT to quartz phase transition rocks. In the Upper Brown Shale, minor fracturing also helps to make it productive. Because the McDonald, Antelope, and Brown shales have such low matrix permeability, most of the oil produced from these rocks comes out of the fractures. In the Belridge Diatomite with its relatively higher matrix permeability, hydrocarbons have saturated the uppermost opal-CT, the opal-A to opal-CT transition, and most of the opal-A rocks. Most of the oil produced from the diatomite comes from the matrix. Lastly, some oil has even migrated into the overlying Etchegoin and Tulare Formations.

The target reservoir for the CO_2 pilot in Lost Hills is the Belridge Diatomite (Figure 2.1-10). In the pilot area, the diatomite is in opal-A phase. The lower half of the Belridge Diatomite is comprised of approximately equal parts of biogenic silica (diatoms), silt/sand, and clay while the upper half is comprised mainly of silt/sand and clay. The diatomite is finely laminated. In general these laminations alternate between a more detritus rich lamina and a more diatomaceous rich lamina. The laminations reflect cyclic variations in yearly runoff (detritus rich) and upwelling (diatomaceous rich).

Superimposed on this depositional cycling are the changes in relative sea level that occurred in the Upper Miocene. As sea level rose, diatomaceous rich deposits were deposited further up on the slope. As sea level fell, sandy diatomite deposits prograded down the slope. These fluctuations in sea level caused the larger scale deposition of sedimentary packages of diatomite and sandy diatomite. The diatomites were deposited under oxygen poor to anoxic conditions that could sustain only a limited sediment-dwelling fauna. Thus laminations are preserved in the diatomites. Meanwhile sandy diatomites were deposited under oxygen poor to oxygenated conditions and are heavily bioturbated. Lastly, superimposed on the sea level changes was the overall progradation of the shelf, which resulted in the coarsening upward of the Belridge Diatomite, and the eventual filling in of the basin in the Pliocene.

As described above, the Belridge Diatomite is comprised of varying amounts of diatomaceous material, clay and silt/sand. In Lost Hills, the Belridge Diatomite ranges in depth from 800 to 3,000 feet. Oil gravity ranges from 28 to 18 degrees API. Although porosity is very high (40 - 65%), permeability is very low (<1 – 10 millidarcies). Oil saturation ranges from 40% to 65% in opal-A and from 10% to 30% in opal-CT (Table 2.1-2). There are over 2 billion barrels of oil in place in the Belridge Diatomite in Lost Hills. To date only 120 million barrels have been produced.

Table 2.1-2. Comparison of rock types at the newly proposed pilot location (Lost Hills) and the original location (Buena Vista Hills).

Parameter	**Lost Hills Pilot**	**Buena Vista Hills Pilot**
Rock Unit	Belridge Diatomite	Upper Antelope Shale
Age	Uppermost Miocene	Upper Miocene
Depositional Environment	Hemipelagic-Turbidite; Slope-Basin	Hemipelagic-Turbidite; Basin
Rock Type	Diatomaceous Mudstone	Siliceous Shale
Silica Phase	Opal-A	Opal-CT
Percent Sand Beds	30%	5%
Sand Description	5-60 feet thick, fine-grained, argillaceous, bioturbated	<1 inch thick, fine-grained, non-bioturbated
Depth to Top of Unit	1,400 feet	4,200 feet
Thickness	700 feet	600 feet
Porosity	50%	29%
Permeability	0.1 – 10.0 millidarcies	<0.1 millidarcies
Oil Saturation	50%	14%

Development of the Lost Hills Field has evolved over the years. From 1910 to the late 1970's, slotted liner completions were used in the upper Belridge Diatomite. From the late 1970's to 1987, small volume hydrofrac completions were performed covering the entire Belridge Diatomite. From 1987 to the present, high volume hydrofrac completions have been performed across the entire Belridge Diatomite and the Upper Brown Shale. Since 1992 a portion of the diatomite has been under waterflood, and in 1998 a pilot steam-drive was started. The Lost Hills Field is developed on a 5 acre (siliceous shale) to 1.25 acre (diatomite) well spacing.

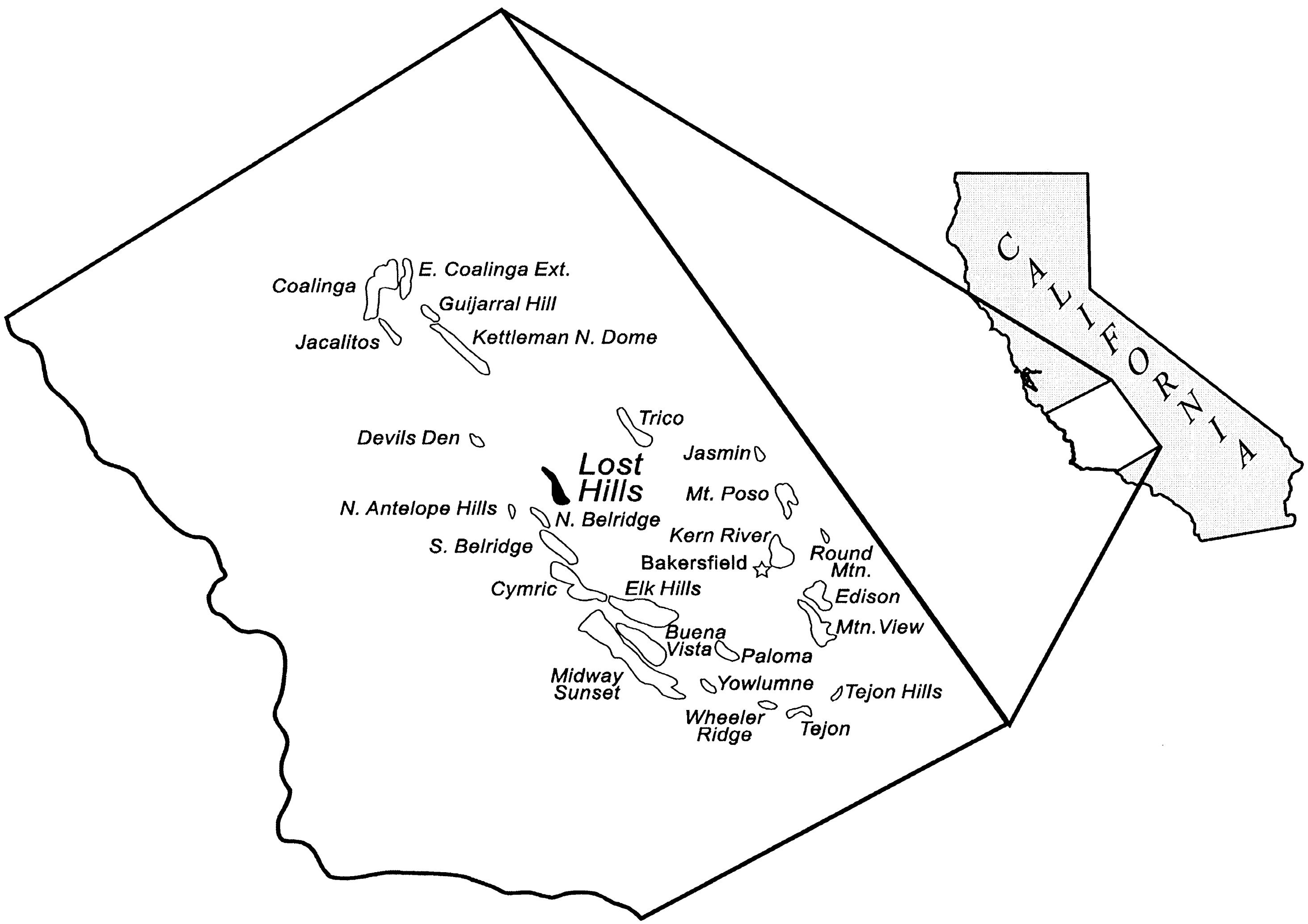
CALIFORNIA
Coalinga
E. Coalinga Ext.
Guijarral Hill
Jacalitos
Kettleman N. Dome
Trico
Devils Den
Jasmin
Lost Hills
Mt. Poso
N. Antelope Hills
N. Belridge
Kern River
S. Belridge
Round Mtn.
Bakersfield
Cymric
Elk Hills
Edison
Buena Vista
Mtn. View
Paloma
Midway Sunset
Yowlumne
Tejon Hills
Wheeler Ridge
Tejon

Figure 2.1-1. Location map of major oil fields in the southern San Joaquin Valley. Lost Hills Field is highlighted.

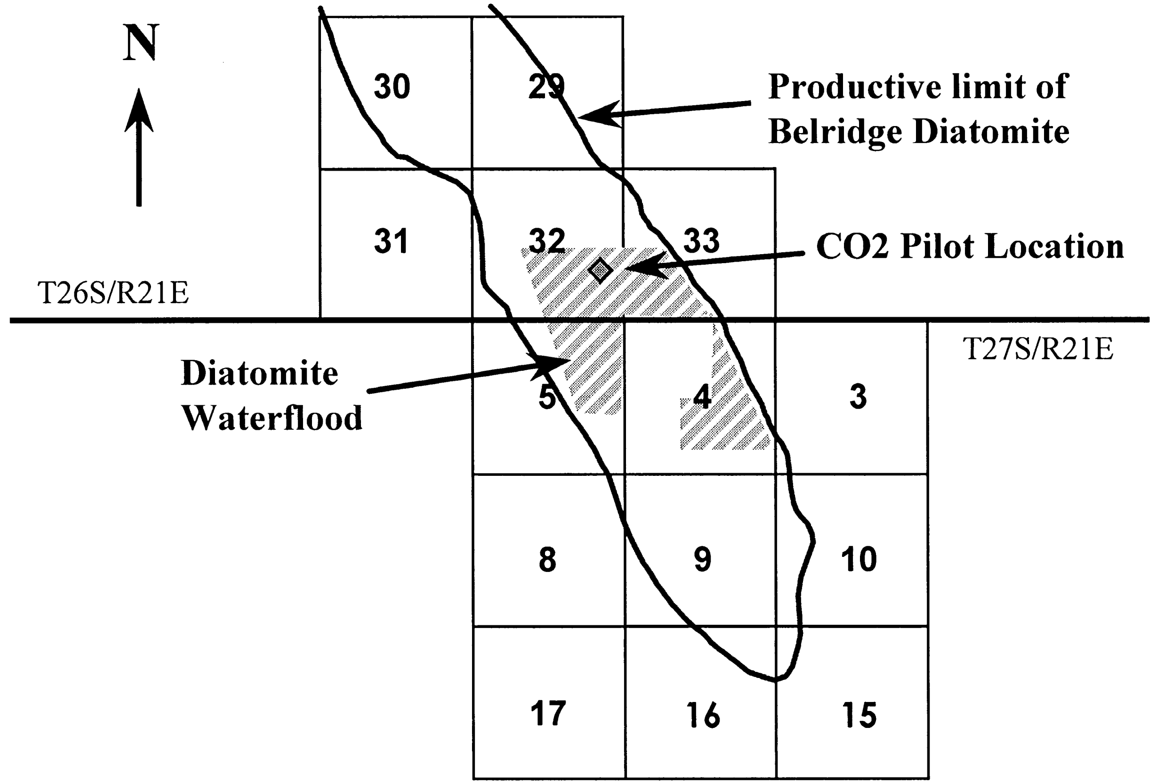
N
30
29
31
32
33
T26S/R21E
T27S/R21E
5
4
3
8
9
10
17
16
15
Productive limit of Belridge Diatomite
CO2 Pilot Location
Diatomite Waterflood

Figure 2.1-2. Productive limits of Belridge Diatomite follows trend of southeast plunge of the Lost Hills Anticline.

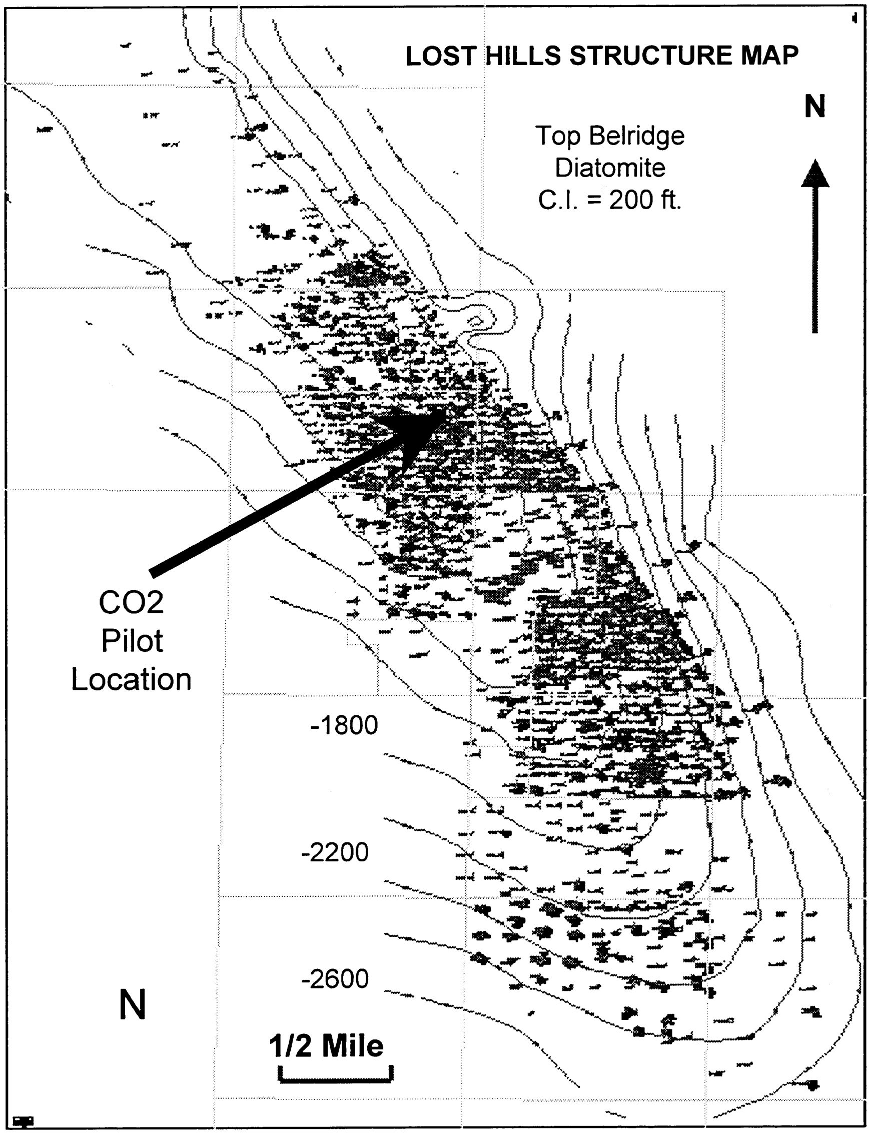
LOST HILLS STRUCTURE MAP
Top Belridge
Diatomite
C.I. = 200 ft.
N
CO2
Pilot
Location
-1800
-2200
-2600
N
1/2 Mile

Figure 2.1-3. Lost Hills top Belridge Diatomite structure map. Contour interval 200 feet.

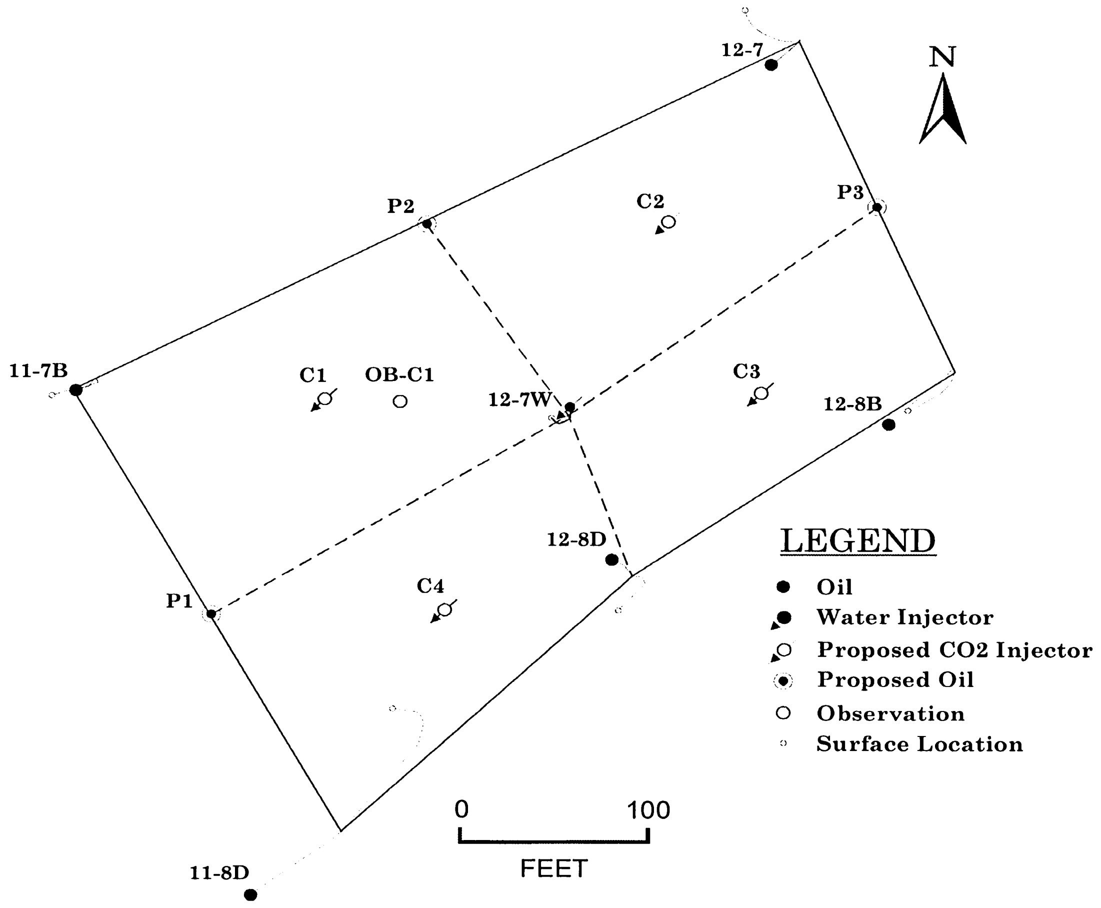
N
12-7
P2
C2
P3
11-7B
C1
OB-C1
12-7W
C3
12-8B
12-8D
P1
C4
11-8D
0
100
FEET
LEGEND
● Oil
Water Injector
Proposed CO2 Injector
Proposed Oil
○ Observation
Surface Location

Figure 2.1-4. Lost Hills CO_2 pilot base map. The planned CO_2 injectivity test on a non-hydraulically fractured well will be performed on well 12-8D. An injectivity test will also be performed on an existing hydraulically propped fractured well, 12-7W.

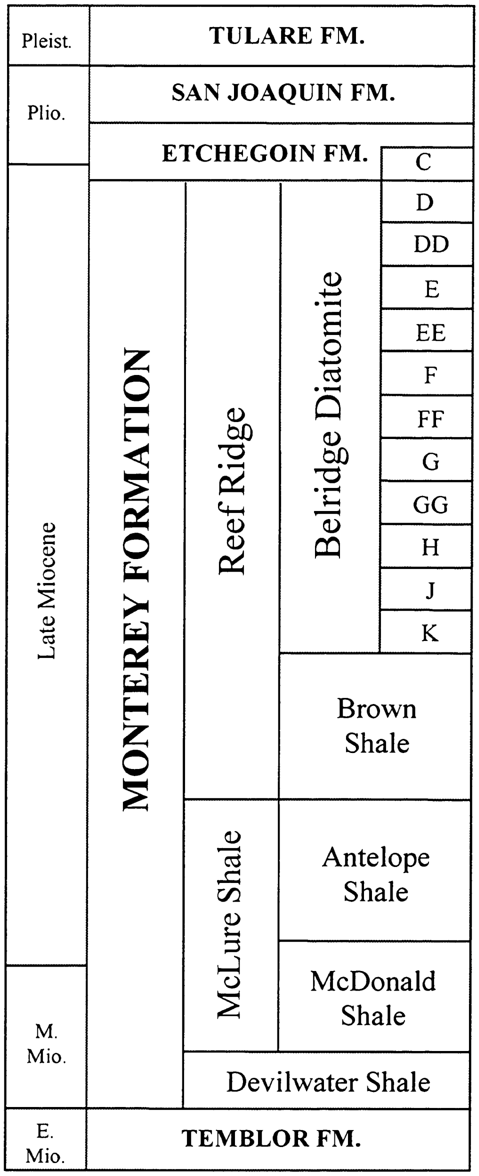
Pleist.
TULARE FM.
Plio.
SAN JOAQUIN FM.
ETCHEGOIN FM.
C
Late Miocene
MONTEREY FORMATION
Reef Ridge
Belridge Diatomite
D
DD
E
EE
F
FF
G
GG
H
J
K
Brown Shale
McLure Shale
Antelope Shale
M. Mio.
McDonald Shale
Devilwater Shale
E. Mio.
TEMBLOR FM.

Figure 2.1-5. Lost Hills stratigraphic column.

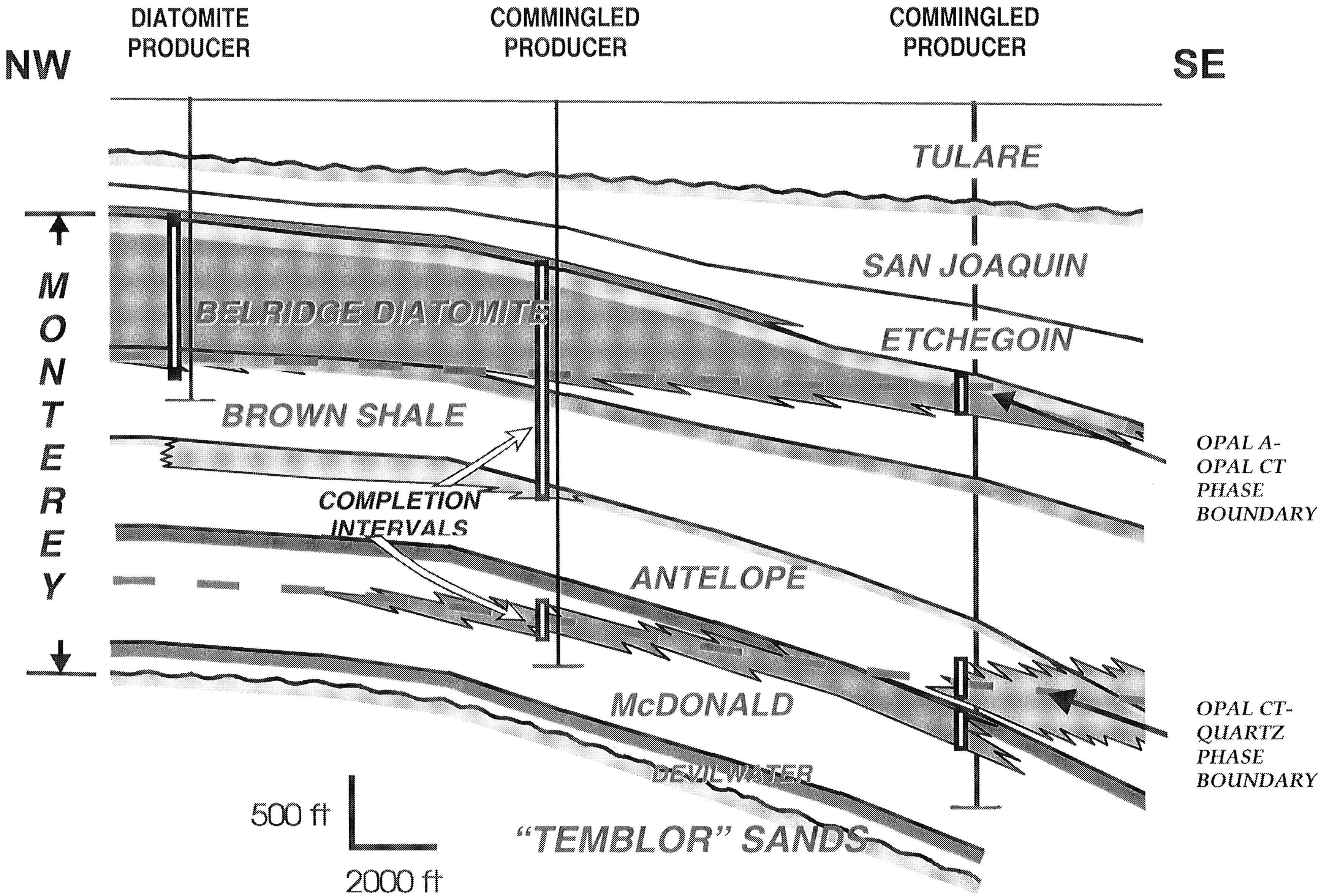
DIATOMITE PRODUCER
COMMINGLED PRODUCER
COMMINGLED PRODUCER
NW
SE
TULARE
SAN JOAQUIN
ETCHEGOIN
BELRIDGE DIATOMITE
BROWN SHALE
COMPLETION INTERVALS
ANTELOPE
McDONALD
DEVILWATER
"TEMBLOR" SANDS
MONTEREY
OPAL A-OPAL CT PHASE BOUNDARY
OPAL CT-QUARTZ PHASE BOUNDARY
500 ft
2000 ft

Figure 2.1-6. Generalized cross section along southeast plunge on Lost Hills. The Belridge Diatomite is the objective of the CO_2 pilot project.

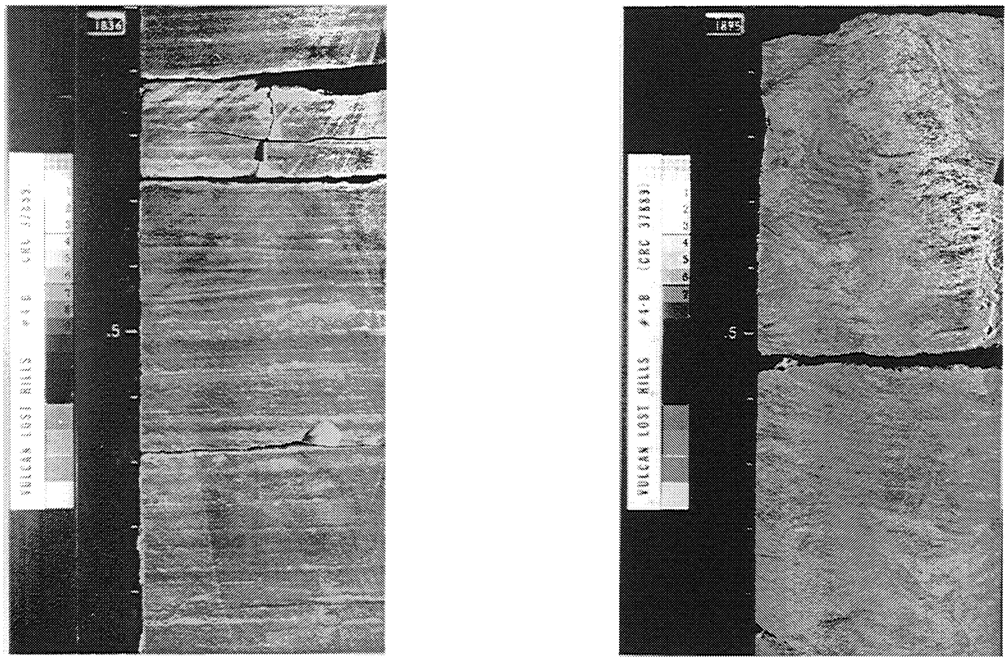
VULCAN LOST HILLS #1-8 (CRC 37835)
.5

Figure 2.1-7. Slabbed core of laminated diatomite (left), and bioturbated sandy diatomite (right).

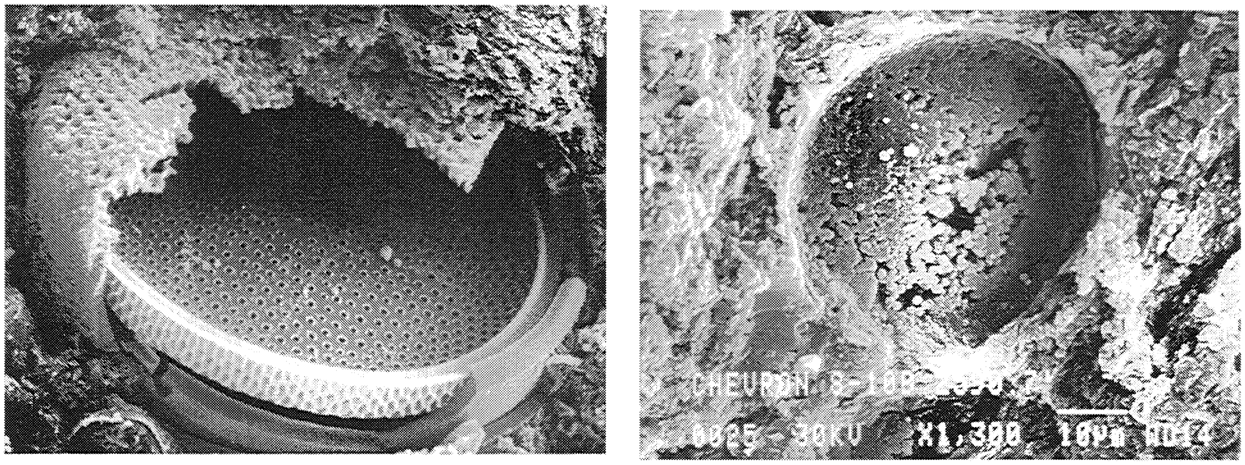
CHEVRON
0025 30KU X1,300 10µm

Figure 2.1-8. SEM photomicrographs of opal-A frustule starting to convert to opal-CT (left), and frustule converted to opal-CT (right). 1,300X magnification.

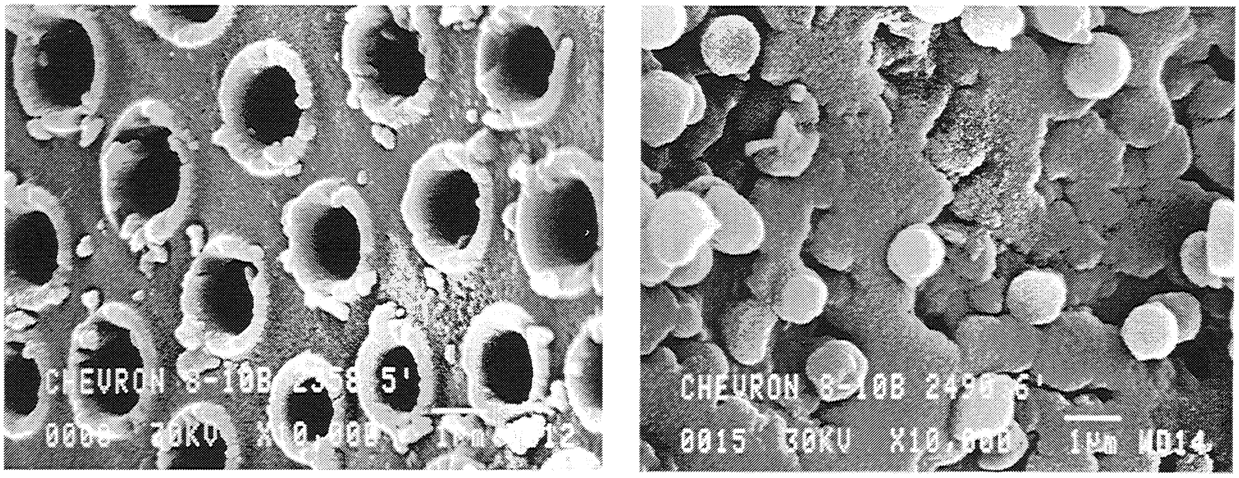
CHEVRON 8-10B 2358.5'
0000 20KV X10,000 1μm WD12
CHEVRON 8-10B 2490.6'
0015 30KV X10,000 1μm WD14

Figure 2.1-9. Opal-A frustule initiating conversion to opal-CT (left), and a frustule after its conversion to opal-CT. SEM photomicrographs, 10,000X magnification.

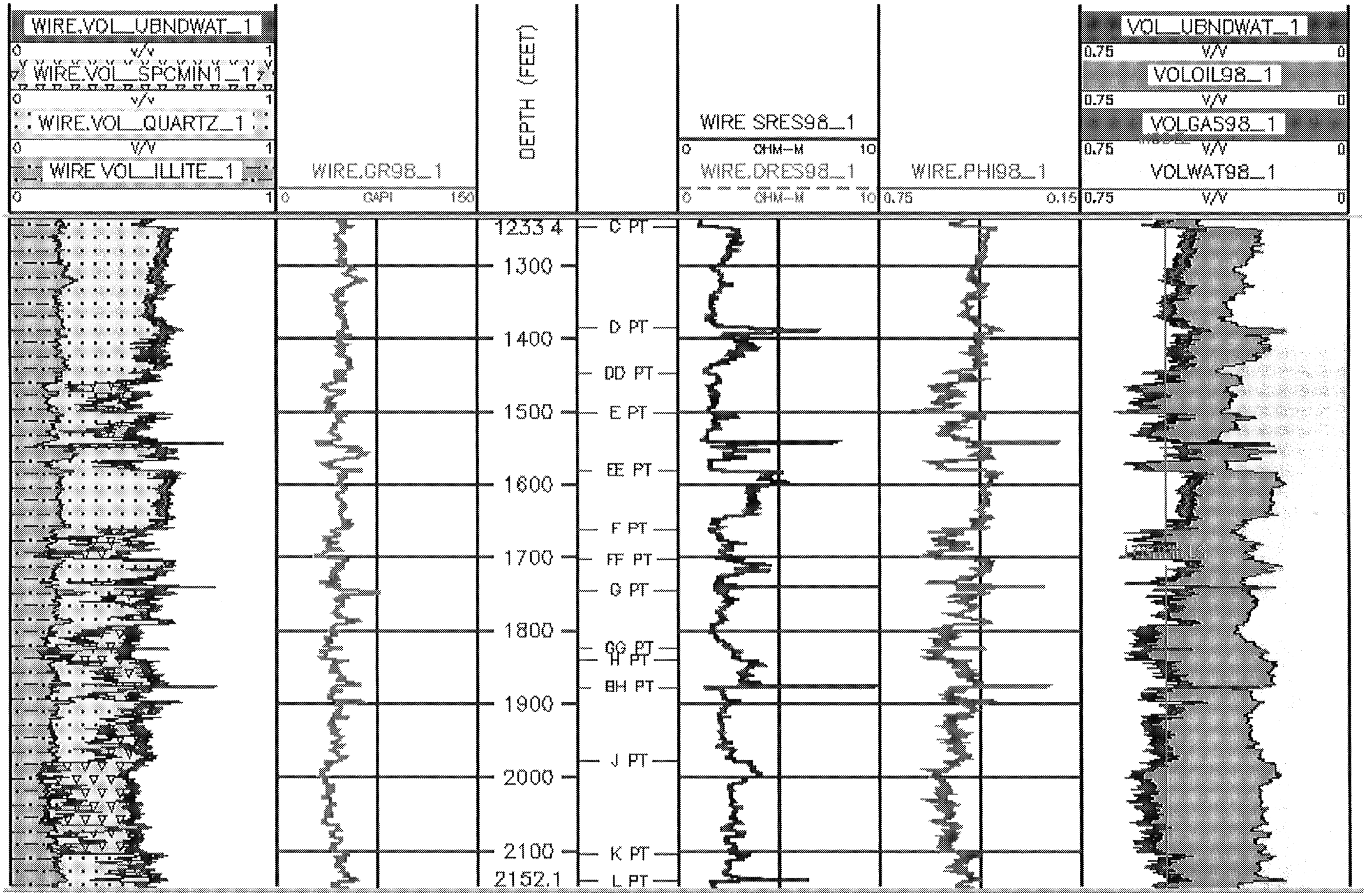

Figure 2.1-10. Type log (12-8D) of Belridge Diatomite in the Lost Hills pilot location. 12-8D will be used for injectivity test.

2.2. CO_2 INJECTIVITY TEST

Mark Emanuele

Chevron USA Production Company

A CO_2 injectivity test is planned for two separate wells located in the Lost Hills Field during the 1st quarter of 1999. The first of two wells to receive CO_2 injection will be a newly drilled well (Dec98), located in the Lost Hills Field. The well, 12-8D Sec 32, is located in an existing waterflood area. This injectivity test will take place in 3 separate lithology types that are typically targeted in both waterflood injection, and production wells. These 3 lithology types will be isolated and individually tested to determine CO_2 injection rates, pressures and profiles under non-hydraulic fracture conditions. Lastly, all lithologies will be commingled and a CO_2 injection test will be conducted to determine injection rates, pressures and profiles to try and determine potential thief and/or low injectivity zones.

Part two of the planned injectivity test will be conducted on an existing hydraulic propped fractured waterflood injector, 12-7W, Sec 32. This injectivity test will be performed on the well as it is currently configured, with all lithologies/zones open to injection. CO_2 injection rates, pressures and profiles will be obtained and compared those in the non-hydraulic propped fractured 12-8D well. Additionally, the injectivity data will also be compared to those data from the subject well during the previous 2 years of water injection.

CO_2 Injectivity Test Monitoring Plan

Aside from monitoring CO_2 injection rates, pressures and injection profiles as mentioned in the description of the injectivity test, additional monitoring will be employed in offset wells to determine what, if any impact CO_2 will make. The monitoring plan is briefly described below:

Injection well monitoring:

- Average CO_2 injection rate (mcf/day or tons/hr).
- Average surface CO_2 injection pressure (psi).
- Average surface CO_2 injection temp. (°F).
- CO_2 Injection profiles by lithology in well 12-8D and by commingled lithologies in well 12-7W.

Producers offset to injectivity test wells: (11-7B, 11-8D, 12-7, 12-8B)

- Daily production volumes (oil/water/gas) pre/during/post injectivity test.
- Oil viscosity samples pre/during/post injectivity test.
- Gas analysis pre/during/post.
- Production flowline (in-line) corrosion monitoring for CO_2.

2.3. LOST HILLS CO_2 PILOT

Pat Perri
Chevron USA Production Company

OVERVIEW

Chevron is proposing a 5/8 acre CO_2 pilot project. The 5/8 acre CO_2 pilot will utilize the current Lost Hills 2-1/2 acre waterflood pattern 12-7W. This 2-1/2 acre waterflood pattern will be converted to a 5/8 acre configuration by drilling four additional producers and four additional injectors as shown in Figure 2.3-1. One of the new producers, 12-8D was drilled in late 1998 and will be used for a CO_2 injectivity test. The remaining three new producers, shown as a circumscribed black circles in Figure 2.3-1 and labeled P1, P2, and P3, will be drilled half-way between the existing producers on the remaining three sides of the current 2-1/2 acre pattern. The center waterflood injector (12-7W) will then be converted to a producer. This thus creates four 5/8 acre patterns as indicated by the dashed lines in Figure 2.3-1. The four new CO_2 injectors, labeled as C1, C2, C3, and C4 in Figure 2.3-1, will be drilled in the center of each of the newly formed 5/8 acre patterns. This will result in one completely confined producer (well 12-7W). All producers will be hydraulically fractured.

It was assumed that the new CO_2 injectors would not have to be hydraulically fractured to meet design CO_2 injection rates. This assumption will be validated during the "un-fractured" testing phase of the CO_2 injectivity test. In addition to the new producers and injectors, an observation well (OB-C1) will also be drilled to monitor changes in oil saturation as CO_2 is injected into the formation.

The Lost Hills Diatomite resource is a unique reservoir and its unusual properties such as extremely small pore size (< 5 microns), high porosity (45 – 70%), and low permeability (<1 md) have led to historically, low primary oil recovery (3-4% of OOIP). Table 2.3-1 is a summary of the average reservoir properties of the proposed CO_2 pilot area. Due to the low primary recovery and large amount of remaining oil in place, Lost Hills presents a large target or resource for EOR.

Figure 2.3-2 shows a comparison of oil response for four different processes under consideration at Lost Hills on 2-1/2 acre well spacing:

- Primary Recovery (Hydraulically Fractured Wells)
- Waterflooding
- Steamflooding
- CO_2 Flooding

These forecasts were generated using Chevron in-house, proprietary reservoir simulation software known as *CHEARS® (CHevron Extended Application Reservoir Simulator).* In this section of the proposal, an overview of simulation results and pilot design will be discussed. More details on the construction of the simulation models including all the geological modeling, gridding, geostatitsics, and fluid properties can be found in the Lost Hills CO_2 Simulation section of this proposal. Analysis of Figure 2.3-2 shows that injecting water has some benefit in arresting the decline over primary depletion. Injecting steam has more or less the same benefit as water injection in arresting the primary decline. At this spacing, not enough steam is injected to improve steam recovery substantially over waterflooding. The one process that really stands out in Figure 2.3-2 is CO_2 flooding. Notice the tremendous oil response relative to the other three processes. The main reason for this is the large difference in CO_2 injectivity relative to the other injectants (water and steam) as shown in Figure 2.3-3.

The injectivity of CO_2 is shown to be at least two to three times greater than that of water or steam. Figure 2.3-4 shows a comparison of oil response for the four different processes (primary, waterflooding, steamflooding, and CO_2 flooding) under consideration at Lost Hills on 1-1/4 acre well spacing. Notice at the tighter well spacing, the improvement of the waterflood and steamflooding processes relative to the 2-1/2 acre case (Figure 2.3-2) in arresting the primary decline. In fact, at this well spacing, steamflooding shows a significant increase in oil response later in the life of the process. Although there is a marked improvement in the waterflooding and steamflooding processes at 1-1/4 acre spacing, these processes pale in comparison to the oil response for CO_2 flooding at 1-1/4 acre spacing. Again, note the substantially higher injectivity for CO_2 at 1-1/4 acre spacing as shown in Figure 2.3-5.

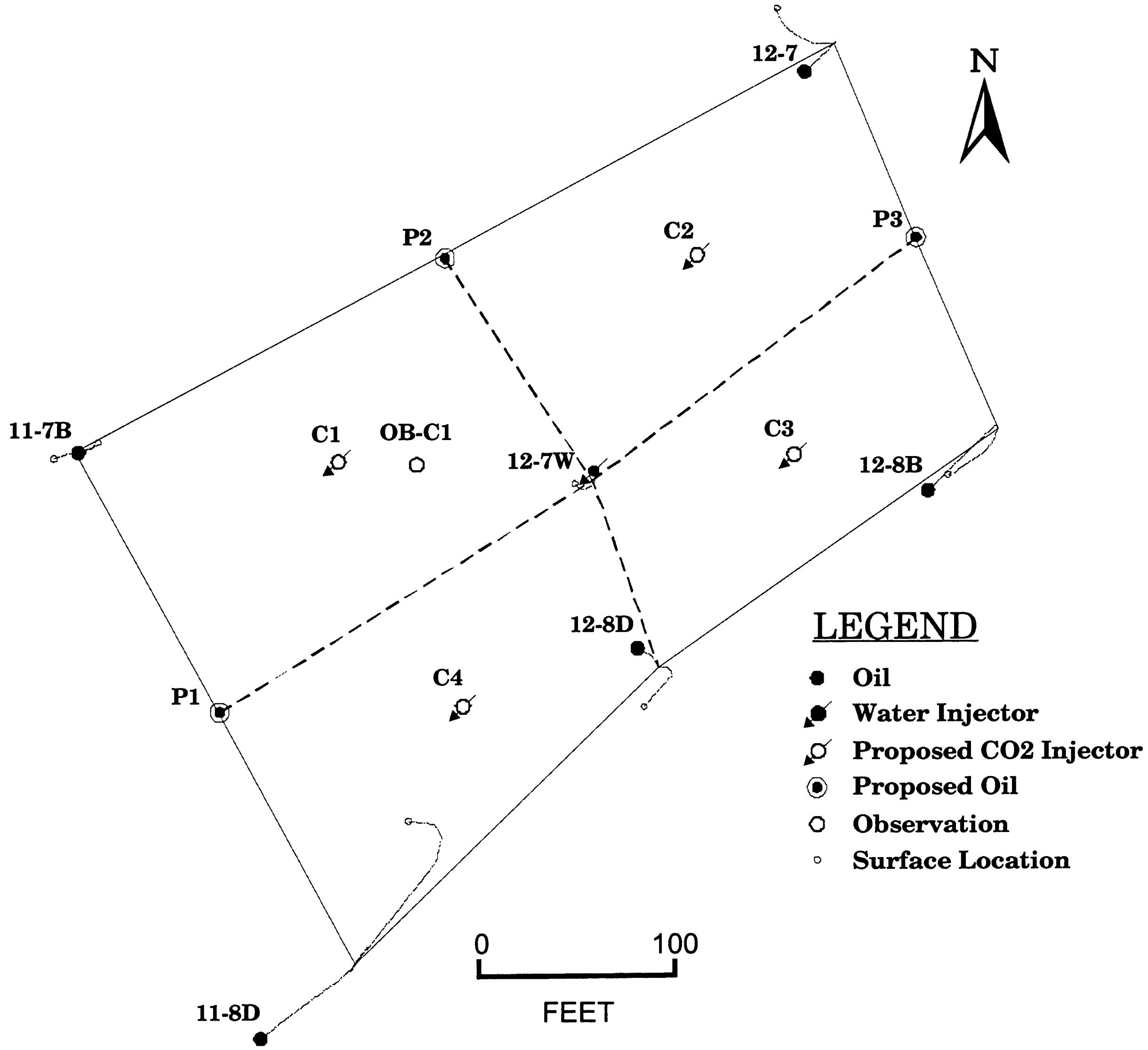
12-7
N
P2
C2
P3
11-7B
C1
OB-C1
12-7W
C3
12-8B
12-8D
LEGEND
Oil
Water Injector
Proposed CO2 Injector
Proposed Oil
Observation
Surface Location
P1
C4
0
100
FEET
11-8D

Figure 2.3-1. CO_2 pilot base map.

Table 2.3-1. Average reservoir properties for Lost Hills diatomite CO_2 pilot area.

Geologic Marker	Depth To Top		Average						
	VSS	Measured	Pressure (psig)	h (ft)	k (md)	ϕ (%)	S_o (%)	S_w (%)	S_g (%)
C Pt.	837	1233	149	139	1.16	43.7	33.4	61.6	5.0
D Pt.	976	1372	234	61	1.44	43.7	41.5	53.4	5.1
DD Pt.	1037	1433	280	79	1.44	52.8	42.2	52.7	5.1
E Pt.	1116	1512	347	48	1.22	51.8	40.3	54.4	5.3
EE Pt.	1164	1560	393	81	1.22	42.8	43.0	51.7	5.3
F Pt.	1245	1641	479	25	0.71	55.0	47.4	47.5	5.1
FF Pt.	1270	1666	507	33	0.71	46.9	45.2	49.7	5.1
G Pt.	1303	1699	547	80	0.47	51.8	46.1	49.0	4.9
GG Pt.	1383	1779	651	62	0.47	60.0	60.9	34.2	4.9
H Pt.	1445	1841	741	46	0.45	53.1	57.9	38.8	3.3
BH Pt.	1491	1887	812	77	0.45	52.2	47.8	48.9	3.3
J Pt.	1568	1964	941	54	0.28	60.0	62.0	37.2	0.8
K Pt.	1622	2018	1039	130	0.29	56.6	55.9	43.6	0.5
L Pt.	1752	2148	1303	100	0.29	51.0	41.1	58.4	0.5
Average	1301	1697	622	73	0.64	51.0	46.4	50.0	3.6
Total				1015					

Figures 2.3-6 and 2.3-7 show a comparison of oil response and injectivity, respectively, for the four different processes (primary, waterflooding, steamflooding, and CO_2 flooding) at 5/8 acre well spacing. Notice as well spacing gets even tighter, the continued improvement of the waterflood and steamflooding processes relative to the 2-1/2 acre case (Figure 2.3-2). In particular, steamdriving shows a substantial improvement as more heat can be injected into the reservoir since there are four times the injectors at 5/8 acre spacing as there are at 2-1/2 acre spacing. What remains to be seen however, is can these additional producers and injectors be economically justified. Although there is a marked improvement in the steamflooding processes at 5/8 acre spacing, CO_2 flooding stills shows the best performance of the four processes evaluated considering the peak of the oil response and the acceleration of recovery relative to the other processes.

It should be noted that although under the current pressure (300 psig to 1000 psig) and temperature ranges (105 – 120°F) for the Lost Hills diatomite, the CO_2 injection process will not be a miscible process (Minimum Miscibility Pressure, or MMP, is estimated to be in the range of 2500 – 3000 psig). Nevertheless, there is significant benefit in injection of CO_2 due to the viscosity reduction and fluid expansion of the reservoir oil under these partial miscibility conditions. In fact, the benefits of CO_2 injection are further demonstrated when comparing it with simply injecting hydrocarbon gas (e.g., methane) as shown in Figure 2.3-8.

The following is a summary of the conclusions reached based on simulation analysis of four processes (primary, waterflooding, steamflooding, and CO_2 flooding) at three different well spacings (2-1/2, 1-1/4, and 5/8 acre):

- Waterflooding does not show a "classical" peak response, only a lessening of the primary decline.
- Steamflooding does not show a significant response unless it is developed on 5/8 acre spacing.

- Of the 4 processes simulated, CO_2 flooding results in the quickest or most accelerated response.
- CO_2 injectivity is significantly higher than water and steam injectivity and is a major reason for the accelerated and higher oil rate response.

In addition, there are a number of other reasons why Lost Hills is a better target than Buena Vista Hills for CO_2 EOR relating to the following reservoir properties:

- Lost Hills reservoir temperature is cooler at 95 – 121°F compared to 160°F at Buena Vista Hills. This will improve the partial-miscibility of the crude oil with CO_2.
- Lost Hills is shallower so operating pressure will be lower.
- Lost Hills has about double the oil saturation and porosity compared to Buena Vista Hills. (See Table 2.3-1 for a summary of the reservoir properties of the proposed Lost Hills CO_2 pilot location).
- Lost Hills oil is heavier at 19 – 25 ^{O}API compared to the 25 - 33 ^{O}API at Buena Vista Hills, which will improve the partial-miscibility of the crude oil with CO_2.
- Lost Hills has much lower overall permeability due to the absence of thin sandstone layers in the targeted intervals.

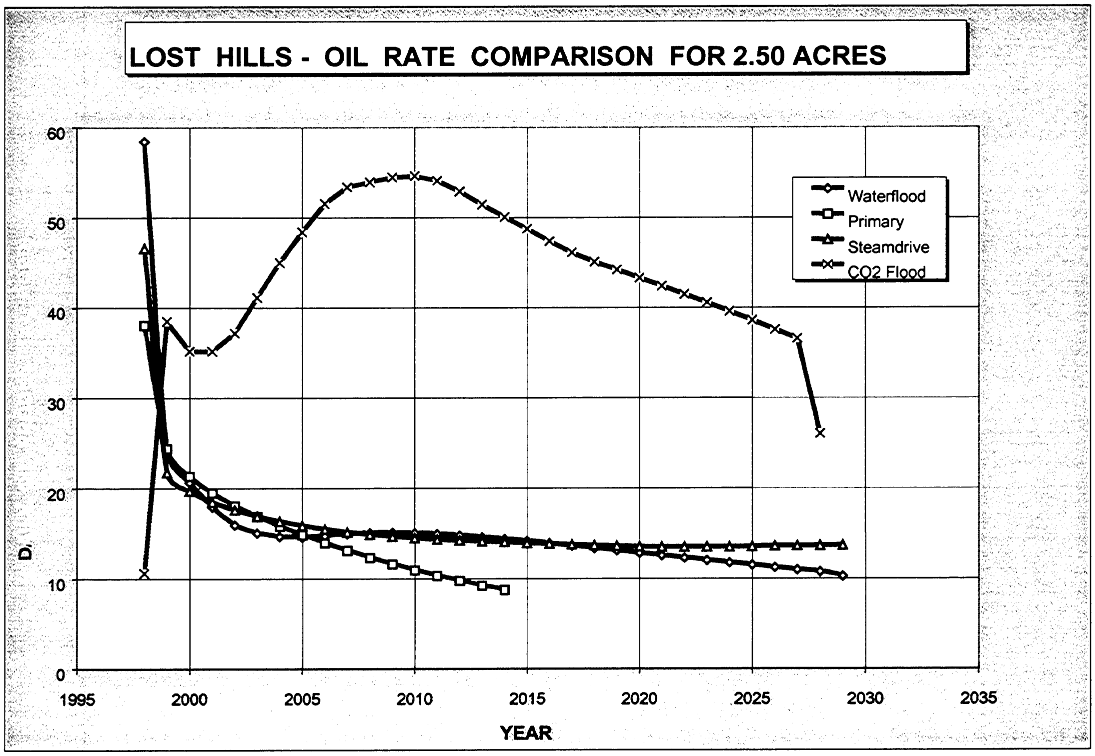

Figure 2.3-2. Oil rate comparison for various processes at 2-1/2 acre spacing.

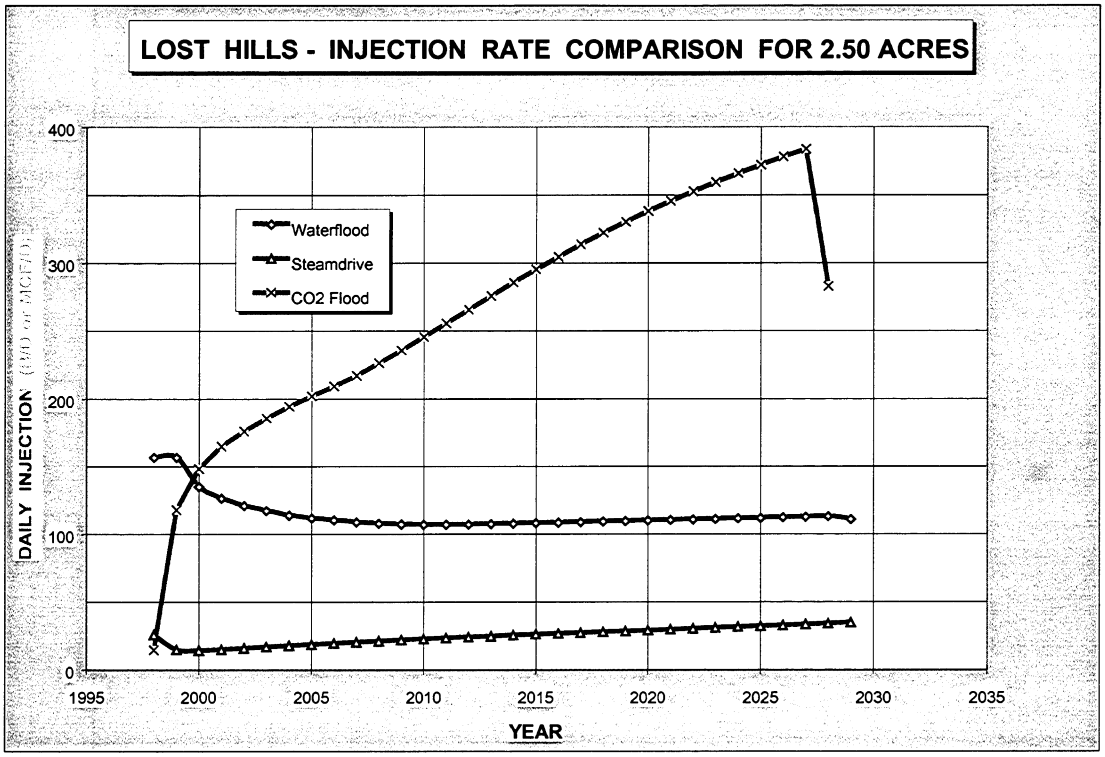

Figure 2.3-3. Injection rate comparison for various processes at 2-1/2 acre spacing.

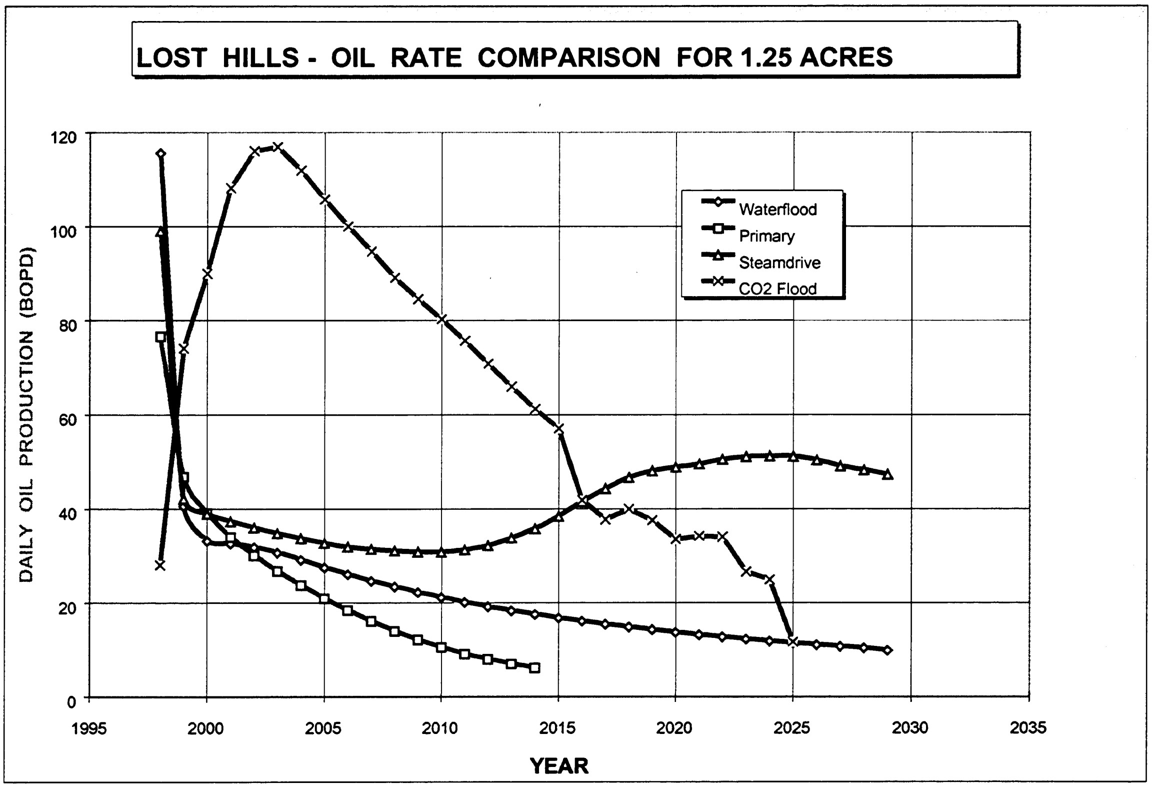

Figure 2.3-4. Oil rate comparison for various processes at 1-1/4 acre spacing.

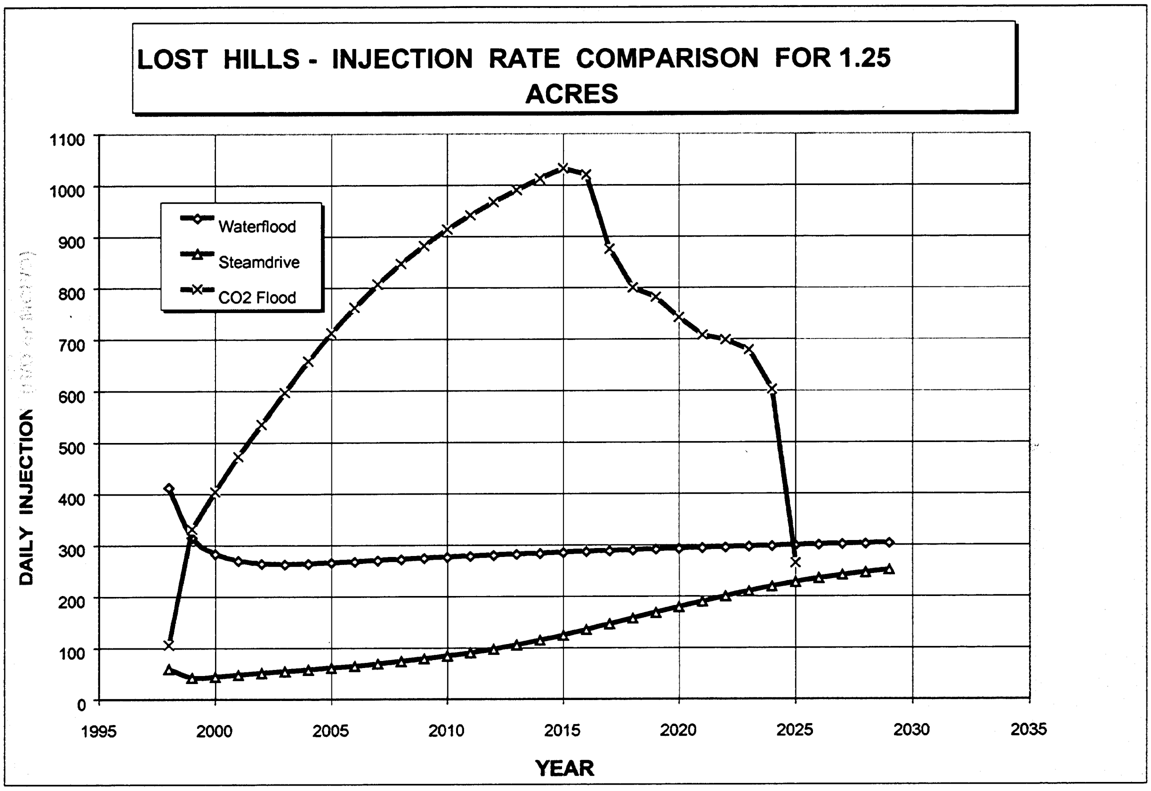

Figure 2.3-5. Injection rate comparison for various processes at 1-1/4 acre spacing.

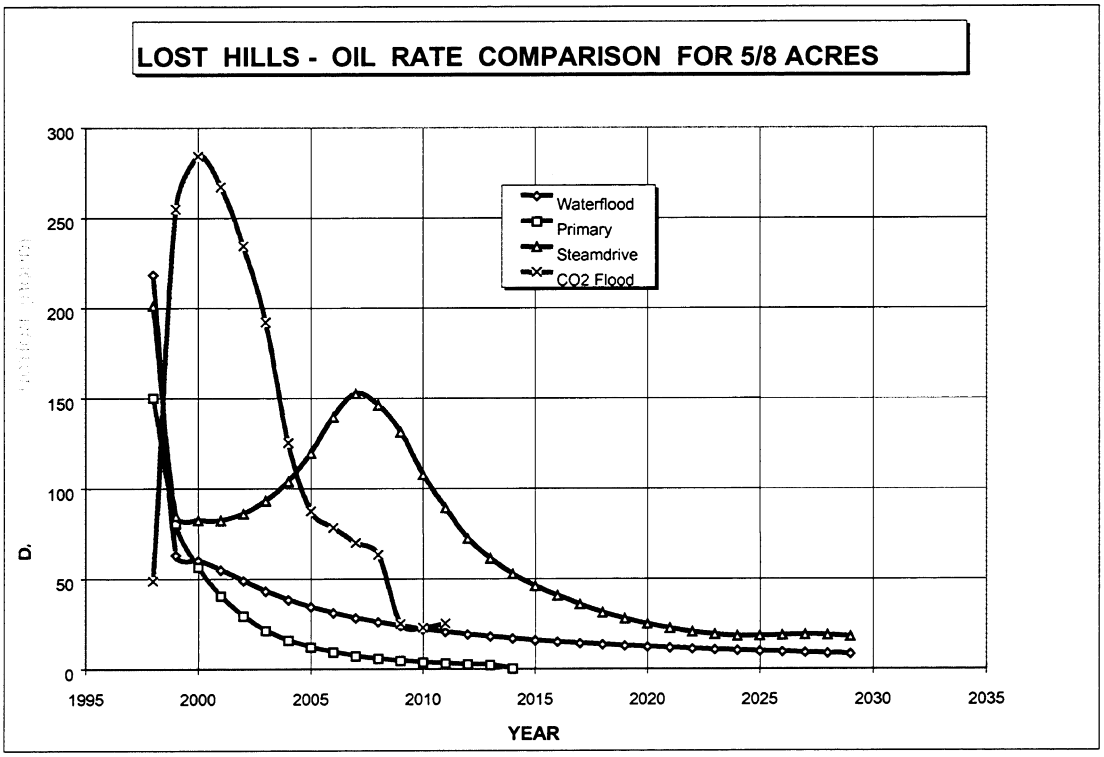

Figure 2.3-6. Oil rate comparison for various processes at 5/8 acre spacing.

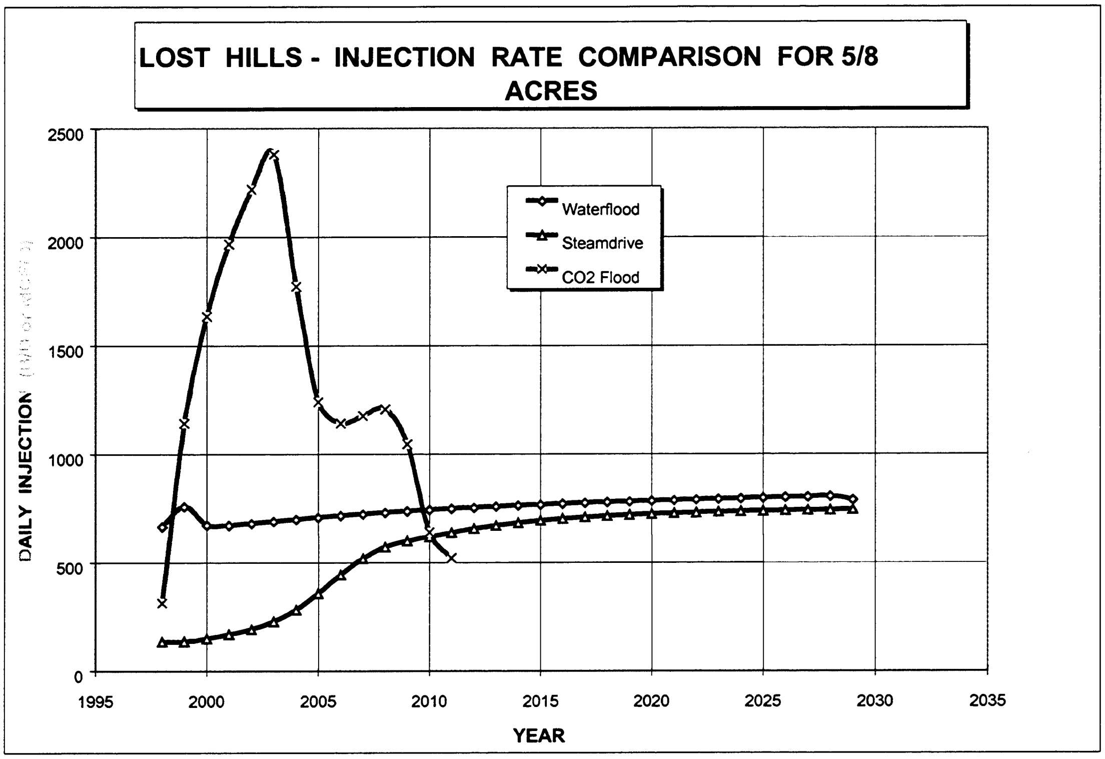

Figure 2.3-7. Injection rate comparison for various processes at 5/8 acre spacing.

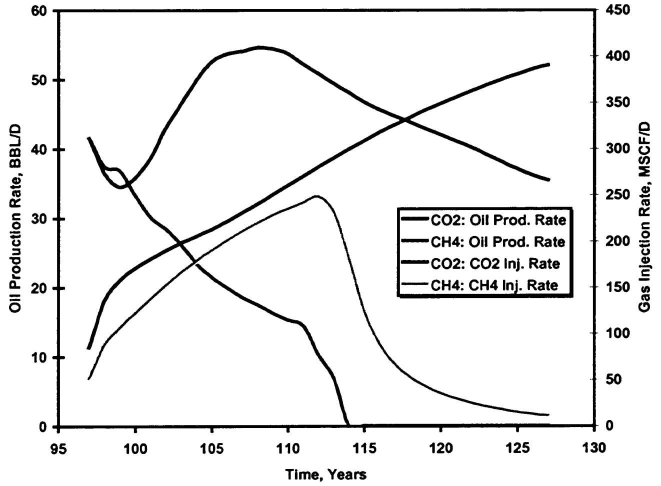

Figure 2.3-8. Comparison of CO_2 vs. CH_4 injection.

PILOT DESIGN

The proposed Lost Hills CO_2 Pilot was designed with the following goals and objectives in mind:

- Test the technical and economic viability of CO_2 flooding the low permeability Diatomite resource, which is one member of California's siliceous shale reservoirs of the Monterey Formation.
- Test the technical and economic viability of CO_2 flooding the Diatomite resource in a timely manner (3 years or less).
- Install a configuration that enhances the chance of process success (oil response).
- Provide an opportunity to gather and analyze reservoir, geologic, and production data and gather facilities design information necessary to commit to a full-field project.
- Install a CO_2 Pilot in Lost Hills safely, without incident, and in accordance with all county, state, and federal environmental rules and regulations.

Two separate pattern configurations were considered for the Lost Hills CO_2 Pilot design:

- 2-1/2 acre well spacing configuration
- 5/8 acre well spacing configuration

The 2-1/2 acre pattern configuration, shown as Figure 2.3-9, is the same configuration used in the existing Lost Hills Waterflood. This arrangement consists of 4 corner producers, with hydraulic fracture half-lengths of approximately 100 feet. The waterflood is configured as an inverted 5-spot with a water injector in the center of a 2-1/2 acre pattern. The waterflood injector is also hydraulically fractured. The current waterflood injector would be used as the CO_2 injector under this scenario. The 2-1/2 acre pattern is approximately 408' x 268' and aligned along the maximum horizontal stress direction of 45°-50° East of North. One observation well would also be utilized to monitor changes in oil saturation as CO_2 is injected into the formation.

The 5/8 acre pattern configuration starts with the current 2-1/2 acre waterflood configuration and is converted to a 5/8 acre configuration by drilling four additional producers and four additional injectors as shown in Figure 2.3-10. The four new producers, shown as squares in Figure 2.3-10, would be drilled half-way between the existing producers on all four side of a current 2-1/2 acre waterflood pattern. The center waterflood injector would then be converted into a producer (shown as a triangle in Figure 2.3-10). This thus creates four 5/8 acre patterns. The four new injectors, shown as stars in Figure 6-2, would be drilled in the center of the newly formed 5/8 acre patterns. The new CO_2 injectors are shown as being hydraulically fractured in Figure 2.3-10, but this may not be necessary if CO_2 injection rates are found to be adequate during the "un-fractured" testing phase of the CO_2 injectivity test. As in the 2-1/2 acre pilot design, an observation well would also be utilized to monitor changes in oil saturation as CO_2 is injected into the formation.

Figure 2.3-11 shows a comparison of oil response for a 2-1/2 acre CO_2 pilot design versus a 5/8 acre pilot design. These forecasts were generated using Chevron in-house, proprietary reservoir simulation software known as *CHEARS® (CHevron Extended Application Reservoir Simulator).* Similarly, Figure 2.3-12 shows a comparison of CO_2 injection requirements for a 2-1/2 acre CO_2 pilot design versus a 5/8 acre pilot design.

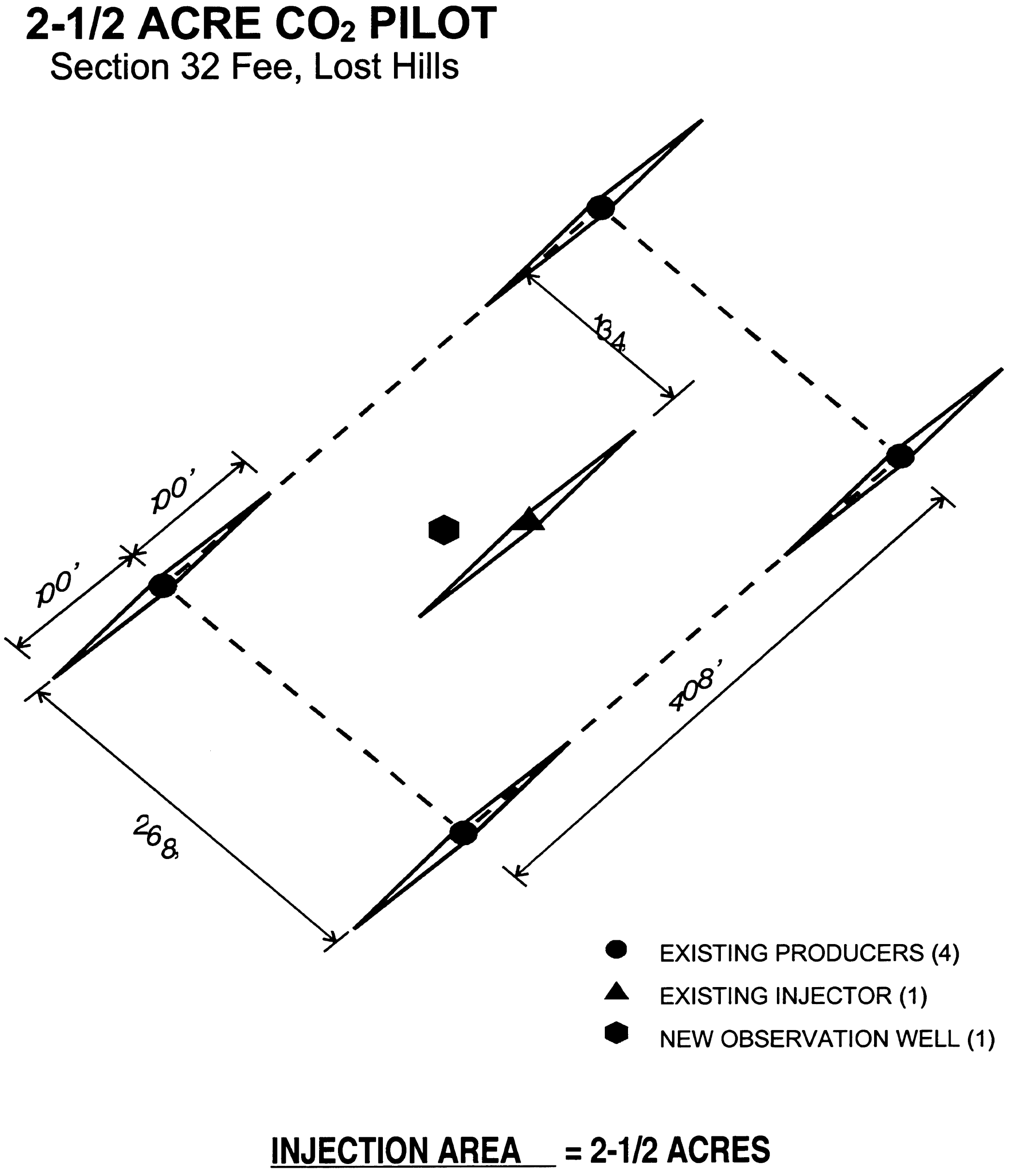
2-1/2 ACRE CO2 PILOT
Section 32 Fee, Lost Hills
134
100'
100'
268
408'
● EXISTING PRODUCERS (4)
▲ EXISTING INJECTOR (1)
⬢ NEW OBSERVATION WELL (1)
INJECTION AREA = 2-1/2 ACRES

Figure 2.3-9. 2-1/2 acre CO2 pilot.

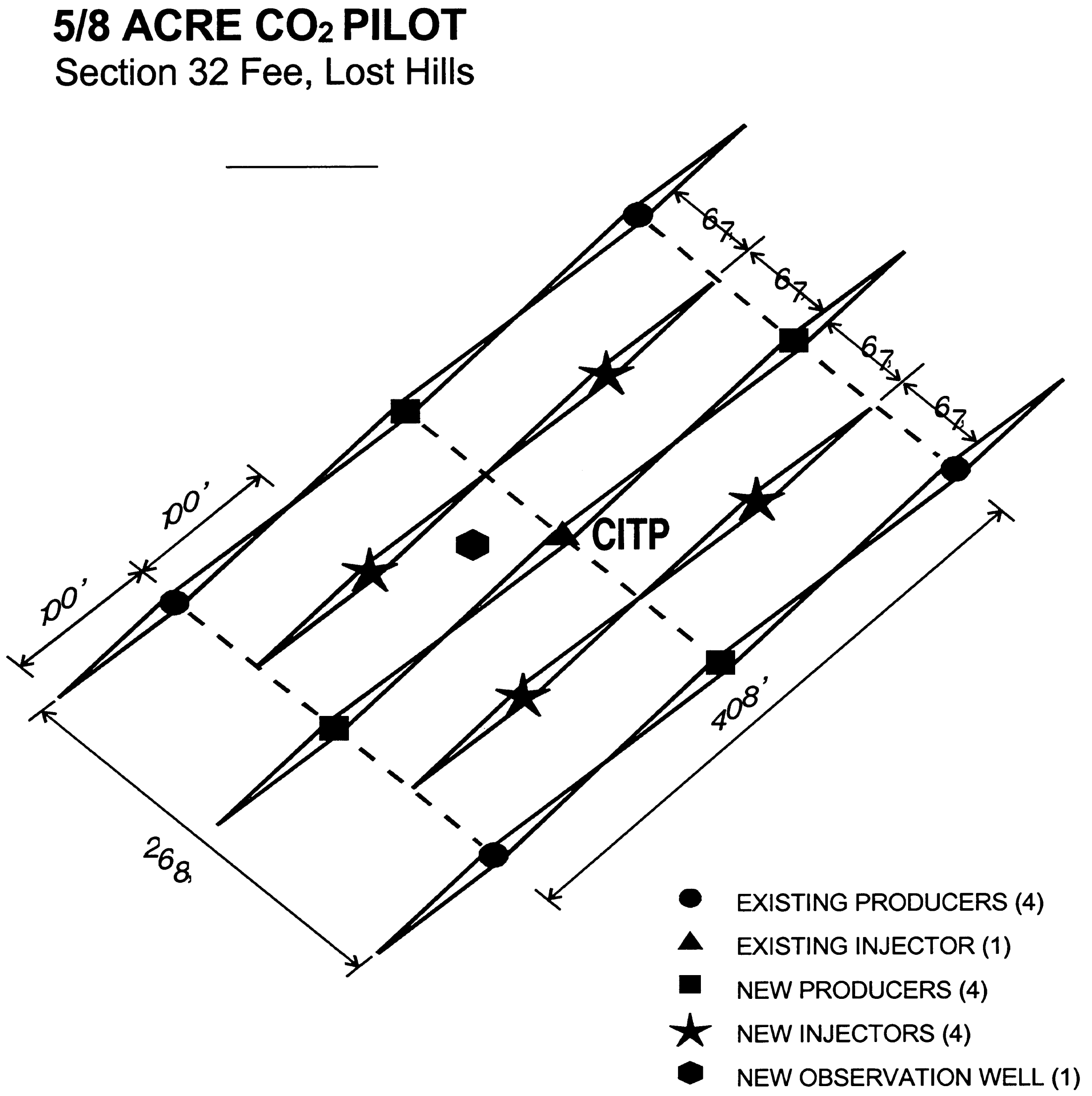
5/8 ACRE CO2 PILOT
Section 32 Fee, Lost Hills
61'
61'
61'
61'
100'
100'
CITP
408'
268'
● EXISTING PRODUCERS (4)
▲ EXISTING INJECTOR (1)
■ NEW PRODUCERS (4)
★ NEW INJECTORS (4)
⬢ NEW OBSERVATION WELL (1)

INJECTION AREA = 5/8 ACRES/PATTERN x 4 PATTERNS = 2-1/2 ACRES

Figure 2.3-10. 5/8 acre CO2 pilot.

Notice the dramatic difference in oil production response between the two design alternatives. The main reason for this is that under the 5/8 acre configuration you have 8 producers and 4 injectors (compared to 4 producers and 1 injectors for 2-1/2 acres) and the injector-to-producer fracture plane distance is reduced from 134 feet to 67 feet. Hence, CO_2 breaks through more quickly and the reservoir is processed more quickly. Also note the nature of the 2-1/2 acre oil response. It is characterized by a gradual increase over an extended period of time. This will make recognizing an actual oil response more difficult to discern and will increase the life of the pilot. It is estimated that pilot life for a 2-1/2 acre configuration (6 years) would be double that of the 5/8 acre pilot (3 years).

An important consideration when designing field pilots is the number of "confined" producers. A "confined" producer is a producing well that is surrounded by injector well when connecting the injectors with straight lines. This is very important considering the unfavorable CO_2 mobility ratio. Having a confined producer improves areal sweep and improves the chances of pilot success. Notice that under the 2-1/2 acre pilot configuration (Figure 2.3-9) there are no "confined" producers, while the 5/8 acre configuration does result in at least one confined producer.

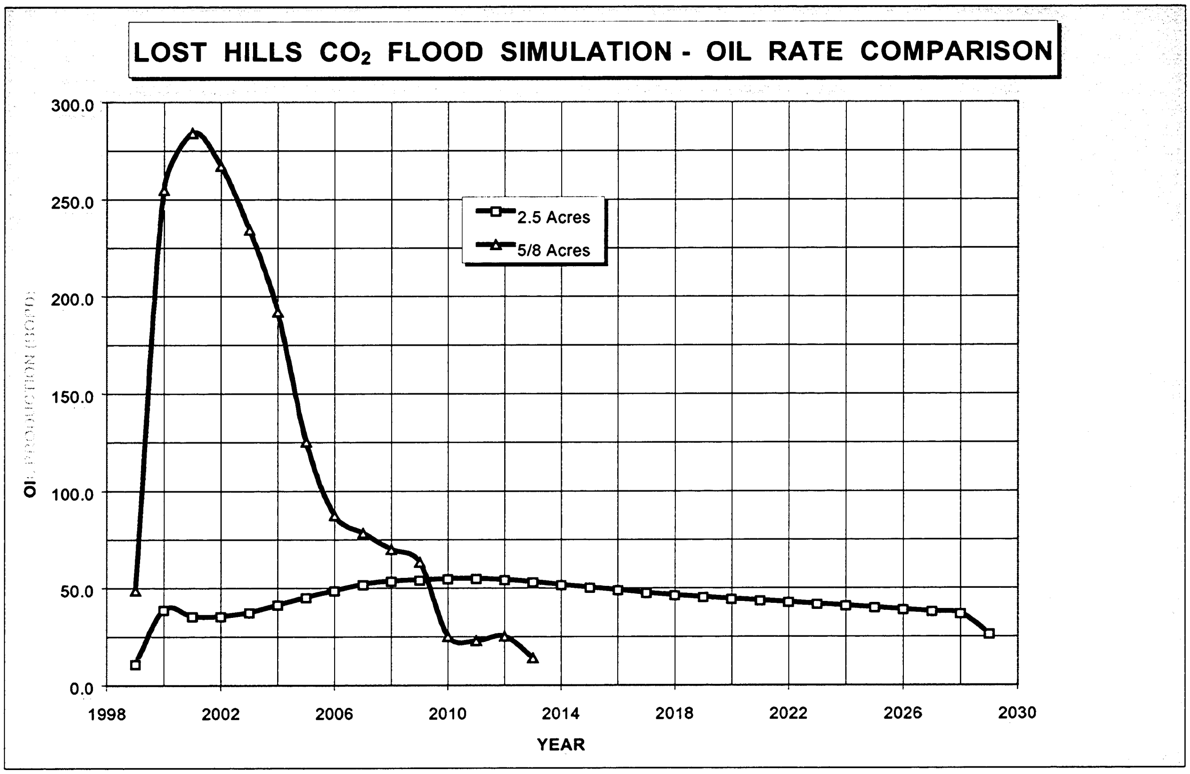

Figure 2.3-11. 2-1/2 acre vs. 5/8 acre simulation results (oil production).

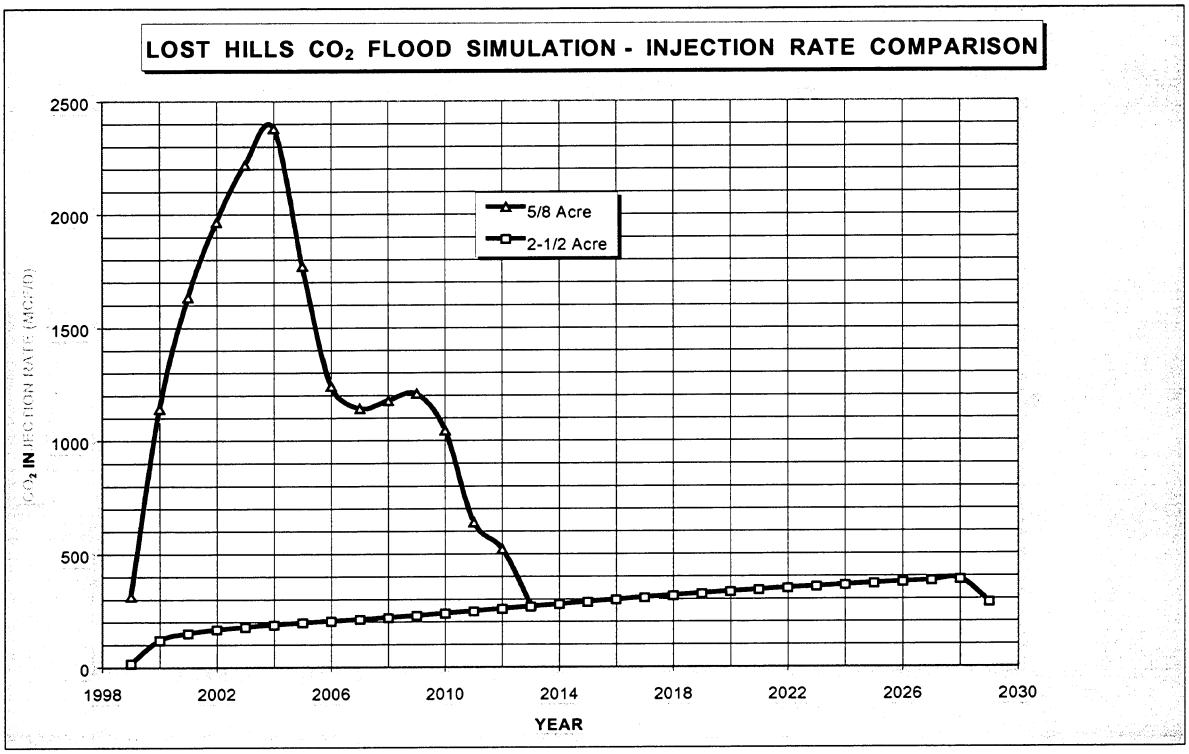

Figure 2.3-12. 2-1/2 acre vs. 5/8 acre simulation results (injection).

The following two tables (Tables 2.3-2 and 2.3-3) summarize the pros and cons for both the 2-1/2 acre pilot design and the 5/8 acre pilot design. The items that make the 5/8 acre pilot design more attractive are the accelerated and increased oil response and the increased probability of success with four injectors and one confined producer. Based on the foregoing analysis, the Lost Hills CO_2 Pilot Team recommends installing a 5/8 acre pilot. This will:

- Accelerate oil response
- Dramatically increase peak oil response
- Shorten pilot life.
- Confine one producer = increase probability of success
- Mature reserves in the shortest, feasible amount of time

Table 2.3-2. Pros and cons for 2-1/2 acre pilot design.

PROS	CONS
Less Expensive ($$$)	Oil Response Delayed
No New Wells	No Confined Producers
Piloting What Will Be Implemented	Injector To Producer Distance Greater
	Oil Response More Difficult To Decipher
	Longer Pilot Life (6 – 7 years)
	Pilot Objectives Delayed
	Catastrophic Breakthrough Destroys The Pilot

Table 2.3-3. Pros and cons for 5/8 acre pilot design.

PROS	CONS
Accelerated Oil Response	More Costly ($$$)
Higher/Larger Oil Response	Not Piloting What Will Be Implemented
One Confined Producer	Accelerated Breakthrough Potential
Injector To Producer Distance Reduced	Potential Hydraulic Fracture Communication
Four Additional Producers (8 Total)	Not Piloting What Will Be Implemented
Four Injectors	
Pilot Objectives Obtained Sooner	

2.4. LOST HILLS CO_2 SIMULATION STUDY

Ray Tang and Minhtrang Doan
Chevron Petroleum Technology Company

SUMMARY

This report presents the results of a 3D-pattern simulation study of Section 32 in the Lost Hills Field. The objective of the study was to estimate a range of recovery performance under various pattern configurations and strategies for CO_2 injection and then contrast this to the current field operation of waterflooding

Table 2.4-1 shows recovery ranges from the models. Acceleration impacts profitability substantially and Table 2.4-2 provides qualitative indicators in the number of years needed to achieve the different recoveries. The base case waterflood recovery at 2.5 acre spacing is estimated to be about 4% OOIP. We found Lost Hills waterflood infill potential, at about 3% OOIP per pattern size reduction similar to in-house and industry experience[1]. Estimated CO_2 recovery performance averages about 6% OOIP above that of waterflooding, less than the West Texas tertiary range of 7-17 %OOIP[2]. Lower recovery for Lost Hills is consistent with the fact that West Texas tertiary projects are miscible and Lost Hills is not.

Table 2.4-1. Summary of recovery efficiency ranges.

Pattern Size acres/pattern	Well spacing acres/well	WBG Case Number	Primary Recovery %OOIP	Post-1997 WF Recovery %OOIP	Post-1997 CO_2 Recovery %OOIP
2.5	1.25	4	4	4 - 9	7 - 19
1.25	0.625	5	NA	7 - 12	7 - 28
0.625	0.312	11	NA	11 - 15	8 - 18
2.5	0.833	12	NA	5 - 8	9 - 18
2.5	0.625	13	NA	5 - 8	11 - 20

Table 2.4-2. Estimated time required to achieve recovery.

Pattern Size acres/pattern	Well spacing acres/well	Waterflood project life, years	CO_2 project life avg. of runs, years
2.5	1.25	30	26
1.25	0.625	30	20
0.625	0.312	30	7
2.5	0.833	30	20
2.5	0.625	30	22

RESULTS AND CONCLUSIONS

1. The simulated primary depletion recovery from discovery to the start of water injection is 4% OOIP. Another 2-3% OOIP was recovered during early waterflood from 1990-1997.
2. Pre-1997 primary infill well and early waterflood (1990-1997) performance, GOR and WOR were used for history matching adjustments. The adjustments include permeability multipliers and relative permeability curvature. The “history matched” conditions at the end of 1997 was the basis for evaluating future waterflooding and CO_2 flooding strategies.

3. Simulated base case (2.5 acre patterns) waterflood recovery over 30 years post-1997 range from 4 to 9% OOIP.
4. Each stage of waterflood pattern size reduction from 2.5 to 1.25 to 0.625 acres is estimated to add about 3% OOIP reserves, about average of in-house and industry experience.
5. Simulated base case CO_2 recovery over 26 years range from 7-19% OOIP. The key sensitivities are maximum allowable bottomhole injection pressure and whether water-alternating-gas (WAG) is needed to control CO_2 breakthrough. WAG (water after gas) substantially reduces CO_2 injectivity.
6. The difference between CO_2 recovery and waterflood recovery averages about 6% OOIP for the different pattern sizes and sensitivities. The difference can be viewed as tertiary incremental for comparison purposes. West Texas tertiary miscible recovery range from 7-17 % OOIP. Spivak's analysis of the Wilmington Tar Zone (14°API) immiscible WAG project[3] suggested tertiary incremental of about 7% OOIP although the project deviated from original design and aborted after 3 years of injection. The Cymric Salt Creek (18.9°API) crestal gas injection project reviewed by Babson[4] showed total recovery of 46% OOIP. A more detailed review of comparable gas injection projects is presented later.

ASSUMPTIONS AND SENSITIVITIES

1. Waterflood simulations assume free imbibition endpoints. Because free imbibition results in significantly higher residual oil saturations, results here show substantially lower incremental waterflood recovery compared with previous simulations. Prior studies assumed that low residual oil saturations obtained from high pressure (typically 1000 psi/ft) gradient experiments are directly applicable in simulations. Free imbibition end-points appears to give more reasonable comparisons to field response; however, the validity of using either free or forced imbibition data or some combination is still ambiguous given our current understanding of the reservoir.
2. Sensitivity runs indicate that injectivity is the dominant factor influencing recovery performance. Factors impacting injectivity, in order of importance, are as follows:
    - Injection interval - base case assumes injection confined to F-L interval. Sensitivities include D-L and C-L injection (also E-L for some CO_2 cases).
    - Fracture length - base case assumes 50 feet half-lengths. Sensitivities include 25 and 90 feet half-lengths.
    - Spacing – base case is 2.5 acre patterns as in current waterflood operations (see Table 7-1 for sensitivities).
    - Operating pressures – all runs assume maximum injection pressure of 1200 psia and minimum producing pressure of 45 psia; both referenced to the C-point.
3. Two relative permeability data sets were used as sensitivities on waterflood response. Data from 12-10 (Terra Tek) and 8-4B (Corey correlation) were adjusted to depletion performance. The adjusted 12-10 data is more restrictive to flow compared to the adjusted 8-4B data.
4. CO_2 simulations were performed with the compositional option in *CHEARS® (CHevron Extended Application Reservoir Simulator).* The CO_2 models were restarted from saturation and pressure distributions from the waterflood model at 1997, with the 12-10 relative permeability data. One gas-oil relative permeability sensitivity case was based on mercury injection data.

5. The CO_2–oil system was represented by a 6-component characterization of a 21.6°API sample. The equation-of-state model is the same as the one used in a previous Chevron (1989-91) CO_2 study, which was calibrated to measurements of oil-CO_2 mixtures.
6. Correlations of bulk density and liquid-permeability data from the 8-4B core analysis were used to construct the *GOCAD/G2* (Chevron's in-house geostatistical modeling software) model.
7. The base case model was used to screen the impact of oil property variations on waterflood response. The results indicate that oil property variation probably has a very significant effect on performance behavior, and probably deserves more robust assessment.

SPECIFICATIONS AND PROCEDURES

The following listing provides a brief outline of the study's procedure:

1. The various CO_2 flooding scenarios evaluated are presented in Figure 2.4-1.
2. The findings of Gould and Munoz[5] in their parametric infill drilling study served as guidelines for gridding. The grid also accommodated hydraulic fractures at all wells.
3. A detailed *GOCAD/G2* model covering an area of about 27 acres was generated from existing (9/97) well log database from Central Lost Hills. The Section 32 model was populated by a transform developed from 8-4B core data. Initial saturation is based on the Archie equation algorithm.
4. A 2.5 acre sector of the *GOCAD/G2* model was extracted to simulate primary depletion performance followed by waterflooding.
5. Reservoir properties including PVT and relative permeability were inherited from the most recent *CHEARS* simulation studies. Rock compressibility was updated with the most recent data.
6. The initial pressure distribution estimated from available pressure transient and RFT data.
7. Pre-1998 production data were used to calibrate the model. The key parameters for calibration were pressures, primary recovery, WOR and GOR behavior during the early waterflood. Global permeability multipliers and relative permeability curve shapes were adjusted to match both WOR and GOR. The 12-10 oil curve (K_{ro}-K_{rg} data) was lowered to match GOR and WOR behavior.
8. Hydraulic fractures were added to the model for waterflood predictions and various sensitivities were simulated.
9. Saturation and pressures distribution at the end of 1997 were used as initial conditions for compositional modeling of CO_2 injection which were performed using the same grid and the same constraints as for the waterflood simulations.
10. The compositional fluid characterization of the reservoir oil was developed using Chevron's in-house fluid modeling software called *CPCP (Chevron Phase Calculation Program).* The equation-of-state (EOS) model consisted of 6 components and is the same one used in a previous (1989-91) Lost Hills study. The EOS model was tuned to CO_2-oil mixture measurements collected for the 1989-91 CO_2 studies on a 21.6°API sample.
11. Additional EOS characterizations for 25°API and 31°API oils were provided by adjusting the 21.5°API EOS and a Buena Vista Hills 34°API EOS. The additional EOS was treated as sensitivities for CO_2 injection for cases 4 and 5.

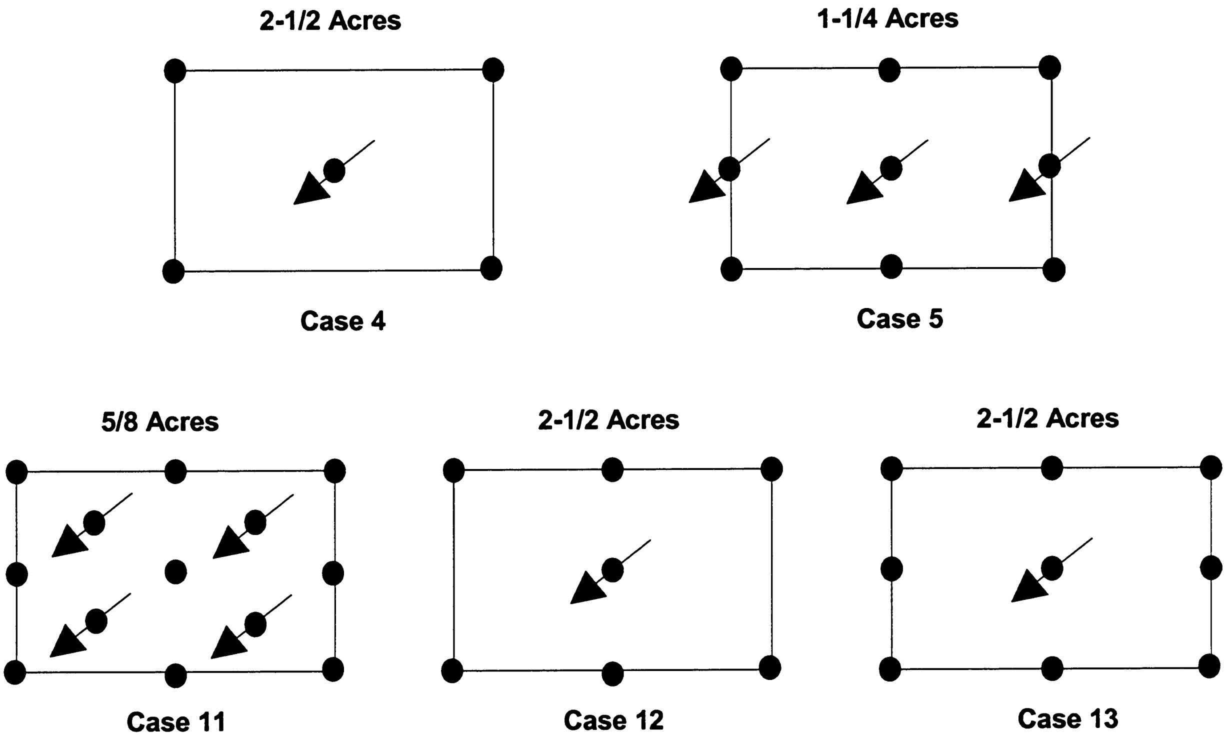

Figure 2.4-1: Five prediction CO_2 configuration scenarios.

GEOSTATISTICAL MODELING PROCEDURE

A 149x149x245 (5.5 million cells) detailed geologic model was created for Section 32 using G2/Gocad++. The model covered approximately 27 acres and included *XPERM*, *POROSITY*, and *SWIR* values for each cell.

SIMULATION MODEL CONSTRUCTION

Extract 2.5 Acre Model from Gocad/G2

The next step in the simulation study was to extract a single 3D pattern model from the central part of the original 5.5 million cell GOCAD model. This single pattern was used to estimate the waterflood behavior of Section 32. GOCAD++ Sgrid Builder option was used to define the size of the 2.5 acre pattern Sgrid, as shown in Figure 2.4-2 below. The pattern model was oriented 55 degrees Northeast (35 degrees counter-clockwise to the east) to coincide with interpreted orientations of vertical fractures in Section 32. After the structure of the pattern Sgrid was created, the Fill Point Wise option was used to copy the *XPERM*, *POROSITY* and *SWIR* values from the nearest 5.5 million cells Sgrid to the pattern model. The pattern Sgrid is (60 x 40 x 245 layers) covering a 408 ft x 268 ft and 920 ft thick portion of the larger Sgrid. The pattern Sgrid has typical DX values of 6.8 ft and DY of 6.7 ft. Figure 2.4-3 shows water saturation cubes of the original 27 acre model and the 2.5 acre pattern model that was extracted.

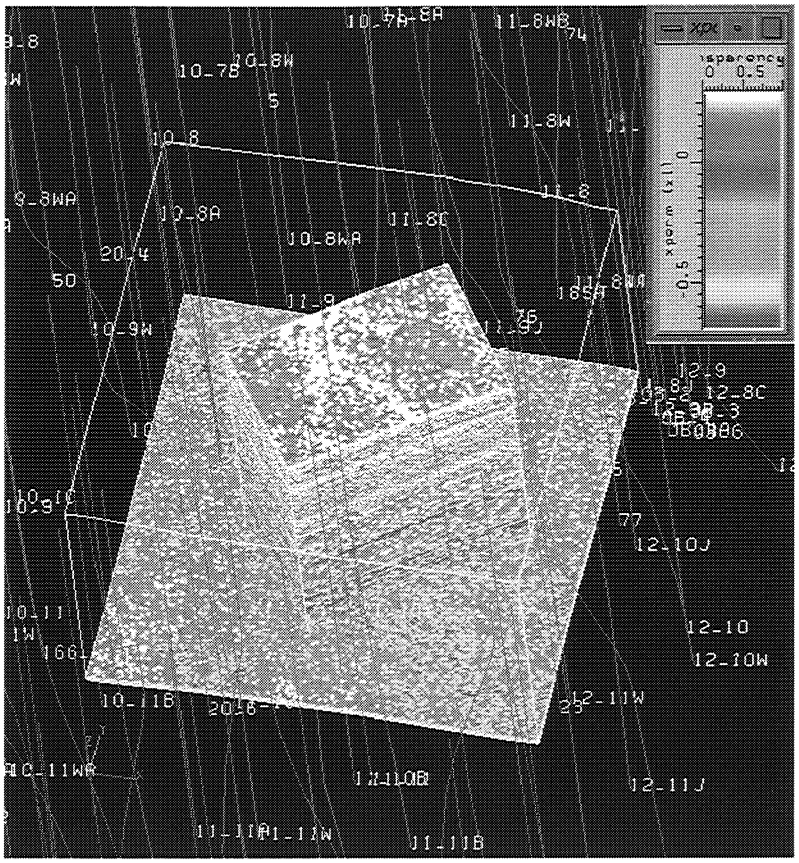
10_7A
11_8A
11_8WB
74
10_7B
10_8W
5
11_8W
10_8
11_8
9_8WA
10_8A
10_8WA
11_8C
20_4
50
11_8WA
185
11_9
76
11_9J
10_9W
12_9
12_8C
77
12_10J
10_9
10_11
166
12_10
12_10W
10_11B
23
12_11W
12_11J
11_10B
11_11W
11_11B
xperm (x1)
-0.5
0
0.5

Figure 2.4-2. The 2.5 acre pattern model (60 x 40 x 245 layers) extracted from central part of the original 27 acre model (149 x 149 x 245).

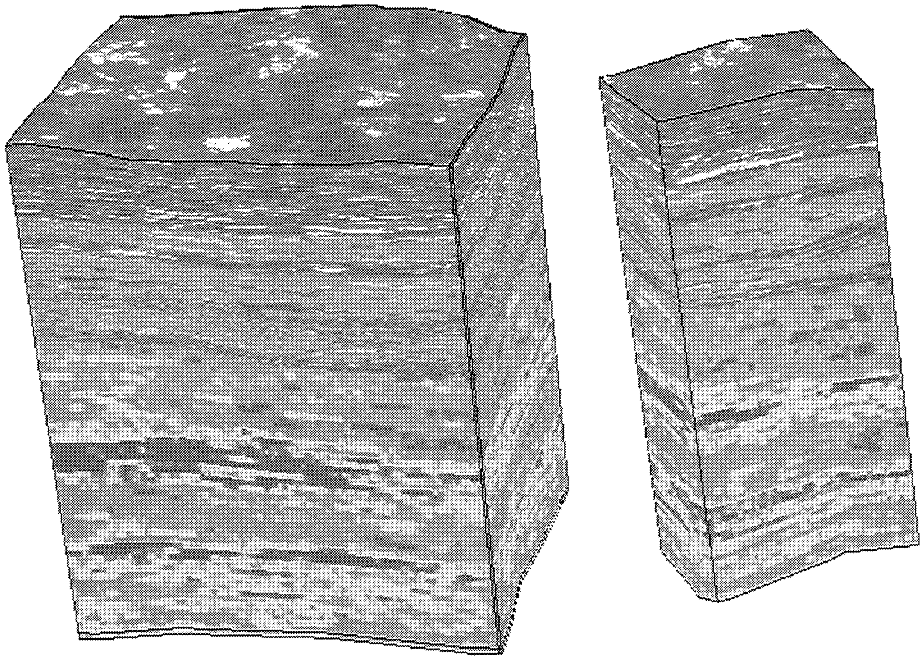

Water Sat. Cube of the 27 Acre Model (149x149x245)

Water Sat. Cube of 2.5 Acre Pattern Model. (60x40x245)

Figure 2.4-3. 2.5 acre pattern model extracted from the central part of the original 27 acre model.

Scale-Up Procedure

Even though the 2.5 acre model has fewer cells than the original fine grid model, it requires coarsening for *CHEARS* simulations. The 2.5 acre pattern model was coarsened using *SCP* (Chevron's in-house scale-up program) both areally and vertically from 60 x 40 x 245 layers to 30 x 20 x 55 (3,300 cells). A kv/kh ratio of 0.3 was used to generate *ZPERM* for each cell (kx, ky, and kz are required inputs for *SCP*). Figure 2.4-4 shows a comparison of the global slice permeability for each coarsened slice in the X and Y directions compared to the fine grid 2.5 acre model (shown in brown). The permeability scale (vertical scale and color scale) ranges from 0 md to 1.8 md and the differences between fine (brown dots) and coarsened (colored bars) slices are generally small. In addition, the fractional flow curves show close agreement for unit mobility displacements. Thus the *SCP* diagnostics show that the coarsened model is close in single phase flow behavior to the 2.5 acre pattern model.

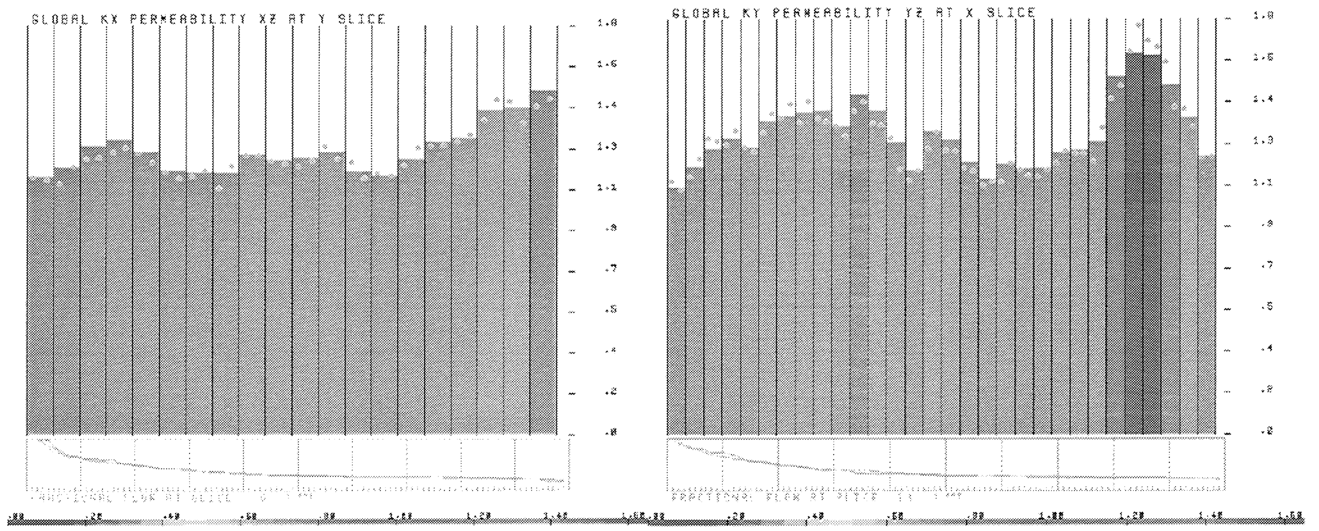

XZ slice YZ slice

Figure 2.4-4. Comparison of single phase flow results in the fine grid 2.5 acre model (60 x 40 x 245 layers) and the scaled-up model (30 x 20 x 55 layers).

Figures 2.4-5 to 2.4-7show a 3D view of the 2.5 acre pattern model (left) and the coarsened model (right) properties: permeability, porosity, and water saturation. In general, the higher property value layers in the fine model have been left as finer layers in the coarsened model and the low property value layers have been lumped into thicker low property value layers. Tables 2.4-3 to 2.4-5 summarize the statistics of permeability, porosity and water saturation of both the fine grid model and the coarsened model. The minimum, maximum, and mean values for each property of both models agree reasonably.

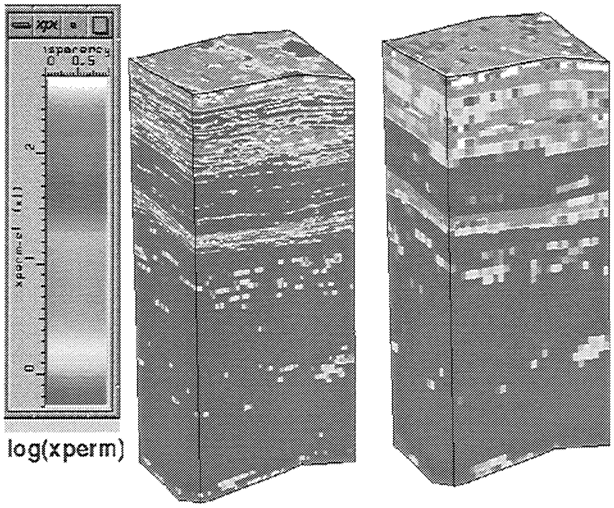

Figure 2.4-5. Comparison of permeability distribution, fine pattern model (60x40x245) and the scaled-up model (30x20x55).

Table 2.4-3. Statistical data of permeability.

Permeability	60x40x245 Model	30x20x55 Model
Minimum	0.17	0.19
Maximum	501.19	501.16
Mean	3.38	4.68

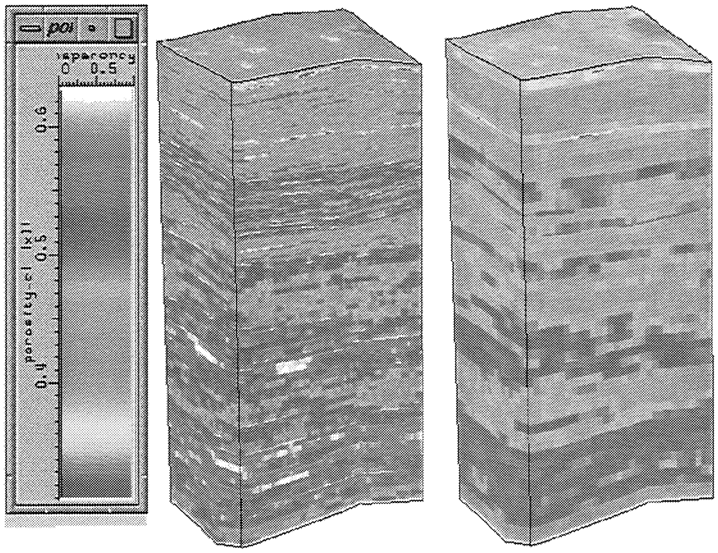

Figure 2.4-6. Comparison of porosity distribution, fine pattern model (60x40x245) and scaled-up model (30 x 20 x 55).

Table 2.4-4. Statistical data of porosity.

Porosity	60x40x245 Model	30x20x55 Model
Minimum	0.29	0.29
Maximum	0.66	0.63
Mean	0.49	0.48

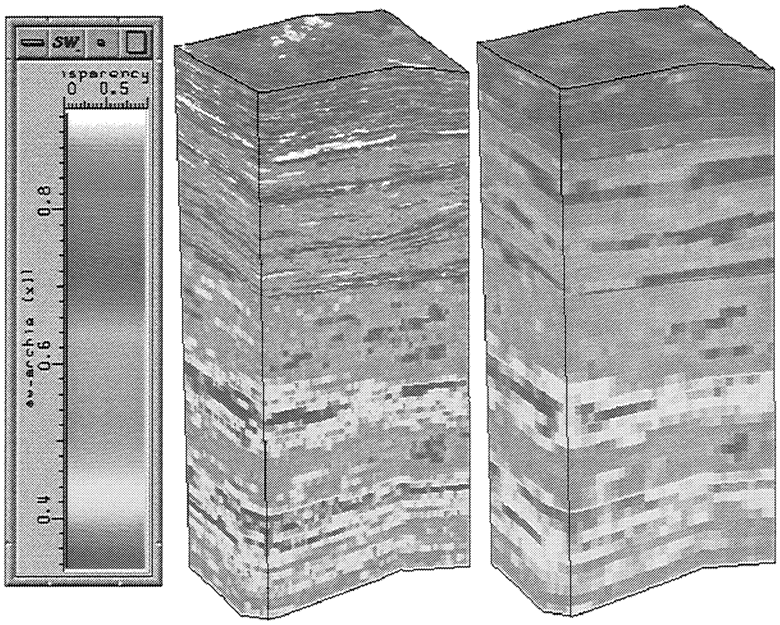

Figure 2.4-7: Comparison of initial water saturation distribution, fine pattern model (60 x 40 x 245) and scaled-up model (30 x 20 x 55).

Table 2.4-5. Statistical data of water saturation.

Water Saturation	**60x40x245 Model**	**30x20x55 Model**
Minimum	0.07	0.20
Maximum	0.99	0.92
Mean	0.57	0.58

In the scaled-up model, the stratigraphic markers' locations were honored (coarsened model layers begin at the top of each marker interval). Table 2.4-6 shows the marker intervals in the coarsened model.

Table 2.4-6. Stratigraphic markers and their depth in the coarsened model.

Marker	**Layer**	**Measured Depth**
C	1	**1250 ft**
D	10	1373 ft
E	19	1505 ft
EE	22	1548 ft
F	26	1616 ft
L	base of 55	2174 ft

Adding Hydraulic Fractures to the Models

To represent the hydraulic fractures, five rows of cells with 0.2 foot width were added as shown in Figure 2.4-8 below. The additional thin cells increased the number of Y direction cells to 25. Fractured cells beyond the fracture half-length were assigned properties from the adjacent Y cells.

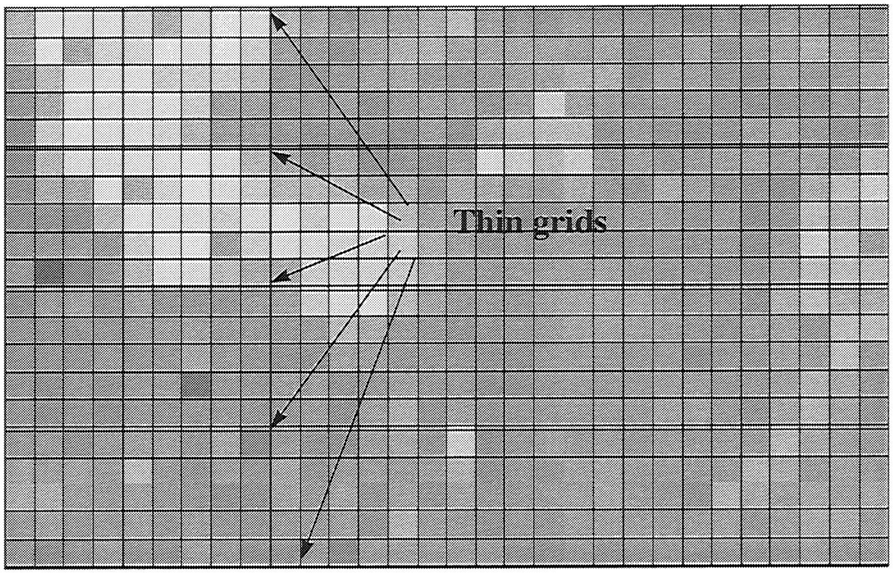

Figure 2.4-8. Five Y slice rows are added to the coarsened model to represent cell hydraulic fractures.

Depending on the location of the well, the completion interval, and the length of the hydraulic fracture, some cells in the Y=1, Y=13, and Y=25 rows were set at kx=ky=kz=1000 md (fracture permeability) as shown in Figure 2.4-9. In addition, certain prediction such as case 11 required that some cells in rows Y=7 and Y=19 also assigned 1000 md permeabilities to represent fractures.

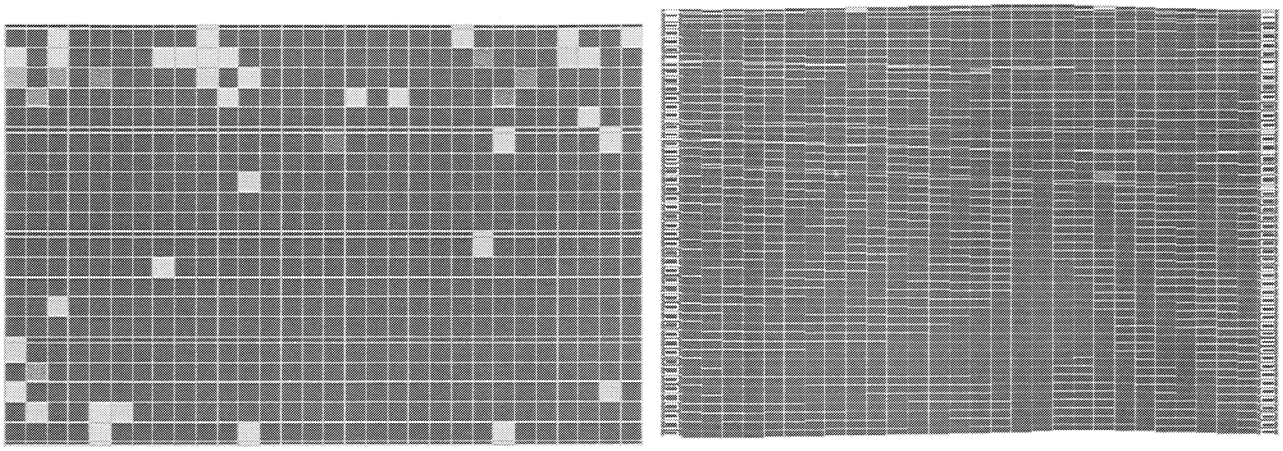

Figure 2.4-9. Plane view and cross section of hydraulic fractures modeled with thin cells (dark blue).

After adding the hydraulic fractures, the simulation input is completed by including reservoir properties such as PVT, relative permeability, well completions and other data.

Waterflood PVT Data

A *CHEARS* black oil simulation deck was created with cell properties from the coarsened model and added fracture cells. Table 2.4-7 shows the deck's oil and gas PVT properties from well 12-10 in Section 32. The bubble point pressure, solution GOR and oil viscosity were adjusted to 1228 psia which is estimated to be the initial conditions at discovery. The FVF and solution GOR were linearly extrapolated from the physical recombination measurements to 1228 psia. Oil viscosity was extrapolated by using the Beal, Chew, and Connally correlation. A dead oil viscosity of 28.94 cp was used in the formula.

Table 2.4-7. Oil and gas input properties for the *CHEARS* model.

Pressure (PSIA)	Oil Formation Volume Factor (RB/STB)	Oil Viscosity (CP)	Solution Gas-Oil Ratio (SCF/STB)	Gas Formation Volume Factor (RB/MCF)	Gas Viscosity (CP)
15	1.020	28.94	0.0	195.32	0.0067
100	1.030	24.80	23.0	28.92	0.0073
200	1.036	22.06	41.0	14.27	0.0080
300	1.042	20.31	58.0	9.39	0.0087
400	1.048	18.68	74.0	6.94	0.0095
500	1.053	17.18	88.0	5.48	0.0104
600	1.058	15.83	104.0	4.51	0.0113
700	1.063	14.73	119.0	3.81	0.0122
860	1.072	13.72	143.0	3.124	0.0139
1000	1.080	14.06	163.0	2.784	0.0154
1228	1.093	11.46	195.5	2.230	0.0178

Stock tank oil properties are as follows:

- Oil Gravity = 21.6 API
- Oil Density = 0.9260
- Gas Density = 0.714

An initial pressure estimate of 1400 psia was made at the top of reservoir at the C-point (1250 ft measured depth, 700 ft vertical subsea). Rock compressibility was 3.3E-5 at a reference pressure of 1000 psia.

Relative Permeability Data

The water-oil and gas-oil relative permeability curves from Terra Tek measurements on Well 12-10 (at 1953.4 ft measure depth) are shown in Figure 2.4-10. Relative permeability end-points (Table 2.4-8) were developed from end-point measurements on 8-4B core. Curve shapes came from Well 12-10 unsteady-state data measured by Terra Tek. The curve shapes were restrictive to flow for all phases. The gas permeability curve was lowered as showed in Figure 2.4-11. Residual oil saturation endpoints reflected the lower efficiency of free imbibition data shown in Figure 2.4-12. For CO_2 sensitivity, pore size dependent curve shapes based on mercury injection data were used as shown in Figure 2.4-13.

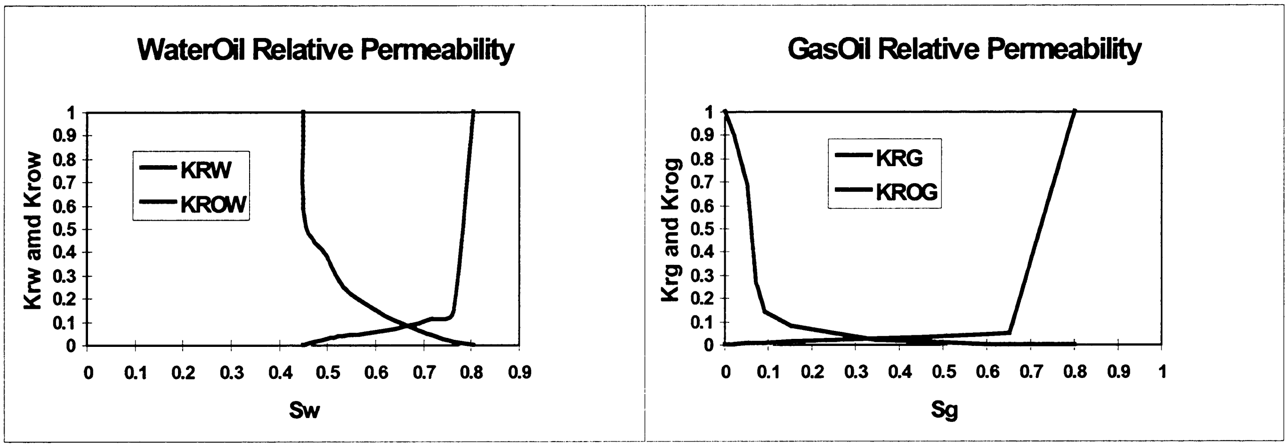

Figure 2.4-10. Relative permeability curves.

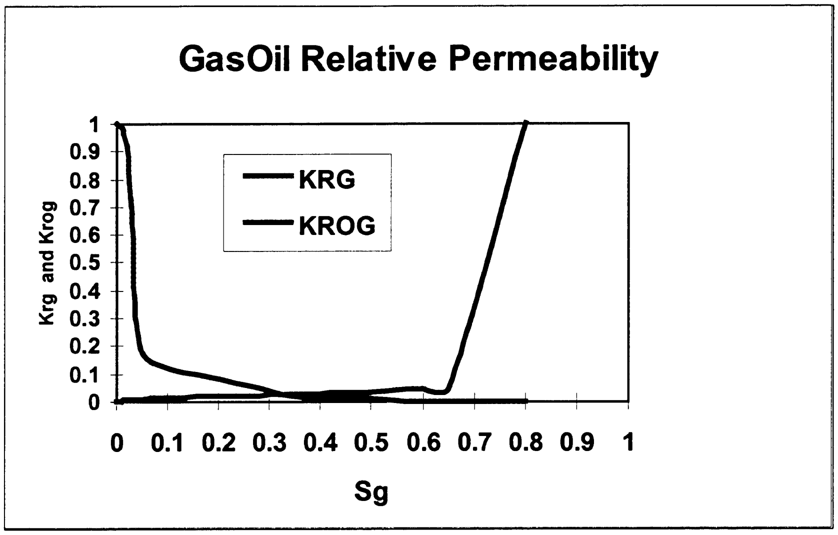

Figure 2.4-11. History adjusted gas-oil relative permeability curves of Well #12-10.

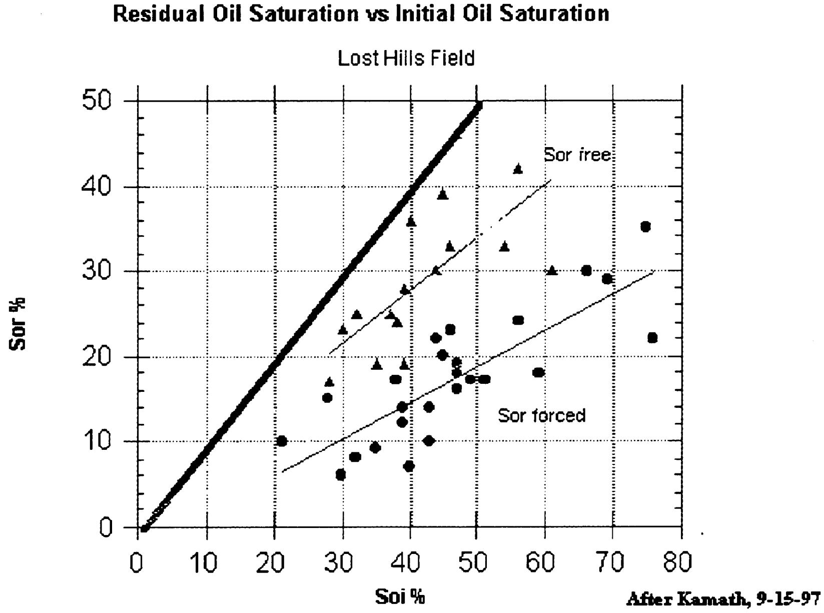

Figure 2.4-12. Free imbibition endpoints compared to forced endpoints from high pressure drop measurements.

Table 2.4-8. Relative permeability end-points.

Swir	Sorw	Krwro	Krocw	Sgc	Sorg	Krgro	Kro (Sg=Sgc)
0.45	0.195	1.0	1.0	0.0	0.20	1.0	1.0

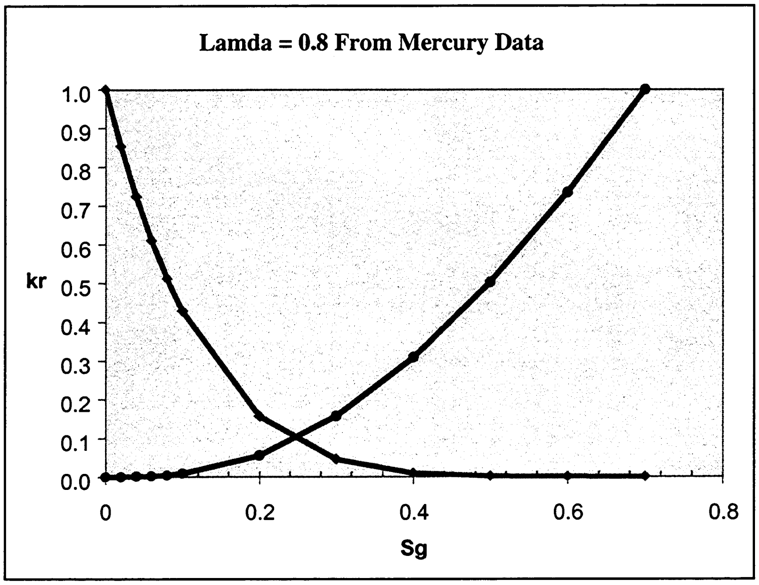

Figure 2.4-13. Oil-gas relative permeability curves derived from mercury injection data, courtesy deZabala and Kamath.

Well Constraints

During primary depletion producers were completed from the C-point to the BH-point or about layer 1-41 and non-fractured. The minimum bottom hole pressure was constrained at a minimum of 45 psia at the C-point with maximum liquid production constraint at 400 b/d for each producer.

After primary depletion and during the waterflood, producers were re-completed to expose all 55 layers from the C-point to the L-point and all wells were fractured. The minimum bottom hole pressure limit remained at 45 psia. Water injectors were installed according to Figure 2.4-1. The injectors were also fractured and limited to a maximum of 1200 psia bottom hole pressure. Water injection interval sensitivities included F-L (base case), E-L and D-L.

History Matching

History matching of the non-fractured primary infill performance suggested that overall permeability might be higher than the permeabilities directly obtained from the *Gocad/G2* model. Two sets of simulations were concurrently performed to capture this uncertainty:

- 1*K model (unadjusted liquid permeability from *G2* model)
- 2*K model (global permeability by multiplying by 2)

The history match was repeated on both models: original permeability (1*K model) and permeability multiplied by two (2*K model). The 1*K model started depletion from January 1968. The depletion took about 23 years and stopped at the end of December 1990. The 2*K model required less time to deplete and started depletion from January 1978. The depletion took about 13 years and stopped at December 1990. As in actual field practice, newly installed waterflood injectors were put on production for 6 months to reduce the near wellbore pressure before the start of injection. For both models during the waterflooding period, all wells were fractured. The producers were re-completed from the top to the bottom of reservoir and the injector(s) were re-completed to the specified injection intervals.

In Figure 2.4-14, the upper left plot shows the history matching of the 1*K model. The GOR and WOR trends of the 1*K model compare reasonably with field GOR and WOR considering the noisiness of the data. Figure 2.4-14 also shows a very good match of the 1*K model's cumulative GOR of 1.65 compared with field cumulative GOR of 1.5. The 1*K model's cumulative WOR of 0.53 also compares well with 0.6. At the end of 1997, Figure 2.4-14 shows the 1*K model's cumulative GOR of 1.57 compared with 1.59 actual. The 1*K model cumulative WOR of 0.79 is consistent with the field's 0.79.

The lower right plot shows the history matched response of the 2*K model. Generally, the 2*K model's GOR was lower than the field's GOR during waterflood period. The 2*K model's WOR during the depletion period is lower than the field and increases rapidly during the waterflood period. However, the trends of the 2*K model's GOR and WOR can be considered just as reasonable as the 1*K model, although not as close. The 2*K model's cumulative GOR of 1.64 compares well with field GOR of 1.5 and cumulative WOR of 0.52 compares well with field WOR of 0.6 for primary depletion. At the end of 1997, the 2*K model's cumulative GOR of 1.43 compares with the field GOR of 1.59 and model cumulative WOR of 1.06 compares reasonably with the field's 0.79.

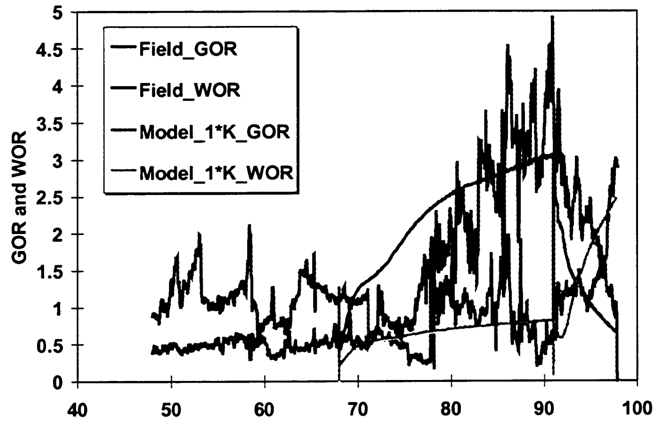

Model 1*K History Match

End of Primary Depletion:
CGOR : 1.65 (historic data 1.5)
CWOR : 0.53 (historic data 0.6)

End of Waterflood:
CGOR : 1.57 (historic data 1.59)
CWOR : 0.79 (historic data 0.79)

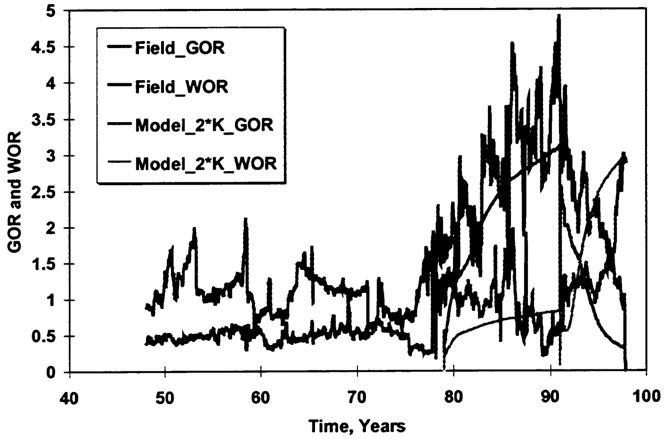

Model 2*K History Match

End of Primary Depletion:
CGOR : 1.64 (historic data 1.5)
CWOR : 0.52 (historic data 0.6)

End of Waterflood
CGOR : 1.43 (historic data 1.59)
CWOR : 1.06 (historic data 0.79)

Figure 2.4-14. Primary depletion and waterflood history match of 1*K and 2*K models.

Reservoir pressure at the end of primary depletion was examined and compared with RFT data. Table 2.4-9 shows the pressure of the 1*K model after 23 years of depletion. The table contains the pressure at the center of the corresponding interval and the average pressure for each corresponding interval. Table 2.4-10 shows the pressure of the 2*K model after 13 years of depletion. Figure 2.4-15 compares the model pressure at the center of the intervals of the reservoir at the end of depletion of the 1*K model (presented in square green dots) and the 2*K model (presented in square light blue dots) to field RFT data (presented in square dark blue).

As expected, the recovery performance of the 1*K model is less than the 2*K model. In depletion the 1*K model took 23 years and recovered 4%. For the same amount of oil recovery, 4 %, the 2*K model took only about half of time, 13 years. In waterflood the 1*K model recovered, 1.8 % compared to 3.0% from the 2*K model. Figure 2.4-11 summarizes the recovery.

Figure 2.4-16 shows that oil production rate of the 2*K model matched better with the more recent waterflood well performance data. The oil production rate of the 1*K model is lower than the field data. The initial production of the 2*K model was about 85 b/d which is between the range of 90 b/d to 55 b/d of field data. After 4 years of waterflood, the oil rate of the 2*K model is about 40 b/d which is between the range of field data 60 b/d to 35 b/d. The trend of oil production rate is slowly going up. However, predicted waterflood response suggest a peaking of response soon followed by a gradual decline, contrary to previous models that showed either a large sustained increase in oil production, or restrained oil production accompanied by a large increase in average reservoir pressure to 3000+ psia.

Table 2.4-9. Reservoir pressure vs. depth at the end of primary depletion of the 1*K model.

Reservoir Zone and Model Layer	Pressure at Center of Middle Layer (psia)	Average Pressure (psia)
C (1-9)	116	108
D (10-18)	201	200
E&EE (19-24)	344	326
25-29	508	457
30-33	689	649
34-37	991	864
38-45	1256	1173
46-55	1640	1629

Table 2.4-10. Reservoir pressure vs. depth at the end of primary depletion and the 2*K model.

Reservoir Zone and Model Layer	Pressure at Center of Middle Layer (psia)	Average Pressure (psia)
C (1-9)	116	108
D (10-18)	210	208
E&EE (19-24)	352	334
25-29	511	468
30-33	686	646
34-37	982	856
38-45	1250	1167
46-55	1635	1616

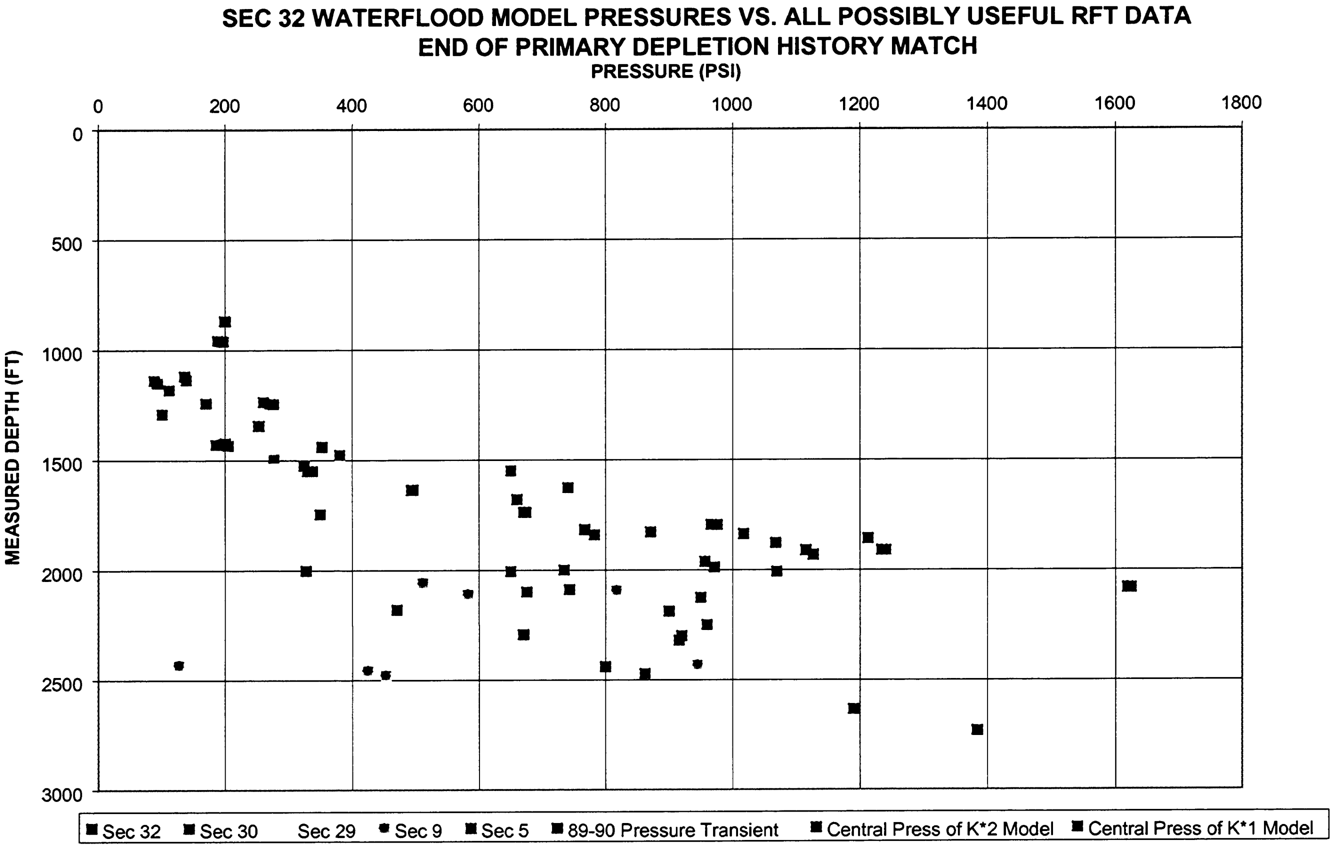

Figure 2.4-15. Pressure of 1*K and 2*K models at the end of depletion with RFT results.

Table 2.4-11. Cumulative oil production during history match of the 1*K and 2*K models.

History Match	Years of Simulation	Cum. Oil Production, Bbls	% Recovery
1*K, Depletion	23 years	148,000	4.0
2*K, Depletion	13 years	148,000	4.0
1*K, Waterflood	6 years and 9 months	68,000	1.8
2*K, Waterflood	6 years and 9 months	110,000	3.0

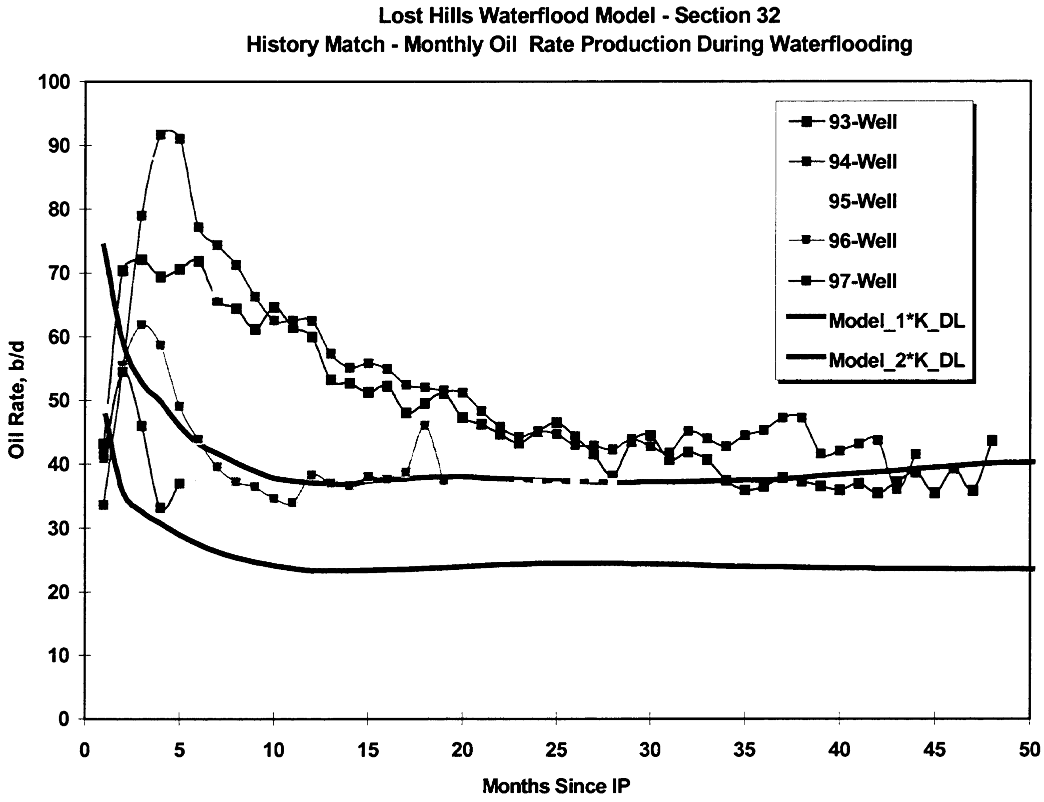

Figure 2.4-16. Oil production rate of 1*K and 2*K models during early waterflood compared to actual.

CO_2 RECOVERY PREDICTIONS

Summary

The waterflood simulation models were extended to evaluate CO_2 injection at Central Lost Hills. The results show significant accelerated and incremental reserves compared to water injection. Incremental reserves result from the favorable effects of CO_2 on oil viscosity and swelling; acceleration directly relates to the improved injectivity afforded by low CO_2 viscosity. Incremental recovery agrees with earlier results from 1991; Table 2.4-12 shows a comparison of recovery estimates from this study compared with 1991 estimates[7, 8]. However, recovery for both water and CO_2 injection is lower compared to the 1991 estimates, which were based on relatively homogeneous models that were very similar to those used for the original waterflood pilot design and predictions.

Table 2.4-12. Summary of base case recoveries compared to 1991 CPTC study (references 7 and 8).

Model	Primary Depletion %OOIP	Water Flood 30 yrs %OOIP	CO_2 Flood 30 yrs %OOIP	Incremental CO_2-WF %OOIP
This study (median scenario)	4	6	14 (continuous)	8
1991	4	22	31 (WAG)	8

Phase Behavior

Compositional simulation is necessary to capture the partial miscibility mechanisms expected at Lost Hills reservoir conditions. The earlier work reported in 1991 included conventional black-oil measurements along with vapor-liquid equilibrium measurements (*VLE*) on a CO_2-oil mixture[10]. The *VLE* provided phase compositions and liquid phase viscosities. The *VLE* data was used to calibrate the Peng-Robinson equation-of-state (*PREOS*) model of the CO2-oil system. Table 2.4-13 presents the *PREOS* parameters used in *CHEARS*. The parameters are in very close agreement with the earlier work by Fong et al.[7,8].

Favorable interaction between CO_2 and oil is one of two key mechanisms (the other is improved injectivity) leading to reserves addition. To delineate the favorable phase behavior of CO_2 and oil, one of the runs injected pure methane to show the difference in predicted performance of a relatively inert gas. A following section will present the methane injection sensitivity.

Initialization

The set of 2*K grid described in the waterflood sections above was used to simulate a range of CO_2 EOR performance at central Lost Hills, using the compositional option of *CHEARS*. The compositional model was calibrated to historic data using the same procedure described for the black-oil waterflood model. Conditions at the end of September 1997 were assumed as initial conditions for the start of CO_2 injection. We used *SIMC* to generate the pressure and saturation arrays and *CHEARS* was able to add hydraulic fractures and initialize the cell compositions using the arrays, after some minor corrections. Figure 2.4-17 shows the comparison of compositional *CHEARS* to depletion and waterflood trends before 1997, essentially identical to the calibration performed for the waterflood models.

Table 2.4-13. CHEARS equation-of-state parameters.

```
0COMPONENTS
0*     NAME     MOL WT
0     C1           16.0430
0     C2-3         32.7800
0     C4-6         71.5000
0     C13         175.7900
0     C37         509.9400
0     CO2          44.0100
0*
0OILVISC    LBC   0.0233640   0.0585330  -0.0407580   0.0093324
0GASVISC    LBC   0.0233640   0.0585330  -0.0407580   0.0093324
0*
0PARACHOR
0       71.0  120.4  239.6  565.0 1563.0   49.0
0*
0EOSPARMS
0*     NAME     PC(PSIA)    TC(F)   VC(CUFT/LBMOL)  W         SC        OMEGAA
OMEGAB
0     C1        667.8010 -116.6260     1.5899     0.0108    -0.1540   0.457240
0.077800
0     C2-3      690.0900  112.8300     2.5400     0.1093     0.0790   0.457240
0.077800
0     C4-6      486.3800  361.3700     5.0000     0.2358    -0.0741   0.457240
0.077800
0     C13       328.9500  778.2800    12.4800     0.4891     0.0481   0.457240
0.077800
0     C37       159.9400 1222.6500    34.6000     1.1289     0.0760   0.457240
0.077800
0     CO2      1070.6040   87.8700     0.3000     0.2280    -0.2942   0.467240
0.077800
0*
0BININTCOEF
0 0.0070
0 0.0100  0.0000
0 0.0200  0.0000  0.0000
0 0.0250  0.0000  0.0000  0.0000
0 0.1000  0.1250  0.1250  0.1200  0.1100
0*
0KVALUES  PREOS     30.000   1500.000
0*
0RESTEMP    105.000
```

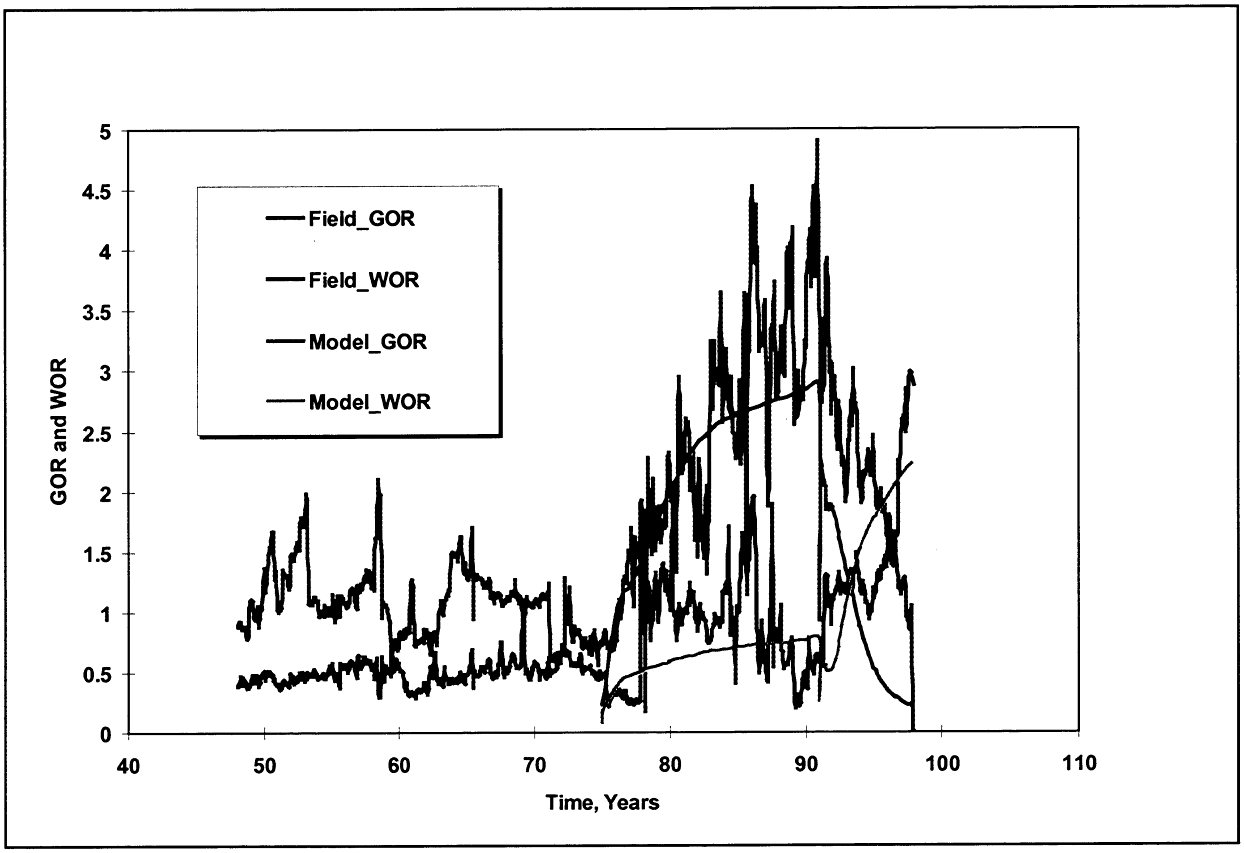

Figure 2.4-17. Comparison of compositional-CHEARS with field GOR and WOR trends, before 9/97.

Run Specifications and Stability Considerations

The completion schemes remained the same as for the waterflood-infill simulations. The only additional sensitivity was water-alternating-gas injection (WAG) to control CO_2 breakthrough, where appropriate. We limited the WAG scenarios to case 4 and case 5 because of the difficulties of obtaining stable simulations. Finite difference compositional simulations of gas injection processes are inherently unstable because of complex phase behavior and rapid changes in pressure gradients especially during WAG cycles. Stability can be improved by adjusting iteration parameters such as time step size and convergence tolerances. However, we found that some scenarios required time step sizes of less than 10^{-3} days and run times in excess of 4 CPU-weeks which makes many of WAG scenarios impractical to simulate without using the simultaneous injection option.

The bottom hole injection was limited to 1200 psi at the F-point, which is more restrictive than the waterflood limit of 1200 psi at the C-point (equivalent to about 1100 psi at the F-point assuming a CO_2 gradient of 0.26 psi/ft). Simulations of WAG were performed using the simultaneous injection option instead of the slugging option to overcome stability problems. Field experience at Rangely indicates that short WAG cycles (situation approximates simultaneous injection at very short cycles) improved well productivity because of more stable artificial lift conditions. However, changes in oil recovery as a function of CO_2 injected were not detected.

Injection pressure is expected to be an important uncertainty at Lost Hills. Bottomhole injection conditions at Lost Hills are near the critical point of CO_2 and as a result, its phase behavior and interaction with reservoir oil is highly sensitive to injection pressure. The sensitivity adds a significant element of uncertainty in performance and we illustrate this uncertainty in the Case 4 sensitivities section. Producing bottomhole pressure of 45 psi was referenced to the F-point. In addition, producing wells have a GOR limit of 20 MCF/STB. Typically, significant NGL volumes can be extracted from the producing gas stream provided that LTS facilities are available. However, our assumed GOR limit is arbitrary. Accurate estimates would require pilot test data and detailed compositional simulations of pilot performance.

Base Case Pattern: Case 4 (2.5 Acre 5-Spot)
Table 2.4-14 provides an overview of recovery factors for this pattern configuration followed by additional details in the subsequent sections. The results in the first row represent base case conditions of injection into a well with a 50 feet half-length hydraulic fracture spanning the F-L interval. The results suggest that it would be more advantages to process the reservoir using a continuous CO_2 injection process rather then WAG, if injection can be controlled to the F-L interval; WAG penalizes processing rate in this case. However, WAG will probably be needed and will improve performance if leakage occurs to the shallower and sandier intervals; injection conformance can only be assessed careful monitoring.

Table 2.4-14. Overview of Case 4 recovery factors, 1997-2027.

Case 4 Model	Project years	Oil Recovery % OOIP	Final oil rate, b/d	Wells shut-in due to GOR limit prior to 30 years injection
F-L, 50'	30	14.3	35	None
Mercury Krg-Kro				
Methane Injection				
BHIP=1350psi	30	19.3	45.2	None
C-L, 50'	6.5	6	63.8	prod3=> 5ys
D-L, 50'	25	17.6	14	Prod1 => 25 ys prod2 => 24 ys prod3 => 25 ys prod4 => 24 ys
E-L, 50'	30	17.3	40.8	None
F-L, 0.25 WAG	30	13.7	37.8	None
F-L, 0.64 WAG	30	12	36.3	None
F-L, 1.3 WAG	30	10.5	32.1	None
D-L. 0.25 WAG	30	20	48	None
D-L, 0.62 WAG	30	18.4	48	None
D-L, 1.3 WAG	30	16	44	None
25' fracture	30	11.8	33.5	None
90' fracture	30	17	33	None
F-L, 31API	30	19	29	None
D-L, 31API	24	21.6	0	Prod1 => 24ys prod2 => 24ys prod3 => 24ys prod4 => 23 ys

Base Case, 50 Feet Fracture Half-Length
Figure 2.4-18 presents the production and injection profile for this case. Stabilize CO_2 injection rate is estimated at 2-3 times that of water injection rate at reservoir conditions (about

1 MCF/bbl). The increased injection rate accelerates production; a key feature of all of the CO_2 simulations presented here and in earlier studies[7, 8].

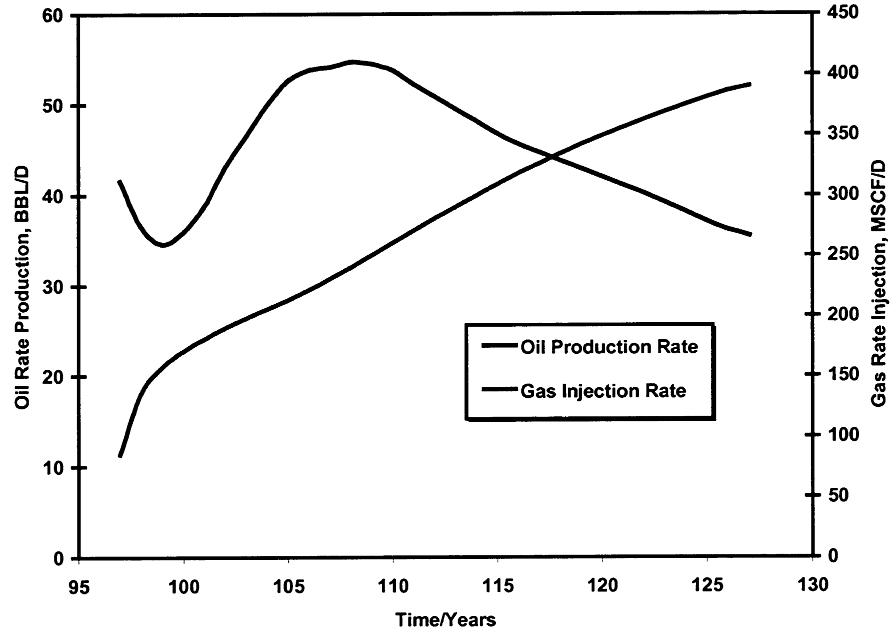

Figure 2.4-18. Base Case CO_2 recovery performance, 2.5 acre 5-spot, F-L injection, and 50 ft. fracture half-length.

Case 4 Sensitivities

Mercury Injection Based Gas-Oil Relative Permeability

With the exception of this sensitivity run, the history (pre-1997) adjusted relative permeability curves were used in all of the simulations. For this simulation, pore size dependent Corey correlations, based on mercury injection data, were used. The mercury based relative permeability is more conductive than the history adjusted shapes where oil permeability drops off rapidly with increasing gas saturation. The resulting recovery results are more favorable as shown in Figure 2.4-19.

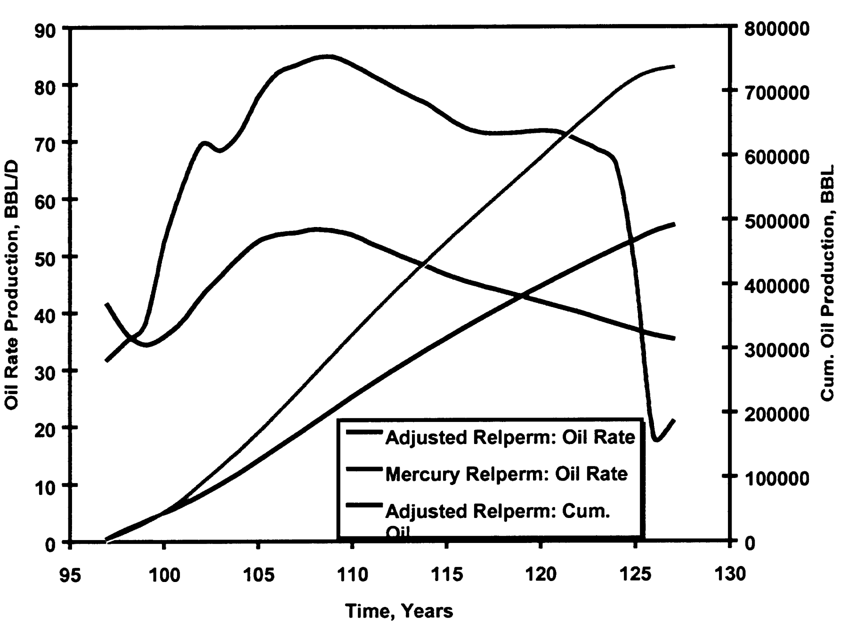

Figure 2.4-19. Relative permeability from mercury injection data increases oil recovery.

Methane Injection

Methane is a relatively inert gas with a molecular weight that is close to nitrogen, and with negligible interaction with oil at Lost Hills reservoir conditions. We simulated methane injection in order to assess the role of CO_2-oil interaction. Methane injection performance is very poor as shown in Figure 2.4-20.

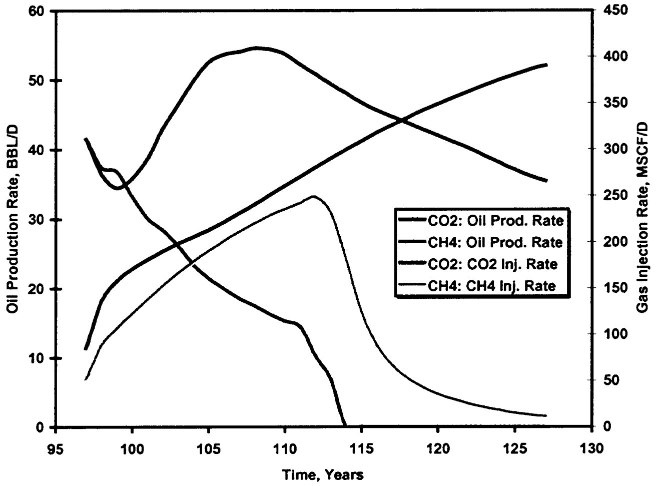

Figure 2.4-20. Comparison of CO_2 and methane injection performance.

Bottomhole Injection Pressure

The risk of fracture extension and the loss of conformance dictate injection pressure limits. The assumption in the other runs is that the fracture extension gradient remains constant with injection. However, in reality fracture extension pressure is dependent on pore pressure, which increases with time as CO_2 invades the reservoir. A rough estimate of the relationship between average pore pressure in the wellbore (injector) region and fracture extension pressure was made. Assuming an increase in average pressure from 600 to 900 psi in the near injector region, fracture extension pressure increases roughly by 150 psi (about half of the increase in pore pressure). As shown in Figure 2.4-21, increasing bottomhole injection pressure by 150 psi increases CO_2 performance significantly as a larger near-wellbore region falls within the critical point of CO_2. Robust assessment of this uncertainty requires field injectivity or pilot testing data.

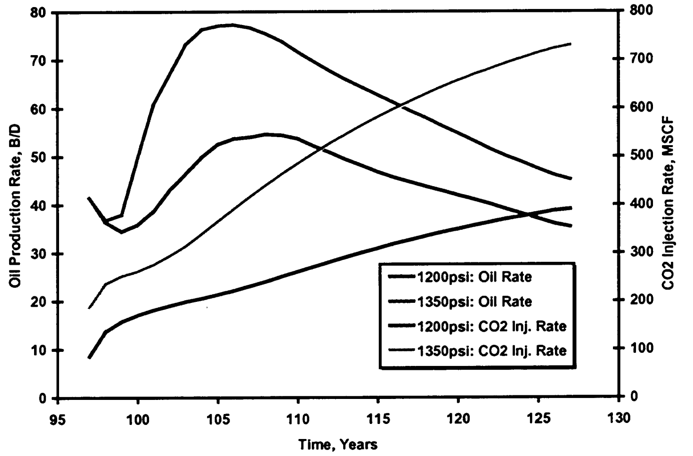

Figure 2.4-21. Effect of increased injection pressure on oil recovery.

Leakage of Injection to C, D and E Intervals

Even in current waterflood operations, significant uncertainties exist regarding injection profiles. The uncertainty is associated with whether hydraulic fractures extend vertically into the shallower intervals. Some observation well data from the original pilot area suggest that water saturation has increased in shallower intervals above the injection interval.

The set of sensitivities presented in Figure 2.4-22 simulates the conditions where leakage occurs to upper intervals. All these simulations assume continuous CO_2 injection and rapid CO_2 breakthrough and peak oil characterize these simulations. The next section presents sensitivities on the corrective action, WAG.

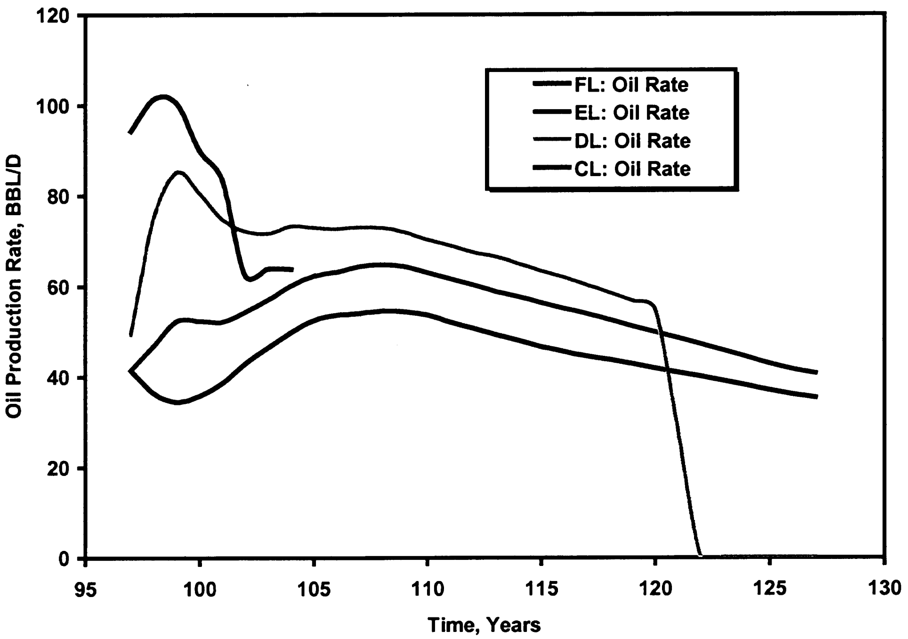

Figure 2.4-22. Recovery sensitivity to interval of injection, continuous CO_2.

Effect of WAG

The rapid breakthrough shown in Figure 2.4-22 requires correction with WAG. Figure 2.4-23 presents recovery performance for WAG for the F-L and D-L injection interval sensitivities. WAG reduces injectivity in both scenarios and particularly in the F-L injection scenario and impacted early performance negatively. WAG marginally improved the performance in the D-L scenario.

The simulations assume that WAG is initiated immediately upon CO_2 injection. The assumption is conservative since most CO_2 operators including Chevron have come to recognize that it would be more optimal to wait for breakthrough problems prior to initiating WAG. Initiating WAG prematurely would risk substantial delayed oil response. Eventually, WAG is required in pattern type projects to stabilize production well behavior. Another alternative is to adapt a CO_2 cycling strategy where wells converted to flowing and WAG is completely avoided and breakthrough is handled by workovers and/or de-spacing, as in a pressure maintenance project.

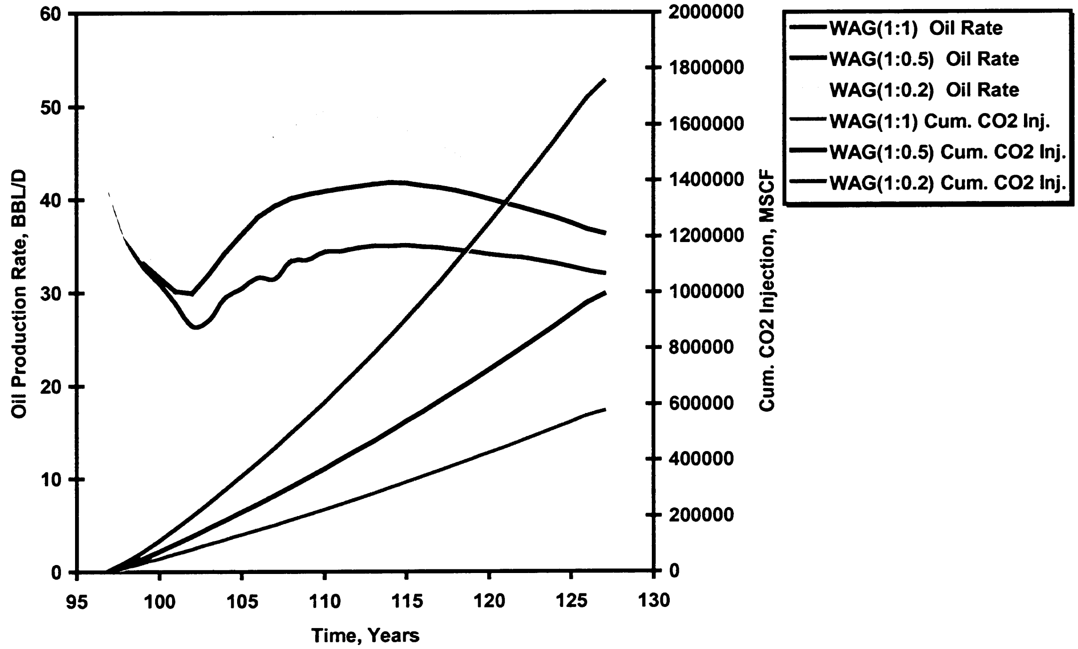

Figure 2.4-23. Effect of using WAG to improve conformance, F-L and D-L injection.

Fracture Half-Lengths of 25 Feet and 90 Feet

Figure 2.4-24 shows that longer fractures are better for this pattern configuration, same as in the waterflood sensitivities.

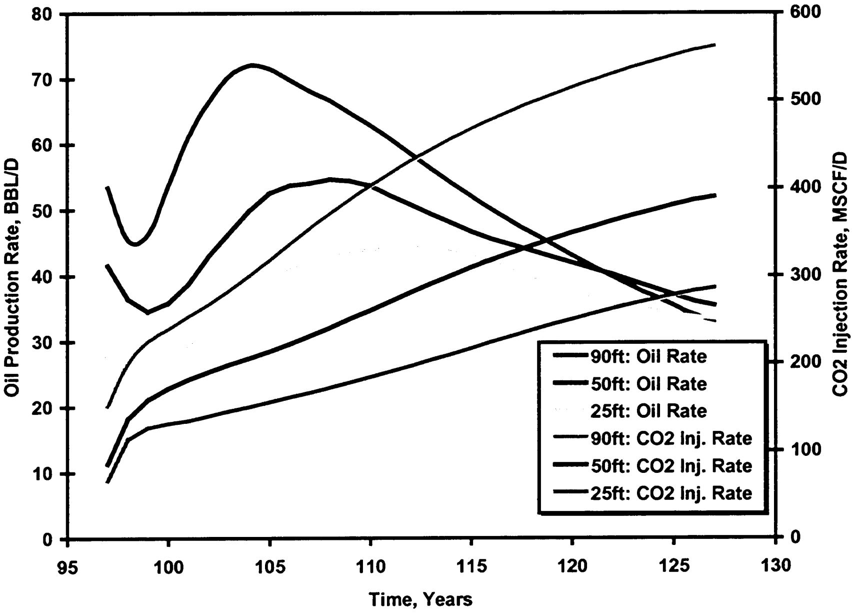

Figure 2.4-24. Effect of fracture length on recovery performance, F-L injection.

Oil Gravity

Better reservoir oil properties improves both processing rate and oil recovery as shown in Figure 2.4-25. Project life is shortened by about 3 years for the D-L injection case and recovery improves. Lower oil viscosity and more favorable CO_2-oil interaction combined to increase predicted oil response.

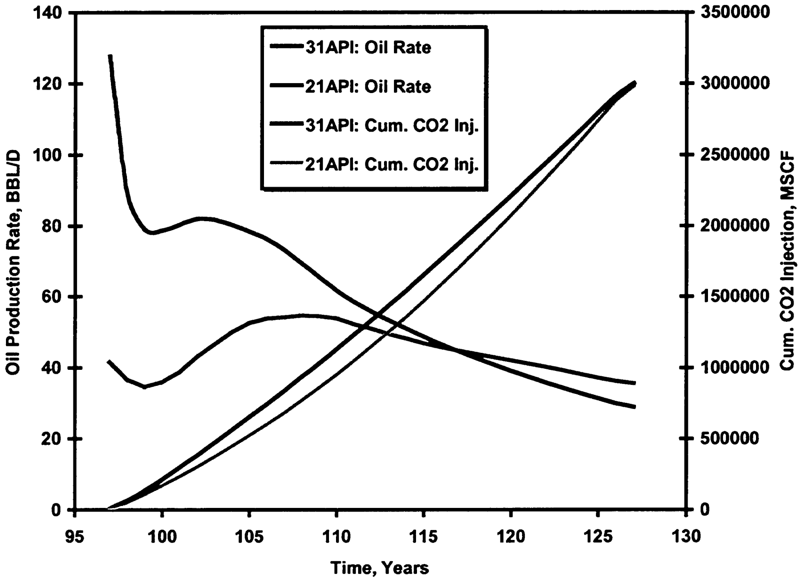

Figure 2.4-25. Effect of oil gravity on recovery performance, F-L and D-L injection.

Case 5 (1.25 Acre Spacing = Direct Line Drive)

Table 2.4-15 presents an overview of recovery factors from case 5 sensitivities. The results in the first row represent base case conditions of injection into wells with a 50 feet half-length hydraulic fracture spanning the F-L interval. Although the behavior of case 5 sensitivities are directionally similar to those in case 4, significant differences in sensitivities to various factors are evident. For cases where CO_2 is leaking into the shallower layers, WAG sensitivities showed significantly improved oil recovery compared to the continuous CO_2 simulations. Pattern alignment and injection-production connectivity seems to be more dominant than in case 4 causing a shift towards more favorable WAG responses. For the same reason, case 5 shows less sensitivity to hydraulic fracture length and oil properties.

Table 2.4-15. Overview of Case 5 recovery factors, 1997-2027.

Case 5 model	Project life, years	Oil Recovery, % OOIP	final oil rate, STB/d	Wells shut in due to GOR limit before 2027
F-L, 50' fracture half-length	26.7	18.36	25	Prod1 => 24 ys prod2 => 18 ys prod4 => 21 ys prod6 => 18 ys
BHIP=1350 psi	13	17.46	46.5	prod2=>14ys prod3=>14ys prod6=>13.5ys
C-L injection	4.5	7.98	86.3	prod2=>4.5ys prod5=> 2.5 ys prod6=>4 ys
D-L injection	10.5	14.23	46	Prod2 => 7ys prod3 => 8 ys prod5 => 7 ys prod6 => 8 ys
E-L injection	15	16	42	prod2=>11ys prod5=>14.5ys prod6=> 14.5ys
F-L, 0.25 WAG	30	20.18	30.8	prod2=>27 ys prod6=>28 ys
F-L, 0.65 WAG	30	19.52	34.8	None
F-L, 1.3 WAG	30	17.73	37	None
D-L, 0.24 WAG	19.5	22.27	57	Prod2=>14 ys prod4=>17 ys prod6 => 14 ys
D-L, 0.61 WAG	30	26.88	39	prod2 => 22ys prod4 => 27ys prod6 => 24 ys
D-L, 1.2 WAG	30	25.25	45	None
F-L, 25' fracture half-length	30	16.05	24.6	prod2 => 21ys prod5 => 22ys prod6 => 22ys
F-L, 90' fracture half-length	23.3	19.8	16.6	Prod2 => 16.5ys prod3=> 16.5ys prod4=> 21ys prod5=> 21ys prod6=> 17 ys
F-L, 25 API	30	19.47	60	prod1=>15ys prod4=>17ys
F-L, 31API	30	21.26	9.6	Prod1=>28ys prod2=>17ys prod3=>29 ys prod5=> 18ys prod6=>18ys
D-L, 25API	8.25	10.16	124	prod1=7 ys prod4=> 7ys
D-L, 31API	12	19.25	0	Prod1=>12ys prod2=>9ys prod3=> 12ys prod4=> 10ys prod5=>10ys prod6=>9ys

F-L, 50 Feet Fracture Half-Length

Figure 2.4-26 presents the production and injection profile for this case. Stabilize CO_2 injection rate is estimated at 2-3 times that of water injection rate at reservoir conditions, the same as for case 4.

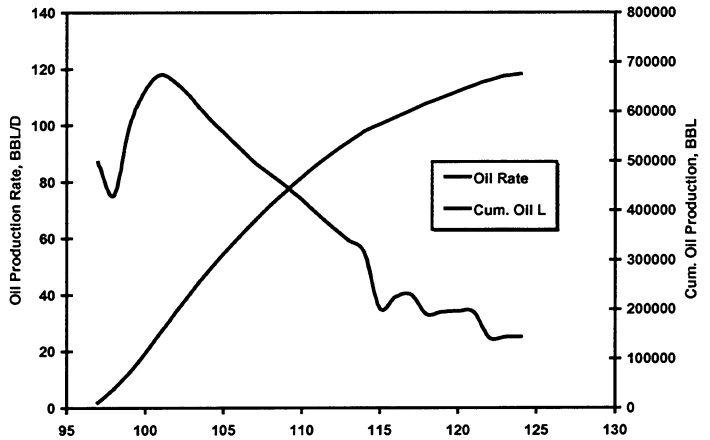

Figure 2.4-26. Case 5 CO_2 recovery performance, F-L injection, and 50 FT fracture half-length.

Case 5 Sensitivities

Bottomhole Injection Pressure

Although recovery factor is marginally lower than the 1200 psi injection case, performance accelerates substantially and the project life is shortened by nearly 14 years (Figure 2.4-27). The acceleration should improve profitability.

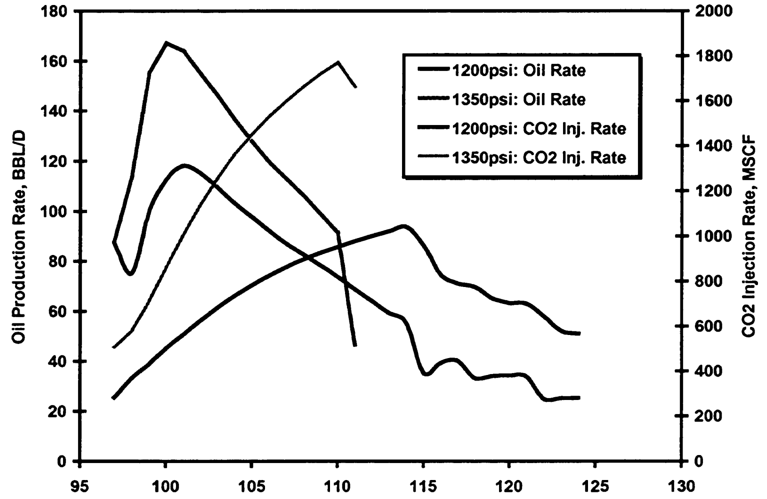

Figure 2.4-27. Case 5, effect of increased injection pressure on oil recovery.

Leakage of Injection to C, D and E Intervals

As in case 4, Figure 2.4-28 shows that leakage to the shallower interval during continuous CO_2 injection negatively impacts performance. The next section presents sensitivities on the corrective action, WAG.

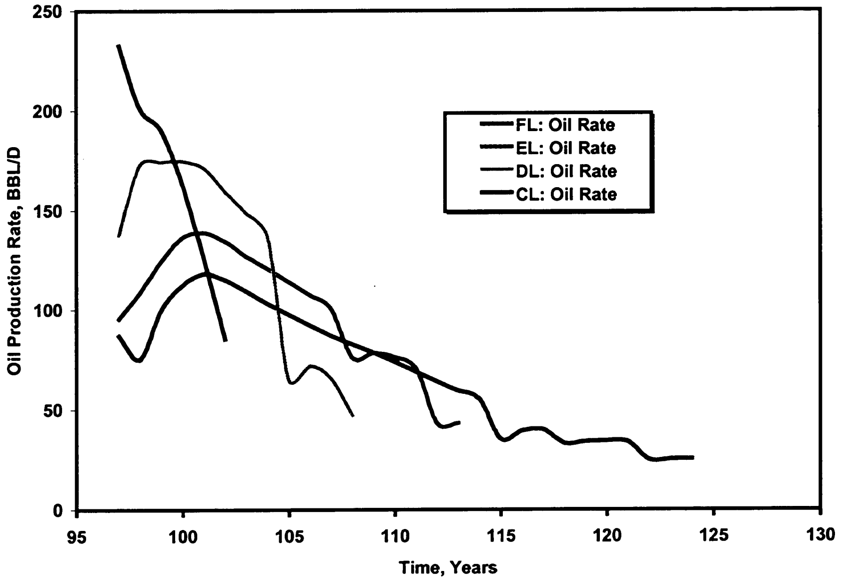

Figure 2.4-28. Case 5, recovery sensitivity to interval of injection, continuous CO_2..

Effect of WAG

Figure 2.4-29 presents recovery performance for WAG for the F-L and D-L injection interval sensitivities. Although increasing oil recovery, WAG reduces injectivity in the F-L injection scenario and impacted early performance negatively. WAG substantially improved the D-L scenario.

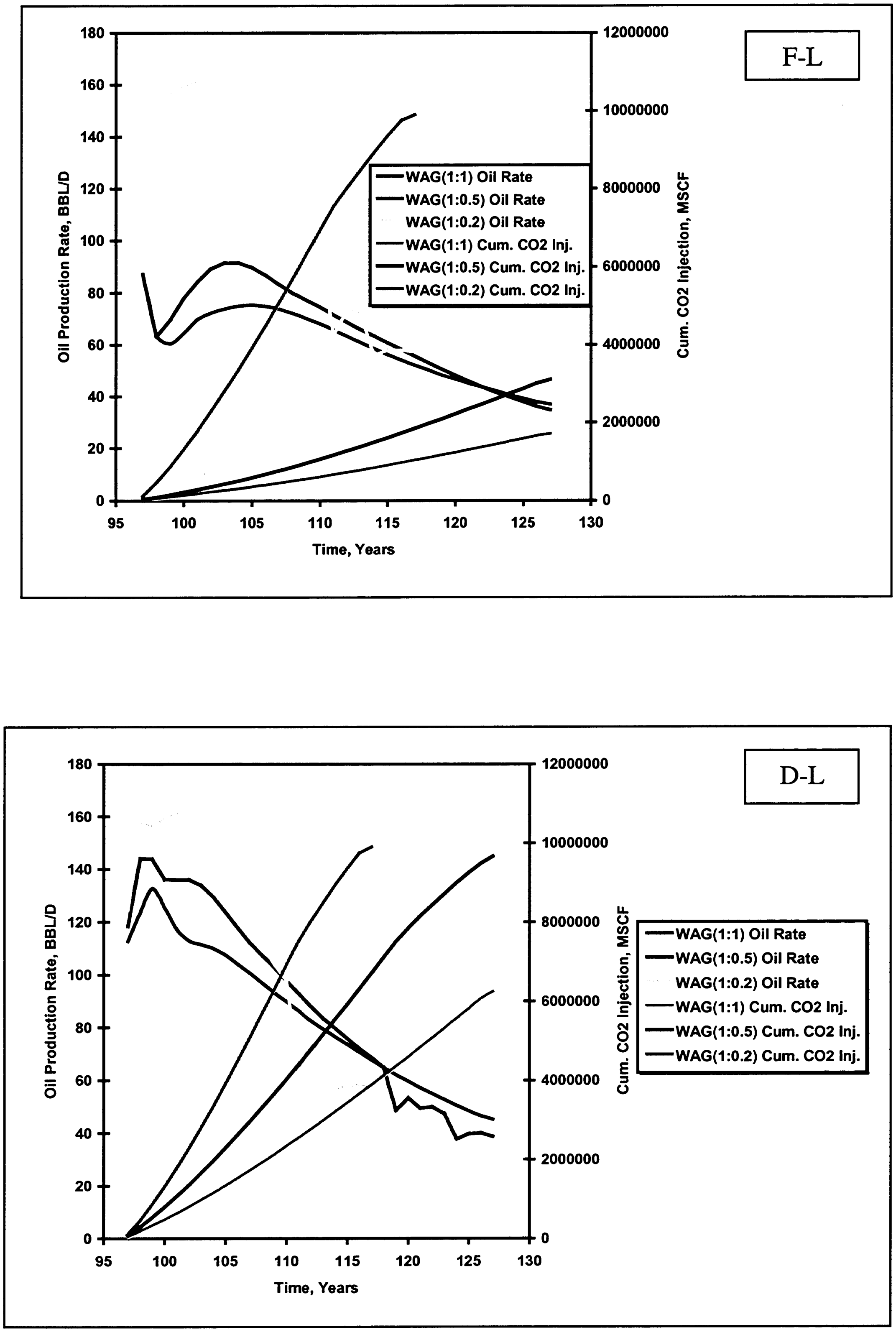

Figure 2.4-29. Effect of using WAG to improve conformance, F-L and D-L injection.

Fracture Half-Lengths of 25 Feet and 90 Feet

Figure 2.4-30 shows that longer fractures are marginally better for this pattern configuration compared to case 4, which showed higher sensitivity to fracture length.

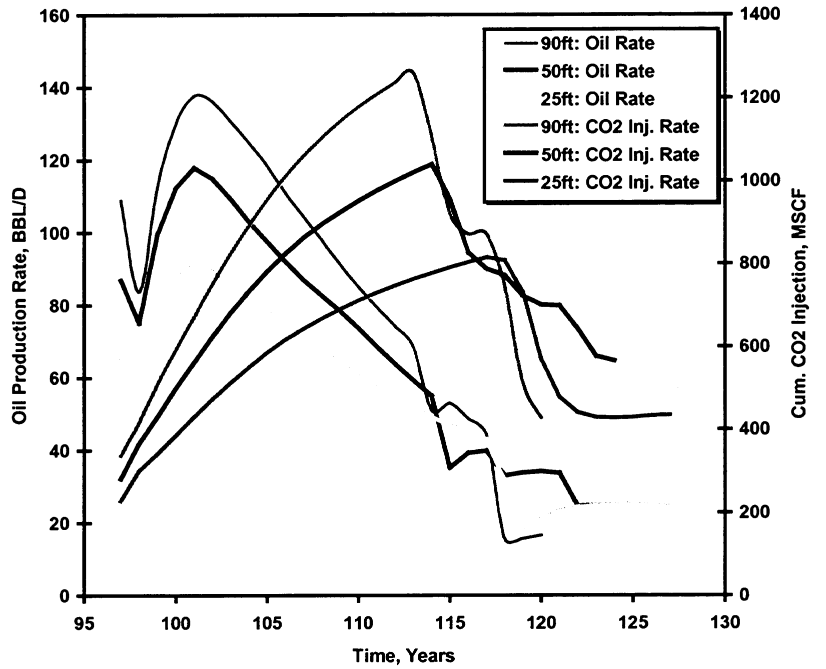

Figure 2.47-30. Effect of fracture length on recovery performance, F-L injection.

Oil Gravity Sensitivity

Reservoir oil properties impacts both processing rate and oil recovery as shown in Figure 2.4-31. However, results are less sensitive compared to case 4. The relative insensitivity to fracture length and oil gravity suggests that pattern configuration and geology dominate case 5 performance.

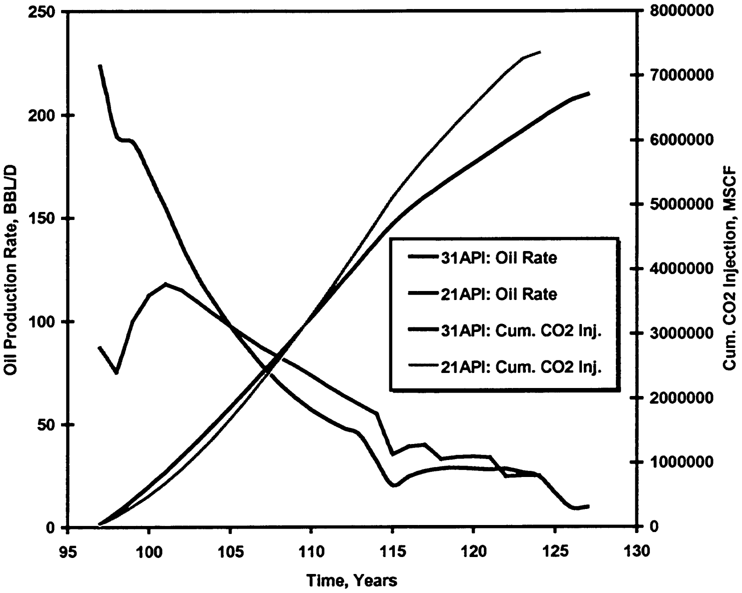

Figure 7-31. Effect of oil gravity on recovery performance, F-L and D-L injection.

Cases 11, 12 and 13

Cases 11-13 represent economically unlikely scenarios based upon the preliminary waterflood-infill simulations. We present these results together for the purpose of brevity. Table 2.4-16 presents an overview of the remaining sensitivities. Figure 2.4-32 shows the sensitivity of oil production to injection interval and Figure 2.4-33 shows the sensitivity of fracture half-length. The results are similar to those for cases 4 and 5.

Table 2.4-16. Overview of Cases 11, 12 and 13 recovery factors.

	Case 11		Case 12		Case13	
	Project Life Years	Recovery %OOIP	Project Life Years	Recovery %OOIP	Project Life Years	Recovery %OOIP
F-L	14	18	30	17	30	18
D-L	3.3	12	8.5	9.5	19	19
C-L	2	9	3.8	5	10	11
E-L	4.6	13	30	20	27	20
F-L 25' fracture half-length	9.5	14	22	11	30	16
F-L 90' fracture half-length	6.3	18	25	18	25	19

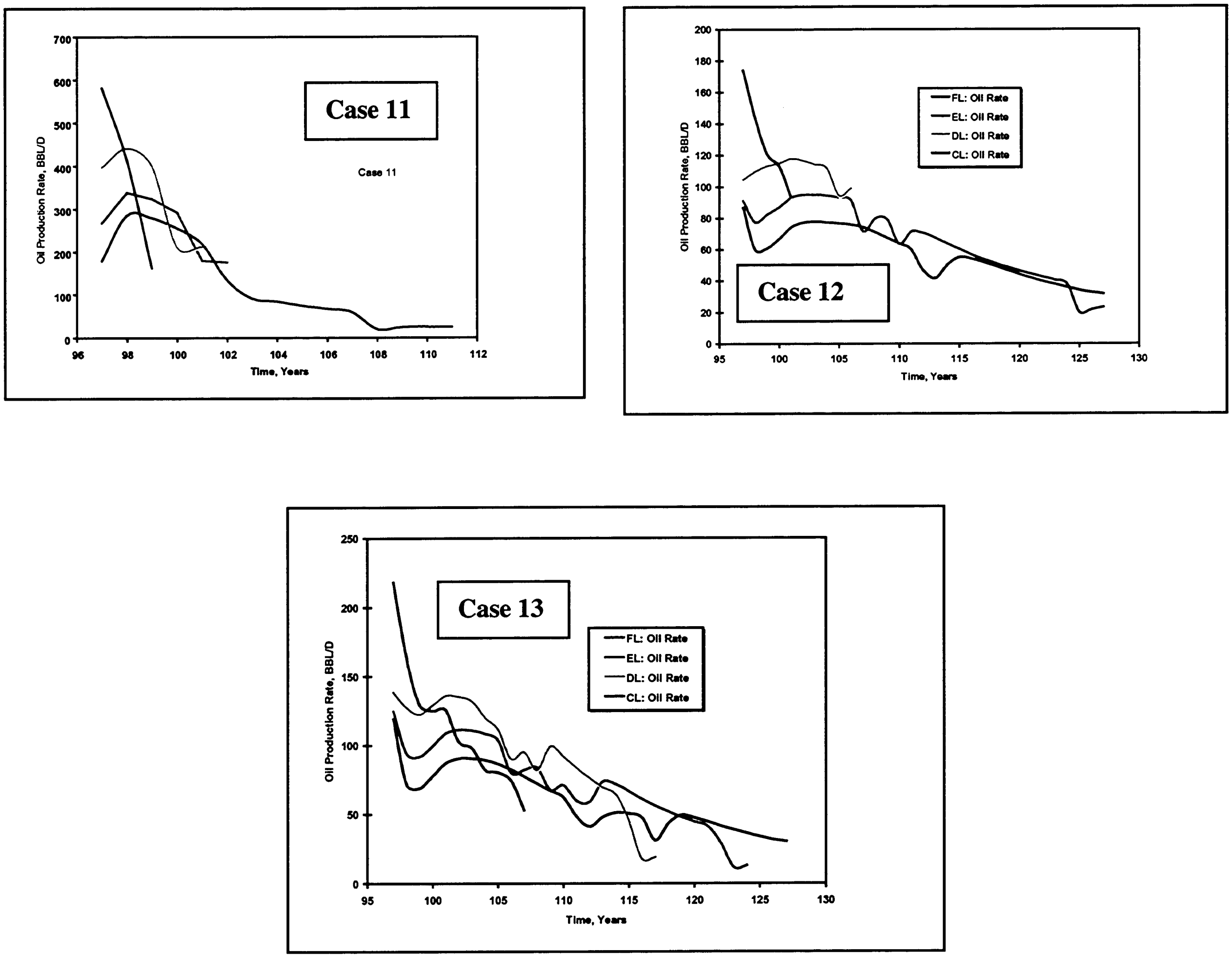

Figure 2.4-32. Oil recovery performance for various injection intervals, Cases 11, 12 and 13.

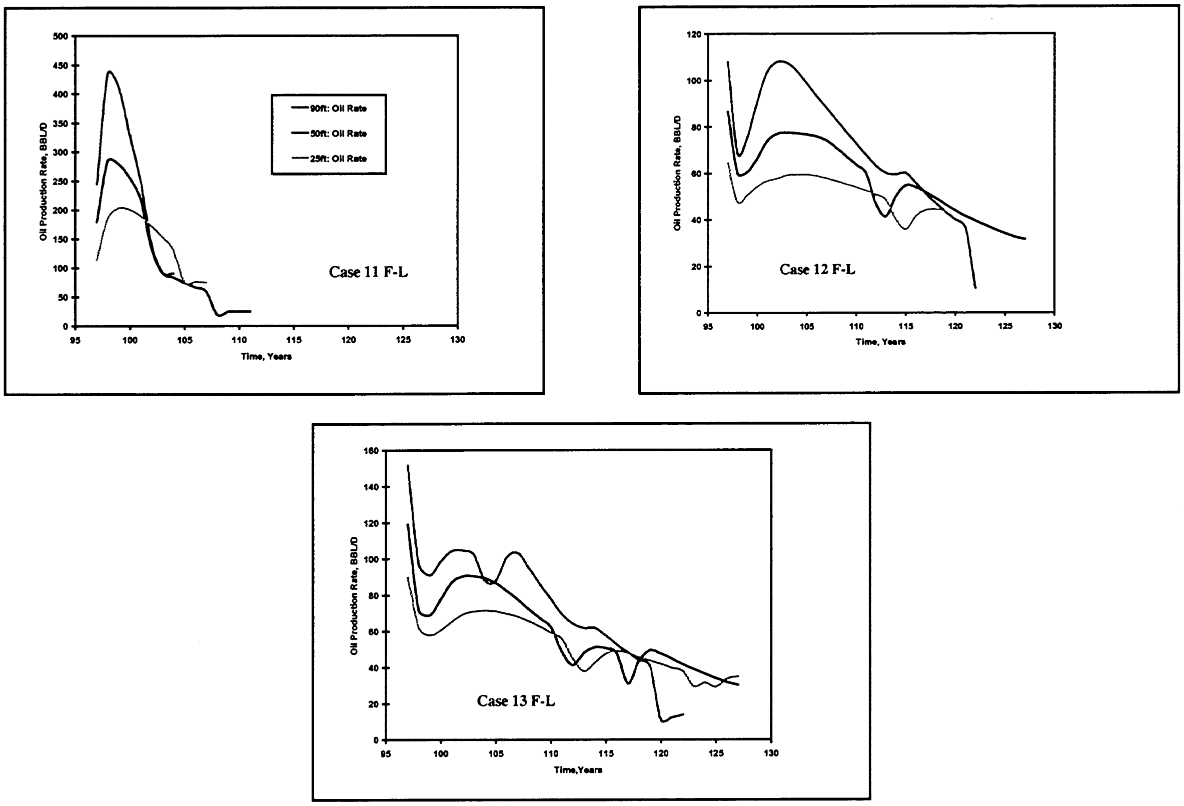

Figure 2.4-33. Oil recovery performance for different fracture half-lengths, Cases 11, 12 and 13.

REFERENCES

1. Tang, R. W., 1987. Infill Drilling as an Oil Recovery Process: Review of Engineering-Evaluation Methods and Case Histories. TM87000213, COFRC.
2. Xue, G. and others, 1994. A Comparative Technical and Economic Analysis of Waterflood Infill Drilling and CO_2 Flood in West Texas Carbonate Reservoirs. SPE 27642, presented at Permian Basin Oil and Gas Recovery Conference.
3. Spivak, A. and others, 1988. A Review of the LBOD Immiscible CO_2 Project, Tar Zone, Fault Block V, Wilmington Field, California. SPE 17407, California Regional Meeting, Long Beach.
4. Babson, E. C., 1989. A Review of Gas Injection Projects in California, SPE 18769, California Regional Meeting, Bakersfield.
5. Gould, T. L. and Munoz, M. A., 1982. An Analysis of Infill Drilling. SPE 11021, Annual Meeting, New Orleans.
6. Standing, M. B., 1977. Volumetric and Phase Behavior of Oil Field Hydrocarbon Systems.
7. Fong, W. S. and others, 1991, Lost Hills Diatomite CO_2 and Flue Gas EOR Potential – Final Report. TM91000809, COFRC.
8. Fong, W. S. and others, 1991. Lost Hills Diatomite CO_2 and Flue Gas EOR Potential – II. TM91000011, COFRC.
9. Simon, R., 1962. Lost Hills Properties of CO_2-Crude Oil Mixtures, TS14667-1, COFRC.
10. Fortner, J, 1989. Special Reservoir Fluid Study, Well 11-11A Lost Hills Field. RFL890338, Core Laboratories, Dallas.
11. Gael, B. T., 1990. Lost Hills Diatomite EOR Pilot Design Phase I – Final Report Volume I. TS90000050, COFRC.

SECTION 3.

TECHNOLOGY TRANSFER COMPLETED TO DATE

3.1. TECHNOLOGY TRANSFER

Aydin, A., 1997, Fault Control on Hydrocarbon Migration and Fluid Flow in Neogene Basins and Related Reservoirs of Central and Coastal California, USA: An Overview, in, Pollard, D. D. and Aydin, A. eds., Proceedings of the Rock Fracture Project Workshop, Stanford University, Stanford, CA.

Aydin, A., Dholakia, S. K., Antonellini, M., and Lore, J., 1996, Fault Control on Hydrocarbon Migration in Neogene Basins in Central and Coastal California, USA, Faulting, Fault Sealing and Fluid Flow in Hydrocarbon Reservoirs, Conference, University of Leeds.

Bilodeau, B. J. and Smith, S. C., 1997, Session Chairmen for Reservoir Characterization and Improving Recovery in Monterey-type Siliceous Shales, Pacific Section AAPG/SEPM Annual Convention, Bakersfield, CA.

Bilodeau, B. J., Smith, S. C., and Julander, D. R., 1997, Comprehensive Reservoir Characterization Using Open-Hole Wireline Logs, Core, and Downhole Video, Buena Vista Hills Field, California, Pacific Section AAPG/SEPM Annual Convention, Bakersfield, CA.

Britton, A.W., Smith, J. L., and Chapman, D., 1997, Continuous Permeability and Porosity Determinations in the Chevron 653Z-26B Well, Buena Vista Field, Kern County, CA, Pacific Section AAPG/SEPM Annual Convention, Bakersfield, CA.

Britton, A. W., Morea M. F., 1998, Acoustic Anisotropy Measurements in the Siliceous Shale, 653Z-26B Well, Buena Vista Hills Field, California, AAPG Annual Convention, Salt Lake City, UT.

Campagna, D. J., Amos, J. F., and Mamula, N., 1998, Influence of Structure, Reservoir Compartments, and Natural Fractures on Oil and Gas Production in the Southern San Joaquin Basin, California, AAPG Annual Convention, Salt Lake City, UT.

Carpenter, A. B., and Moore, T. S., 1997, Origin of Boron-Rich Pore Water in the Monterey Formation, San Joaquin Valley, CA, Pacific Section AAPG/SEPM Annual Convention, Bakersfield, CA.

Decker, D. and Bilodeau, B. J., 1997, Antrim Shale Resource and Reservoir Characterization as an Analog for Diffusion Controlled Gas Production from the Monterey Formation Pacific Section AAPG/SEPM Annual Convention, Bakersfield, CA.

Dholakia, S. K., 1995, An Integrative Study of Fractures and In Situ Stress in the Antelope Shale, Monterey Formation, Stanford Rock Fracture Project, Stanford University, Stanford, CA.

Dholakia, S. K., 1996, Outcrop to Reservoir: Importance of Faulting to Hydrocarbon Migration in the Monterey Formation, CA, Stanford Rock Fracture Project, Stanford University, Stanford, CA.

Dholakia, S. K., Aydin, A. Pollard, D. D., and Zoback, M. D., 1995, Relationship between Hydrocarbon Transport and Shearing Deformation in the Antelope Shale, Monterey Formation, San Joaquin Valley, California, GSA Annual Convention.

Dholakia, S. K., Aydin, A., Pollard, D. D., and Zoback, M. D., 1996, Hydrocarbon Transport and Shearing Processes in the Antelope Shale, Monterey Formation, San Joaquin Valley, California, AAPG Annual Convention San Diego, CA.

Dholakia, S. K., Aydin, A., Pollard, D. D., and Zoback, M. D., in press, Development of Fault-controlled Hydrocarbon Pathways in the Monterey Formation, California, AAPG Bulletin.

Dholakia, S. K., Aydin, A., Pollard, D. D., Zoback, M. D., and Barton, C., 1996, Integration of Geological and Borehole Image Data for the Interpretation of Conductive Structural Inhomogeneities in the Monterey Formation, California, Geological Application of Borehole Imaging Conference, Houston, TX.

Dholakia, S. K., Aydin, A, Pollard, D. D., Zoback, M. D., Barton, C., and Bilodeau, B. J., 1997, Integration of Surface Geology and Borehole Geophysics for Reservoir Characterization in the Monterey Siliceous Shales for the Purpose of Facilitating Improved Recovery Designs, Pacific Section AAPG/SEPM Annual Convention, Bakersfield, CA.

Dholakia, S. K., Aydin, A., Zoback, M. D., and Pollard, D. D., 1995, Plan for an Integrative Study of Fractures and In Situ Stress in the Antelope Shale, Monterey Formation, Stanford Rock & Borehole Geophysics Project Annual Report, Stanford University, Stanford, CA.

Dholakia, S. K., Lore, J., Brankman, C. M., and Roznovsky, T., 1996, Fault Control on Hydrocarbon Migration in the Monterey Formation, CA, Proceedings of the Stanford Rock Fracture Project Field Workshop, Stanford University, Stanford, CA.

Dholakia, S. K., Zoback, M. D., and Aydin, A., 1996, Stress State, Shearing Deformation and Implications for Hydrocarbon Transport in the Monterey Formation, California, Stanford Rock & Borehole Geophysics Project Annual Report, Stanford University, Stanford, CA.

Dholakia, S. K., Zoback, M. D., Barton, C., Aydin, A. and Pollard, D. D., Active Faults and Hydrocarbon Migration and Production in the Monterey Formation, California, Geophysics (in prep).

Fargo, D., 1997, Advanced Coring and Wellsite Handling Add Pizazz to Buena Vista Hills Core, Pacific Section AAPG/SEPM Annual Convention, Bakersfield, CA.

Fargo, D., 1997, Advanced Coring and Wellsite Case Study of Chevron/DOE Well 653Z-26B, Core Technology Meeting, Anchorage, AK.

Fargo, D., 1997, Case Study: Chevron/DOE Buena Vista Field Core Project, Technology Meeting, AERA Energy, Bakersfield, CA.

Jacobs, J. L., 1997, Characterization and Formation of En Echelon Fracture Arrays in the Monterey Formation, California. In, Pollard, D. D. and Aydin, A. eds., Proceedings of the Rock Fracture Project Workshop, Stanford University, Stanford, CA.

Kuuskraa, V., 1997, Incorporating Reservoir Characterization into Optimized Production of Siliceous Shales and Other Gas Bearing Shales, Pacific Section AAPG/SEPM Annual Convention, Bakersfield, CA.

Langan, R. T., 1997, Crosswell Reflection Imaging in the San Joaquin Valley: Buena Vista Hills, Society of Exploration Geophysicists, Development and Production Forum, Vail, CO.

Langan, R. T., 1997, Crosswell Seismology, Where We've Been and Where We're Going, Producers Executive Committee, Gas Research Institute, Chicago, IL.

Langan, R. T., 1997, Crosswell Imaging in West Texas and the San Joaquin Valley, Geosciences Department, Princeton University, Princeton, NJ.

Langan, R. T., Julander, D. R., Morea, M. F., Addington, C. M., and Lazaratos, S. K., 1998, Crosswell Seismic Imaging in the Buena Vista Hills, San Joaquin Valley: A Case Study, Annual International Meeting, Society of Exploration Geophysicists, New Orleans, LA.

Mamula, N., and Campagna, D. J., 1997, Determination of Reservoir Compartmentalization Using Mesoscopic Scale Fracture Analysis in the Buena Vista Hills Area of the Southern San Joaquin Valley, CA, Pacific Section AAPG/SEPM Annual Convention, Bakersfield, CA.

Morea, M. F., 1997, Advanced Reservoir Characterization in the Antelope Shale to Establish the Viability of CO_2 Enhanced Oil Recovery in California's Monterey Formation Siliceous Shales, Oil Technology and Gas Environmental Program Review Meeting, Houston, TX.

Morea, M. F., Zalan, T. A., and Jacobs, J. L., 1997, Buena Vista Hills Reservoir Characterization Study, Chevron/DOE Class III Reservoir Project. In, Advances in Reservoir Description Techniques as Applied to California Oil and Gas Fields Workshop, Pacific Section AAPG/SEPM Annual Convention, Bakersfield, CA.

Morea, M. F., 1998, Advanced Reservoir Characterization in the Antelope Shale to Establish the Viability of CO_2 Enhanced Oil Recovery in California's Monterey Formation Siliceous Shales, DOE/BC/14938-8, (DE98000484), 1997 Annual Report, National Petroleum Technology Office, US Department of Energy, Tulsa, OK.

Morea, M. F., Julander, D. R., Zalan, T. A., and Beeson, D. C., 1998, Advanced Reservoir Characterization of the Siliceous Shale, Buena Vista Hills, California, Pacific Section AAPG Convention, Ventura, CA.

Morea, M. F., Zalan, T. A., Julander, D. R., Beeson, D. C., and Britton, A. W., 1998, Advanced Reservoir Characterization of the Siliceous Shale, Buena Vista Hills, California: Integration of

Geological, Geochemical, and Petrophysical Data, AAPG Annual Convention, Salt Lake City, UT.

Morea, M. F., and Zalan, T. A., in press, Chapter 3, Buena Vista Hills Field, California, Borehole Imaging, DOE/AAPG Advanced Logging Volume, Tulsa, OK.

Morea, M. F., and Zalan, T. A., in press, Chapter 4, Buena Vista Hills Field, California, Advanced Logging Tools, DOE/AAPG Advanced Logging Volume, Tulsa, OK.

Tang, R. W., Zhou, D., Beeson, D. C., Ulrich, R. L., and Morea, M. F., 1998, Immiscible CO_2 Floods in Low Permeability Reservoirs, International Energy Agency, Collaborative Project on Enhanced Oil Recovery, 19th Workshop and Symposium, Carmel, CA.

Wang, G. Y., 1997, 3-D Attenuation Imaging, Annual International Meeting, Society of Exploration Geophysicists, Dallas, TX.

Wang, G. Y., Harris, J. M., Magalhaes, C. G., Julander, D. R., and Morea, M. F., 1998, Buena Vista Hills 3-D Attenuation and Velocity Tomography, Annual International Meeting, Society of Exploration Geophysicists, New Orleans, LA.

Zalan, T. A., Morea, M. F., Julander, D. R., and Denoo, S. A., 1998, Applying Integrated Formation Evaluation to Advanced Reservoir Characterization in California's Monterey Formation Siliceous Shales, DOE/BDM OK/ PTTC Class Project Logging Workshop, Advanced Applications of Wireline Logging for Improved Oil Recovery, Denver, CO.

Zalan, T. A., Morea, M. F., Julander, D. R., and Denoo, S. A., 1998, Integrated Formation Evaluation in California's Monterey Formation Siliceous Shales, Buena Vista Hills Field, California, 1998, SPE Western Regional Meeting, Gems Session, Bakersfield, CA.

Zalan, T. A., Morea, M. F., Julander, D. R., and Denoo, S. A., 1998, Applying Integrated Formation Evaluation to Advanced Reservoir Characterization in California's Monterey Formation Siliceous Shales, Society of Professional Well Log Analysts, 39th Annual Logging Symposium, Keystone, CO.

Zoback, M. D., Barton, C., Finkbeiner, T., and Dholakia, S. K., 1996, Evidence for Fluid Flow along Critically-Stressed Faults in Crystalline and Sedimentary Rock, Faulting, Fault Sealing and Fluid Flow in Hydrocarbon Reservoirs, Abstracts, Conference, University of Leeds.

Data from this project has been given to Southwest Research Institute, San Antonio, TX and included in their project:
Parra, J. O., Characterization of Fracture Reservoirs using Static and Dynamic Data: From Sonic and 3D Seismic to Permeability Distribution, BDM Subcontract No. G4S51-731, and Prime Contract No. DE-AC22-94PC91008.